UNIVERSITA' DEGLI STUDI DI GENOVA

SCUOLA POLITECNICA - DITEN

DIPARTIMENTO DI INGEGNERIA NAVALE, ELETTRICA, ELETTRONICA
E DELLE TELECOMUNICAZIONI

DOCTORAL THESIS IN
NAVAL ARCHITECTURE & MARINE ENGINEERING

UNCERTAINTY QUANTIFICATION IN CFD SHIP RESISTANCE EVALUATION

TUTORS:

PROF. DIEGO VILLA
C.V. (GM-GN) SERGIO ALLEGRO PONTANI

AUTHOR:

C.F. (GM-GN) SIMONE BOZZO

This page is intentionally left blank

"Alla mia Famiglia, per il tempo sottrattoLe
ed in memoria della Nonna Maria"

This page is intentionally left blank

Summary

Abstract

Ships are the largest moving devices ever created by humans. In the design phase, it is important to define the main characteristic for a ship to run; one of the key features that must be addresses is the power estimation to reach the design speed. Over the years, different attempts to define this value can be listed, once the ships moved from both the muscular and the wind energy to a mechanical propulsion plant. In this scenario, based on Froude's findings about the similarity between a ship and its scale model, the Experimental Fluid Dynamics (EFD) began its activity in the second half of the XIX century. By that time, the need for a constantly updated and freely accessible guidance grew up in importance among the scientific community. These requirements have been addressed by the International Towing Tank Conference (ITTC). From the second half of the XX century, a new resource became available in order to replicate the EFD experiences; indeed, based on the computing available sources, the Computational Fluid Dynamics (CFD) began its estimations. Both the EFD and CFD approaches, accounts for uncertainties connected with the results obtained. The Uncertainty Assessment (UA) issue began in the last couple of decades of the XX century. With the respect to the CFD, the uncertainty assessment can be estimated based on the following two main phases: the Verification and the Validation.

With the respect to a towing tank test, in current research a single numerical set-up has been defined to compare the numerical results with the experimental one with the attempt to define the accuracy for a CFD calculation compared with an EFD result. In order to generate a database where all the results can be stored, 142 simulations have run for 22 different hulls tested at different speeds. The results obtained have been used to define some statistical correlation among the differences recorded and the other input parameters like the hydrodynamic coefficients and the main dimension for the models.

With the respect to the UA, two different hulls have been tested at different speeds and configuration for a total number 72 different simulations with the attempt to test the literature available approaches to get the numerical uncertainty assessment. These approaches have been divided into two families, as follows: three and multiple solutions (at least four) families.

Finally, based on the findings from current research, the possible answer to the question “how precise is a CFD resistance calculation” can be described as follows: in the towing tank test, if a blind CFD simulation has run, a difference of below 5% can be experienced with a confidence on 80%.

Keyword: CFD, EFD, Uncertainty Assessment, Verification&Validation.

1 Introduction

Earth is the lonely planet, according to the current state of art, covered by 71% water [1] and continents represent the remaining part, which surface is approximately $148 \cdot 10^6$ km^2 [2]. As reported by Camprubí et al. [3], who cite Oparin [4] and Haldane hypothesis dated back in 1920s, the first building block arose from the "primordial soup", and more in details, life could appear within the range from $800 \cdot 10^6$ to $200 \cdot 10^6$ years ago, as reported by Pearce et al. [5]. From that time onward, additional time elapsed before the arrival of the first *Homo sapiens*, who has been estimated at approximately 315 thousand years ago, as reported by Hublin et al. [6]. Over years many inventions have been performed and many other probably follow.

Since the beginning, the mankind has to phase with the water. Over the years, humankind started to understand the advantages offered by this kind of resource, and started to design wooden floating object to navigate on it.

At the beginning, muscular power represented the only available kind of energy to move these objects which belong to the raft or dugout canoe families; indeed, the oldest one find is from the Pesse swamp in the Netherlands, from around 8265 ± 275 years before present, as reported by Osipowicz [7].

Later on, humans implemented a way to join the power of the wind through sails with the first floating rafts. Some evidence of this ancient Egyptians technology was found on iconography and trade patterns dating back to the Naqada II Period (3500-3200 years before common era), as reported by Mark [8]. That period of time can be considered as the beginning for the era of sailing boat, and by that time many several configurations have been designed. This kind of boat led the people to sail all over the oceans and being forced to face with both the storms and the flat calm, moving amid myths and legends. In order to achieve these results, the knowledge about the physical description for a ship sailing and floating on rough waters has been investigated by several people, nowadays identify as scientists. As reported by Bettini [9], shipbuilding processes were based on three main contributions, until 1700. The first one is represented by the Archimedes' principle (Syracuse, 287÷212 years BC), which postulates that an object immersed in a fluid obtain an upward thrust (buoyancy) equal to the weight of the fluid where it lays in, as reported by Mohazzabi [10]. The second contribution is given by Stevin’s law (Bruges, 1548÷1620), which defines the connection among pressure (P) and depth (h) for a fluid, as reported by Kontomaris et al. [11] and displayed in equation (1):

$$P = \rho \cdot g \cdot h \left[\frac{N}{m^2}\right] \tag{1}$$

where, $\rho\ [kg/m^3]$ and $g\ [m/s^2]$ represents the liquid density and the acceleration of gravity, respectively. Hence, considering an elementary unity area, the force acting on it is connected with the weight for the above water column. Finally, the third contribution is represented by the Pascal’s law (Clermont, 1623 ÷1662), which defines the behaviour of pressure in a fluid and it represents an extension for Stevin’s law.

Across the XVI and XVII centuries, a framework based on the influences played by Humanism and the Reformation on typographic printing, the evolution for the technical drawing and the perspective led to the definition of the modern naval architecture [9]. By that time, a scientific approach started to characterize all the activities; at the beginning the main features to phase with can be identify with the materials, hull deformation, goods storage and firefighting systems. A rule of thumb for the sailors can be listed as follows: “innovation among tradition”; indeed, at that time it sometimes occurred that ships designed with great attention to detail would display unfortunate seakeeping performances. Moreover, based on this sort of “tradition”, the evaluation for the resistance for the ship exerted a lower level of interest and the hull shapes follow. It was only in the second half of the XIX century when that the scenario changes completely.

At the beginning of XVIII century, a new type of energy was found; indeed, Newcomen realized in 1712 a steam engine enabling mines to pump water [12], and later on, in 1763, Watt improved Newcomen’s engine [13]. Being this new engine suitable for common industrial uses, the “age of steam” was directly connected to the new technology, as reported by Landes [14]. This new age is commonly called as The First Industrial Era (RI1), as reported by Sharma et al. [15], ranging from 1750-1760 to 1820-1840, as reported by Mohajan [16]. With the respect to the naval fields, in this scenario ships changed their propulsion plants shifting form the “sail propulsion” to the mechanical one. A landmark for this shifting in propulsion plant can be dated back to 15 July 1783; indeed, Francois Dorothèe, Comte de Jouffroy D’Abbans, tested a steam boat 46 meters long, at Lyon on the Saône, as reported by Chatterton [17] and the name for this boat was “*Pyroscaphe*” [18]. In

1807, Fulton set in motion the paddle wheels named Clermont, the first ship being considered the first commercial example of ship.

This new kind of propulsion changed the design for the ship, although at the beginning of this new shipbuilding phase both the sails and the combustion engine were installed on board. Indeed, the interest for the best hull-shape with the respect to the forward speed for a ship, started to become one driver issue in the design phase. This period was full of technological innovation, besides the mechanical energy, other improvements like the screw propeller and new materials (like iron and steel) to replace wood were tested and implemented. All these innovations, led designers to phase with the hydrodynamical integration among engine, propeller and hull shape not separately, but jointly. As reported by Oosterveld [19], the development for the screw propeller got underway approximately in 1800; within roughly 60 years, screw propellers were installed on nearly all seagoing ships, replacing the paddle wheels system. Moreover, the availability of internal combustion engine rather than the only external one, led to the MS Selandia, the first ship powered with a diesel motor in 1912, as reported by Pedersen [20]; by that time several other examples followed. This technological scenario is commonly called as the Second Revolution of industry (RI2), and can be related to the invention of the production of electricity in the 19th century. More in details, considering Landes work [14], this historical period developed from about 1870 to the beginning of the first World War in 1914.

With the respect to the naval field, the engineering solution to the evaluation for the performances in the design phase resulted in the implementation of an experimental procedure to derive the results obtained from a scaled ship model to the ship one; additionally, for this procedure to work, a towing tank facility is required. Berd performed the first attempt in 1756 working with ship models in a 10 meters towing tank; in 1775, D’Alambert, Bossu and Condorcet performed the first systematical tests in a gravitational type towing tank, as reported by Gotman [21]. Subsequently, further experiments were conducted; however, Froude’s expertise was required to define an experimental procedure able to evaluate the resistance for a ship based on its model scale hull. In 1859, Swan and Raven, two wooden model hulls, were tested on Dart River for three different scales by Froude; this experience led Froude to define the general law for the similitude; indeed, when the model is tested at the corresponding speed at two different scales, a similar wave pattern is registered. Based on this result, in 1860 Froude succeeded in persuading the British Admiralty to build the first towing tank, which name was Admiralty Experiment Works (AEW) and placed in Torquay, as reported by Boccalatte [22]. Therefore, this new type of facility overcame the limitation for the gravitational towing tank; indeed, the presence of a carriage to pull the model was installed over a pool, which dimensions were 90m length, 12m width and 3.5m depth at the centerline of the tank

[19]. This framework can be considered as the forerunner of the towing tanks which are used today; by that time, several towing tanks have been built [19]. In the 1930s, several Institutions were fully operational and they used their own procedure to work. At Hamburg in 1932, the international Hydro-mechanical Congress was held; following the congress, the contributors agreed to plan a series of meetings, in alternate years, under the name of "International Conference of Ship Tank Superintendents"; therefore, this can be considered as the origin for the International Towing Tank Conference (ITTC), as reported by the ITTC's website [23] and the main idea for this conference was to define a common mutually agreed procedure along with a way to present the results. The first conference dates back to 1933 in The Hague, and others followed, as listed below: London (1934) Paris (1935) and Berlin (1937); after the interruption for the Second World War, the conference was resumed and the fifth one was held in London in 1948. By this last one conference, the "Standing Committee" was established to give continuity between the conferences; it was in the 1954, when the name for the conference shifted from International Conference of Ship Tank Superintendents into International Towing Tank Conference. Nowadays, it is possible to access to the procedures, as they are available on the ITTC website [24]; moreover, they are constantly updated and freely accessible.

Over the years, different types of facilities have been developed. Nowadays, as reported by ITTC facilities list [25], it is possible to perform experimental tests using the main following infrastructures: towing tank, manoeuvring basin, offshore basin, ice tank, cavitation tunnel, ship simulator wind tunnel, rotating arm facility, circulating water channel, shallow water facility; for the sake of completeness, all the towing tanks on ITTC facilities are listed in Table 1:

Across the 1940s and 1950s several changes have been registered. Historically, it is possible to assess across the 1950s the beginning for the Third Industrial Revolution (RI3), as reported by Mohajan [16], and in his view, it continues until 2021 (research edition period).
This period can be defined even as "The Digital Revolution" because of the shifting from the mechanical and analogue electronic to the digital one. Indeed, changes in education, Information Communication Technology (ICT) and financial can be considered as the most important sectors for the RI3, as reported by Szeszák [26]. Moreover, it is worth nothing that in this period the space exploration was open and the mankind changes its habits, indeed the transport exhibit a great improvement. It is reasonable to assume that the RI3 maybe directly connected with the innovative technology represented by the computer. Indeed, Copeland et al. [27] attribute the first working program-controlled digital computer in 1941 to Konrad Zuse; this machine was later called "Z3". From this specific point onward, several additional technological advances were registered; for instance, Abramovitch [28] reports that in 1956 International Business Machines Corporation (IBM)

brought the first disk to market; in 1957 the first computer controlled by a keyboard and used by one person was designed by IBM, as reported by Mohajan [16].

Table 1: towing tank facilities from ITTC website [25], listed by alphabetical order.

Facility	Nation	Facility	Nation	Facility	Nation
Australian Maritime College	Australia	Kyushu University - Research Institute for Applied Mechanics	Japan	Seoul National University	Korea
Bulgarian Ship Hydrodynamics Centre	Bulgaria	Marine Design and Research Institute of China (MARIC)	China	Shanghai Ship and Shipping Research Institute (SSSRI)	China
Canal de Experiencias Hidroninámicas de El Pardo (CEHIPAR)	Spain	Maritime Advanced Research Centre (CTO S.A.)	Poland	Sharif University of Technology	Iran
Changwon National University	Korea	Maritime Research Instutute Netherlands (MARIN)	The Netherlands	SINTEF Ocean (formerly MARINTEK)	Norway
China Ship Scientific Research Centre (CSSRC)	China	Mitsubishi Heavy Industries, Ltd.	Japan	Tallinn University of Technology	Estonia
CNR-INM	Italy	National Iranian Marine Laboratory (NIMALA)	Iran	Technische Universität Berlin	Germany
École Centrale de Nantes	France	National Maritime Research Institute	Japan	TSUNEISHI AKISHIMA LABORATORY Co., Ltd.	Japan
Escuela Técnica Superior de Ingenieros Navales (ETSIN)	Spain	National Research Council of Canada	Canada	United States Coast Guard Academy	USA
FORCE Technology	Denmark	National Technical University of Athens	Greece	Universidad Austral de Chile	Chile
Gdansk University of Technology	Poland	Naval Science and Technological Laboratory	India	University College London	United Kingdom
Hamburgische Schiffbau-Versuchsanstalt GmbH (HSVA)	Germany	Naval Surface Warfare Center, Carderock Division	USA	University of California, Berkeley	USA
Hanwha Ocean	Korea	NTNU - Norwegian University of Science and Technology	Norway	University of Galati	Romania
Hyundai Heavy Industries Co. Ltd.	Korea	Osaka Metropolitan University	Japan	University of Michigan	USA
IIHR-Hydroscience & Engineering	USA	Osaka University	Japan	University of Southampton	United Kingdom
Imabari Ship Model Basin	Japan	QinetiQ	United Kingdom	University of Strathclyde	United Kingdom
Institut Teknologi Sepuluh Nopember	Indonesia	Research Institute of Medium & Small Shipbuilding (RIMS)	Korea	University of Tokyo	Japan
Instituto de Pesquisas Tecnológicas do Estado de São Paulo – IPT	Brazil	RISE	Sweden	University of Zagreb, Faculty of Mechanical Engineering and Naval Architecture	Croatia
Japan Marine United Corporation	Japan	Samsung Heavy Industries	Korea	Zhejiang Ocean University	China
Korea Research Institute of Ships and Ocean Engineering (KRISO, formerly MOERI)	Korea	Schiffbau Versuchsanstalt Potsdam GmbH	Germany		
Krylov State Research Centre	Russia	Schiffbautechnische Versuchsanstalt in Wien	Austria		

Furthermore, by that time, computing power had improved, and it continues to expand to this day; this increase of computer facilities led the floor open to the development of numerical methods. These methods began to influence the hydrodynamical research performed by towing tank in 1970s and new formerly impenetrable issues became affordable, as reported by Oosterveld [19]; indeed, in 1975 Michell's theory was applied to predict the resistance of water for a ship, as reported by Gotman

[21]. Therefore, adhering to Ansys guide [29], Computational Fluid Dynamics (CFD), which can be considered that science able to predicts fluid behavior by solving equations numerically on computers, registered the first results in this period.

With the respect to the results, the scientific debate on the precision of a CFD calculation is still nowadays opens. Over the years, several computational codes and theories have become fully applicable in order to find an answer to this question "how precise is a CFD calculations?"; to achieve this, three different kinds of approaches can be listed, as follows: *Single Participant To One* (SPTO), *Multiple Participants To One* (MPTO) and *Single Participant To Multiple* (SPTM). More in details, considering SPTO, a single CFD expert performs a CFD study for a single case without comparing and sharing his result with nobody else; while, in MPTO, several participants submitted their works, with the attempt to assess the required issues for the case and later on they share their results among each other participants. Finally, in SPTM, one participant performs several simulations with the same parametrical numerical set-up to several cases. The MTPO approach is the one commonly implemented by the CFD workshops. The typical configuration for a workshop is made by four steps, as follows: firstly, the organizers generate the repository where the participants can find the case (or cases) description, the hull geometries and the data submission format, secondly the participants perform their simulations with their respective best practice, thirdly the participants submit their results, and finally, all the results are discussed and compared to find trends and general conclusions. For the sake of completeness, this kind of workshops are usually blind, meaning that the experimental results are shared only after the submission of the works. With the respect to viscous flow, several MPTO workshops have been registered from the beginning of CFD. The first international workshop on numerical prediction of ship viscous flow took place in Gothenburg in 1980 (1G1980), as reported by Larsson et al. [31]. The target for the workshop consisted in the boundary layers for the ship; 17 groups submitted their works for two model ship, as reported by Wilson [30]. At that time, integral methods were the most used and performed well for a two-dimensional case but issues arise when cross-flow velocity profile exists, as reported by Stern et al. [32] who cited Von Kerczek [33]; indeed, the methods fail completely the evaluation for the flow into the intake and at the stern [30]. Ten years later, in 1990, a second workshop took place again in Gothenburg (2G1990), and a shifting to RANS methods had been registered. 19 different research groups submitted their works with the respect to the HSVA Tanker and "mystery" tanker, as reported by Bekhit [34]. Most of the methods were able to reproduce the gross features [30]. In 1994, another workshop took place in Tokyo (3T1994). This time, the double model approximation disappeared and the free surface was implemented. The lack of an accurate discretization for the grid across the free surface led to a dumping in the numerical results, when compared with the experimental data for the test case, which was the Serie 60 profile

[30]. In 2000, the fourth workshop took place in Gothenburg (4G2000). Modern hull shapes have been implemented as test cases; indeed, a fast twin screw propeller ship from David Taylor Model Basin (identify as DTMB 5415), a crude carrier from Korea Research Institute of Ships and Ocean Engineering (KRISO, and identify as Korean Very Large Crude Carrier 2, KVLCC2) and a Container Ship from KRISO (identify as KCS) were submitted to the participants, whose total number was 20 and use 16 different software [30]. For the first time both the self-propulsion and the Verification and Validation (V&V) procedures were introduced [31]. In 2005, the fifth workshop took place in Tokyo (5T2005). The hulls used for the workshop were the same of the fourth one, but other tasks were required to the participants as follows: self-propulsion at propulsion point and static drift. The number of participants was equal to 20 groups and the results displayed differences, when compared with the one from 4G2000. Indeed, for the KVLCC the force prediction exhibited a higher dispersion, but a better representation for the wake was obtained; with the respect to the free surface, a well predicted wave pattern was obtained, even because a higher refinement for the grids was registered [34]. Another workshop, the sixth one, took place in Gothenburg in 2010 (6G2010). The hulls employed were DTMB 5415, KCS, and KVLCC2; while, the total number of participants was 33 groups. The following different computations were required: local flow at fixed condition, resistance, sinkage and trim, self-propulsion, heave and pitch in waves, forward speed diffraction and free roll decay [31]. With the respect to the ship resistance, the results highlighted that the mean error was practically zero, and comparing the mean standard deviation for 6G2010 was reduce by half, if compared with 4G2000 [31]. In 2015, the seventh workshop took place in Tokyo (7T2015). In this workshop two new hulls have been introduced: the Japan Bulk Carrier (JBC) and the Office of Naval Research (ONR) model Tumblehome 5613 (ONRT), preliminary design of a modern surface combatant ship. 88 participants submitted their works for the JBC case without and with the Energy Saving Device (ESD), as reported by Bekhit [34]; moreover, the participants had to submitted their work with the Verification and Validation procedures. With the respect to the resistance accuracy, it can be observed that the systematic error lays within the experimental accuracy range for all the results collected in 7T2015, which is marginally better than the 6G2010, but the standard deviation for computations is around 2%, which is worse than deviation is worse 6G2010. Moreover, a greater scatter was observed in the results for 7T2015 when compared with 6G2010, the same accuracy limit of 4% is reached with 10M or 3M cells for 7T2015 and 6G2010, respectively; finally, a turbulence model more complex than the two-equations one doesn't exhibit any advantage. Even though it doesn't represent a workshop, Jasak et al. [35] demonstrate in 2018 the opportunity to use a high-fidelity method to predict the characteristics at full-scale for two different hulls, a general cargo and a car carrier ship, respectively. As reported by Ratten [36], the digital technologies exhibited a rapid

advance during COVID-19. Indeed, after the pandemic period, these new technologies have opened the door to new types of events, such as hybrid workshops, held both in person and via remote connections. In 2024, the Lucy Ashton blind full-scale CFD workshop was held in 2024 (8V2024) on the resistance prediction, as reported by Lopes for the Lucy Ashton ship [37]. 40 participants submitted their work for the following three different sets: grid refinement study, full-scale simulations varying the speed and model-scale simulation varying the scale at a constant Froude's number. Results for the full-scale test exhibit a decrease in the difference as the Froude's number was increased, with a median absolute deviation not higher than 2.3%. The 8V2024 first set presented the full-scale comparison along with a detailed numerical uncertainty assessment. The outputs highlight the possibility of outliers; these could be related to post-processing or typographical errors and could impact the statistical measurements, represented by the mean and the standard deviation. The last workshop took recently place in Wageningen in November 2025 (9W2025) [37]. A common feature of all previous conferences is the intent to assess the state-of-the-art CFD methods applied on well specified test cases. The ship used as test cases were JBC, KCS, ONRT, JoRes1 Tanker (full scale), and Nawigator XXI (for the underwater radiated sound), which last ship was previously presented by ITTC [38]. The last two cases show the tendency to investigate the ability to CFD to predict in full-scale model and the underwater radiated sound. Results aren't still available. From 1G1980 to 9W2025, 45 years have passed. Across this period, CFD replicate the towing tank experiences and evaluate the uncertainty; in last years, the CFD is moving to the full-scale to replicate the full-scale experiences.

In addition to the findings for resistance, another issue has to be considered. When an experimental measure takes place, an uncertainty for the quantity measured occurs. The experimental fluid dynamics and the computational one do not constitute an exception. Even for this issue, sensitivity to the topic has evolved over the years. It was Galileo who first exposed considerations on the random errors on astronomic observations in 1632 [39]. Later on, Gauss in 1809 defined a procedure to account for the errors [40], which later on was identify as "Gaussian curve" [41]. While, in 1875, through the "Convention du Mètre", the ground for the international collaborations had opened; indeed, in the same year this entity created the "*Bureau International des Poids and Measures*" (BIPM), established the "*Conférence Générale des Poids et Mesures*" (CGPM) and the "*Comité International des Poids et Mesures*" (CIPM), as reported by Débarbat [42] and Fanton [43]. Later on, across the XX century, new theories about error formulations have been assessed. It was in 1977 when CIPM asked BIPM to phase with the absence of international consensus on the expression for the uncertainty in measurements [44]. In 1993, seven international organizations presented the "*Guide to the expression of uncertainty in measurement*" (GUM) [45]. With the respect to the naval architecture field, two kinds of uncertainty can be listed: the experimental and the numerical ones. Among the ITTC procedures [24], some of them addresses the issues related to these two kinds of uncertainties. More in details, the experimental ones are consistent with the GUM guide; while, for the numerical uncertainty assessment, the procedure has been revised in 2024 [46] and accounts for the main used procedures to assess it. With respect to numerical uncertainty, the evaluation of the calculation's confidence level is performed through two different phases, respectively defined as Verification and Validation, usually referred to as V&V. When dealing with the verification, the mathematical correctness for the computational model is tested while, in validation phase, the modelling errors are evaluated among the numerical results and the experimental data; finally, Uncertainty Assessment (UA) evaluates all the sources of uncertainties arising from the numerical calculation versus the experimental one. Therefore, a recent definition for this issue can be represented by the acronym of VVUA, which stands for Verification, Validation, and Uncertainty Assessment. Different kinds of theorical approaches can be implemented to assess the numerical uncertainty, but each one of them accounts for the results in its proper way, for the subsequent use of the Richardson extrapolation [47]. Indeed, after 1986, when The American Society of Mechanical Engineers (ASME) Journal of Fluids Engineering [48] published a declaration reporting the need for the evaluation of the numerical uncertainty, as reported by Groves [49], the international scenario has changed leading the researchers to define a method to assess this kind of uncertainty. Some of the main approaches commonly adopted by literature can be chronologically listed as follows: in 2001 Stern et al. [50], in 2008 Celik et al. [51], in 2010 Xing and Stern [52] and in 2014 Eça and Hoekstra [53].

How precise a CFD calculation is, even today, still something not entirely clear. Over the years, several workshops have taken place and a general idea of the precision for a CFD calculation has been obtained for few hulls. Indeed, by considering the CFD viscous resistance workshop, the following conclusions arise. Even if a numerical dumping affected the results, it takes 14 years form 1G1980 to get the free surface considered into a calculation for 3T1994; indeed, at that time, the computational sources weren't so powerful to get a detailed description for the free surface. By that workshop, only eight hulls have been used as benchmark cases to run the comparisons among EFD and CFD; indeed, the hulls considered are listed as follows: DTMB 5415, KVLCC2, KCS, JBC, Lucy Ashton (full scale), ONRT, JoRes1 Tanker (full scale) and Nawigator XXI (for the underwater radiated sound). With the respect to the resistance prediction, it possible to assess the differences with the EFD results through a percentual value represented by E_{MEAN}, evaluated through equation (2):

$$E_{MEAN} = \frac{D - S_{MEAN}}{D} \; [\%] \tag{2}$$

where, D represents the measured data value and S_{MEAN} the mean among the numerical results. The results obtained by the MPTO workshops are summarized in Table 2 for the resistance evaluation; number between brackets represent the number of available data to assess the representative values.

Table 2: MPTO workshops, results for the CFD resistance evaluation.

Hull	Configuration	F_r	E_{MEAN} [%] 2005 (1)	2010 (1)	2015 (2) (3)	2024 (4)
KVLCC2	Fixed	-	0.0 (13)	-1.7 (5)	-	-
	Free	-	-	-2.1 (1)	-	-
KCS	Fixed	$F_r = 0.260$	-1.1 (11)	-1.3 (8)	-	-
	Free	$F_r = 0.110\sim0.280$	-	-0.2 (27)	$F_r = 0.108$: -0.4 (12)	-
					$F_r = 0.152$: 0.3 (10)	
					$F_r = 0.195$: 1.3 (10)	
					$F_r = 0.227$: 0.5 (12)	
					$F_r = 0.260$: -0.2 (10)	
					$F_r = 0.282$: 0.7(11)	
DTMB 5415	Fixed	-	1.6 (11)	2.5 (5)	-	-
	Free	$F_r = 0.138$	-	-2.8(5)	-	-
		$F_r = 0.280$	-1.9 (1)	0.1 (6)		
		$F_r = 0.410$	-	4.3 (5)		
JBC	Free w/o ESD	-	-	-	1.0 (22)	-
	Free with ESD	-	-	-	1.0 (20)	-
Lucy Ashtown	Set 1 (5)	-	-	-	-	2.3 (40)

(1) Data form [31];
(2) Data form KCS_2015, Tokyo 2015 A Workshop on CFD in Ship Hydrodynamics [54];
(3) Data form JBC_2015, Tokyo 2015 A Workshop on CFD in Ship Hydrodynamics [54];
(4) Data form Lucy Ashtown [37];
(5) Maximum median absolute deviation.

Considering the standard deviation, σ, expressed as a percentage of measured data value D, it is possible to display the results as reported in Table 3; number between brackets represent the number of available data to assess the representative values.

Table 3: MPTO workshops, results for the CFD resistance evaluation standard deviation.

Hull	Configuration	F_r	σ [%] 2005 (1)	2010 (1)	2015 (2) (3)	2024
KVLCC2	Fixed	-	6.2 (13)	1.3 (5)	-	-
	Free	-	-	- (1)	-	-
KCS	Fixed	$F_r = 0.260$	4.2 (11)	1.2 (8)	-	-
	Free	$F_r = 0.110\sim0.280$	-	1.2 (27)	$F_r = 0.108$: 4.2 (12)	-
					$F_r = 0.152$: 3.1 (10)	
					$F_r = 0.195$: 2.4 (10)	
					$F_r = 0.227$: 2.7 (12)	
					$F_r = 0.260$: 1.5 (10)	
					$F_r = 0.282$: 2.9 (11)	
DTMB 5415	Fixed	-	5.3 (11)	3.8 (5)	-	-
	Free	$F_r = 0.138$	-	4.4 (5)	-	-
		$F_r = 0.280$	- (1)	2.1 (6)	-	-
		$F_r = 0.410$	-	1.4 (5)	-	-
JBC	Free w/o ESD	-	-	-	2.4 (22)	-
	Free with ESD	-	-	-	2.0 (20)	-
Lucy Ashtown	Set 1	-	-	-	-	-

(1) Data form [31];
(2) Data form KCS_2015, Tokyo 2015 A Workshop on CFD in Ship Hydrodynamics [54];
(3) Data form JBC_2015, Tokyo 2015 A Workshop on CFD in Ship Hydrodynamics [54].

Considering the estimated data uncertainty, U_D, expressed as a percentage of measured data value D, it is possible to display the results as reported in Table 4; number between brackets represent the

number of available data to assess the representative values. Following the overview about the data, results display a general decreasing trend in error between the comparison among EFD results and CFD calculations; indeed, the statistical analysis for the average error of the results of all resistance test simulation shows a decrease from 4.17% to 2.1% by considering 5T2005 and 6G2010, respectively [31]. Moreover, with the respect to different hulls, the uncertainty related to simulation exhibits a value close to 4%, as reported by Mancini [55]. Based on these kinds of analysis, it is possible to derive the following statistical conclusion: the analysis is based on data, but the total number of results isn't so large to obtain a robust conclusion. Moreover, the number of freely accessible benchmark, where both the geometries and the experimental results are available, is not so extensive; indeed, considering the ITTC benchmark repository for ship resistance and propulsion [56], it is possible define 14 different hulls, sometimes not so easy to access.
Another example to assess the accuracy for a CFD calculation can be listed. Indeed, through the SPTM approach, Islam et al. [57] perform the uncertainty analysis with the respect to 4 different hulls: DTC, JBC, KCS, and KVLCC2. This study concluded that the results for the uncertainty estimations differs when the methods to assess them have changed; moreover, it can be observed that the hulls tested belong to the ITTC benchmark repository. To partially overcame this lack of information, and in order to assess the accuracy for a CFD calculation when compared with the towing tank experience with the respect to the advance resistance evaluation, an heterogenous database containing both the hull geometries and the experimental results along with their uncertainty assessment is required. Once these mandatory elements are available, it is possible to perform investigation through the *Multiple Participants To One* (MPTO) or the *Single Participant To Multiple* (SPTM) approaches and define a statistical description about the accuracy obtained by a CFD calculation when compared with an EFD result.

Table 4: MPTO workshops results, for the CFD resistance estimated uncertainty.

Hull	**Configuration**	F_r	U_D [%]			
			2005 (1)	**2010** (1)	**2015** (2) (3)	**2024**
KVLCC2	Fixed	-	0.7 (13)	1.0 (5)	-	-
	Free	-	-	1.0 (1)	-	-
KCS	Fixed	$F_r = 0.260$	-1.1 (11)	1.0 (8)	-	-
	Free	$F_r = 0.110 \sim 0.280$	-	1.0 (27)	-	-
DTMB 5415	Fixed	-	2.2 (11)	0.6 (5)	-	-
	Free	$F_r = 0.138$	-	1.3 (5)	-	-
		$F_r = 0.280$	2.2 (1)	0.6 (6)	-	-
		$F_r = 0.410$	-	0.6 (5)	-	-
JBC	Free w/o ESD	-	-	-	1.0 (22)	-
	Free with ESD	-	-	-	1.0 (20)	-
Lucy Ashtown	Set 1	-	-	-	-	-

(1) Data form [31];
(2) Data form KCS_2015, Tokyo 2015 A Workshop on CFD in Ship Hydrodynamics [54];
(3) Data form JBC_2015, Tokyo 2015 A Workshop on CFD in Ship Hydrodynamics [54].

At the University of Genova, more than 200 experimental tests have been found inside a collection of ancient volumes, where both the geometries and the experimental data are available. In order to generate a diversified enough database to assess the CFD ability to reproduce the experimental results, among all the available cases, 16 have been selected. Moreover, to overcome the latent limitations inherent to the use of old fashion hull shapes deriving from the available database, 6 additional hulls from the one suggested by I.T.T.C. benchmark-repository [56] were investigated. Therefore, a number of 22 hulls have been used to generate a database where the characteristics for the hulls, the CFD calculation (142 computations) and the EFD results are stored in order to assess the accuracy for a CFD calculation. Moreover, based on this repository, different kinds of analysis have been performed with the attempt to define any possible correlation among the differences and other parameters (like speed, configuration for the hull during the test, hydrodynamical parameters). A key parameter for the analysis is the coefficient ΔR_{T_M}, defined by equation (3):

$$\Delta R_{T_M} = \left(\frac{R_{TM_{CFD}}}{R_{TM_{EFD}}} - 1\right) \begin{cases} < 0\,\%, & CFD\ underestimate \\ = 0\,\% & No\ difference \\ > 0\%, & CFD\ overestimate \end{cases} \quad [\%] \tag{3}$$

where, $R_{TM_{CFD}}$ and $R_{TM_{EFD}}$ represent the single computation result and the experimental one, respectively.

Current research presents the accuracy evaluation of CFD calculations compared with EFD results. Chapter 2, entitled “Theoretical background”, provides EFD and CFD characterizations, defining the ship resistance and accounting for the UA. In Chapter 3, entitled “Numerical set-up”, the definition of a parametrical numerical set-up to be implemented in the SPTM approach is discussed. The workflow and the checks for the population of experimental results and numerical calculations database are presented in Chapter 4, entitled “Repository of EFD and CFD results”. The conclusion for the pure towing accuracy along with the uncertainty assessment are reported in Chapter 5, entitled “Data analysis”. Based on the findings from the research, a so called “future work” is addressed in Chapter 6, entitled “Model self-propulsion, experimental and numerical results”, in which a preliminary analysis is presented to define a possible procedure to assess the precision of a CFD calculation compared with an EFD result, taking into account the interaction between the propeller and the hull.

2 Theoretical background

In the second part of the XX century, computer science registered a high increase in computational resources and this growth has shifted to lead to attract interesting from a wide range of sectors like industrial applications, research and developing. Even in naval architecture, this new kind of technology has moved to gradually consider the Computational Fluid Dynamics (CFD) as a possible alternative to the Experimental Fluid Dynamics (EFD). With the respect to the resistance evaluation for a model hull, debates on how the CFD can properly replicate the EFD are still open, moreover the precision about a CFD calculation when compared with a result from EFD is something still not well defined.

In this scenario, current Chapter has been divided into three layers: physical description of the experimental tests, technologies for CFD and uncertainty assessment, respectively. Therefore, after a brief introduction about the experimental models used to perform a resistance evaluation, in the second part the actual state of art along with the most advanced technologies and methodologies nowadays available are described, while, in the latest part, a detailed description of the available techniques able to perform the Verification and Validation (V&V) in order to define the uncertainty assessment is provided.

2.1 Experimental Fluid Dynamics (EFD) and resistance test

During the design phase of a new vessel, the initial characteristics and a "first tentative" hull shape for the vessel under studied are defined, once the design constraints have been appropriately evaluated. When the power propulsion plant is free from any constraint, the first unknown to be evaluated is the power to install on board to achieve the contractual speed. One of the most consistent and robust way to assess this data is represented by the towing tank test.

The towing tank test represents an experimental procedure, where a model scale for the ship under design is towed inside a basin to assess the resistance for that hull. The first application of this procedure is dated back in XIX century, when William Froude in 1872 developed a new type of facility under the name of "Admiralty Experiment Works" (A.E.W.) in Torquay [22], to test a model hull under controlled conditions. Indeed, at that period of time, ships had moved from a sailing propulsion system to a mechanical one and the designers addressed to phase with a new technical problem, consisting in the need to evaluate the resistance for the new hull. By that time, several towing tanks have been realized, as reported in the International Towing Tank Conference (ITTC) website under the page "Facilities". While, with the respect to the procedure and guidance, the origin of the International Towing Tank Conference can be dated by in Hamburg in 1932 [23], when the "International Hydro-mechanical Congress" established to schedule, in alternate years, meetings referred to as "The International Conference of Ship Tank Superintendents" to foster and disseminate the generation for mutually agreed procedures related to all aspects of ship model work. After Oslo conference (1954), held later on several other conferences (Hague 1933, London 1934, Paris 1935, Berlin 1937 and London 1948), the name has changed in "International Towing Tank Conference" (ITTC), as nowadays recognized among the scientific community. The ITTC makes available procedures and best practices with the aim of standardizing the results in the experimental field (and more recently even in the numerical one); these procedures are constantly updated and open-source. Among all the procedures, the ones for the experimental test are addressed here.

When a body is close or across the free surface of the fluid, it interacts with the fluid generating waves on the free surface and obtaining viscous-pressure variations; moreover, the wave generation requires energy, leading to a resistance and giving that the fluid has its own viscosity, tangential forces arise generating a second type of resistance. These are identified as wave-making and viscous (or frictional) resistances, respectively. Because of the presence of the viscosity for the fluids, the velocity field next to the hull changes. The effects of the viscosity can be split into air and water; when considering only conventional displacement hull without any dynamical support and tested for a Froude's number (F_r) smaller than 0.45, the effects of air are considered negligible. Indeed, by considering the data for air (data at 15°C: kinematic viscosity, $\upsilon_{AIR} = 1.460\text{x}10^{-5}\ [m^2/s]$ and density $\rho_{AIR} = 1.225\ [kg/m^3]$), as reported in ISO 2533:1975 [58] and the one for water (data at 15°C $\upsilon_{WATER} = 1.1386\text{x}10^{-6}[m^2/s]$ and density $\rho_{WATER} = 999.1026\ [kg/m^3]$), as reported in ITTC Recommended procedure and guidelines 7.5-02-01.03 [59], the magnitude of the respective ratios are $\upsilon_{WATER}/\upsilon_{AIR=} \cong 0.1$ and $\rho_{WATER}/\rho_{AIR=} \cong 800$, and therefore neglect the effects of air represents a reasonable approximation for this framework. Due to the presence of this pressure field close to the hull and connected with the viscosity, sometimes the viscous effects are termed as “viscous pressure resistance” or “form resistance”, as reported by Tupper [60]. This last way to identify this influence is directly connected to the hull shape with respect to the trajectory for the streamlines; indeed, when a transom hull is considered, the flow field next to the aft doesn’t follow the hull shapes but generates eddies and they cause an increase in the resistance. Given that the simultaneous agreement of Froude’s and Reynolds’ numbers for both the ship and the model, the resistance obtained for the model cannot be directly scaled for the ship. As reported by Lewis [61], Froude ”first recognized the practical necessity of separating the total resistance into components, based on the general law of mechanical similitude, from observation of the wave patterns of models of the same form but of different sizes”. Indeed, when the model runs at an equivalent speed (with respect to the ship), it is possible to measure the model’s total resistance and calculate the frictional one (based on similar model); considering the proportion among the displacements, the remaining components (residuary resistance) can be scaled and added to the frictional resistance for the ship. This approach exhibits sufficient accuracy, although based on the simplification for the flat plate to evaluate the frictional components and on the independence among the resistances.

A dedicated infrastructure is required to perform a single towing tank experiment. As an example, the “Umberto Pugliese” towing tank from the Institute of Marine Engineering (INM) may be considered. As shown in the schematic plan view of basin Figure 1a and for its cross section in Figure 1b, a general view about the infrastructure is reported. Indeed, from the instrumentation available on the carriage, it is possible to get the information required to define the value for the resistance of the model from the experimental point of view (EFD) along with other quantity of interests depending on the case to be investigate; among these, it is possible to enlist: the 3D wake, the vertical and the horizontal planar motion and the longitudinal wave cut.

A synthetic description about the experimental fluid dynamics and the resistances is describe below.

2.1.1 Wave-making resistance

When a body moves through the free and undisturbed surface, it generates a pressure field that alters the shape of the surface, and waves arise. The system seems to be stationary when the body moves at constant speed and the wave pattern is similar to the one described by Kelvin for a moving pressure point, composed of diverging and transversal waves inside an isosceles triangle (on the plane) with the angle of about 40°, described in Figure 2.

When considering a ship, if the thrust of the propeller equilibrates the resistance, the waves seem to remain the same, and the force required to keep on this system of waves is the so called “wave-making” resistance.

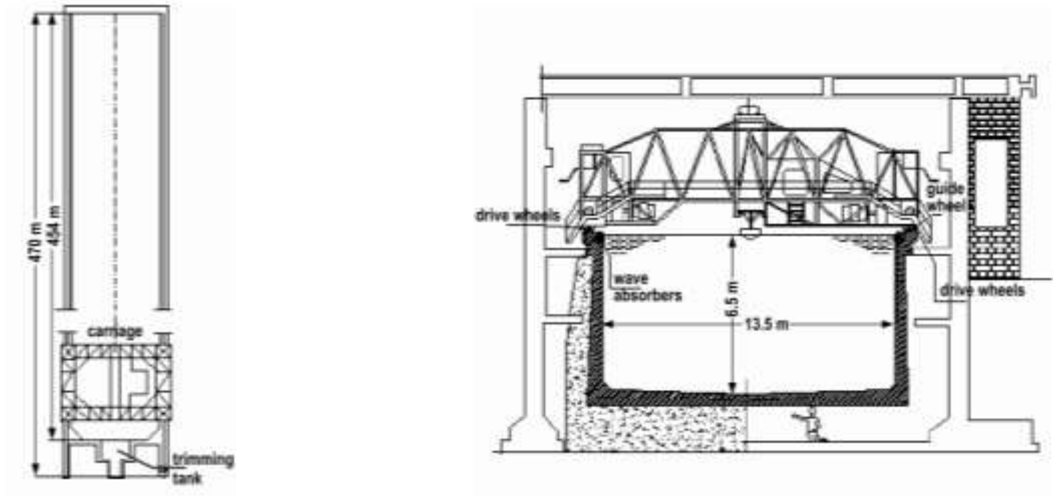

(a) (b)

Figure 1: Institute of Marine Engineering, "Umberto Pugliese" towing tank (NO. 1 -1974)[1]; basin schematic plan view (a) and cross section (b).

The waves generated by the relative motion among hull and water exhibit interferences effects connected with the wave generation system; indeed, two systems of waves move from the hull: the first one has its origin on the bow and moves aft, till the interaction with the second wave-system, whose origin is the aft part of the hull.

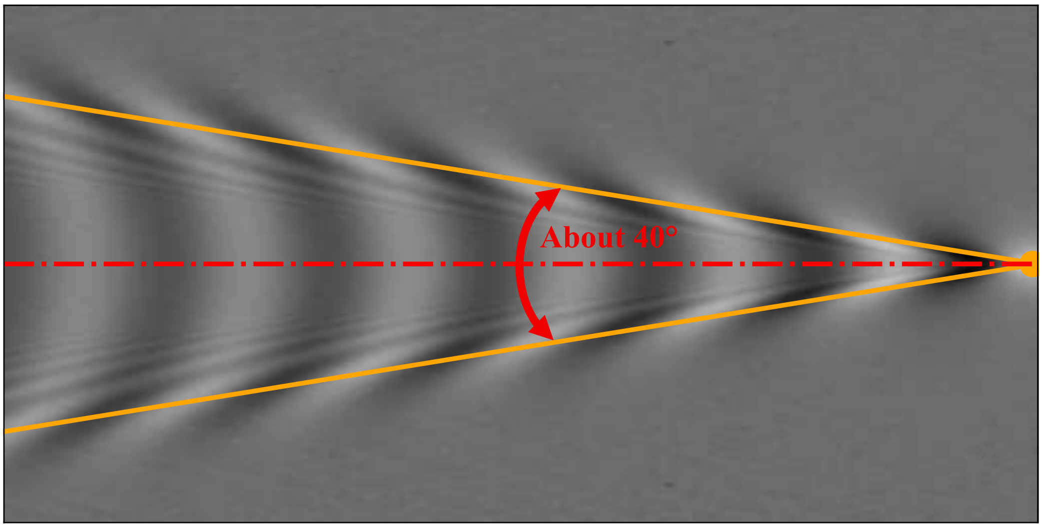

Figure 2: Kelvin's wave pattern.

This interaction plays a crucial role with the respect to the wave-making resistance, as demonstrate by the Figure 3 where, varying the speed, hump and hollows may be seen in a resistance-type curve. A mathematical role of thumb connects the presence of a troughs (or a crest) from the bow system to the presence of a crest of a trough in the stern one, as defined in equation (4):

[1] From https://www.inm.cnr.it/wp-content/uploads/2019/04/ITTC-CoF-1.pdf.

$$\frac{V^2}{0.9L} = \frac{g}{N\pi} \tag{4}$$

where, V stands for the advance speed, L the ship lenght and g the gravitational acceleration; moreover, by assessing whether the integer value of N are odd or even, it is possible to define whether a crest or a trough attains the stern system. This behavior changes by changing the speed and justify the hollows and the humps exhibit by the picture.

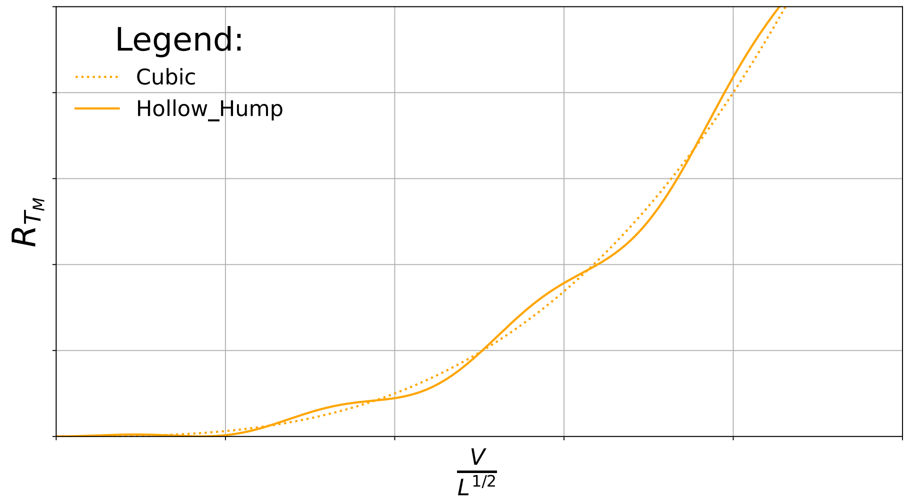

Figure 3: hollow-hump in resistance-type curve.

The wave making resistance can be scaled from the model to the ship by the ratio among their displacements. This represents an approximation and it is still nowadays accepted. As reported by the results from "A summary of the Lucy Ashton resistance prediction workshop" [37], it can be demonstrated that this approximation is acceptable being the tendency for the C_P quite the same by changing the scale and so unaffected by the scale effects.

2.1.2 Frictional resistance

The viscosity leads a fluid to be considered non-ideal, and water falls under the same rule. Considering the case for a body moving inside a physical domain composed by water, experimental tests demonstrated the presence for three zones: a zero-speed zone close to the body, a zone where the speed is the relative one (being one the value for the undisturbed velocity among water and body) and finally, a transition zone from the zero to the speed. This last field is the so-called "boundary-layer" and its thickness is usually given by a function of the characteristic length and depends on the fluid characteristics. With the respect to the fluid's characteristics, based on Reynolds' number, which is defined as reported in equation (5), two kinds of flow can be listed: laminar and turbulent flow, and the change among them depends on the critical Reynolds' number:

$$R_e = \frac{VL}{\upsilon}[adim] \tag{5}$$

where, V represents the speed (expressed in $[m/s]$), υ represents the kinematic viscosity (expressed in $[m^2/s]$) and L the characteristic length (expressed in $[m]$). Based on this subdivision and with the respect to the frictional resistance, a proportional mathematical law can describe the trend in the laminar case, while in the transition zone (across the critical R_e) a properly defined law isn't available and finally in the fully turbulent range the increase for the resistance adhering to an exponential law, which typical value for the exponent is 1.723. These subdivisions play an important role with the respect to the naval architecture field; indeed, being the model length different from the ship one, the two Reynolds' number are different and if the model isn't big enough it may be tested at a different regime from the ship one. To account for this, in towing tank experiences turbulence stimulation (like wires, studs and strip of sandpaper) are installed firstly to ensure the equivalence for both the flow regime at model and the full scale, as reported by ITTC recommended procedure for ship models, 7.5-01-01-01 [62].

At the beginning, in early 1870s, several planks have been tested with the attempt to define a fitting formula for the frictional resistance. Later on, the frictional resistance coefficient (C_F), as reported in equation (6), has been introduced as a function of the Reynolds' number:

$$C_F = f(R_e) = \frac{R_F}{\frac{1}{2}\rho S V^2}[adim] \tag{6}$$

where, ρ represents the mass density of fluid (expressed in $[Kg/m^3]$), S the wetted surface (expressed in $[m^2]$), V the speed (expressed in $[m/s]$) and R_F the frictional resistance (expressed in $[N]$). Among all the available approaches, the Shoenherr and the ITTC 1957 ones are reported in equations (7) and (8), respectively.

$$\frac{0.242}{\sqrt{C_F}} = log_{10}(R_e C_F)[adim] \tag{7}$$

$$C_F = \frac{0.075}{(log_{10}R_e - 2)^2}[adim] \tag{8}$$

Schoenherr's and ITTC approaches display similar results, when applied in the range $10^5 \leq R_e \leq 10^{10}$, as demonstrated by Figure 4 (where the green and brown lines represent the traces for the formulations, respectively).

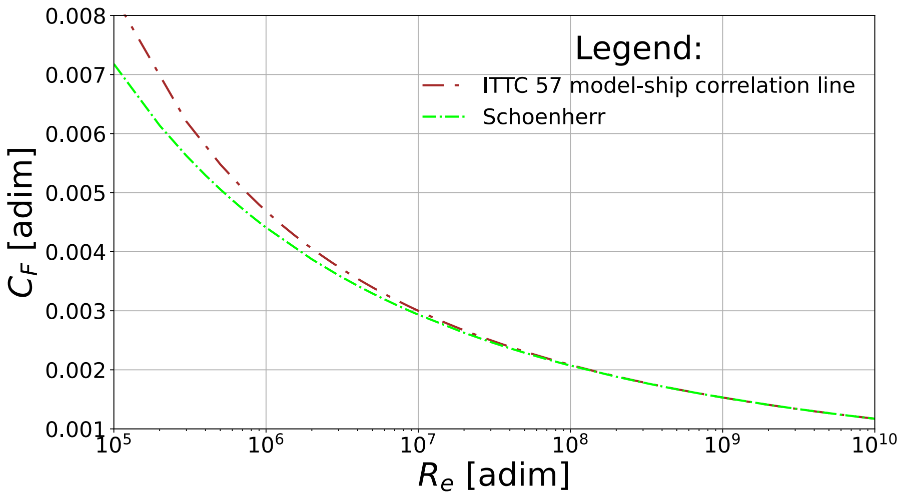

Figure 4: frictional coefficient evaluation through Schoenherr's and ITTC 1957 formulations.

Viscous pressure resistance (or eddy making resistance) has to be evaluated. Indeed, considering a symmetric hull shape, the resultant component on the diametral plane displays a non-zero value, and this difference is directly connected with the differences among the pressures at the bow and the one at the stern part of the hull. Moreover, moving aft, the pressure can change because of the shape and all the appendages (like rudder, struts, bilge keel, bossing) representing other sources for eddy resistance. These appendages have their own characteristic length (and therefore a specific R_e); this, can lead them to be tested to a different regime with the respect to the model hull. Therefore, usually model hulls are naked when tested, and their appendages evaluated separately and scaled to the ship. Even if differences can occur, usually the global addition is small and the errors aren't critical. Nevertheless, it is important that the appendages are aligned with the flux to avoid eddy resistance generation; moreover, with the respect to the struts for the shaft line, they display a crucial role for the propellers, allowing them to work with a perturbation as less as possible [63].

With the respect to the air resistance, usually it is neglected; but, if design constraint declares the presence of wind, its effect can be evaluated through Tupper approach [60]; indeed, the Ahead Resistance Coefficient (ARC), as described by equation (9):

$$ARC = \frac{R_{A_AFT} + R_{A_FORE}}{\frac{1}{2}\rho A_T V_R^2}\,[adim] \tag{9}$$

where, V_R represents the relative velocity among air and model, A_T the value for the area of the transversal cross section.

2.1.3 Total Resistances components

Once all the kinds of resistance have been described, it possible to assess their composition with the respect to a hull (at model or full scale) sailing on the water. Indeed, the total resistance (R_T) can be split into the frictional (R_F) and in the pressure (R_P) components, as reported in (10), (11), (12):

$$R_T = R_F + R_P [N] \tag{10}$$

$$R_F = \int_{SUF} \tau_x dA \, [N] \tag{11}$$

$$R_P = \int_{SUF} p_x dA \, [N] \tag{12}$$

where, τ_x represents the shear stress component along x-axis (lays on the longitudinal plane of symmetry) and p_x the pressure normal component in x-direction. With the respect to the advance direction for the ship, it can be noted that the sign for R_P changes based on the surface normal, while the sign for R_F is always opposed to the advance of the hull and, following the flat plate theory, it possible to assess its value based on the one obtained from an equivalent flat wetted surface towed at the same speed $\left(R_{F_0}\right)$ scaled on the form factor coefficient $(1 + k)$, as reported in equation (13):

$$R_F = (1 + k) R_{F_0} [N] \tag{13}$$

As described later on, the form factor is an experimental coefficient, which accounts for the 3D hull geometry instead of the 2D flux formulation for the flat plate. With the respect to the pressure resistance (R_P), it is possible to consider two kinds of contributions: the viscous pressure (R_{VP}) and the wavemaking (R_W) resistances. The first one mainly accounts for the pressure variation due to the presence of the boundary layer; while, the second one represents the force required to keep on the wave system. Moreover, the latter one resistance can be sub-divided into the wave pattern (R_{WP}) and wavebreaking pressure (R_{WB}) resistances. As suggested by the names, R_{WP} accounts for the force required by the stationary wave system which moves with the hull, and R_{WB} is connected with the non-stationary wave breaking close to the hull. Therefore, it is possible to consider each single component to get the value for the total resistance, as reported in (14):

$$R_T = R_F + R_P = (1 + k) R_{F_0} + R_{VP} + R_{WP} + R_{WB} [N] \tag{14}$$

Based on equation (14), it is possible to split the total resistance into viscous (R_V) and wavemaking (R_W) resistance components, as performed in (15); therefore, the total resistance can be evaluated through equation (16):

$$R_V = (1 + k)R_{F_0} + R_{VP}[N] \quad (15)$$

$$R_T = R_V + R_W[N] \quad (16)$$

Still based on equation (14), considering the residuary resistance components (R_R), as reported in (17), it possible to define another way to assess the value for the total resistance, as reported in (18):

$$R_R = (k)R_{F_0} + R_{VP} + R_W[N] \quad (17)$$

$$R_T = R_{F_0} + R_R[N] \quad (18)$$

The total resistance shown in equation (18) was the first form to be used, as proposed by Froude; indeed, R_{F_0} accounts for the relative contribution to the total resistance from an equivalent flat plate, and all the other contributions have been evaluated by the residuary resistance R_R. A hull running across the free surface exhibits all the sources of resistance, these values change by mainly three factors: the speed, the characteristics (mainly connected to viscosity, as shown in Figure 4) and on the shape for the hull. As shown with the respect to the frictional resistance coefficient (C_F) in equation (6), resistances are expressed by dimensionless coefficients, where the generic force (R_i, expressed in $[N]$) is divided by the mass density of fluid (ρ, expressed in $[Kg/m^3]$), the wetted surface area (S, expressed in $[m^2]$) and the speed (V, expressed in $[m/s]$), as reported in (19):

$$C_i = \frac{R_i}{\frac{1}{2}\rho S V^2}[adim] \quad (19)$$

Therefore, all the formulations from equation (10) to equation (18) can be expressed in dimensionless form. All these kinds of contributions are reported following Ween representation in Figure 5 along with the Table 5, where the possible ways to account for the total resistance are listed.

With the respect to all this contribution, considering as test case the data for the INSEAN 2340 model, which is an identical geometrical similitude of the DTMB 5415 [64], it is possible to assess the resistance contributions for the model total resistance coefficient C_{T_M} varying Reynolds' number, as plotted in Figure 6. Indeed, considering the brown lines as the representative for the model-ship correlation lines (solid line represents the ITTC-1957 line; dashed line for the form factor approach) and the solid orange line as the experimental results for C_{T_M}, one speed has been considered ($R_e = 9.39x10^6$) and two vertical lines have been generated (graphically divided to appreciate the differences but related to the same R_e). The first one, the red vertical line, represents Froude's formulation $\left(C_{F_0} + C_R\right)$, as detailed in equation (18), where all the residuary coefficient is integrally transferred to the ship, while the green label C_{FORM_M} reports the part to subtract to C_{R_M} before the transfer procedure, as prescribed by form factor theory; while, the blue line represents the contributions for C_{T_M} as used by the 1978-ITTC procedure.

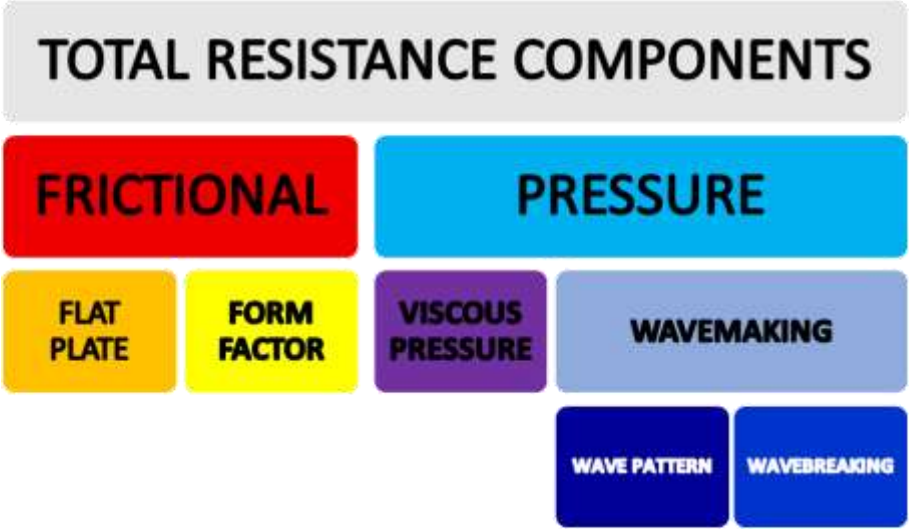

Figure 5: total resistance contributions.

Table 5: schematical representation about the way to split the total resistance contributions.

TOTAL RESISTANCE CLUSTERS				R_T FORMULATION
FLAT PLATE R_{F_0}	RESIDUARY R_R			$R_{F_0} + R_R$
FLAT PLATE R_{F_0}	FORM DRAG $(k)R_{F_0} + R_{VP}$		WAVEMAKING R_W	$(1+k)R_{F_0} + R_{VP} + R_W$
FRICTIONAL R_F		VISCOUS P. R_{VP}	WAVEMAKING R_W	$R_F + R_{VP} + R_W$
VISCOUS R_V			WAVEMAKING R_W	$R_V + R_W$

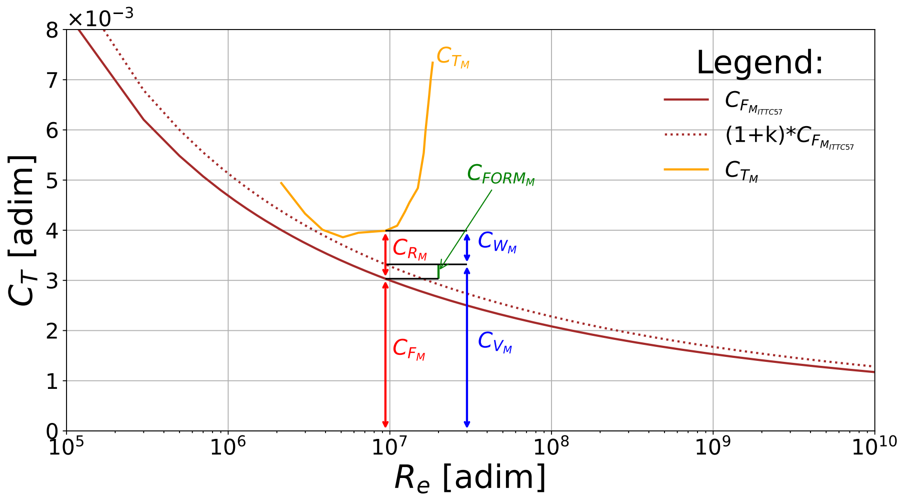

Figure 6: experimental results for INSEAN 2340 model.

This representation is full of details and it enables the opportunity to directly compare results for different hulls and their extrapolated results to full scale (subscript "M" indicates model, while "S" full scale), tested at different speed. Indeed, as reported in Figure 7, where the experimental results for three different hulls have been plotted (solid red line for Hull A, fuchsia for Hull B and green for Hull C, respectively) with the brown traces (representative for the model-ship correlation line) just for Hull A, it is possible to define for each one of them the contributions for the resistance along with the differences for the total resistant coefficient, otherwise hidden when the total resistance is exhibited because of its variation with the speed (quite close to a cubic trend for a displacement hull).

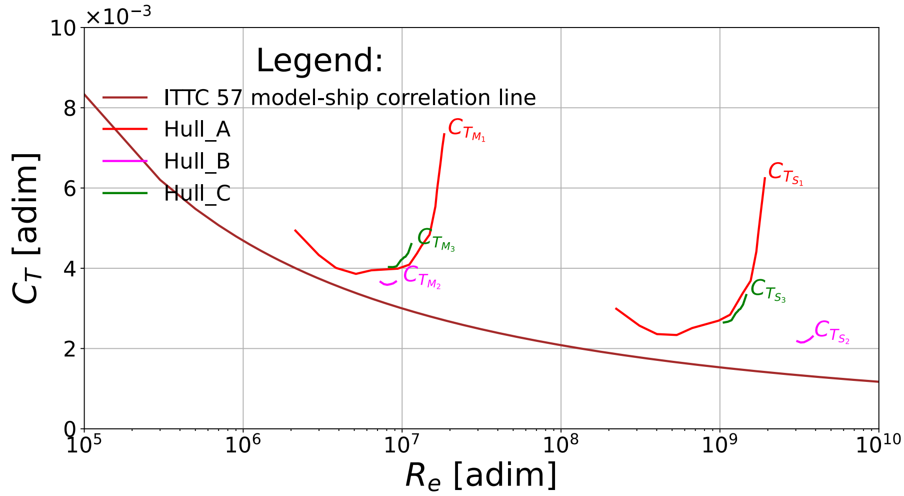

Figure 7: comparisons among experimental results for three different hulls, tested at different speed, along with the extrapolated results for full scale.

2.1.4 Full scale prediction

As stated by Froude, a way to assess the resistance for a ship consists in performing a towing tank test on a model, tailed by a procedure to transfer the result from model to ship scale. This procedure can be split into the following steps: measure the resistance for the model towed at a correspondent F_r with the ship, subtract the evaluated frictional resistance to the total read one, scale the model residuary resistance with the ratio of the displacements, evaluate the frictional resistance for the ship, finally add the scaled residuary, the frictional and the appendages resistance to achieve the resistance for the ship (if necessary, allowances has to be performed with the respect to the air resistance).

Adhering to the resistance test procedure from ITTC 7.5-02-03-01.4, even known as 1978 ITTC Performance Prediction Method [65], and considering hull "C5-3ª" as the bare hull test case [66], which main dimensions are stored in

Table 6 along with a 3D view in Figure 8, a three dimensions extrapolation to full scale has been performed as follows.

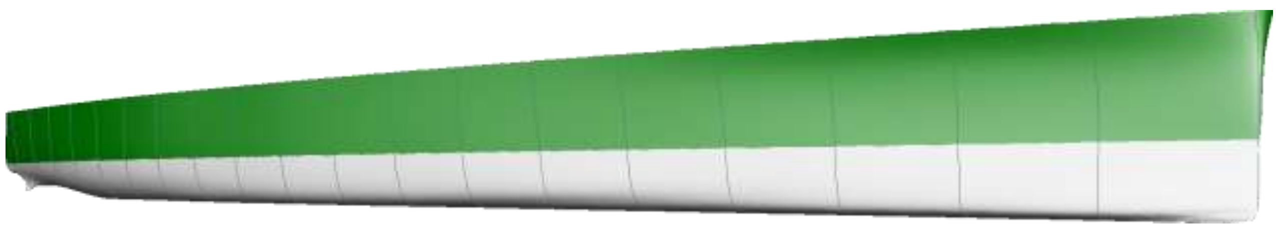

Figure 8: overview on hull C5-3ª.

Table 6: hull "C5-3[a]" main characteristics.

Model characteristics	Symbol	Values	UNIT
Length between perpendiculars	L_{PP}	6.000	m
Length, overall submerged	L_{OS}	6.008	m
Length of waterline	L_{WL}	6.008	m
Maximum moulded Breadth at design WL	B_{WL}	0.654	m
Draught at forward perpendicular	T_F	0.184	m
Draught at midship	$T_M = (T_A + T_F)/2$	0.184	m
Draught at aft perpendicular	T_A	0.184	m
Displacement volume	∇	0.412	m^3
Area of wetted surface	S	4.025	m^2
Ratio L/B	L_{WL}/B_{WL}	9.186	-
Ratio B/T	B_{WL}/T_M	3.546	-
Block coefficient	$C_B = \nabla/LBT$	0.569	-
Froude's length coefficient, or length-displacement ratio	$M^C = \nabla^{1/3}$	8.073	-
Scale ratio	$\lambda = L_s/L_M$	25	-
Area of water-plane	A_W	-	m^2
Longitudinal centre of buoyancy	L_{CB}, X_{CB}	2.980	m

Firstly, the characteristics for the air and the water (density, kinematic viscosity and temperature) have to be established in accordance with ITTC Recommended Procedure 7.5-02-01-03 [59]. More in details, a sampling for the water has to be performed before the run in order to assess the temperature and the density for the water, and later on it is possible to scale the results for the standard condition. Secondly it is possible to perform the resistance tests; once the total resistance, R_T, has been evaluated for the model hull by the dynamometer on the carriage for the speeds of interests, the dimensionless number of Reynolds' and Froude can be respectively evaluated by equations (5) and (20), along with the resistance frictional coefficient, C_{F_M}, and the total resistance coefficient, C_{T_M}, as respectively described by equation (8) and by (21).

$$F_r = \frac{V}{\sqrt{gL_{WL}}}[adim] \tag{20}$$

$$C_{T_M} = \frac{R_T}{\frac{1}{2}\rho S V^2}[adim] \tag{21}$$

where, L_{WL} represents the characteristic length (the length between the perpendiculars for the hull), ρ the mass density of fluid (expressed in $[Kg/m^3]$), S the wetted surface of the hull without the transom area and any appendance (expressed in $[m^2]$), V the speed (expressed in $[m/s]$) and R_T the total resistance (expressed in $[N]$). Data can be stored into a datasheet, as reported in Table 7. Considering this particular case, where the results for low speed exhibits a clustered tendency, the stern is cruiser type and there isn't a bulb, Prohaska proposed procedure [67] has been applied in the range $0.1 \leq F_r \leq 0.25$ to assess the value for the for coefficient $(1+k)$; indeed, applying an interpolating straight line with a slope among the data, the interception among the line and the y-axis (which physically represents $F_r = 0$), represents the value for the form coefficient, as described in equation (22):

$$\frac{C_{T_M}}{C_{F_M}} = (1+k) + c\,\frac{{F_r}^4}{C_{F_M}}\,[adim] \tag{22}$$

where, c represents the slope and assessed with the least squares line (for this case $c = 0.1684$ and $1 + k = 1.0503$). It is possible to plot the experimental results (orange line and markers) within the fixed range with Prohaska's line (red dashed line) and define the intercept for y-axis (red pentagon), as reported in Figure 9.

Table 7: hull "C5-3a" experimental results.

V_M $[m/s]$	F_r $[adim]$	$10^{-6}R_e$ $[adim]$	$10^3 C_{T_M}$ $[adim]$	$10^3 C_{F_M}$ ITTC 57 $[adim]$	$(F_r)^4/C_{F_M}$ $[adim]$	C_{T_M}/C_{F_M} $[adim]$
1.500	0.195	8.55	3.470	3.084	0.473	1.125
1.600	0.208	9.12	3.526	3.049	0.619	1.156
1.700	0.221	9.69	3.588	3.017	0.798	1.189
1.800	0.235	10.25	3.652	2.987	1.012	1.223
1.900	0.248	10.82	3.730	2.959	1.269	1.261
2.000	0.261	11.39	3.806	2.933	1.571	1.297
2.100	0.274	11.96	3.872	2.909	1.926	1.331
2.200	0.287	12.53	3.906	2.886	2.339	1.354
2.300	0.300	13.10	3.920	2.864	2.815	1.369
2.400	0.313	13.67	3.896	2.843	3.361	1.370
2.500	0.326	14.24	3.919	2.824	3.985	1.388
2.600	0.339	14.81	3.970	2.805	4.693	1.415
2.700	0.352	15.38	4.083	2.788	5.492	1.465
2.800	0.365	15.95	4.263	2.771	6.391	1.539
2.900	0.378	16.52	4.554	2.755	7.397	1.653
3.000	0.391	17.09	4.960	2.739	8.519	1.811
3.100	0.404	17.66	5.483	2.724	9.766	2.013
3.200	0.417	18.23	6.027	2.710	11.147	2.224
3.300	0.430	18.80	6.407	2.696	12.671	2.376
3.400	0.443	19.37	6.690	2.683	14.348	2.493
3.500	0.456	19.94	6.831	2.670	16.189	2.558

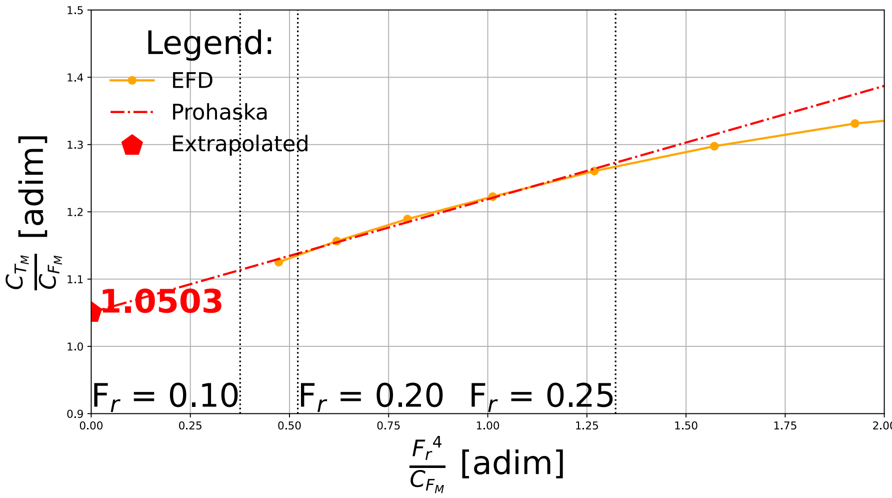

Figure 9: Prohaska's method to assess the form factor $(1 + k)$ value.

To evaluate the resistance and the effective power for a ship without roughness at i-th speed, the ship total resistance coefficient, C_{T_S}, can be expressed as reported in formulation (23):

$$C_{T_S} = C_{V_S} + C_{W_S} = (1+k)C_{F_S} + C_W + \Delta C_F + C_A + C_{AA_S}\ [adim] \quad (23)$$

where, with the respect to the ship hull, the total viscous resistance coefficient, C_{V_S}, as reported in (24), can be derived from the form factor $(1+k)$, as defined in equation (22), and the frictional coefficient, C_{F_S}, can be evaluated through the ITTC-1957 correlation line, as reported in (8); while, by considering Froude's theory, the wave making resistance coefficient for the ship, C_{W_S}, is the same for the model, as reported in (25).

$$C_{V_S} = (1+k)C_{F_S}\ [adim] \quad (24)$$

$$C_W = C_{W_S} = C_{W_M} = C_{T_M} - C_{V_M} = C_{T_M} - \left[(1+k)C_{F_M}\right]\ [adim] \quad (25)$$

Moreover, the other coefficients account for other specific contribution as follows. With the respect to the roughness allowance, the value for the coefficient ΔC_F has been defined in the 19th ITTC [68] and its formulation in reported in (26):

$$10^3 \Delta C_F = 44\left[\left(\frac{AHR}{L_{WL}}\right)^{\frac{1}{3}} - 10R_e^{-\frac{1}{3}}\right] + 0.125[adim] \quad (26)$$

where, AHR represents the average hull roughness and in 1978-ITTC it has been shifted into the k_S coefficients, whose standard value, when data aren't available, is $k_s = 15x10^{-5}$. When considering the correlation allowance, although ITTC recommends to the institutions to always use the same model to assess the differences between the prediction from the model to the ship scale at sea trials, based on 19th ITTC congress, 1978-ITTC proposes the formulation (27) for the coefficient:

$$C_A = (5.68 - 0.6\, log\, R_e)x10^{-3}[adim] \quad (27)$$

Finally, considering the air resistance coefficient, C_{AA_S}, its value can be calculated with equation (28):

$$C_{AA_S} = C_{DA}\frac{\rho_A \cdot A_{V_S}}{\rho_S \cdot S_S}[adim] \quad (28)$$

where, C_{DA} is a coefficient evaluated by wind tunnel experiences and a coherent value is 0.8, with the respect to the ship, ρ_A and ρ_S represent the air and the water density, respectively; while, A_{V_S} and S_S the transversal projected area above the water plane and the wetted surface area. If the ship exhibits bilge keel appendages of limited dimensions, C_{T_S} can be evaluated by equation (29):

$$C_{T_S} = \frac{S_S + S_{WBK}}{S_S}\left[(1+k)C_{F_S} + \Delta C_F + C_A\right] + C_R + C_{AA_S}[adim] \tag{29}$$

where, S_{WBK} represents the wetted surface of these appendages. While, as reported in ITTC Resistance Test procedure 7.5-02-02-01 [69], if fixed appendages are displayed on the ship, the model has to be fitted with all of them, except for the ones which are considered as propulsors, the movable ones and the bilge keels (if their contribution is expected small and evaluable through equation (29), otherwise they have to be fitted on the model). Therefore, the total resistance coefficient for the ship can be expressed by equation (30):

$$C_{T_S} = \frac{S_S + S_{WBK}}{S_S}\left[(1+k)C_{F_S} + \Delta C_F + C_A\right] + C_W + C_{AA_S} + C_{APP_S}[adim] \tag{30}$$

Debates on how to scale the appendages are still ongoing today; among the available theories, 1978-ITTC last release (2021) suggests the following two: the first one consists of scaling by the fixed fraction $(1+\beta)$ the value obtained for the appendages resistance coefficient at model scale $\left(C_{APP_M}\right)$, which value lays on the range 0.6 ÷ 1.0, as reported in (31):

$$C_{APP_S} = (1+\beta)C_{APP_M}[adim] \tag{31}$$

In the second case, considering a local Reynolds' number based on the surface for the appendage (S_{APP}) or on its length (L_{WL}), it is possible to scale the appendages, as defined by (32), (33), respectively:

$$R_e = \frac{V\sqrt{\frac{S_{APP}}{2}}}{v}[adim] \tag{32}$$

$$R_e = \frac{VL_{APP}}{v}[adim] \tag{33}$$

The appendages drag components are evaluated separately and then summed together, using a local form factor $(1+k_i)$, being the index "i" representative for the "i-th" appendance on "n" installed (the k_i value can be assessed by model tests if available or from published data), as reported in (34):

$$C_{APP_S} = \sum_{i=1}^{n}(1+w_i)^2\,(1+k_i)C_{F_{S_i}}\frac{S_i}{S_S}[adim] \tag{34}$$

where, with the respect to the "i-th" appendance, the wake fraction evaluated at the position for the appendance is represented by w_i, the frictional component by $C_{F_{S_i}}$, and the ratio among S represents the percentage between the wetted surfaces area of the "i-th" appendance and the hull, respectively. This approach doesn't scale the model appendages drag, but evaluates the full-scale appendages drag. Finally, considering equation (23), it is possible to assess the value the total resistance for the ship R_{T_S}, with all the other quantities numerically evaluable; once the total resistance has been evaluated, the effective power for the ship $\left(P_{E_S}\right)$ can be evaluated with equation (35):

$$P_{E_S} = R_{T_S} V_S [W] \tag{35}$$

Therefore, it is possible to scale the results from the model hull "C5-3[a]" to the ship scale by applying this procedure; results are summarized in Table 8.

Table 8: hull "C5-3[a]" experimental results.

F_r (20) $[-]$	R_{T_M} (-) $[kN]$	$10^{-6}R_{e_M}$ (6)[1] $[-]$	C_{F_M} (8)[1] $[-]$	C_{V_M} (15)[1,2] $[-]$	C_{T_M} (21)[1,2] $[-]$	C_W (25)[1,2] $[-]$	$10^{-8}R_{e_S}$ (6)[1] $[-]$	C_{F_S} (8)[1] $[-]$	C_{V_S} (15)[1,2] $[-]$	ΔC_F (26)[1] $[-]$	C_{T_S} (23)[1,2] $[-]$	R_{T_S} (21)[1] $[Mw]$	P_{E_S} (35)[1] $[MW]$
0.195	15.691	8.546	3.084	3.239	3.470	0.231	9.477	1.541	1.618	0.117	1.966	0.143	1.071
0.208	18.142	9.116	3.049	3.202	3.526	0.324	10.109	1.529	1.605	0.126	2.056	0.170	1.358
0.221	20.839	9.685	3.017	3.168	3.588	0.419	10.741	1.517	1.593	0.135	2.148	0.200	1.702
0.235	23.781	10.255	2.987	3.137	3.652	0.515	11.373	1.506	1.582	0.143	2.240	0.234	2.108
0.248	27.066	10.825	2.959	3.108	3.730	0.622	12.004	1.496	1.572	0.151	2.345	0.273	2.595
0.261	30.597	11.394	2.933	3.081	3.806	0.725	12.636	1.487	1.562	0.158	2.445	0.316	3.156
0.274	34.323	11.964	2.909	3.055	3.872	0.817	13.268	1.478	1.553	0.164	2.534	0.361	3.787
0.287	38.001	12.534	2.886	3.031	3.906	0.875	13.900	1.470	1.544	0.171	2.590	0.404	4.449
0.300	41.678	13.104	2.864	3.008	3.920	0.912	14.532	1.462	1.536	0.176	2.624	0.448	5.151
0.313	45.111	13.673	2.843	2.986	3.896	0.910	15.163	1.455	1.528	0.182	2.620	0.487	5.843
0.326	49.229	14.243	2.824	2.966	3.919	0.953	15.795	1.447	1.520	0.187	2.660	0.536	6.706
0.339	53.937	14.813	2.805	2.946	3.970	1.023	16.427	1.441	1.513	0.192	2.728	0.595	7.736
0.352	59.821	15.382	2.788	2.928	4.083	1.155	17.059	1.434	1.506	0.197	2.858	0.672	9.075
0.365	67.176	15.952	2.771	2.910	4.263	1.353	17.691	1.428	1.500	0.201	3.054	0.772	10.815
0.378	76.982	16.522	2.755	2.893	4.554	1.661	18.323	1.422	1.493	0.205	3.360	0.912	13.220
0.391	89.731	17.092	2.739	2.877	4.960	2.084	18.954	1.416	1.487	0.209	3.780	1.098	16.467
0.404	105.91	17.661	2.724	2.861	5.483	2.622	19.586	1.411	1.481	0.213	4.317	1.339	20.748
0.417	124.05	18.231	2.710	2.846	6.027	3.181	20.218	1.405	1.476	0.217	4.874	1.610	25.767
0.430	140.23	18.801	2.696	2.832	6.407	3.575	20.850	1.400	1.470	0.220	5.266	1.850	30.533
0.443	155.43	19.370	2.683	2.818	6.690	3.872	21.482	1.395	1.465	0.224	5.561	2.074	35.264
0.456	168.18	19.940	2.670	2.805	6.831	4.026	22.113	1.390	1.460	0.227	5.713	2.258	39.523

[1] Footers in formulations refer indistinctly both to ship (identify with S) and model (identify with M).
[2] In formulations the notation can be referred to coefficients (for instance C_{T_M}) and resistances (for instance R_{T_M}).
[3] Number between brackets represents the reference equation.

It is possible to plot the total resistance coefficient for the model $\left(C_{T_M}\right)$ and the ship $\left(C_{T_S}\right)$ varying R_e, as reported in Figure 10a and Figure 10b, and appreciate the different ways to account for the different contributions for the total resistance for the test case. While, considering the effective power varying the speed, it is possible to assess the effective power curve varying the speed, as reported in Figure 11.

For the sake of completeness, another procedure to extrapolate data from the model to the ship scale can be performed by considering equation (36) and (37), where based on the equivalence for the residuary resistance coefficient, it is possible to assess the various contribution for the total resistance coefficient at model and ship scale, respectively.

$$C_{T_M} = C_{F_M} + C_R[adim] \tag{36}$$

$$C_{T_S} = C_{F_S} + C_R + C_W + \Delta C_F + C_A + C_{AA_S} + C_{APP_S}[adim] \tag{37}$$

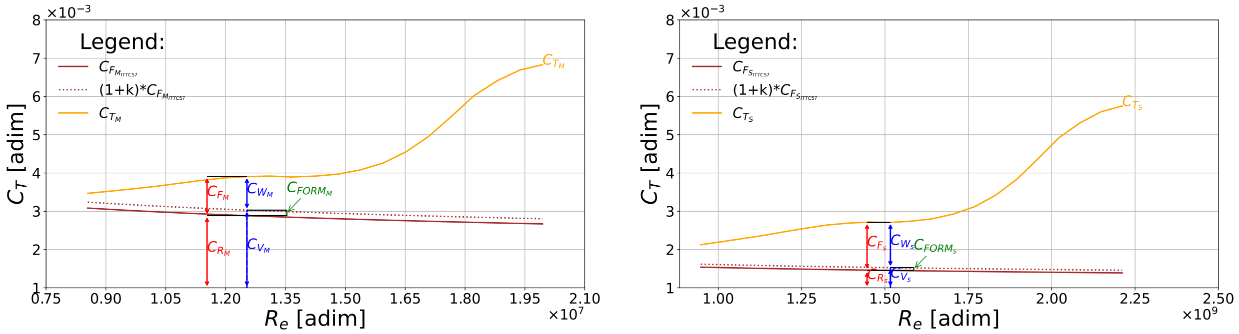

(a) (b)

Figure 10: representation about the total resistance coefficient with its resistance contributions for hull at model (a) and ship (b) scale.

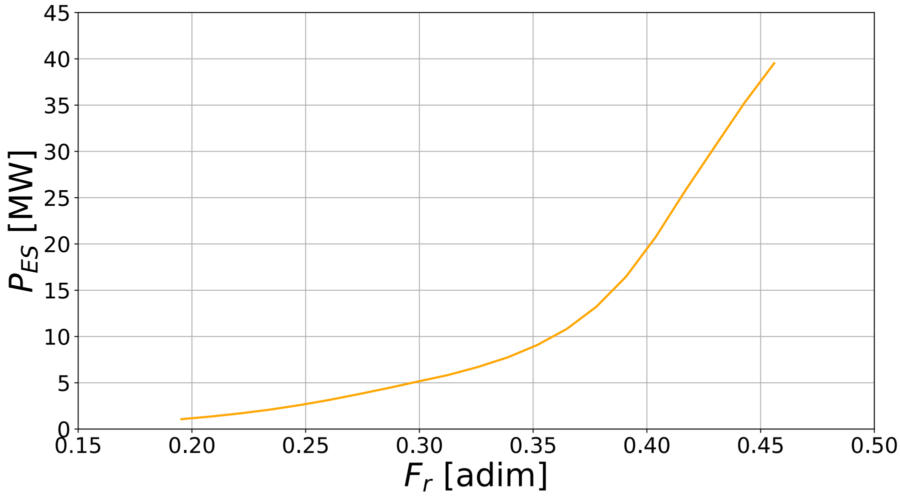

Figure 11: effective power curve at ship scale for hull "C5-3[a]".

Therefore, a comparison among the two ways to get the results for the full-scale ship can be performed. Indeed, considering the most pivotal factors, C_F, C_R, C_W, and C_V, with the respect to the C_T and integrating all the other contributions under the term "other", it is possible to plot all these indexes by varying the speed, as reported in Figure 12a for the ITTC-1978 procedure. Moreover, it is possible to compare the scaling results for the two procedures, as reported in Figure 12b and it is possible to plot the recorded differences, as shown by Figure 12c.

In this case, the differences for the total resistance coefficient at full scale can be evaluated with equation (38):

$$\Delta = \left(\frac{C_{T_{S-ITTC78}}}{C_{T_{S-ITTC57}}} - 1\right)[\%] \tag{38}$$

Results display as maximum negative deviation of -7.55% for the lower speed ($F_r = 0.195$); moreover, a clear trend can be noted by considering the decrease for the difference when the speed increase, reaching the minimum value of -0.64%, at the higher speed ($F_r = 0.455$).

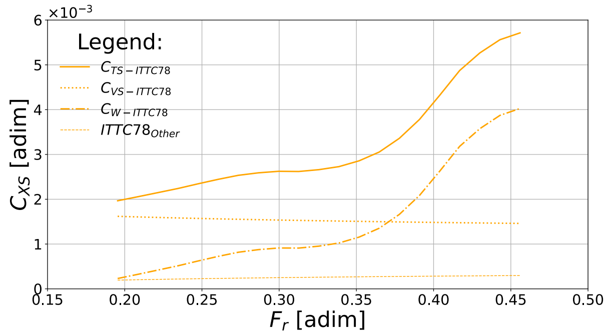

(a)

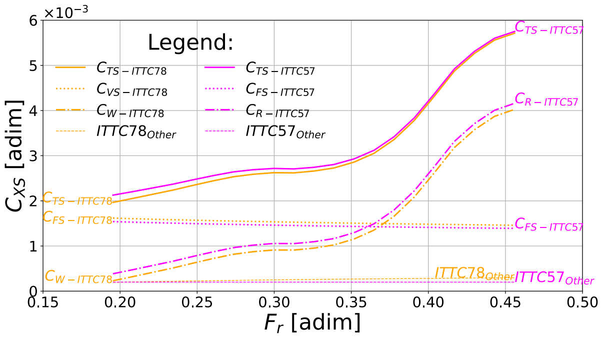

(b)

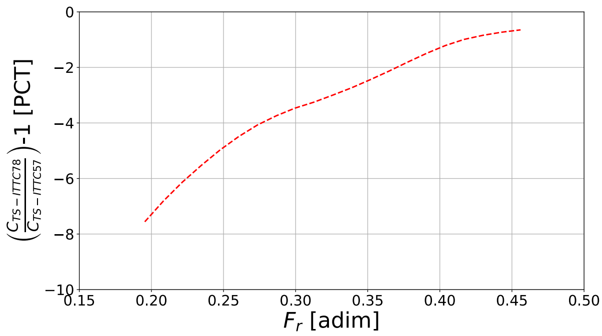

(c)

Figure 12: representation for the extrapolation of C_T, C_F, C_R, C_W and C_V, with the respect to the speed variation for hull "C5-3[a]"; results are clustered as follows: 1978-ITTC procedure (a), comparison among 1978-ITTC and ITTC-1957 procedures (b) and the differences for the two procedures (c).

With the respect to the shortcomings of 1978-ITTC method, Molland et al. [70] exhibited that towing tanks are used to implement an overall "correlational allowance" (C_A) instead of the roughness allowance coefficient (ΔC_F), which formulation is empirical and approximate. Moreover, as reported on Principles of Naval Architecture [61], the value for $(1 + k)$ may depends on Reynolds' number and therefore, if a single value is considered varying R_e, it represents an approximation. In 1979, Tanaka [71] proposed a way to assess the value for the form coefficient, as reported in equation (39):

$$k = a + \frac{b}{\sqrt{C_F}} + \frac{c}{C_F}[adim] \tag{39}$$

where, a, b, c represent coefficient depending on hull shapes. Based on these considerations, and considering that the form factor may also be R_e dependent, the issue remains open, as a universally validated solution is currently unavailable within the towing tank community.

2.2 Computational Fluid Dynamics (CFD)

The Computational Fluid Dynamics (CFD) numerically solves mathematical equations describing the physical phenomena to be investigated in order to assess the motion of fluids and the forces on them. Nowadays, the CFD techniques involve a wide range of engineering or scientific applications such as engines (e.g. turbines and internal combustion engine), thermal management (e.g. exhaust systems and cooling units) and fluid-surface interaction (e.g. wind farm, ship resistance prediction). Based on these examples, a modern definition for CFD can be given by Greenshields et al. [72], as follows: "the prediction of fluid motion and forces by computation using numerical analysis, generally extended to include heat, thermodynamics, chemistry and solids".

A CFD calculation performs through the three following main steps, as reported by Patil [73]: Pre-processor, Flow solver and Post-processor. More specifically, when performing a CFD calculation, the description for the problem is required; indeed, considering the fluid flow along a prism with a square cross section, the following data are required: the volume geometry occupied by the fluid, its motion characteristics equations and the boundary conditions. This physical description has to be implemented into the CFD environment; therefore, the mesh is used to discretize the physical domain, the governing equations can be decomposed into a sum of discrete contributions and the boundary conditions enable the Partial Differential Equations (PDE) to be solved.

Based on the resolution of the Reynolds Averaged Navier-Stokes (RANS) equations with the open-source software for computational fluid dynamics (CFD) OpenFOAM-8, in this Chapter will be defined the characteristics for the fluid, the governing equations, the turbulence models, the discretization methods with the algebraic algorithm to solve the matrixes displaying the discrete representation of the computational domain and the boundary conditions.

Figure 13: physical description for the fluid flow along a prism with a square cross section (a) and CFD description of the fluid flow along a meshed prism with a square cross section (b).

2.2.1 Fluids description and approximations

The fluids exhibit a molecular structure offering no resistance with the respect to external shear forces; deformations can occur when small forces act on the fluid. Both liquid and gases obey to the same laws of motion and they are considered as continuum in most of the applications, due to their macroscopic properties. Indeed, each fluid has its own characteristics and the constitutive models represent their mathematical formulation.

The viscosity affects each fluid generating shear stress. Indeed, based on the speed variations from low to high speeds (values depends on each single case), it is possible to cluster the properties as creeping flow (very low speed), laminar, transition and turbulent, respectively. Moreover, based of Mach's number (40):

$$M_a = \frac{V}{c}[adim] \tag{40}$$

where, V is the speed and c represents the sound speed in that fluid, another subdivision can be performed: incompressible ($M_a < 0.3$) and compressible ($M_a > 0.3$) fluids.

In current research simulations have been performed to assess the main characteristics for hulls tested inside a virtual towing tank and a steady-solutions are expected. Therefore, the flow has been considered as steady and 3D.

2.2.2 Governing equations

Mass, momentum and Reynolds Averaged Navier-Stokes (RANS) equations have been considered as the governing equations.

Firstly, the mass conservation equation is also called continuity equation; as the name suggests, it can be stated that the mass cannot be generate or destroyed inside a close system. Indeed, the flux of mass in a tiny control volume (but great enough to describe the characteristics for the fluid) can be obtained by the rate of mass flux through the volume bounding surface, as reported in equation (41):

$$\frac{\partial \rho}{\partial t} + \nabla \cdot (\rho \boldsymbol{u}) = 0 \tag{41}$$

where, $\rho, \boldsymbol{u} = (\boldsymbol{u}, \boldsymbol{v}, \boldsymbol{w})$ and $\nabla = (\partial/\partial x, \partial/\partial y, \partial/\partial z\,)$ represent the fluid density, the velocity vector and the space differential operator for a generic fluid, respectively. While, considering an incompressible fluid, the density can be considered as constant ($\partial \rho/\partial t = 0$); therefore, the continuity equation can be simplified and it can be represented in compact form or with the Einstein summation convention in Cartesian coordinate, as reported in equations (42) and (43), respectively:

$$\nabla \cdot \boldsymbol{u} = 0 \tag{42}$$

$$\frac{\partial u_i}{\partial x_i} = 0 \tag{43}$$

Secondly, the momentum equation reports that the flux among a control volume can be obtained by the rate of mass flux through the volume bounding surface added by the sum of forces acting on the control volume, as reported by equation (44):

$$\frac{\partial \rho \boldsymbol{u}}{\partial t} + \nabla \cdot (\rho \boldsymbol{u}\boldsymbol{u}) = \boldsymbol{F} + \nabla \cdot \boldsymbol{\sigma} \tag{44}$$

where, body forces are evaluated by $\boldsymbol{F}$ and $\boldsymbol{\sigma}$ represents the Cauchy's stress tensor.
With the respect to a Newtonian fluid, the Cauchy's stress tensor can be re-defined as reported in (45):

$$\boldsymbol{\sigma} = -\left(p + \frac{2}{3}\mu \nabla \cdot \boldsymbol{u}\right)\boldsymbol{I} + \mu[\nabla \boldsymbol{u} + (\nabla \boldsymbol{u})^{\boldsymbol{T}}] \tag{45}$$

where, μ represents the dynamic viscosity.
Considering both the generic momentum equation (44) and the Cauchy's stress (45), it is possible to define the momentum equation for a compressible Newtonian fluid, as reported in (46):

$$\rho\left(\frac{\partial \boldsymbol{u}}{\partial t} + \boldsymbol{u} \cdot \nabla \boldsymbol{u}\right) = -\nabla p + \nabla \cdot \mu[\nabla \boldsymbol{u} + (\nabla \boldsymbol{u})^{\boldsymbol{T}}] - \nabla\left(\frac{2}{3}\mu \nabla \cdot \boldsymbol{u}\right) + \boldsymbol{F} \tag{46}$$

Now, considering the incompressible fluid approximations, as defined by (42), and considering (45), it is possible to write the momentum equations for an incompressible fluid as reported in (47) and in (48), where the Einstein summation convention has been applied with the respect to the Cartesian coordinates, as proposed in Linde [74]:

$$\left(\frac{\partial \boldsymbol{u}}{\partial t} + \boldsymbol{u} \cdot \nabla \boldsymbol{u}\right) = -\nabla p + \mu \nabla^2 \boldsymbol{u} + \boldsymbol{F} \tag{47}$$

$$\frac{\partial u_i}{\partial t} + u_j \frac{\partial u_i}{\partial u_j} = -\frac{1}{\rho}\frac{\partial p}{\partial x_i} + \upsilon \frac{\partial}{\partial x_j}\left(\frac{\partial u_i}{\partial x_j}\right) + \frac{1}{\rho}F_i \; i,j = 1,2,3 \tag{48}$$

where, i, j represent the "i-th" element for the vector and υ the kinematic viscosity. Cao [75] reported that the momentum equations are also called the Navier-Stokes equations. Fefferman [76] defined the set regarding the problem of existence and smoothness for the 3D Navier-Stokes equations; indeed, Navier-Stokes equations are still nowadays unsolved for 3D turbulent flow cases and their solution figure among the seven Millennium Prize Problems, as announced by Clay Mathematics Institute (CMI) at a meeting in Paris held on May 24, 2000 [77].

A way to assess an approximate solution for the Navier-Stokes equations, when a turbulent flow occurs, is represented by the Reynolds Averaged Navier-Stokes (RANS) equations. In this approach, the Reynolds' decomposition is implemented; indeed, the flow variables can be divided into a mean component (time-averaged part) and a fluctuating component. Therefore, considering the mean values for the pressure, the velocity and the stress (denoted by P, U_i, and T_{ij}, respectively), and their fluctuating components (denoted by p', u_i', and τ_{ij}', respectively), it is possible to write their components as reported in (49), (50), (51), respectively:

$$p = P + p_i' \tag{49}$$

$$u_i = U_i + u_i' \tag{50}$$

$$\tau_{ij} = T_{ij} + \tau_{ij}' \tag{51}$$

Muzamal [78] reported that the mean value for the fluctuating components in equal to zero; this condition can be mathematically expressed as reported by equation (52):

$$\bar{p}' = \bar{u}_i' = \bar{\tau}_{ij}' = 0 \tag{52}$$

By dividing the flow variables, the time-averaged part and the fluctuating components, the mass conservation equation (41) can be written as (53); while, considering the zero value for the fluctuating components, the results are expressed by (54):

$$\frac{\partial(U_i + u_i')}{\partial x_i} = 0 \tag{53}$$

$$\frac{\partial U_i}{\partial x_i} = 0 \tag{54}$$

Moreover, considering both the momentum equations (47), (48) with the Cauchy's stress tensor applied on a Newtonian incompressible fluid with the Reynolds' decomposition for flow variables and the Reynolds' averaged approach, equation (55) can be obtained:

$$\frac{\partial U_i}{\partial t} + \frac{\partial\left(U_j U_i\right)}{\partial x_j} = -\frac{1}{\rho}\frac{\partial(P)}{\partial x_i} + \frac{1}{\rho}\frac{\partial\left(T_{ij} + R_{ij}\right)}{\partial x_j} + \frac{1}{\rho}F_i \tag{55}$$

where, the Reynolds' Stress is represented by R_{ij}, which formulation is reported in equation (56).

$$R_{ij} = R_{ji} = -\rho\overline{u_i' u_j'} \tag{56}$$

This stress denotes the connection among the fluctuating velocities components and represents an additional unknown quantity; therefore, considering the system of equations given by the mass conservation (54) and the RANS (55), it exhibits a not closed solution since the number of unknowns is higher than the number of equations. To assess the value for the Reynolds' Stress tensor, it is required a turbulence model.

2.2.3 Turbulence modelling

All the turbulence models deal with the need to model the Reynolds' stress tensor R_{ij}. Indeed, the turbulence modelling process works on defining a connection among the fluctuating component and its mean value in order to solve RANS equations. Over years many models have been developed as follows: Layton [79] reported that, in 1877, Boussinesq's assumption [80] postulated a dissipative effect on the mean flow exerted by the turbulent fluctuations, later on, adhering to Davidson's et al. historical recap on the "major events in the history of turbulence" [81], other approaches have been proposed by Prandtl (1925). While, in the past 40 years a great effort has been dedicated to define turbulence models, as Linde's declared [74] based on Wilcox et al., 1988 [82]. The presence of some constant among all these proposed methodologies represents their general formulas, and the values for these constants have been empirically evaluated; moreover, nowadays a turbulence model exerting for all the cases of interests is still undefined. Based on the formulation, the models can be divided into families, as follows: Reynolds' stress, both linear and nonlinear. With the respect to the linear ones, all of them works on the Boussinesq's approximation and it is possible to perform another sub-division based on the kind and quantity for the equations, such as models with zero-equation without transport equations for turbulent quantity and one or two equations based on turbulence transport can be listed.

As far as the viscous marine flows, as the resistance prediction for a hull running across the free surface, the RANS two-equations turbulence models are widely used, as reported by Pena et. al [83] who cited Terziev et al. [84]; more in details, most of their studies on these fields are based on $k-\varepsilon$ and $k-\omega$ models.

The $k-\varepsilon$ model, defined in 1973 by Lauder and Spalding [85], represents one of the widely used models in CFD applications. In this model, the turbulence kinetic energy k (which quantifies the mean kinetic energy per unity of mass connected with eddies) and its dissipation rate ε are defined through the transport equations solved at the same time with the once governing the mean flow characteristics. The first formulation for this model exhibits issues regarding particular conditions; indeed, as reported by Pena et al. [83] and considering Paterson et al. [86], the SST $k-\omega$ model exhibits ability to model fluids in particular conditions like pressure gradients, flow separation (which represent the typical condition for the stern part on modern ships). Despite these considerations, Dashtimanesh et al. [87] reported that the $k-\varepsilon$ model can give accurate results with the respect to the resistance evaluation for a ship running across the free surface.

The $k-\omega$ model postulate the existence for the turbulent eddy viscosity υ_t (which is not a fluid property but it represents a model assumption to work) evaluated through the analysis for some fashion to the mean flow variables, as reported by Day [88]. These statement account for the effects of the turbulence providing a measure about the intensity of the momentum transferred. The value for the eddy viscosity allows the estimation for the Reynolds' stresses and finally the equations system can be considered closed allowing the evaluation for an approximate result by CFD solvers. In order to define the value for υ_t, two equations account for the flow turbulent kinetic energy k and its specific dissipation rate ω (and as the symbol suggests, sometimes it is even called as the turbulent frequency), which represents the effects for the smallest turbulent structures, where flux energy is transformed into heat because of the viscosity.

Moving from Wilcox [82], who performed a critical review about the other turbulence modelling and defined a more suitable choice for the variables to better describe fluxes exhibiting adverse pressure gradient, the shear stress transport $k-\omega$ model ($k-\omega$SST) formulation has been proposed by Menter [89]. It is reported that improvements in performance with the respect to the original $k-\varepsilon$ and $k-\omega$ models have been achieved. Indeed, by considering Wilcox's methodology in the inner region of the boundary layer and switching through a blending function to the other model in the outer region, improved accuracy has been achieved near the boundary layer along with a sensitivity reduction for the freestream turbulence linked to the $k-\omega$ model. Moreover, as indicated by $k-\omega$SST model, in the near wall region an additional function limits the turbulent viscosity.

2.2.4 Discretization

Computational Fluid Dynamics uses computers to solve the governing equations in a discretized form. In order to discretize, the computational domain is divided into discrete points (nodes) and volumes (cells); the process to define this configuration is called meshing process (or grid generation). The grids can be divided into structured and unstructured. In the first case, each grid point is uniquely defined by indexes (i.e. i, j, k) and the cells type is hexahedral. This approach leads to easy correlate the cells and therefore, data can be evaluated by subtracting or adding indices by an integer and this is the great advantage; meanwhile, complex geometries cannot be regularly divided and this represents the disadvantage of this approach. Conversely, unstructured meshes are created without a specific order for the points and many kinds of grid can be listed (i.e. hexahedral, prisms, pyramids). When comparing this methodology with the structured one, the following advantages arise: a greater flexibility (based on the generation for the cells which is easier if compared with the other case), and refinements for the grid can be handled with ease, as reported by Johnson [90]; while, looking at the disadvantages, a higher memory is required along with a more complex data structure. Moreover, a comparison for a square of unit length (2D case) domain is reported in Figure 14: a structured discretization (rectangles in a 2D case with a stretching of 1.2 among the "i-th" row and the "i-th+1" one) is displayed in Figure 14a and an unstructured one (triangular shape for a 2D case) is reported in Figure 14b. Once the grid is available, the equations have to be discretized; among the available methodologies, three have been considered and listed from the most recent to the oldest, as follows: Finite Volume Method (FVM), Finite Element Method (FEM) and Finite Difference Method (FDM).

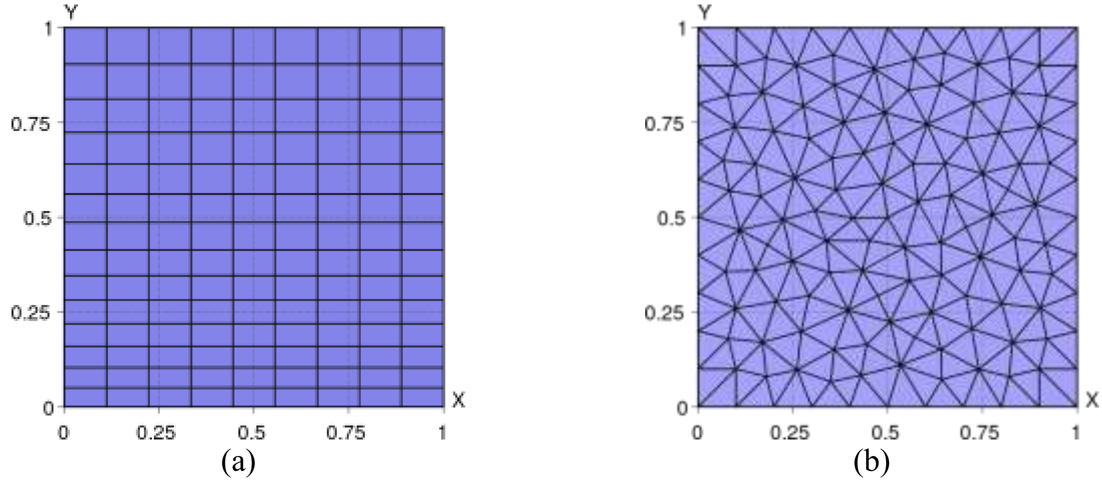

Figure 14: mesh discretization, structured (a) and unstructured (b) meshes.

Each computational method has to respect consistency, stability and convergence as primary properties; conservation, boundedness and accuracy as secondary. A brief description for each one of them follows. The consistency criteria postulates that the discrete equations should tend to the continuum PDE as the grids spacing tends to zero (which is true if an infinite number of cells is used in the computational domain); while, an algorithm can be considered as stable if it doesn't augmented the input or internal errors while running, and finally, considering the convergence, the scheme is said convergent if the solution for the equations tends to the exact solution for the continuum equation (The Lax Equivalence Theorem for Linear problem as reported by Mountain [91], and grid independence analysis for the non-linear problems).

As reported by Ortigueira [92], the first infinitesimal theory was developed by Newton and Leibniz in the 17th century. In 1798, Euler most likely utilized the finite difference method (FDM) to the numerical solution of the differential equations by employing the Taylor series expansion to equation (57), which can be approximated as a first order approximation by equation (58).

$$U(x_0 + \Delta x) = U(x_0) + \Delta x \left.\frac{\partial U}{\partial x}\right|_{x_0} + \frac{\Delta x^2}{2}\left.\frac{\partial^2 U}{\partial x^2}\right|_{x_0} + \cdots \tag{57}$$

$$\left.\frac{\partial U}{\partial x}\right|_{x_0} = \frac{U(x_0 + \Delta x) - U(x_0)}{\Delta x} + o(\Delta x) \tag{58}$$

This formulation can be applied to the governing equations and high-order derivatives can be used to increase the level of accuracy. This approach performs properly only if simple geometries have to be considered.

The Finite Element Method (FEM) was originally proposed in 1956 by Turner [93] for a structural analysis case; while, at the beginning of 90's it was applied to solve the Euler and Navier-Stokes equations. This approach is based on a rigorous mathematical foundation and uses an integral formulation working even on unstructured grids too; moreover, when a non-Newtonian fluid is considered, it is particularly appropriate. With the respect to the computational effort, FEM requires a significative amount; it can be assessed, for particularly cases, an equivalence among FEM and FVM and it can explain why this last one approach became more popular.

The Finite Volume Method (FVM) was originally proposed by McDonald in 1971 [94] for a two-dimensional gas turbine cascade. This method works with the integral formulation for the Navier-Stokes equations and discretizes the domain into control volumes; the surfaces integrals are evaluated on the volume surfaces, as reported by Johnson [90]. The cell-centered schemes can be used in order to define the position and the shape for the volumes; indeed, the flow variables are stored in the cell centre, and they are evaluated by considering the numerical fluxes across the cell faces. Considering a square of unit length (2D case) domain, a graphical representation displaying the cell-centered is depicted in Figure 15; indeed, the blue squares represent the control volumes, the red dots represent the cell centers, the blue dots represent the nodes and the orange lines represent the borders for the volumes.

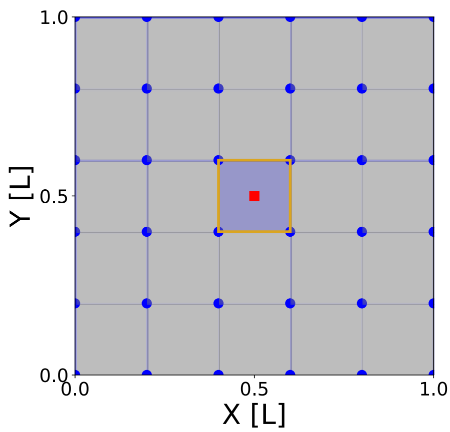

Figure 15: cell-centred discretization for Finite Volume Method (FVM).

With the respect to the evaluation for the quantity of interest on the face from the cell centers, different theoretical approaches are available, as follows: Central Differencing Scheme (CDS), Upwind Differencing Scheme (UDS), hybrid differencing scheme, Quadratic Upstream Interpolation for Convective Kinetics (QUICK) and the Total Variation Diminishing (TVD).

2.2.5 Free surface modelling

Two fluids are involved in the hydrodynamic behaviour of a ship sailing; indeed, when it runs, air and water interact with the hull generating perturbations with the respect to the velocity and pressure fields. Therefore, a numerical scheme is required to model the free surface and replicate the physics of this dynamic. Over years, several different theoretical approaches have become available. The first can be considered the Harlow and Welch' one [95] and defined as "marker and cell" method (MAC), where Lagrangian markers particles follows the distribution for the fluids into a fixed Eulerian field. Rider et al. [96] reported that in the early of 1970s, the first three volume tracking methods were published, and at that date can categorized into one of among piecewise constant, piecewise constant/stair-stepped, or piecewise linear categories, as follows: DeBar [97] algorithm implemented a sharper linear approximation, Nichols and Hirt [98] proposed the "volume of fluid" (VOF) approach according to which a single scalar displaying the fluid fraction for each cell of the domain replaced the Harlow and Welch' markers and finally Noh and Woodward's [99] implemented the Simple Line Interface Method (SLIC) where a constant by interval approximation was used. At the end of 1980s, Osher [100] proposed the so called the Level Set Method (LSM) to describe a propagating front with curvature dependent speed through an algorithm based on Hamilton-Jacobi Formulations.

Nowadays, one the most used approaches consists in the VoF approach considering its stability, accuracy and an affordable computational effort. In this method, the volume fraction α is described through a transport equation, as reported in (59) for incompressible fluids, for all the cells inside the numerical domain and can assumes a value among the value zero (which physically represents a cell full of air) and one (which represents a cell full of water); moreover, the free surface lies in the zone where α assumes the particular value of 0.5.

$$\frac{\partial \alpha}{\partial t} + \frac{\partial (\alpha u_i)}{\partial x_i} = 0 \tag{59}$$

To better define the free surface capturing approach and considering as test case the discretization for a 2D field where a generical sinusoidal wave (red curve) lays on, it is possible to assess the volume fraction α for each cell; moreover, considering the grid refinement, it is possible to better approximate the free surface based on the value for α=0.5. Based on this refinements, Figure 16 displays seven different cases, each one the them has been obtained by the following grids size (x- axis division equal to the y-axis one): 3x3 for Figure 16a, 5x5 for Figure 16b, 10x10 for Figure 16c, 15x15 for Figure 16d, 25x25 for Figure 16e, 50x50 for Figure 16f and 100x100 for Figure 16g. The pictures report the wave trace along with the volume fraction for each cell; red number exhibit the volume fraction for the cell across the free surface (for grid size bigger than 25x25 the values are not displayed as they would have been indecipherable); moreover, the comparison among the sinusoidal wave and free surfaces obtained by each one of the grids is available in Figure 16h and it is possible to appreciate the degree of approximation by changing the grid size.

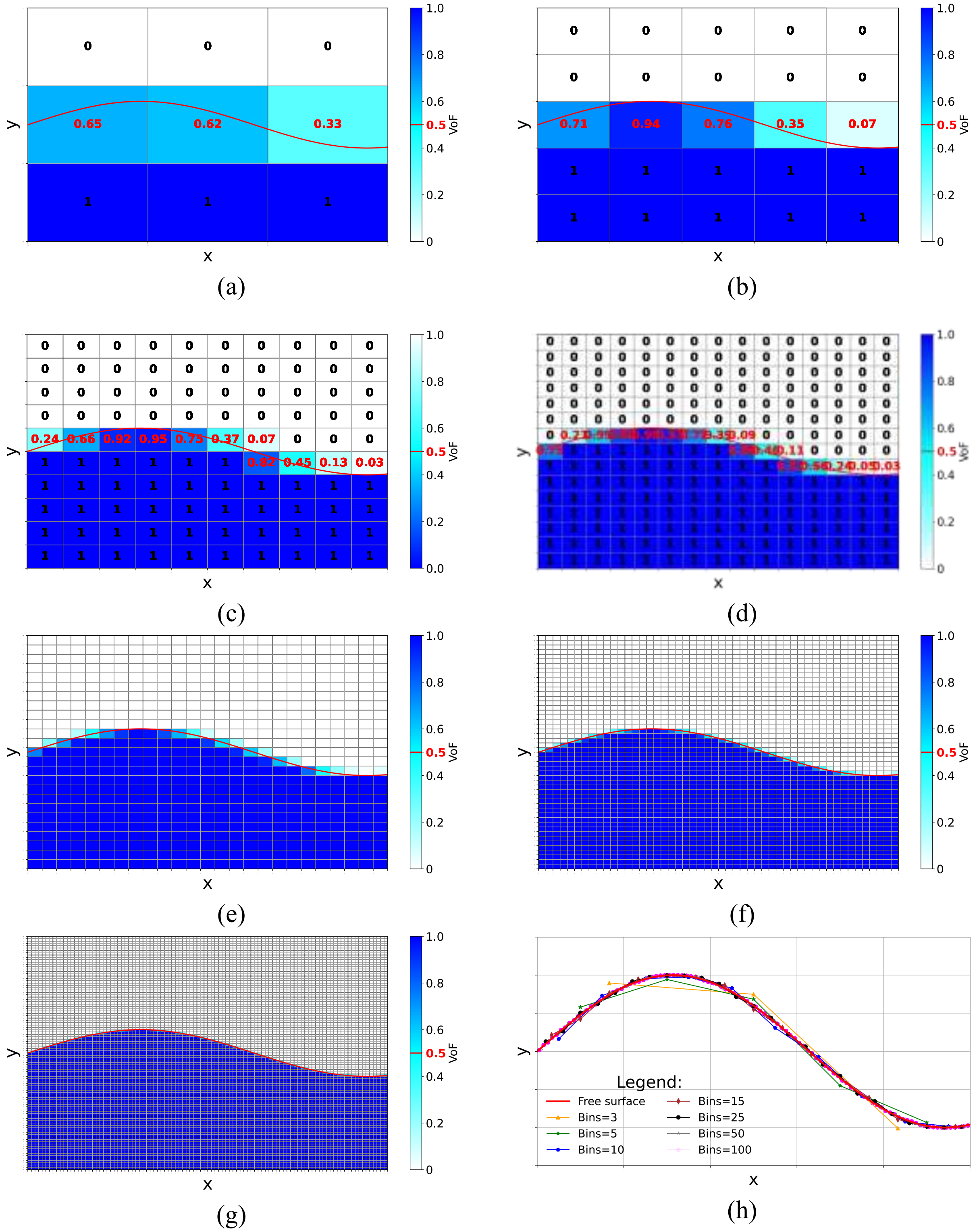

Figure 16: VoF approach to define the free surface for different grids size as follows: 3x3 (a), 5x5 (b), 10x10 (c), 15x15 (d), 25x25 (e), 50x50 (f) and 100x100 (g); free surface approximation (h).

2.2.6 Boundary conditions

To find a solution for the equations (48) describing the physical phenomena, boundary conditions are required. These descriptions have to reflect the physical condition, lead to get a unique, physical and stable solution, and finally to perform across all the equations, as reported by Greenshields [72]. The mesh boundary is divided into different regions, which name is defined as patches; each one of them has its own boundary condition.

Several type (theoretically infinite) of conditions can be derived on the patches. With the respect to a virtual towing tank study, which represents the case of interest for this work, the patches are identified as follows: upstream (inlet), downstream (outlet), side, centre symmetry plane, bottom, top and model, as reported in Figure 17a where each single patch has its own color and the trace for the free surface is painted is red; while, in Figure 17b the patches are reported at the course level grid along with the traces of the free surface (red lines).

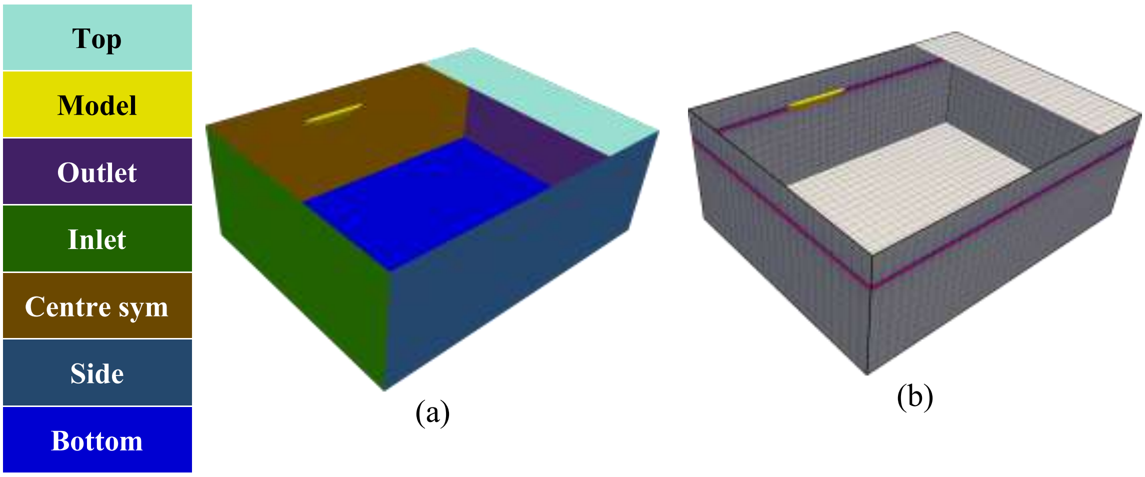

Figure 17: boundary patches name and position(a), discretization on boundaries (b); red lines represent the free surface.

With respect to the boundary of a mesh representing the limits for the computational domain and sometimes nothing physically (i.e. for a virtual towing tank the inlet boundary doesn't represent a physical wall), the most common types are described in next section as follows: fixed variable value (or Dirichlet condition, "fixedValue" in OpenFOAM suite) or its gradient along one direction, usually the normal to the surface (or Neumann "zeroGradient" in OpenFOAM suite) or their combination, as reported by Ferziger and Peric [101]; while, considering the wall boundary (as the hull of the ship inside the virtual towing tank), the no-slip condition can be applied. Table 9 exhibits the boundary conditions for current research; while, next to Figure 18a, where the boundary names are listed, their types are plotted and labelled in Figure 18b.

Table 9: boundary conditions.

Boundary Name	Type
Top	Symmetry plane
Model	Wall
Outlet	Pressure outlet
Inlet	Velocity inlet
Centre sym	Symmetry plane
Side	Symmetry plane
Bottom	Symmetry plane

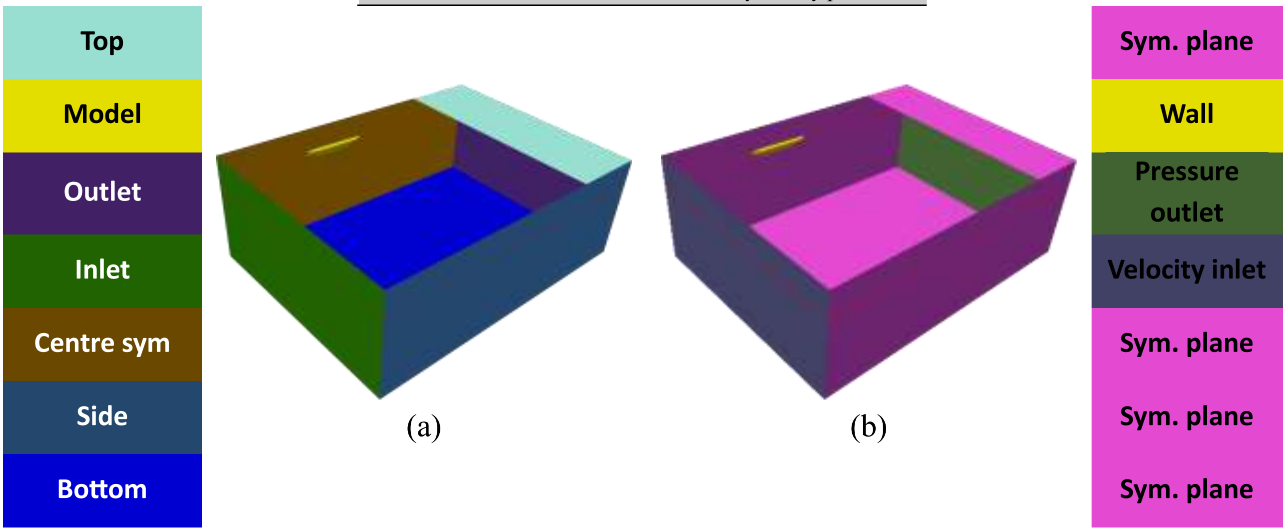

Figure 18: boundary patches name and position(a), boundary patches type (b); red lines represent the free surface.

2.2.7 Boundary layer

With the respect to the hull, the associated boundary type corresponds to a wall; a detailed focus is required to better identify the main feature connected to the physical description for the fluid behaviour. Indeed, when a bounded flux occurs, the evaluated quantities on the boundary (i.e. forces) are directly connected with the solver's ability to evaluate the behaviour in the boundary layer. From a numerical point of view, the characteristics for the flux can be evaluated through the nondimensional distance (normal) away from the wall (y^+) and the nondimensional velocity in the boundary layer and parallel to the surface of the wall (u^+); their formulations are available in equation (60) and (61), respectively:

$$y^+ = \frac{y u_\tau}{\upsilon} = \frac{y}{\delta_\upsilon} \qquad (60)$$

$$u^+ = \frac{u}{u_\tau} \qquad (61)$$

where, the normal distance to the wall is given by $y\,[m]$, the viscous scale $\delta_\upsilon = \upsilon/u_\tau$ and the frictional velocity by u_τ and it can be evaluated through the ratio among the square of the wall shear stress τ_w on the fluid density ρ as reported in equation (62):

$$u_\tau = \sqrt{\frac{\tau_w}{\rho}} \tag{62}$$

The nondimensional distance and velocity can describe the fluid within the boundary layer; indeed, considering a flat plate in a fully turbulent flow, all turbulent boundary layers obey to a universal behaviour when density and viscosity remain the same, as reported by Lauder and Spalding [85]. Different formulations are available to give a mathematical representation for the experimental results; moreover, three different zones (layers) can be observed in the range $y^+ = 0 \div 300$, as follows: viscous sub layer, buffer zone and log-law layer. Each one of them has its own characteristics, as reported in Figure 19. Considering the first one, u^+ and y^+ exhibit a linear connection because the viscous shear stress dominates among other contributions leading to a laminar flow within this layer; indeed, in the range $y^+ = 0 \div 5$, the red line represents the equation (63) which describe the linear correlation among parameters as follows:

$$u^+ = y^+ \tag{63}$$

While, the buffer zone lies within the range $y^+ = 5 \div 30$, which is in the middle among the other two regions. In this rage, it is not possible to appreciate any specific mathematical formulation; moreover, considering Figure 19, the green line connects the results from the borders of the two contiguous regions and a mix among turbulent and laminar flows can be observed. Finally, the log-law region exhibits a logarithmic trend among u^+ and y^+, within the range $y^+ = 30 \div 300$; the fuchsia line represents the equation (64), which is even known as "law of the wall":

$$u^+ = \frac{1}{k} ln(y^+) + C \tag{64}$$

where, $k = 0.4$ represents the von Kàrmàn constant and $C = 5$ another coefficient, as reported by Zhang [102]. Moreover, fluids exhibit turbulent characteristic within this range, as reported in the schematical representation in Figure 19.

For the sake of completeness, among all the mathematical formulation, it is possible to list the logarithmic–exponential (LOG-EXP) one, as recently proposed by Zhang [102] and reported in equation (65):

$$u^+ = \frac{1}{k} ln(1 + ky^+) + AB^2\left(1 - e^{-\frac{y^+}{B}} - \frac{y^+}{B} e^{-\frac{y^+}{B}}\right) + \prod sin^2\left(\frac{\pi}{2}\frac{y}{\delta}\right) \tag{65}$$

where, the second term in the right-hand side represents the added exponential part and A=0.314, $B = 4.775, \pi = 0.793$ represents the constant terms.

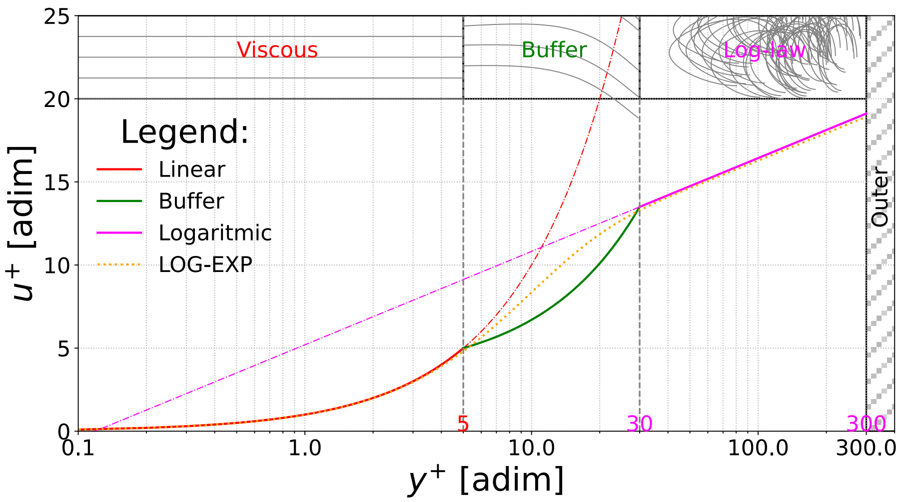

Figure 19: law of the wall in semi log coordinates.

Once the fluids' behaviour has been identified, it is possible to move through the numerical approach to solve the near-wall region; among all the available methodologies, two strategies can be implemented, as follows: the semi-empirical one, named "wall function", and the "wall-resolved" one. With the respect to the wall-function approach, if the height for the centroid of the first cell is in the log-law region (y^+ values within the range $30 \div 300$), as reported in Figure 20 where the first cell and its centroid are displayed, wall functions can be implemented to get the results in this region without directly solving the numerical issue and therefore, a lower computational effort is required.

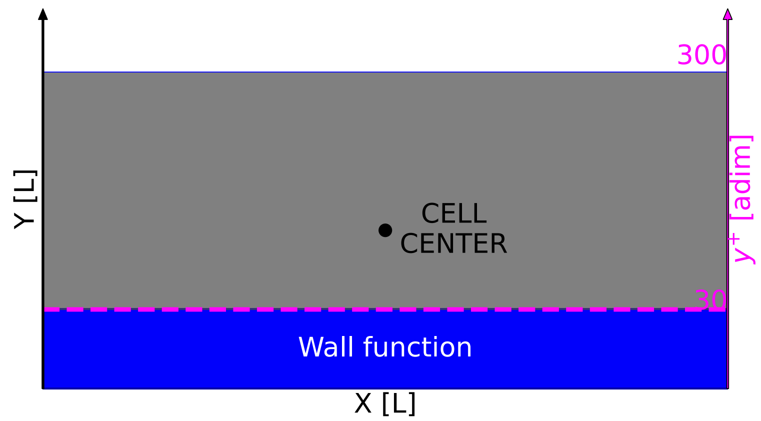

Figure 20: first cell mesh with centroid.

The height for the first cell can be defined based on the requested y^+. Its value can be therefore assessed by following a simple procedure: defining the theoretical height for the boundary layer thickness[2] by means of the estimated R_e and friction coefficient C_F with the respect to the characteristic length for an equivalent flat plate[3] and estimating the friction velocity (62) the first layer of the prism layer can be obtained. Despite the selected value, variations may be observed on

---

[2] The theoretical thickness for the boundary layer can be defined through $BL_{TH} = 0.16L\left(R_e^{-\frac{1}{7}}\right)$

[3] The one-seventh power law can be used, where $C_f = 0.0576R_e^{-\frac{1}{5}}$

the wall results because the effective y^+ is local velocity dependent. Therefore, if the computed y^+ values exceed the limit, the wall function approach is activated otherwise a wall resolved approach is considered by the code. While, for the near-wall solved approach, it is possible to solve directly the boundary layer flow. Indeed, by considering the y^+ value if this value lays within the range $0 \div 5$, the boundary layer flow can be numerically solved. In order to qualitatively compare the two kinds of approaches, two representations are available: Figure 21a shows the wall function approach and Figure 21b the other one. With the respect to the boundary layer, it is possible to appreciate the difference in the number of cells among the two approaches; indeed, the near-wall solved one requires a higher number of cells in order to get a higher level of accuracy.

In this study, among the theoretical available formulations, the $k - \omega$ SST one has been applied. These formulation account for the near wall region through the $k - \omega$ formulation, and far from the wall for the $k - \varepsilon$ one, which is a common way to deal with this kind of issue. As an example for this approach, Hull 20 ($F_r = 0.270$, yellow color) is displayed in Figure 22; more in details, result for y^+ are painted for the wetted surface in Figure 22a (model surface equal to $9.71945\ m^2$), Figure 22b accounts for the y^+ values below 30 (model surface equal to $0.09122\ m^2$) and Figure 22c reports the y^+ values within the range $30 \div 300$ (model surface equal to $9.62823\ m^2$). For the sake of completeness, 99% of the wetted surface belongs to the range $30 < y^+ < 300$, the lower values are recorded for two appendances: the rudder and the boss; therefore, with the respect to the y^+ value, the numerical set-up can be considered as affordable. These results have been obtained by running the DSUP numerical set-up described in paragraph 3.2.4.

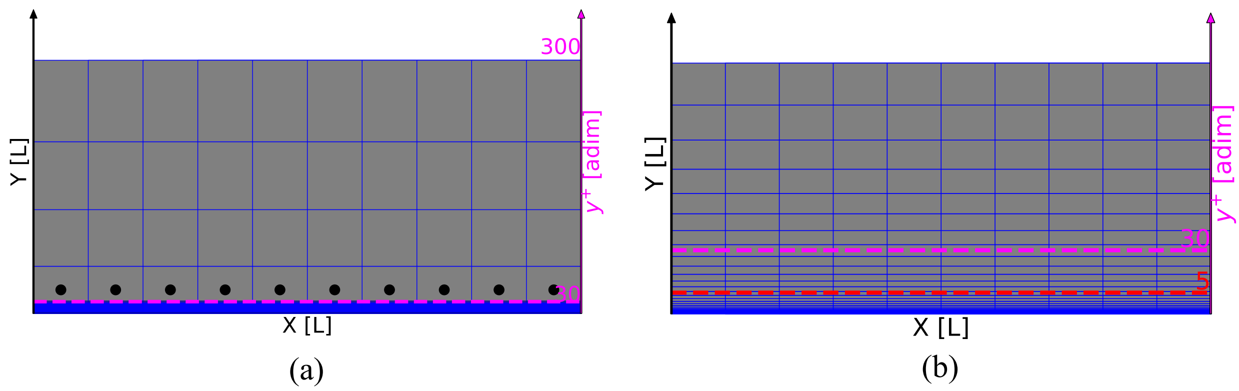

Figure 21: near wall region, wall-function modelling approach (a) and resolved approach (b).

2.3 Verification, Validation and Uncertainty assessment (VVUA)

When dealing with a physical measure, its value isn't something exact but exhibits an uncertainty; this uncertainty accounts for all the sources for the measurement errors. Before describing the procedures and the methodology to perform the uncertainty estimations, the concept of uncertainty has to be introduced. As the name suggests, the word "uncertainty" leads to the concept of doubt.

When different instruments measure the same physical quantity, different values arise and therefore the lack of exact knowledge for the representative value arises. The uncertainty assessment phases with the quantification of the level of confidence for that measure; even if the “truthfulness” about the result cannot be achieved, as reported by ITTC guide 7.5-02-01-01 [103]. This concept follows the International Organization for Standardization (ISO) Guide to the Expression of Uncertainty in Measurement (GUM and JCGM). More in details, the uncertainty can be considered as the error estimation, indeed the true value lays in the range $\pm U$ with a confidence of 95%, as reported by Mancini [55].

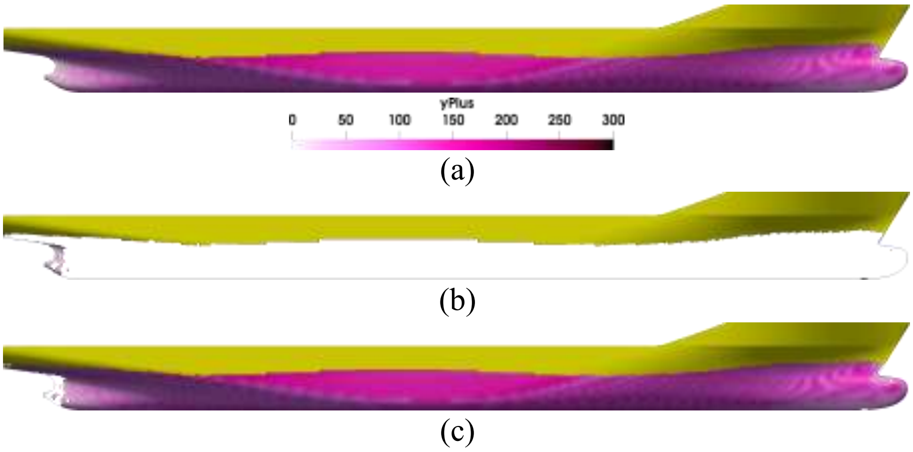

Figure 22: y^+ evaluation for Hull 20 in ballast condition ($F_r = 0.270$) with field function on the wetted surface; y^+ values (a), only $y^+ < 30$ (b), only $30 < y^+ < 300$ (c).

With the respect to the naval architecture field, two kinds of experiences can be performed to reproduce the reality: the experimental and the numerical ones.

In the first scenario, the experimental measures follow the ITTC procedure to assess the uncertainty. In the ITTC Register [24] it is possible to find different procedures to deal with the uncertainty; more in details, the procedures can be split into two different layers, as follows: instrumentation/calibration and testing/extrapolation. All these procedures account for the experimental errors (δ_D).

With the respect to the numerical description for the reality, the uncertainty issues are also present. In last 20 years different procedures has been developed to phase this issue. All the procedures perform the uncertainty assessment through the Verification and the Validation processes, commonly known as V&V. Based on this distinction it is possible to assess both the numerical and the modelling errors. Recently, the so called VVUA, acronym for Verification, Validation and Uncertainty assessment has been introduced by the ITTC procedure 7.5-03-01-01 [46] to deal with all the issues related to the uncertainty estimation.

Among all the theoretical probabilistic available approaches to phase with the VVUA, two families can be listed: statistical and non-statistical. The main difference among the approaches consists in the effort required to assess the uncertainty; indeed, the statistical methods usually require a higher effort when compared with the non-statistical one. The statistical methods account for a large number of variables as input parameter to assess the output repeatedly and use statistics (mean and variance) to evaluate the output; while, the other type of methods implement an analytical structure which requires less computational effort. With the respect to the probabilistic statistical method, the following one can be listed: Monte Carlo (MC), Latin Hypercube Sampling (LHS), Stochastic Collocation (SC); while, considering the probabilistic non-statistical methods, the Moment (or perturbation) and the Spectral methods can be listed.

In current research, being the *Single Participant To Multiple* (SPTM) approach implemented to multiple hulls shapes and following to the practical published methods usually implemented among the ITTC members, the non-statistical approach has been followed. More in details, among the non-statistical methods, the perturbation one has been selected and based on the sensitivity derivatives.

2.3.1 Uncertainty assessment, key concepts

Adhering to Oberkampf and Blottner approach [104], the uncertainty arises from each phase of the modelling and simulation process; the sources for the uncertainty can be divided into sub components, as follows: physical modelling, discretization-solution, programming and computer round-off. Moving from the reality and considering both the experimental and the numerical set-up, the workflow to assess the VVUA is presented in Figure 23. As depicted by the pink field, the uncertainty assessment accounts for both the verification (blue rectangle) and the validation (brown rectangle) parts; each one of them phase with a particular issue. Indeed, adhering to Oberkampf and Blottner [104], Verification and Validation try to assess if the governing equations are solved right and if the governing equations are able to describe the physics of the problem, respectively. In both cases, mathematical and procedural algorithms are implemented by the theories to perform the VVUA.

In order to find the VVUA, all the sources of uncertainty are considered separately and connected with the modelling assumptions, the numerical solutions and the experimental field. The first source of uncertainty comes from the modelling error, δ_{SM}; all the doubts about the model geometries, graphical simplifications, boundary conditions, fluid properties and mathematical equations are evaluated through δ_{SM}. It can be mathematically expressed by equation (66), as proposed by Stern et al. [50]:

$$\delta_{SM} = M - T \tag{66}$$

where, M and T represent the model value and the true one, respectively.

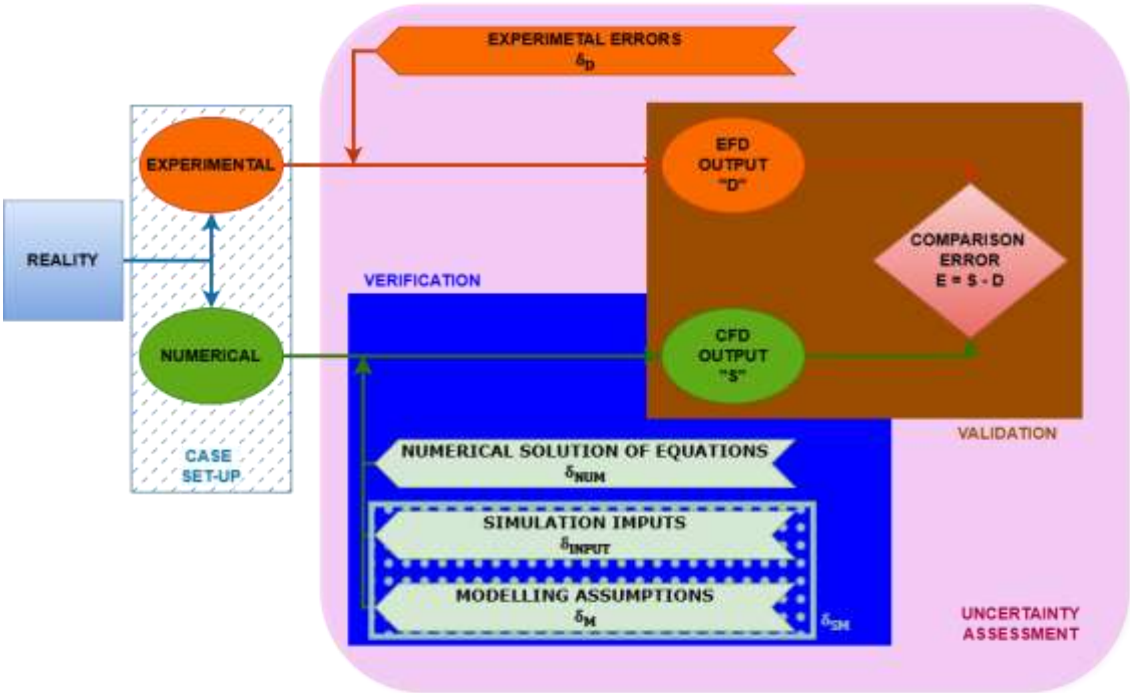

Figure 23: Verification, Validation and Uncertainty assessment workflow.

The second source of uncertainty to phase with is represented by the numerical error for the solution of the mathematical equations, δ_{SN}; this error accounts for the discretization issues and the round-off errors and can be mathematically expressed by equation (67):

$$\delta_{SN} = S - M \tag{67}$$

where, S represents the simulation result. Therefore, combining these two errors, it is possible to both assess the simulation error, δ_S, and uncertainty, U_S, as reported by equations (68) and (69):

$$\delta_S = \delta_{SM} + \delta_{SN} = S - T \tag{68}$$

$$U_S = (U_{SM}^2 + U_{SN}^2)^{0.5} \tag{69}$$

where, S and T represent the simulation result and the truth, respectively and the subscripts "M" and "N" stand for Modelling and Numerical, respectively. Under particular conditions (such as when an exact mathematical solution exists), it is possible to define the numerical simulation error through equation (70):

$$\delta_{SN} = \delta_{SN}^* + \varepsilon_{SN} \tag{70}$$

where, δ_{SN}^* represents the sign with the magnitude for the numerical simulation error and ε_{SN} stands for the error estimation. In a similar manner it is possible to derive the correct simulation value, S_C, its error, δ_{S_C}, and its uncertainty U_{S_CN}, as reported by equations (71), (72), (73):

$$S_C = S - \delta_{SN}^* = S - (\delta_{SN} - \varepsilon_{SN}) \tag{71}$$

$$\delta_{S_C} = S_C - T = \delta_{SM} + \varepsilon_{SN} \tag{72}$$

$$U_{S_CN} = \left(U_{SM}^2 + U_{S_CN}^2\right)^{0.5} \tag{73}$$

With the respect to the evaluation for the errors, the stochastic and deterministic approaches can be listed to assess them; scientific debate is still opened in order to define which method performs better along with the way to account for them in the uncertainty analysis, as reported by Stern et al. [50].
In the following two sub-paragraphs, a detailed analysis about the verification approaches to assess the numerical uncertainties and about the validation procedure to define the simulation modelling assumption are presented. For the sake of completeness, the validation procedure is based on the comparison among the results for the towing tank experience and the numerical one.

2.3.2 Verification

All the theoretical available approaches for the verification procedure aim to assess the numerical uncertainty, U_{SN}, and when it is possible, the sign and the magnitude for the error, δ_{SN}. The verification has to be performed both on the code and the solution. In current research the open-source code OpenFOAM has been used to perform all the simulations, and therefore, the code verification isn't required because it is considered as already achieved by the code developers and the verification procedure has to phase with the uncertainty estimation for the solution.
As reported by equation (74), (75), the analysis for U_{SN} and δ_{SN} can be carried out by considering the following sources of uncertainty and errors separately: grid size (U_G, δ_G), iteration number (U_I, δ_I), time step (U_T, δ_T) and other parameters (U_P, δ_P).

$$U_{SN} = (U_I^2 + U_G^2 + U_T^2 + U_P^2)^{0.5} = U_I^2 + \sum_{j=1}^{J} U_j^2 \tag{74}$$

$$\delta_{SN} = \delta_I + \delta_G + \delta_T + \delta_P = \delta_I + \sum_{j=1}^{J} \delta_j \tag{75}$$

The error estimate can be similarly decomposed, as reported by equation (76):

$$\delta_{SN}^* = \delta_I^* + \sum_{j=1}^{J} \delta_j^* \tag{76}$$

By considering the "corrected approach" it is possible to define the corrected simulation, S_C, and its numerical uncertainty as reported by equations(77), (78):

$$S_C = S - \left(\delta_I^* + \sum\nolimits_{j=1}^{J} \delta_j^*\right) = T + \delta_{SN} + \varepsilon_{SN} \longrightarrow S = S_C + \left(\delta_I^* + \sum\nolimits_{j=1}^{J} \delta_j^*\right) \quad (77)$$

$$U_{S_C N} = U_{I_C}^2 + \sum\nolimits_{j=1}^{J} U_{j_C}^2 \quad (78)$$

The second part of equation (77) leads to consider the simulation value as the corrected one added with a correction based on the numerical error.

The non-statistical methodologies nowadays available implement different ways to account for the numerical results based on the theory proposed by Richardson and known as Richardson Extrapolation (RE) [47]. This theory is based on the power series expansion, and when it is applied on discrete numerical results (as for instance the results from different simulations), it is able to extrapolate other value addressing the variation for one input parameter. With the respect to the CFD, in what follows different theoretical approaches are going to be described. Even if the discretization can be performed by using structured and unstructured meshes, these theories remain equally pertinent.

2.3.2.1 Convergence study

When dealing with discrete results, the convergence study represents the first step toward the numerical uncertainty evaluation. This approach accounts for the change of one parameter (the one of interest), while the others remain unchanged. A minimum number of three solution is required to let the procedure working. When dealing with the uncertainty for the numerical towing tank where a steady-state solution is expected, equation (74) can be simplified to equation (79) by considering as main sources for the uncertainty the grid size and the iteration number, as defined by Stern et al. [106]:

$$U_{SN} = (U_I^2 + U_G^2 + U_T^2 + U_P^2)^{0.5} \cong (U_I^2 + U_G^2)^{0.5} \quad (79)$$

Adhering to the findings from Huang et al. [107] and Lakatoš et al. [108], it is possible to perform another approximation; indeed, usually the most relevant contribution to the uncertainty arises from the grid size, and therefore, the iteration number uncertainty can be neglected, as reported by equation (80) for the uncertainty and by equation (81) for the numerical error:

$$U_{SN} \cong (U_I^2 + U_G^2)^{0.5} \cong U_G \quad (80)$$

$$\delta_{SN} \cong \delta_I + \delta_G \cong \delta_G \quad (81)$$

Based on these simplifications, the input parameter for the convergence study can be represented by the ratio among the characteristic measure for the mesh. This ratio is commonly called as refinement ratio parameter, r_K, and can be expressed as reported by equation (82):

$$r_K = \frac{\Delta X_{K_i}}{\Delta X_{K_{i-1}}} \tag{82}$$

where, X_{K_i} represents the characteristic dimension for the mesh "i-th"; for a 3D case, it can be evaluated as proposed by Celik et al. [51], and as reported by equation (83), or it can be represented by grid cells number.

$$\Delta X_{K_i} = \frac{\sqrt[3]{\sum_{i=1}^{N} \Delta V_i}}{N} \tag{83}$$

where, ΔV_i represents the single "i-th" volume cell and N the total number of cells. The choice for the refinement parameter operates among two antithetical conditions: adequate diversification among the two-grid considered to assess it and computationally affordable. Among the scientific community, a mutually agreed value for the grid refinement factor, $\widetilde{r}_K$, hasn't been yet defined, the suggested value is 2 but in a 3D case it means an increase of 2^3 for the number of cells and it may be computationally unaffordable. Based on literary review, the value for the refinement factor can be chose equal to $\sqrt{2}$ [57] or 1.3 [51].

When a structured mesh is used to discretize the domain, a hierarchical decrease/increase for the cells size occurs and the refinement factor remains unchanged, as reported by equation (84):

$$r_K = \frac{N_1}{N_2} = \frac{N_2}{N_3} = const. \tag{84}$$

with, $N_1 > N_2 > N_3$; conventionally it is possible to define $r_{21} = N_1/N_2$ and $r_{32} = N_2/N_3$. While, considering the cases where unstructured meshes are used to discretize the domain, the hierarchical decrease/increase cannot be obtained *tout court* all over the domain. This last finding, differently to equation (84), leads to account for a possible variation among the grid refinement factor when considering three different results, as reported by equation (85):

$$r_{21} \neq r_{32} \tag{85}$$

Adhering to the same footer notation, the solution for the grid 1 (N_1) can be indicated as $\hat{S}_1$, the one for grid 2 (N_2) as $\hat{S}_2$ and so on till the "N-th" grid (N_N), where the solution can be indicated as $\hat{S}_N$. Based on three solutions, it is possible to define the convergence ratio parameter, R, as reported by equation (86):

$$R = \frac{\varepsilon_{21}}{\varepsilon_{32}} = \frac{\left(\hat{S}_2 - \hat{S}_1\right)}{\left(\hat{S}_3 - \hat{S}_2\right)} \tag{86}$$

Once the value for the convergence ratio parameter has been evaluated, it is possible to define the relation among the results. Indeed, as reported by Table 10, it is possible to understand the tendency displayed by the results varying the refinements based on R. Therefore, it is possible to define the numerical uncertainty by applying RE only when the monotonic convergence is achieved; while, if an oscillatory convergence occurs, it is only possible to bound the numerical uncertainty through equation (87):

$$U_{SN} = 0.5 \cdot \left(\hat{S}_{UP} - \hat{S}_{LOW}\right) \tag{87}$$

where, $\hat{S}_{UP}$ represents the higher value solution and $\hat{S}_{LOW}$ the one with the lower.

Table 10: types of convergence.

ID	Function properties	R	Richardson Extrapolation	Numerical Uncertainty assessment	
				Possible	U_{SN}
R_01	Monotonic convergence	$0 < R < 1$	YES	YES	Different approaches
R_02	Oscillatory convergence	$-1 < R < 0$	NO	Bounded Uncertainty	Equation (87)
R_03	Monotonic divergence	$R > 1$	NO	NO	NO
R_04	Oscillatory divergence	$R < -1$	NO	NO	NO

Finally, when divergence or oscillatory divergence are achieved, nothing can be said about the numerical uncertainty and further investigations are required. The graphical characteristics for these types of convergence are displayed in Figure 24; the dots represent the simulations results varying the grid refinement along with the interpolant function, which trace is a dashed-dotted line. The monotonic increasing convergence $(R = 0.12)$ and the decreasing one $(R = 0.16)$ are shown in Figure 24a and Figure 24b, respectively; while the oscillatory convergence $(R = -0.54)$ is represented in Figure 24c. Finally, the divergence $(R = 1.20)$ and the oscillatory divergence $(R = -1.83)$ conditions are displayed in Figure 24d by red and purple colors, respectively. The three solutions approach accounts for the hill dependence issue. Indeed, considering a generic curve exhibiting a sinusoidal behaviour (which can be considered as representative for a numerical noise issue), when the three points lays on this didactical curve, a local trend can be identified as the global one. Therefore, based on R value, it is possible to identify an incorrect trend; Figure 25 graphically demonstrate this issue, where the results (green dots) can be approximate by a sinusoidal function (dashed-dotted green line). Based on the available results, it is possible to choose R_01 $(r_K = 1.0, 1.25, 2.25)$ and R_03 $(r_K = 1.5, 2.75, 3.75)$ as representative different triplets of points and later on it is possible to assess the R values; with the respect to the two cases, R_01 (blue squares) displays a monotonic convergence $(R = 0.25)$, while, in the second one (red squares) a divergence condition can be observed based $(R = 1.25)$.

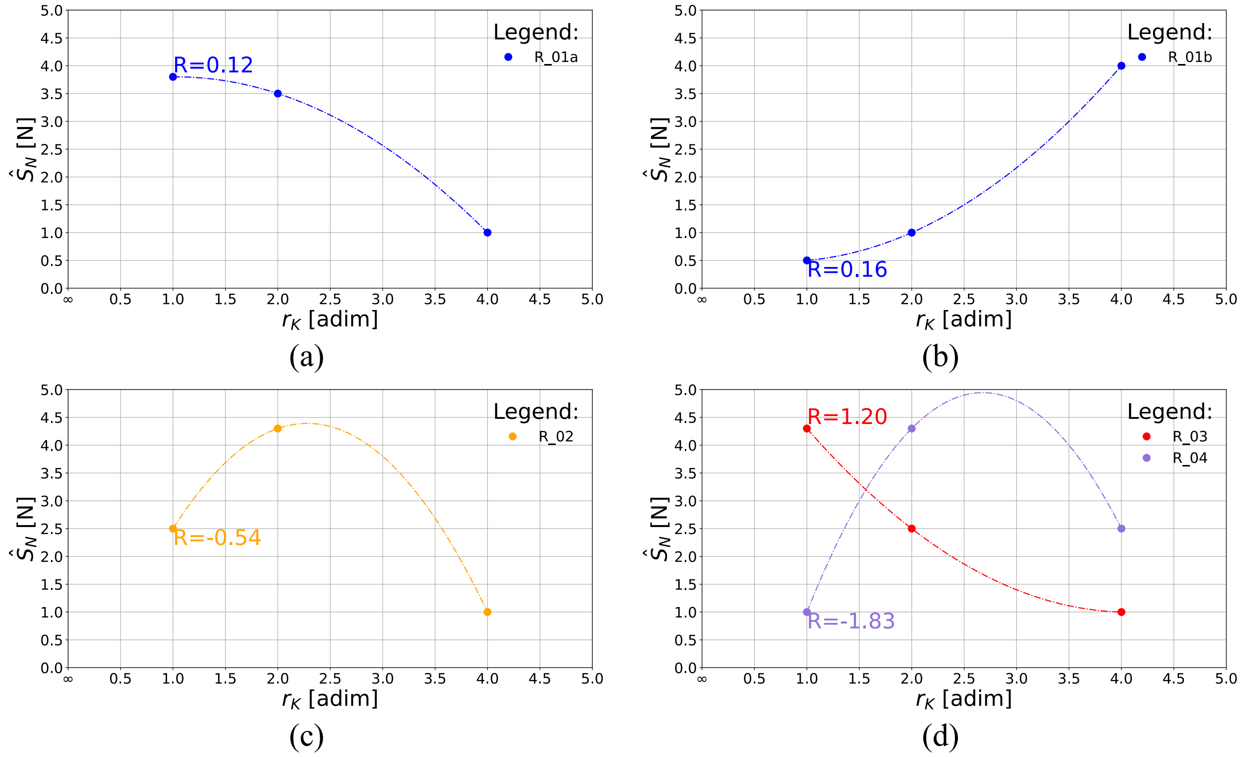

Figure 24: type of convergence, monotonically increasing convergence (a), monotonically decreasing convergence (b), oscillatory convergence (c), divergence and oscillatory divergence.

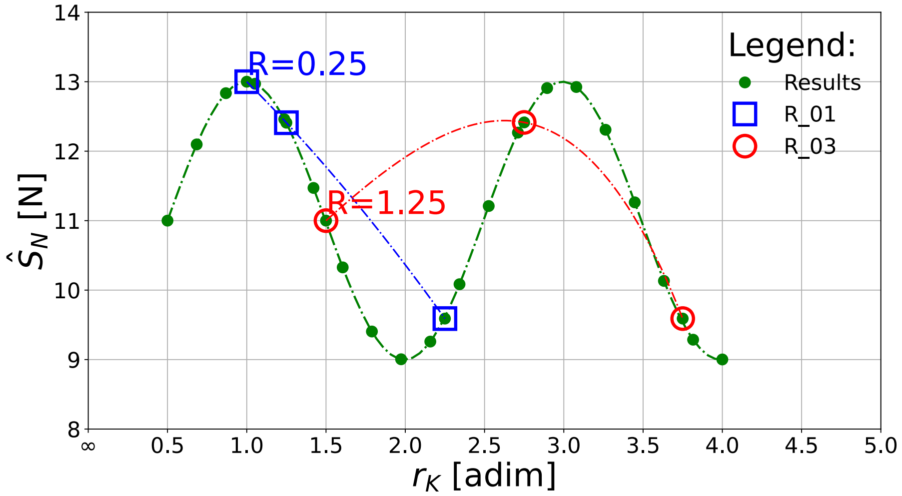

Figure 25: characterizations of the convergence of a sinusoidal function.

To further address these issues, other theoretical approaches are available as described later on. The Eça and Hoekstra's one [53] has been chosen among the available methodology because it is based on the Least Squares Root (LRS) approach, and by definition it can phase with discrete variables with the attempt to overcome the described limitations by using at least four different results.

When dealing with pointwise variables, as usually happens for the numerical naval architecture, and before describing the theoretical approaches to assess the numerical uncertainty, the convergence analysis leads to a first preliminary conclusion. Indeed, in order to assess the type of convergence, a minimum number of three solutions is required; moreover, based on their values, two different conditions can occur: firstly, a “false” trend can be identified because of the hill dependance issue, and secondly, it is possible to assess the numerical uncertainty only if the results account for a monotonic convergence. It is just possible to bound U_{SN}, when the oscillatory convergence is achieved, or nothing else can be said in the other cases. To overcame the hill dependance issues, and the type of convergence, other approaches account for different techniques to approximate the mean behaviour for the results. When comparing these techniques with ones based on the grid convergence issue, the number of required solutions changes (at least four versus three), but the power series expansion is always used to estimate the error based on RE considering the variation for the mesh size. With the respect to both the number of solutions and the required minimum increase for the grid refinement, the increase of one more solution to account for the numerical uncertainty can represent a significantly greater computational effort. Indeed, based on the available computing infrastructure, it is possible to assess the computational time required to solve the same simulation changing the number of cells; as reported by the data, the increase in the computational time exceeds the linear factor as the number of cells increase. This behaviour can be observed in Figure 26a, where the dots represent the trace for time required by each simulation. Therefore, based on this data, it is possible to extrapolate the computational time required to solve the simulation changing the number of cells. With the respect to Figure 26b, and considering as coarser mesh a computational domain composed by 1M cells (Simulation ID=1), it is possible to perform a couple of refinements based on the following values for the refinement factor: $R_1 = 1.3$ (blue dots) and $R_1 = 2$ (red squares). If the computational time required to solve the 1M cells mesh is 8 hours, it is possible to appreciate how rapidly this time grows up; indeed, if one refinement occurs (Simulation ID=2), the computational time reaches 25 hours for the lower refinement factor and 125 for the other, respectively.

In the following, different theoretical available approaches to perform a Verification analysis are described, based on these general considerations regarding the mesh sensitivity analysis.

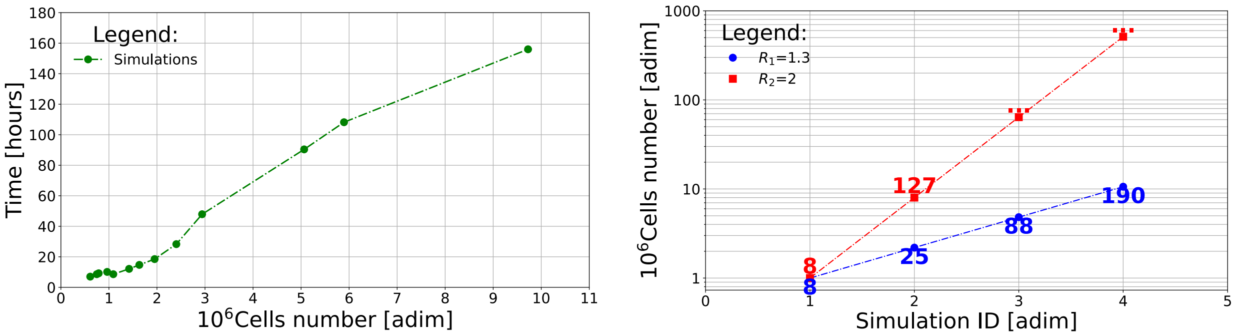

(a) (b)

Figure 26: computationally time effort varying the number of cells (a) increase in computational effort varying the number of cells for the mesh sensitivity analysis (b).

2.3.2.2 Generalized Richardson Extrapolation (RE)

When three solutions are available, among all the theoretical cases for R, generalized Richardson Extrapolation (RE) can be used to assess a result for the numerical uncertainty estimation only when a monotonic convergence occurs. In RE theory, the numerical solution can be defined using the apparent order of accuracy, p, defined in equations (88):

$$p = \frac{ln(\varepsilon_{k_{32}}/\varepsilon_{k_{21}})}{ln(r_k)} \tag{88}$$

through the asymptotic error expansion $\hat{S}_i = \hat{S}_\infty + kr_i^p + \ldots$, where k is a coefficient. Therefore, the discretization error is assumed to asymptotically converge to zero as an infinitely fine discretization occurs (the grid spacing tends to zero).

2.3.2.3 Celik et al.

A procedure for estimation and reporting the numerical uncertainty has been proposed by Celik et al. [51]. This procedure defines a guidance in order to apply RE, bases on three different simulation results through five different steps. The first step intents to identify a representative measure to define the following refinements; while, in the second phases the refinement factor among two different meshes is proposed (as previously defined, the suggested value for r should be no smaller than 1.3) and suggested as constant by varying the meshes, as reported by equation (84). With the respect to the third step, the apparent order of accuracy, p, is defined based on the results from the three available solutions, as reported by (89), (90), (91). These equations can be solved using a fixed-point iteration, starting from $q(p) = 0$ until a constant refinement is achieved. Once p has been defined, it is possible to implement RE and assess the extrapolated value, S_{ext}^{21}, as defined by (92).

$$p = \frac{1}{ln\, r_{21}} |ln|\varepsilon_{32}/\varepsilon_{21}| + q(p)| \tag{89}$$

$$q(p) = ln\left(\frac{r_{21}^p - s}{r_{32}^p - s}\right) \tag{90}$$

$$s = 1 \cdot sgn(\varepsilon_{32}/\varepsilon_{21}) \tag{91}$$

$$S_{ext}^{21} = \left(\frac{r_{21}^p S_1 - S_2}{r_{21}^p - 1}\right) \tag{92}$$

This value represents the evaluated value, when the cells number tends to ∞, which denotes the physical condition of a continuum domain. Finally, it is possible to define the numerical uncertainty through the so-called Grid Convergence Index, GCI, after the evaluation of the approximated (e_a^{21}) and the extrapolated (e_{ext}^{21}) relative errors as reported by equations (93), (94), (95), respectively:

$$GCI_{fine}^{21} = \frac{1.25 e_a^{21}}{r_p^{21} - 1} \tag{93}$$

$$e_{ext}^{21} = \left| \frac{S_{ext}^{21} - S_2}{S_{ext}^{21}} \right| \tag{94}$$

$$e_a^{21} = \left| \frac{S_1 - S_2}{S_1} \right| \tag{95}$$

For the sake of completeness, even if non directly reported, the 1.25 value in equation (93), can be considered as the correction based on a factor of safety, as proposed by Roache [105].

2.3.2.4 Stern et al.

As stated by Wilson and Stern et al. [106], a correction for the approximation can be fitted based on the availability of an analytical benchmark. In this scenario, the correction factor [106] and/or the factor of safety approaches, as proposed by ITTC 7.5-03-01-01 [46] with the respect to Roache [105] can be listed. Therefore, based on equation (76), it is possible to assess the accuracy for the error based on the power series expansion; indeed, considering a constant grid refinement factor and the leading term for the expansion, δ_{RE}^* and p can be evaluated through equations (96) and (88), respectively:

$$\delta_{RE_k}^* = \frac{\varepsilon_{k_{21}}}{r_k^{p_k} - 1} \tag{96}$$

When the grid refinement factor isn't constant, the transcendent implicit equation (97) leads to the evaluation of the theoretical order of accuracy:

$$p = \frac{ln\left(\varepsilon_{k_{32}} / \varepsilon_{k_{21}}\right)}{ln\left(r_{k_{21}}\right)} + \frac{1}{ln\left(r_{k_{21}}\right)} \left[ln\left(r_{k_{32}}^p - 1\right) - ln\left(r_{k_{21}}^{p_k} - 1\right) \right] \tag{97}$$

With the respect to the factor of safety approach, F_S, adhering to Roache's theory [108], it is possible to multiply the evaluated numerical uncertainty by the factor itself, as reported in (98):

$$U_{SN} = F_S \left| \delta_{RE_k}^* \right| \tag{98}$$

The value for the factor of safety can be assessed through different formulations. Roaches proposed $F_S = 1.25$.

While, based on the statistical analysis for both analytical and numerical benchmarks samples, as reported by the last ITTC procedure for the Uncertainty Analysis [46], Xing ed al. [52] defined a formulation based on the distance metric P and the statistical analysis. Indeed, considering both the value of the distance among the theoretical order of accuracy and the one obtained from RE and the statistics, the P value and the factor of safety one can be defined through (99), (100), respectively:

$$P = \frac{p}{p_{th}} \tag{99}$$

$$U_{SN} = F_S(P)\left|\delta^*_{RE_k}\right| = \begin{cases} (2.45 - 0.85P)\left|\delta^*_{RE_k}\right| & 0 < P \leq 1 \\ (16.4P - 14.8)\left|\delta^*_{RE_k}\right| & P > 1 \end{cases} \tag{100}$$

2.3.2.5 Eça and Hoekstra

As reported by Eça and Hoekstra [53], when dealing with the numerical uncertainty estimation, different contributions lead to the global assessment for it; among the contributions, the grid refinement error exhibits the highest influence, when compared with the iterative and the round off errors. The power series expansion represents one way to account for the grid refinement error. The following assumptions lead the procedure to perform properly: all the results for the grids have to be in the asymptotic range and a single parameter enables the description for the grid. When complex geometries and turbulent flow represent the case to study, it becomes very had to satisfy both of the described conditions. Indeed, these issues affect the unstructured meshes, where noisy data appears both because it is not possible to guarantee a geometrical similarity of the grids and by the presence in the turbulence model of flux limiter and damping functions. In order to overcame these limitations, typical for approaches to three solutions, the Least Squares Root method (LSR) has been introduced by Eça and Hoekstra. Indeed, when four different simulations results are available by changing the grid size (usually evaluated through the number of cells), it is possible to define a fit curve which minimize the differences among the scattered results, and apply the power series expansion as reported by equation (101):

$$S_i = S_0 + \alpha h_i^p \tag{101}$$

where, S_0 represents the exact solution, and the refinement factor $h_i = \sqrt[3]{1/N_i}$. The order of accuracy usually implemented by the codes is a second-order scheme, it is possible to assess the error by considering the contributions from equations (102), (103), (104), (105).

Considering the data range parameter, Δ_S, to evaluate the quality for the fit as reported by (106), it is possible to assess the value for the numerical uncertainty U_{SN} for the "i-th" solution, based on (107).

$$\epsilon_S \cong \delta_{RE} = S_i - S_0 = \alpha h_i^p \tag{102}$$

$$\delta_1 = \alpha h_i \tag{103}$$

$$\delta_2 = \alpha h_i^2 \tag{104}$$

$$\delta_{12} = \alpha h_i + \alpha h_i^2 \tag{105}$$

$$\Delta_S = \frac{(S_i)_{max} - (S_i)_{min}}{(n_g) - 1} \tag{106}$$

$$U_{SN_i} = \begin{cases} F_S \epsilon_S + \sigma + |S_i - S_0| & \sigma < \Delta_S \\ \dfrac{3\sigma}{\Delta_S}(\epsilon_S + \sigma + |S_i - S_0|) & \sigma \geq \Delta_S \end{cases} \tag{107}$$

where, based on the p value, the following value for the ϵ_S can be considered. If $p > 2$, ϵ_S value coincides with minimum value for the standard deviation (σ) evaluated among the δ_1 function and δ_2 one, defined through equations (103) and (104), respectively; while, if the p value lays in the interval $0.5 \leq p \leq 2$, the error is equal to the RE one, as reported by equations (102); finally, when $p < 0.5$, the minimum value among the standard deviations defined for the δ_1, δ_2 and δ_{12} cases is considered. With the respect to the factor of safety, F_S, its value can be defined based on the observed order of accuracy (p) and the data range parameter, Δ_S, as follows: $F_S = 1.25$ if p lays in the interval if $0.5 < \mathrm{p} \leq 2.1$ or $F_S = 3$ otherwise.

2.3.3 Validation

Once the numerical uncertainty has been evaluated, it is possible to move the validation analysis. The simulation modeling errors, U_{SM}, and the δ_{SM} comparison error, when conditions permit, can be evaluated through current the verification procedure. In this scenario, the recorded differences among the experimental results and the numerical ones are considered along with the mathematical modelling errors.

As reported by equations (68), the difference between the simulation result (S) and the truth (T) is named simulation error (δ_S); this error can be further subdivided into the modelling error (δ_{SM}) and the numerical error for the solution of the mathematical equations (δ_{SN}) components. Using equation (108), it is possible to define the comparison error, E:

$$E = D - S = \delta_D - (\delta_{SM} + \delta_{SN}) \tag{108}$$

where, D represents the data value and δ_D the error in data and defined as reported in equation (109).

$$\delta_D = D - T \tag{109}$$

The comparison error δ_{SM} can be split into the error from use of previous data (δ_{SPD}), and error from modelling assumption (δ_{SMA}). Therefore, it is possible to assess E and the uncertainty for the comparison U_E, as reported by equation (110) and (111):

$$E = \delta_D - (\delta_{SMA} + \delta_{SPD} + \delta_{SN}) \tag{110}$$

$$U_E = \sqrt{U_D^2 + U_{SMA}^2 + U_{SPD}^2 + U_{SN}^2} \tag{111}$$

Based on the unavailability for U_{SMA}^2, it is theoretically impossible to assess U_E. As reported by equation (112), the validation uncertainty (U_V) considers all the uncertainties and leads to define if the verification has been achieved:

$$U_V = \sqrt{U_D^2 + U_{SN}^2} \tag{112}$$

When dealing with the obtained values for the validation uncertainty, the comparison error and the programmatic uncertainty, U_{REQD}, six different combinations can occur, as reported by Table 11:

Table 11: validation cases.

ID	**CASE**	**V&V**	**BELOW REQUEST UNCERTIAINTY**	**REQUEST FOR MODEL INVESTIGATIONS**
1	$\|E\| < U_V < U_{REQD}$	ACHIEVED	COMPLIANT	NO
2	$\|E\| < U_{REQD} < U_V$	ACHIEVED	COMPLIANT	NO
3	$U_{REQD} < \|E\| < U_V$	ACHIEVED	NOT COMPLIANT	YES
4	$U_V < \|E\| < U_{REQD}$	NOT ACHIEVED	COMPLIANT	NO
5	$U_V < U_{REQD} < \|E\|$	NOT ACHIEVED	NOT COMPLIANT	YES
6	$U_{REQD} < U_V < \|E\|$	NOT ACHIEVED	NOT COMPLIANT	YES

With the respect to the cases defined in Table 11, the validation is achieved at the validation uncertainty level for cases ID1, ID2 and ID3; while, being the validation uncertainty lower than the comparison error, the validation isn't achieved for the other cases (ID4, ID5 and ID6). Moreover, when comparing the value for the comparison error with the value for the requested uncertainty, if further investigations need to be addressed for the cases where $U_{REQD} < |E|$ (ID3, ID5 and ID6).

This page is intentionally left blank

3 Numerical set-up

When tackling a scientific problem with the objective of deriving information and results, to be sure and confident about them, the analyzed data have to cover all the possible scenario. Therefore, considering the question "how precise is a Computational Fluid Dynamics (CFD) calculation when compared with an Experimental Fluid Dynamics (EFD) result?" as driver activity for current research, ensuring that the full spectrum of relevant factors has been considered is of paramount importance. To get an answer to this question, with the respect to the total advance resistance for the model to test without the presence of the propeller behind the hull, two kinds of data have been considered: the towing tank experimental result $\left(R_{T_{M}\_EFD}\right)$ and the numerical one $\left(R_{T_{M}\_CFD}\right)$, respectively. As the names suggest, although both of them want to represent the same physical force, the methods used to evaluate the total advance resistance for the model change substantially: in the first case, based on Froude's law, the value for the force is obtained by means of the towing tank experiment, where a model hull is towed by a carriage equipped with sensors able to read the quantity of interest; while, following Froude's law even in the second case, a virtual representation for the model hull and the towing tank is replicated inside a numerical environment to get the same quantity acting on the surfaces of the model.

Considering the virtual towing tank, differently from the EFD case, the evaluation for the advance resistance and the other quantity can be carried out without the need for a very expensive dedicated infrastructure, as it only requires computing resource nowadays quite easily found on the market. During the height of the Fifth Industrial Revolution (RI5) even known as "Society 5.0", as reported by Ziatdinov [109], and which is still running nowadays, a single commercial workstation is able to compute this resistance and all the other quantities of interests (like the 3D wake, the vertical and the horizontal planar motion and the longitudinal wave cut). If another type of computing infrastructure, like a High-Performance Computing (HPC), is available, it possible to perform the same calculation in a much shorter time compared with the one required from the workstation, alternatively, a simulation may be carried out with a significantly higher number of cells (of the order of tens millions), thereby offering a more precise depiction of the physical discretization of the problem. Indeed, as reported by Abidin et al. [110], if a higher number of cells is implemented (i.e. 97 million), the error obtained is smaller when compared to the one obtained with the case with few cells (13 million).

In this Chapter, the workflow used to identify the numerical set-up implemented to replicate the physical experience is presented. Firstly, the model length has been considered as the driver parameter to get a scalable tool and all the other dimensions are defined accordingly to specific rules arising from the best practice. Secondly, the initial in-house developed set-up (later on defined through the acronyms of ASUP) is tested and iteratively modified in different ways (BSUP and CSUP configurations) to derive the final version (later on defined as DSUP) used to perform all the simulations. Moreover, in order to implement the *Single Participant To Multiple* (SPTM) approach to all the simulations performed, as defined in the first Chapter, a detailed analysis on the tuning for the numerical set-up is going to be described in current Chapter.

3.1 The numerical set-up

Single Participant To Multiple (SPTM) approach requires a numerical set-up to run. In order to perform for all the cases from the available database (22 different hulls), this set-up has to be parametrized based on the ship dimensions and needs to be validated before run all the simulations.

When performing a simulation, three main parts have to be addressed, as follows: pre-processing analysis, solving and post-processing. In order to perform all the analysis, the software used in this study are the one listed as follows:

- Open-Source Field Operation and Manipulation (OpenFOAM) version 8: it is an open-source code for CFD simulations; it is able to solve turbulent-multiphase flows and generate unstructured meshes. It is used for the all the three parts of the simulation because of the presence of utilities, meshing tools and other application able to perform in each one of the parts for the simulation.
- ParaView (version 5.6.0): it is an open-source software able to visualize and analyze 3D cases. It is used in the post-processing analysis to check the consistency for the simulations.
- python (version 3.11): it is a high-level, multi-purpose and interpretate programming language. It is used both to match the simulations tools available in the OpenFOAM environment and the representation (graph) for the results.

With the respect to the pre-processing and the solve phases, a finite volume method with cells centered variables performing for a multiphase physic for two fluids (air and water) considered as immiscible and isothermal has been used inside a numerical domain discretized by unstructured mesh. Moreover, based on the results from Bozzo et al. [63] for a fast twin-screw propeller ship, the volume of fluid approach has been used to model the interface among the two fluids, and because of a steady state solution is expected for the physical issue, a quasi-steady approach has been selected. Considering the OpenFOAM environment, the following utilities has been used to generate an unstructured mesh: cfMesh and blockMesh; while, in the solve phase, the interFOAM solver with the Local Time Step (LTS) option have been used. Moreover, following the outcomes from Villa et al. [111], in order to define the dynamical attitude for the model with the respect to the trim and sinkage, a mesh morphing approach has been considered in correspondence of four different check-points, where the dynamical and statical buoyancy are compared with the displacement and the new is evaluated. A characterization process has run to calibrate all these utilities and libraries to define the standard test case.

In the next three sub paragraphs, a systematical analysis for refinements, domain dimensions, turbulence models and Courant number selection, are described. Courant number (C_O) is defined as reported in equation (113):

$$C_O = \frac{u\Delta t}{\Delta x} \leq C_{MAX}\ [adim] \tag{113}$$

where u represents the flow speed, Δt the local time step and Δx the cell dimension. In current research, this kind of study represent a key point because when considering the number of hulls to be tested, the required computational effort isn't negligible, and therefore, a compromise among effort and accuracy has to be found.

3.2 Mesh generation

In the pre-processing analysis, the geometries for the hull to be tested and the numerical domain have to be considered. The hulls described in current research are designated in accordance with the nomenclature reported in Annex 1, adhering to the following code identification: Hull XX, where XX stands for the identification number.

With the respect to the hull, the geometry has to be implemented in STereoLithography (STL) format. The hull description is made by triangular planar surfaces; considering a single triangular surface, its sides must coincide with those of the adjacent boundary triangular surfaces; the expression "water tight" refers to a hull surface made by triangular planar surfaces displaying this property. Usually, the geometries for the hull are in available in Initial Graphics Exchange Specification (IGES) format. This format accounts for curves and surfaces and needs to be remeshed in order to get a STL format, as described in Chapter 4. Moreover, each triangular surface should, ideally, display an equal length among the sides; it rarely happens but if the ratio among the sides is high, convergence issues can occur in the code. Figure 27 exhibits the geometry for Hull 20; while, the comparison among the surface and the triangulated one along with a red rectangle are reported in Figure 27b, and finally, the surface inside the red rectangle from Figure 27b displays the details for the STL surface of the hull in Figure 27c. It is possible to verify how the borders from each triangle are mutually connected.

Once the hull geometry has been defined, it is possible to move to the mesh generation. To get a parametrical set-up, it is important to define the key parameter to use in order to replicate the same configuration for each one of the 22 hulls. The ITTC "Practical Guidelines for Ship Resistance CFD" (7.5-03-02-04) [112] refers the minimal dimension for the domain to the model length; therefore, in current research the model length has been chosen as the key parameter to scale the dimensions for the domain, adhering to the ITTC recommendation. Indeed, based on the model length, the dimensions for the domain are defined along with the refinements inside the domain.

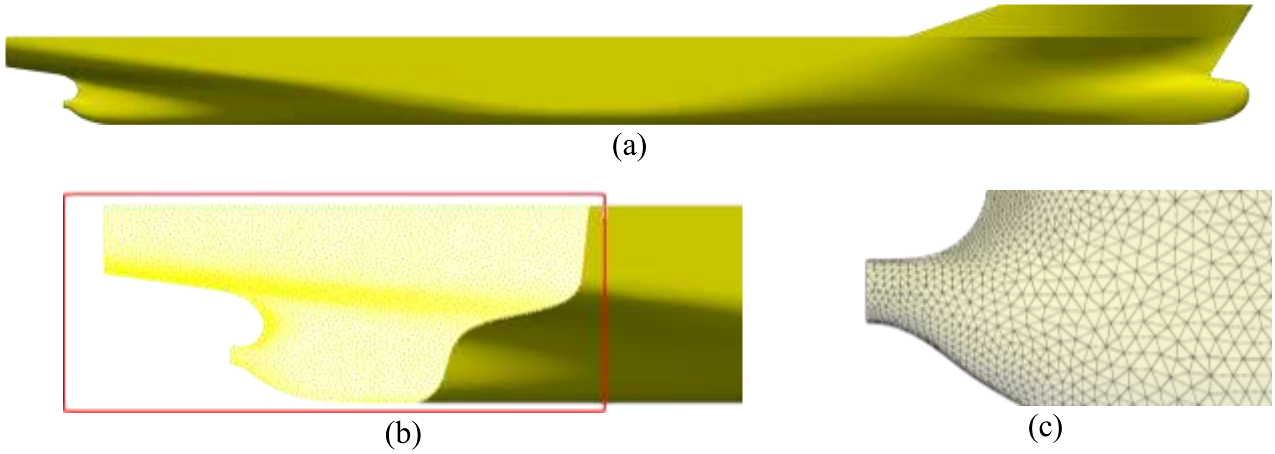

Figure 27: STL representation for Hull 02.

Therefore, based on the symmetry condition connected to the expected symmetry for the case to study and considering an initial numerical set-up, later on identify as Alpha Set-Up (ASUP), it is possible to define the parametrical dimensions for both the domain and refinements. Considering just as an illustrative example a model length between perpendiculars is 7.278m and the geometries for Hull 20, the computational domains and characteristics are reported in Table 12 and displayed in Figure 28. As previously defined in Chapter 2, among the available options for the boundary condition, the one reported in Table 13 have been implemented. The wall condition occurs for the hull, and if necessary, even in the presence of appendages. Based on this condition, it is possible to phase with the boundary layer. As reported in Chapter 2, it is expected a boundary layer close to the surfaces for the model. The velocity profile changes moving forward to the wall, indeed the value for the speed is null next to the wall and reaches the nominal value at the end of the boundary layer.

Table 12: domain size for Hull 20.

Boundary distances	Value [m]	Times Model length [adim]
Upstream	18.195	2.50
Down-stream	18.195	2.50
Lateral(*)	9.243	1.27
Top	3.639	0.50
Bottom	9.461	1.30
Domain_X	36.390	5.00
Domain_Y(*)	9.243	1.27
Domain_Z	13.100	1.8

(*) Dimension referred to the semi-domain.

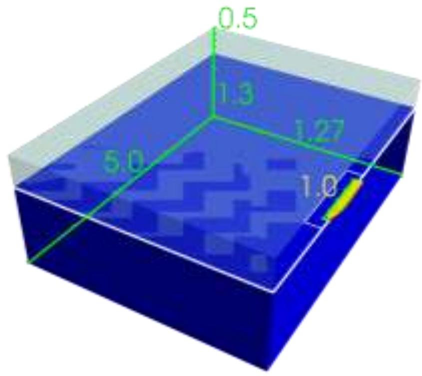

Figure 28: domain parametric dimension.

Table 13: boundary conditions.

Boundary Name	Type
Top	Symmetry plane
Model	Wall
Outlet	Pressure outlet
Inlet	Velocity inlet
Centre sym	Symmetry plane
Side	Symmetry plane
Bottom	Symmetry plane

As initially proposed by Prandtl and later on balanced with coefficients, the height for the boundary layer can be evaluated through the “one-seventh power law” profile for turbulent flows, as reported in equation (114):

$$BL = \frac{0.16 \cdot L}{{R_e}^{(1/7)}} \ [L] \tag{114}$$

where, R_e represents the Reynold’s number and L the characteristic length (for the hull it is equivalent to the model length, for the appendages it can be expressed as the chord length for the rudder, and so on for the others one). In order to reduce the computational effort to solve the boundary layer, a wall function approach has been selected. To get affordable results, the value for the non-dimensional distance from the wall (y^+) has to be within a well-defined range. Equations (60), (61), (62) report the mathematical formulation for y^+, $u^+$and u_τ, respectively.

Adhering to ITTC recommendations for Ship CFD Applications (7.5-03-02-03) [113], the non-dimensional distance from the wall has to lay within the range $30 \div 100$; while, in Cui et al. [114] it is possible to find a range $30 \div 300$. In current work a maximum value of 150 has been fixed along with a prescribed grading on of 1.2. Therefore, once the value for y^+ has been fixed, it is possible to generate a number of layers to lead the centroids of the first cells to the right value for the non-dimensional distance from the wall. In order to get this kind of set-up, the cells have to be trimmed, and therefore, from a structured mesh generated in the far field, with a predominance of hexahedral volumes, a trimmed one is obtained. Considering a hull without appendages as Hull 20, the results for the near-wall region are depicted across a longitudinal view in Figure 29a, and other detail like the stern part, the shaft and the forebody are displayed by Figure 29b, Figure 29c and Figure 29d, respectively.

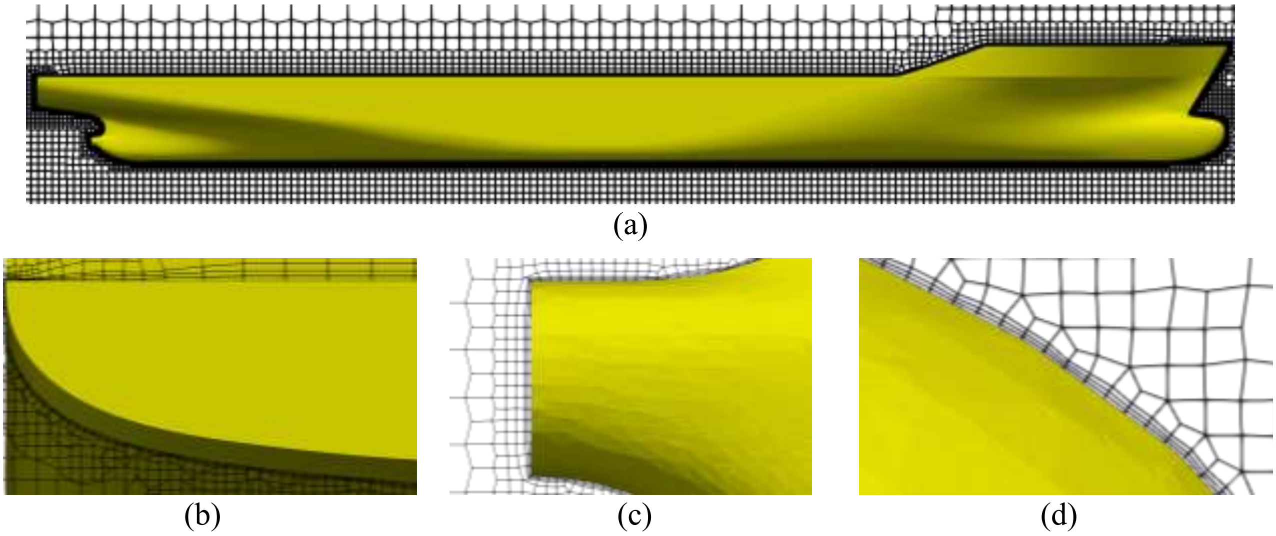

Figure 29: near-wall region for Hull 20, global view (a), detail for the stern (b), the shaft (c) and forebody (d); scale among representations differs.

While, considering a case for a model tested with appendages, the boundary layer thickness has to be evaluated for each one of the appendages in the same way as described for the hull. Indeed, considering Hull 03 as test case, the mesh for the near-wall region is reported in Figure 30 and other details like the stern part, the shaft-end-part, and the forebody are displayed by Figure 30b, Figure 30c and Figure 30d, respectively.

Moving away from the hull, mesh refinements have to be designed; indeed, three types of refinements are implemented to capture the flow field. With the respect to the Hull 20, Figure 31 displays a 3D view about the boundary for the refinements with the following code color: red for the box across the hull position, green for the prismatic one with isosceles triangular-base (with the Kelvin's angle, 38° 56', in the vertex position) and blue for the free surface. Each type of refinement has its own characteristics as listed below. The red case contains 5 boxes, and with the respect to the trace for the central symmetry plane, each one of them exhibits a hierarchical mesh coarsening, with cell size doubling as the distance from hull increases. Figure 32a reports a 3D representation for the boxes, and Figure 32b displays the detail with the halving of the number of cells when moving away from the wall. Moreover, changing the color for the boxes, the refinements change moving from the coarsest (red), passing thought intermediate (respectively pink, cyan, and violet) to reach the finer one (green).

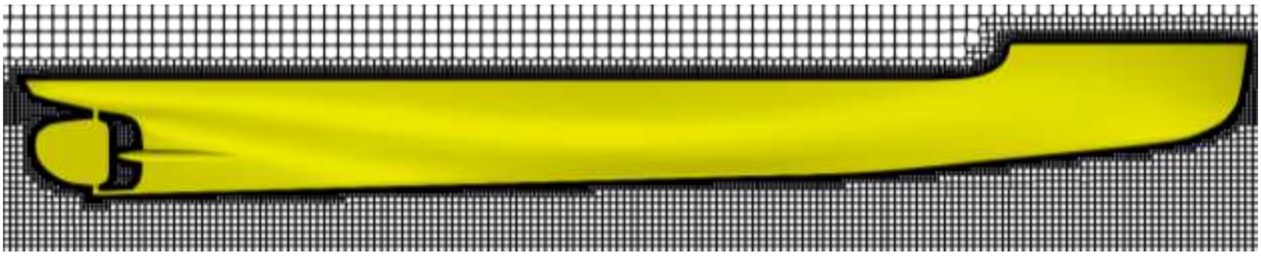

(a)

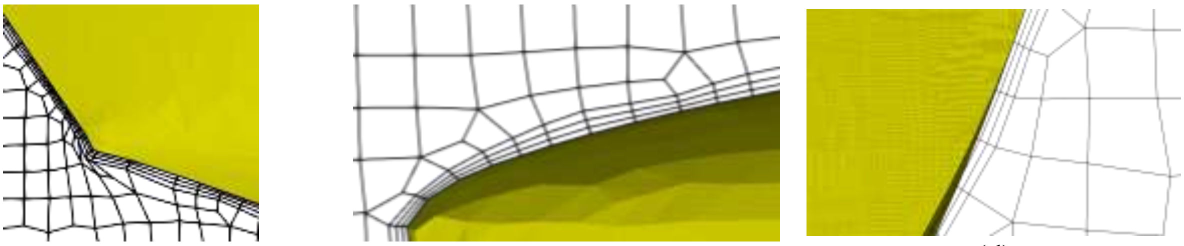

(b) (c) (d)

Figure 30: near-wall region for Hull 03, global view (a), detail for the stern (b), the shaft line (c) and forebody (d); scale among representations differs.

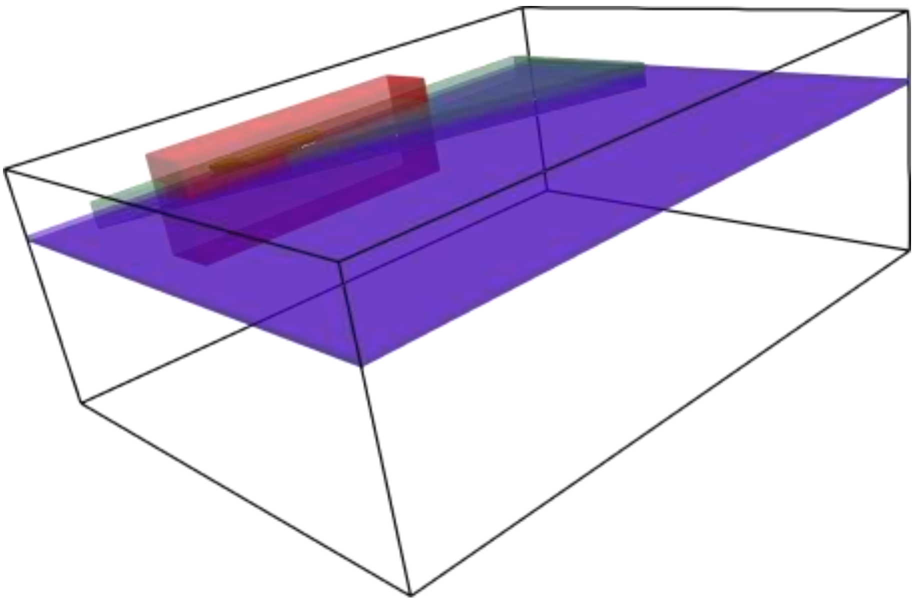

Figure 31: domain and refinements considering Hull 20 as test case.

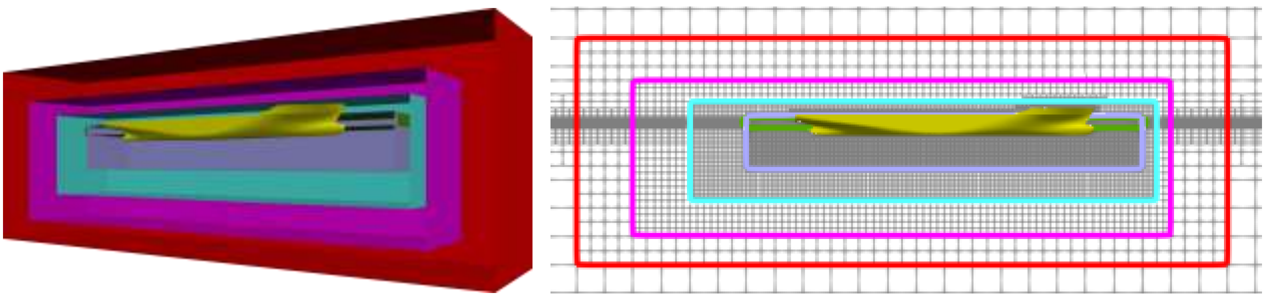

(a) (b)

Figure 32: domain refinement for Hull 20; 3D view about the 5 boxes (a) and symmetry plane details across the hull position (b). Different scales have been used to better capture the details.

While, the green prismatic refinement with isosceles triangular-base is made by two different prisms. Figure 33a reports a 3D representation for the prisms, and Figure 33b displays the detail with the halving of the number of cells when moving away from the wall. Moreover, changing the color for the prisms, the refinements change moving from the coarsest (dark green), to reach the finer one (orange).

(a)

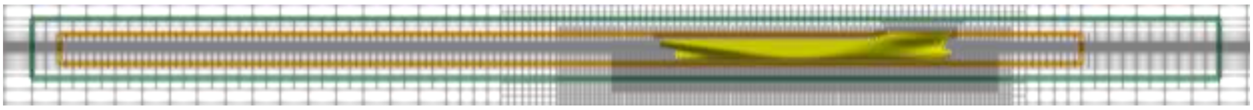

(b)

Figure 33: domain refinement for Hull 20; 3D view about the prismatic refinement with isosceles triangular-base (a) and symmetry plane details across the hull position (b). Different scales have been used to better capture the details.

Lastly, for the free surface an anisotropic refinement with the respect to the vertical direction has been implemented across all the surface, as reported by Figure 34.

(a)

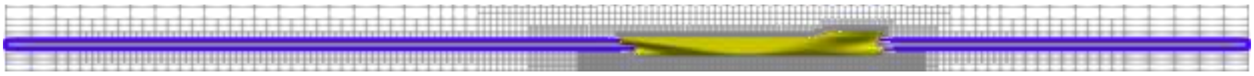

(b)

Figure 34: domain refinement for Hull 20; 3D view about the free surface refinement (a) and symmetry plane details across the hull position (b). Different scales have been used to better capture the details.

Finally, it is possible to get a general overview about the refinements by considering all the representations for Figure 35, where refinements and their traces are displayed on the symmetry plane (Figure 35a), on the water plane (Figure 35b) and the transverse plane (Figure 35c). Changing the hull dimension, the refinements display always the same ratio among them because of the presence for a parametric tool to generate them.

Considering the boundary layer for the walls and the three typologies for the refinements, the ASUP has run on Hull 15 ($F_r = 0.350$). With the respect to the advance resistances, the post processing analysis displayed a noisy signal for the total resistance of the hull and it doesn't achieve the convergence in less than 30000 iterations, as reported in Figure 36.

Based on both this noisy signal and the modern, complex hull shape (a bulb and a transom stern are both present), Hull 15 has been selected as "the test" case for performing the numerical set-up customization.

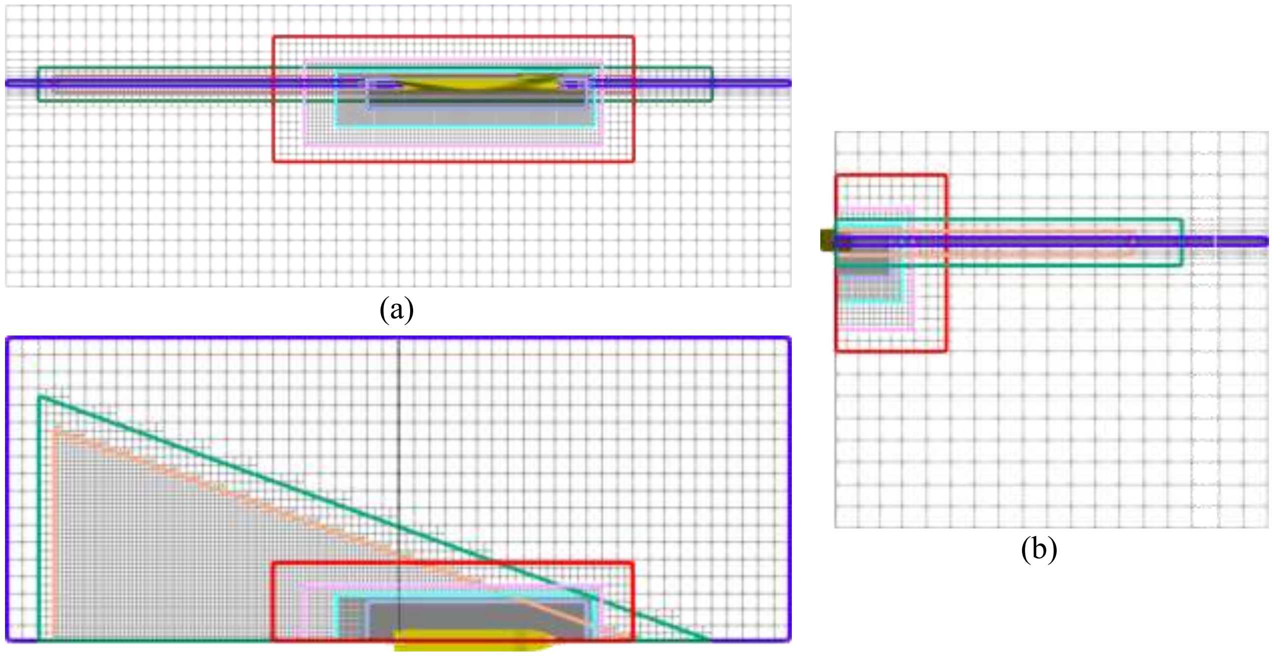

Figure 35: domain refinement for Hull 20; symmetry plane (a), the transverse plane (b) and the water plane (c). Different scales have been used to better capture the details.

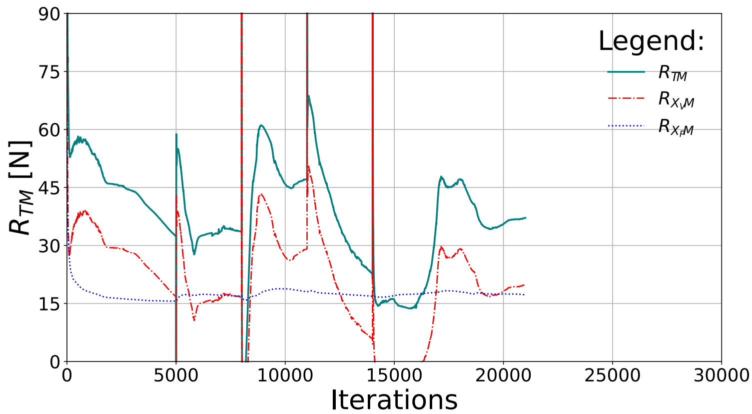

Figure 36: ASUP set-up applied on Hull 15 ($F_r = 0.350$).

Based on the available computing power for this research, the value of 30000 iterations for each simulation has been considered as the maximum computational affordable effort to run all the simulations. A critical review about these trends leads to a couple of issues dealing with the definition of dynamical attitude based on four check points and the size of the domain. With the respect to the check-points, two different speeds for the same hull have been considered and different set-up have been tested. The first speed to be tested corresponds to a $F_r = 0.150$ and five different configurations for the model dynamical attitude have been tested; each one of them differs alternatively for the total number of iterations, for the total number of equilibrium checks and for their spacing over iterations. A detailed overview about the cases is reported in Table 14; with the respect to the domain section (which accounts for just one-half hull for the symmetry condition), the refinements (Ref.) and the dimensions along the three-coordinate axis (X, Y and Z) have been reported with then respect to the ASUP characteristics, identified as standard (STD).

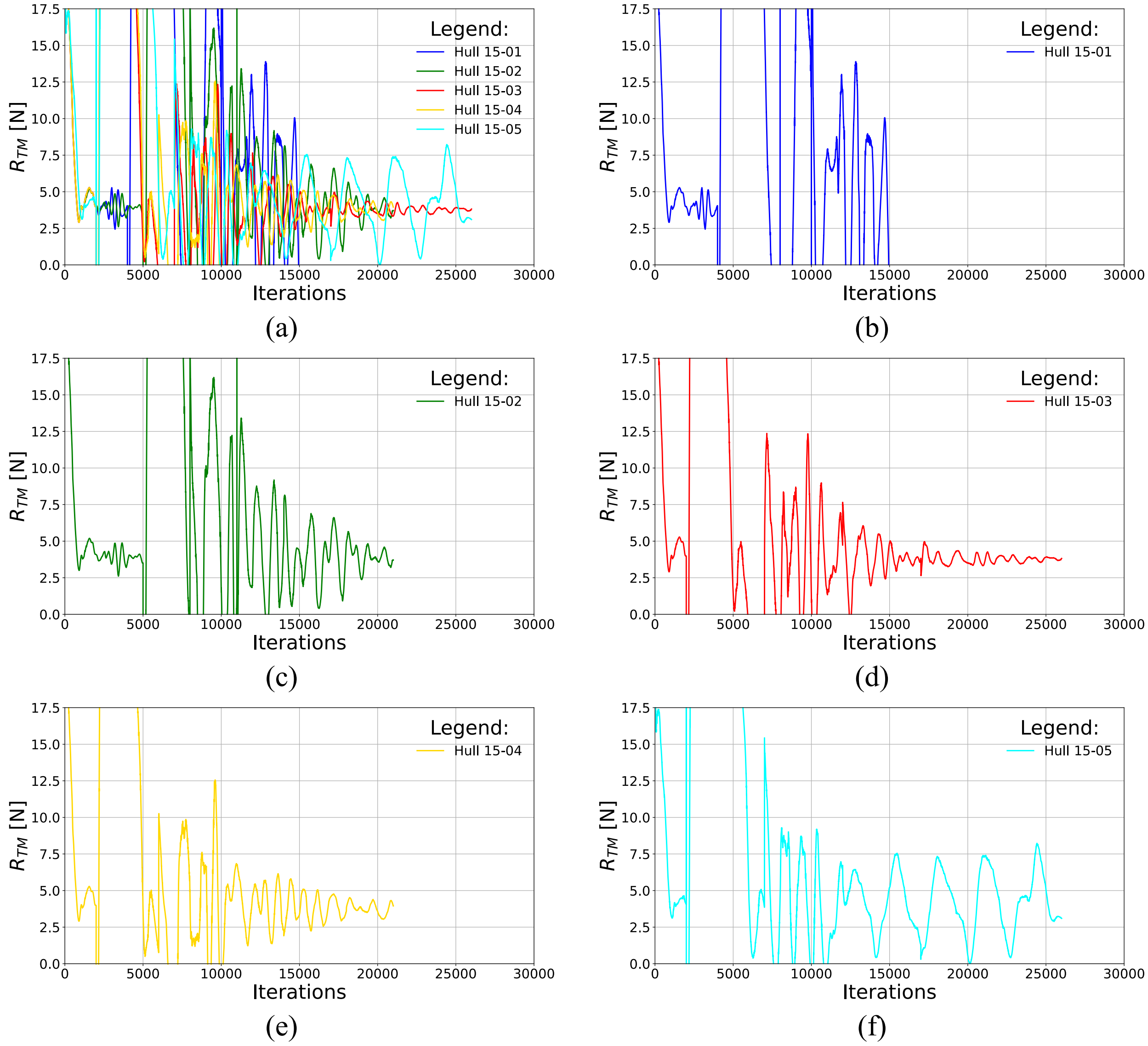

Figure 37: $R_{T_{M\_CFD}}$ analysis based on ASUP set-up for Hull 15 at $F_r = 0.150$; graphs exhibit different configurations, as follows: all the cases together (a), Hull 15-01 (b), Hull 15-02 (c), Hull 15-03 (d), Hull 15-04 (e) and Hull 15-05 (f).

Table 14: numerical set-up for Hull 15 ($F_r = 0.150$).

Hull	DOMAIN[(1)]					ITERATIONS	EQUILIBRIUM CHECKs							NOTES
ID	Cells[(2)]	Ref.	X	Y[(2)]	Z		Total	1°	2°	3°	4°	5°	FINAL	
15-01	0.769	STD	STD	STD	STD	15000	4	4000	6000	8000	10000	-	15000	-
15-02	0.769	STD	STD	STD	STD	21000	4	5000	8000	11000	14000	-	21000	-
15-03	0.769	STD	STD	STD	STD	26000	4	2000	7000	12000	17000	-	26000	-
15-04	0.769	STD	STD	STD	STD	21000	4	2000	6000	10000	14000	-	21000	-
15-05	1.350	STD	STD	STD	STD	26000	4	2000	7000	12000	17000	-	26000	-

(1) Where "STD" is present, it is referred to the dimension reported in Table 12.
(2) Millions of cells referred to half domain, based on the symmetry condition.

More in details considering Table 14, the refinements columns don't refer to the three types of refinement for the ASUP case but accounts for extra refinements as later on shown in current analysis. Comparing the iterations-history for the $R_{T_{M\_CFD}}$ changing the cases, it is possible to perform a trends

analysis based on Figure 37. Indeed, Figure 37a shows all the cases together, while Figure 37b, Figure 37c, Figure 37d, Figure 37e and Figure 37f show each single case, respectively. This first analysis leads to define the configuration 15-03 as the best candidate, based on its trend to convergence.
The same kind of analysis has run for the same hull, tested at $F_r = 0.350$. As reported by Table 15 all the cases are listed along with their characteristics.

Table 15: numerical set-up for Hull 15 ($F_r = 0.350$).

Hull ID	DOMAIN[(1)] Cells[(2)]	Ref.	X	Y[(2)]	Z	ITERATIONS	EQUILIBRIUM CHECKs Total	1°	2°	3°	4°	5°	FINAL	NOTES
15-06	0.807	STD	STD	STD	STD	26000	5	2000	7000	12000	17000	-	26000	-
15-07	0.808	STD	STD	STD	STD	21000	5	2000	6000	10000	14000	18000	21000	-
15-08	0.808	STD	STD	STD	STD	21000	4	5000	8000	11000	14000	-	21000	-
15-09	1.376	STD	STD	STD	STD	21000	4	5000	8000	11000	14000	-	21000	-

(1) Where "STD" is present, it is referred to the dimension reported in Table 12.
(2) Millions of cells referred to half domain, based on the symmetry condition.

As reported by the graphs in Figure 38, a general overview about the cases tested is reported. More in details, all the configurations are compared in Figure 38a, while Figure 38b, Figure 38c, Figure 38d and Figure 38 report the data for the cases 15-06, 15-07, 15-08 and 15-09, respectively. The post-processing analysis leads to phase with the convergence issue for all the cases; indeed, none of the tested configurations account for the convergence in the prescribed range. Therefore, other investigations have been performed to assess the right numerical set-up. As first step, the convergence is checked; therefore, simulations 15-06, 15-07, 15-08 and 15-09 were extended by an additional step considering the last configuration for sinkage and trim, leading to the cases 15-06L, 15-07L, 15-08L and 15-09L, respectively. The details for the new set-up are reported in Table 16. While, considering the post-processing analysis, the convergence issues remain for all the cases. Indeed, none of the tested configurations account for the convergence neither in the extended range.

Table 16: numerical set-up for Hull 15 ($F_r = 0.350$).

Hull ID	DOMAIN[(1)] Cells[(2)]	Ref.	X	Y[(2)]	Z	ITERATIONS	EQUILIBRIUM CHECKs Total	1°	2°	3°	4°	5°	FINAL	NOTES
15-06L	0.807	STD	STD	STD	STD	36000	5	2000	7000	12000	17000	-	36000	-
15-07L	0.808	STD	STD	STD	STD	31000	5	2000	6000	10000	14000	18000	31000	-
15-08L	0.808	STD	STD	STD	STD	36000	4	5000	8000	11000	14000	-	36000	-
15-09L	1.376	STD	STD	STD	STD	31000	4	5000	8000	11000	14000	-	31000	-

(1) Where "STD" is present, it is referred to the dimension reported in Table 12.
(2) Millions of cells referred to half domain, based on the symmetry condition.

As reported by the graphs in Figure 39 , a general overview about the cases tested is reported. More in details, all the configurations are compared in Figure 39a, while Figure 39b, Figure 39c, Figure 39d and Figure 39 report the data for the cases 15-06L, 15-07L, 15-08L and 15-09L, respectively. This analysis leads to disconnect the link among the convergence issue and the dynamic behaviour, and so the dynamical attitude for the hull can be evaluated through the configuration defined for 15-03, based on the results obtained.

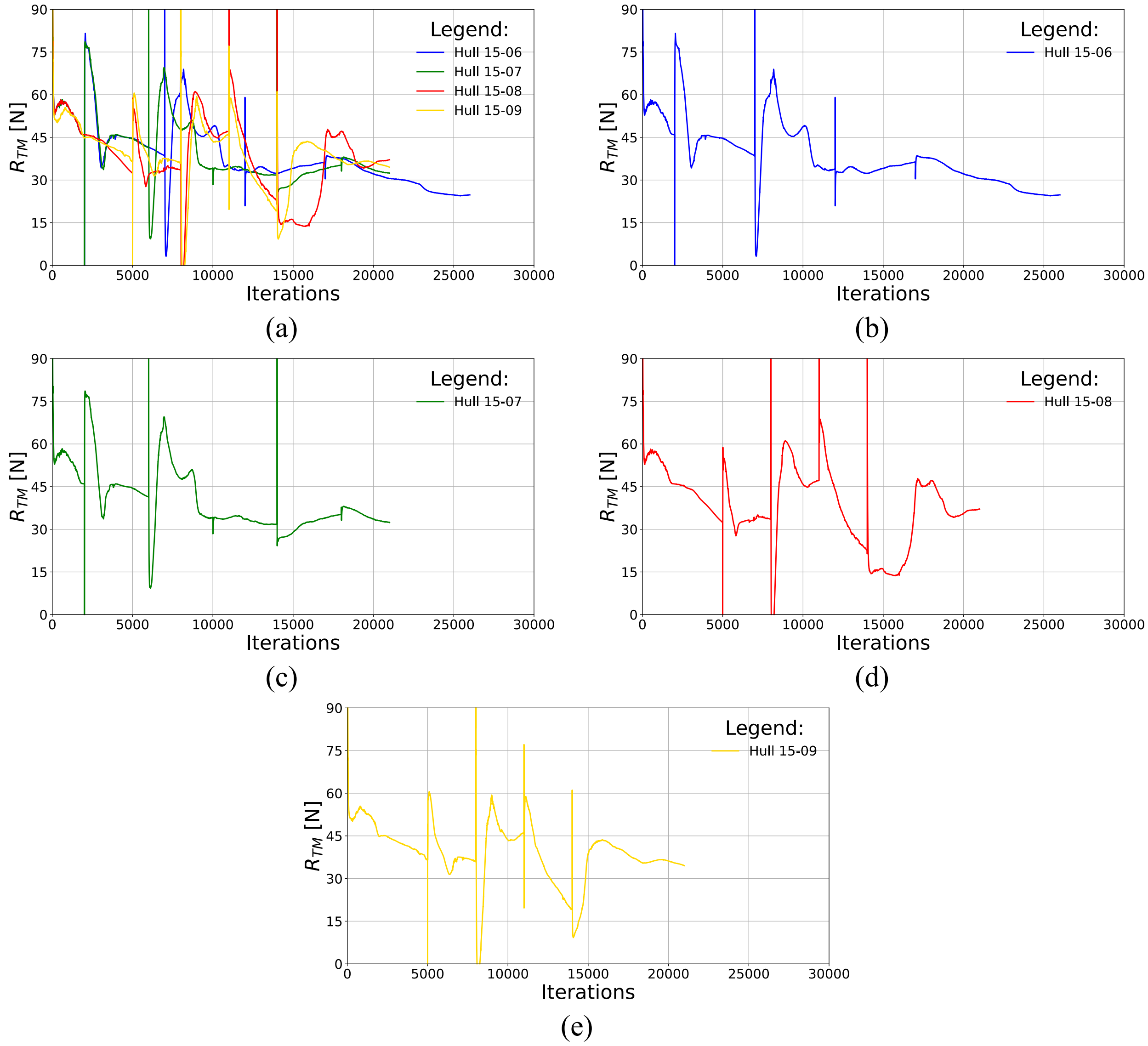

Figure 38: $R_{T_M\_CFD}$ analysis based on ASUP set-up for Hull 15 at $F_r = 0.350$; graphs exhibit different configurations, as follows: all the cases together (a), Hull 15-06 (b), Hull 15-07 (c), Hull 15-08 (d) and Hull 15-09 (e).

Therefore, the converge issue has to be investigated considering other parameters. Considering Hull 15-06 as the test case, a simulation has been performed considering a fix value for sinkage and trim considering an iterations step of 100000. The values of sinkage and trim were obtained from the convergence value for Hull 15 ($F_r = 0.350$), 2 Degree of Freedom (DoF). The "0 DoF" results obtained are reported in Figure 40a, while in Figure 40b a detailed overview is displayed. The iterations history exhibits convergence issue, because of the presence for crests and troughs; this attitude becomes particularly evident in the region starting from iteration numbers greater than 30000.

A detailed analysis of this attitude has been performed to identify any possible key parameter to get the convergence for the signal in the prescribed range.

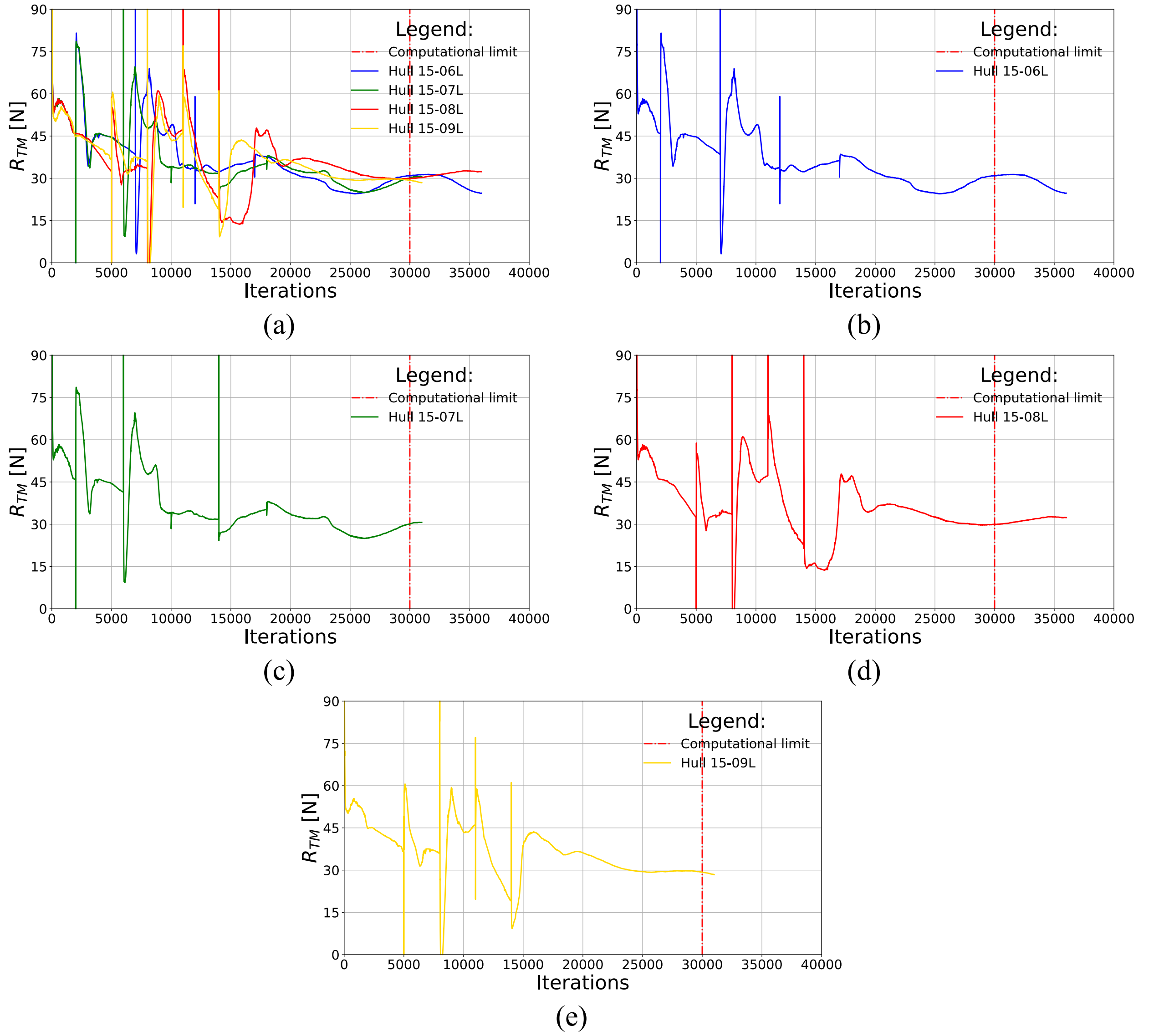

Figure 39: $R_{T_{M\_CFD}}$ analysis based on ASUP set-up for Hull 15 at $F_r = 0.350$ with extended range; graphs exhibit different configurations, as follows: all the cases together (a), Hull 15-06L (b), Hull 15-07L (c), Hull 15-08L (d) and Hull 15-09L (e).

A total number of 7 different conditions has been investigated. As reported by Figure 41a, numbers 1,2,3,5,6 account for crests, while 4 and 7 for troughs. A combined analysis for wave pattern and the free surface has run for each one of the seven listed conditions, as reported by the picture from Figure 41b to Figure 41h where the images display the free surface at 14000, 33000, 55000, 64000, 75000, 79000 and 88000 iterations, respectively. Based both on the number of iterations and the type of simulations, a steady-state solution is expected, while the images exhibit the presence of a sort of wave moving inside the domain (clearly visible in Figure 41g). This wave is supposed to be the responsible for the variation in the resistance evaluation and other investigations have been performed. In order to verify this founding, the analysis for the wave have been performed.

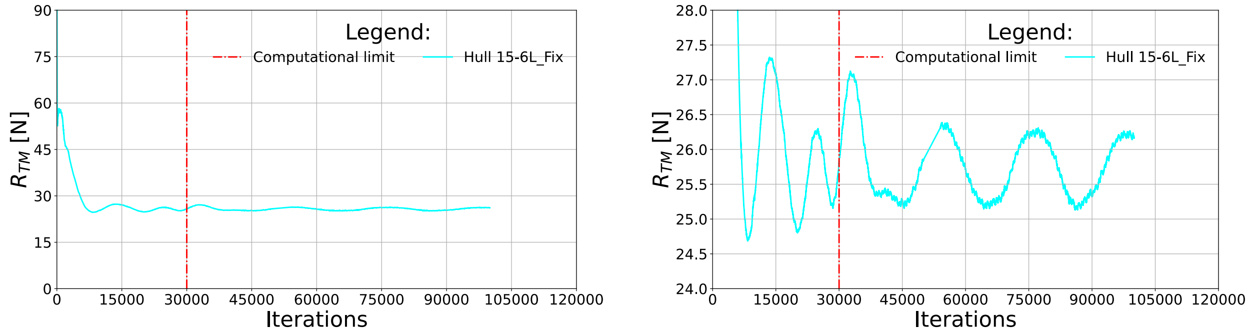

(a) (b)

Figure 40: $R_{T_{M\_CFD}}$ analysis based on ASUP set-up for Hull 15 at $F_r = 0.350$ with fix trim and sinkage (a) and its detailed view (b).

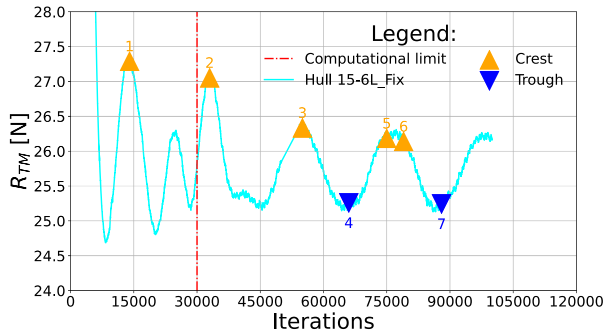

(a)

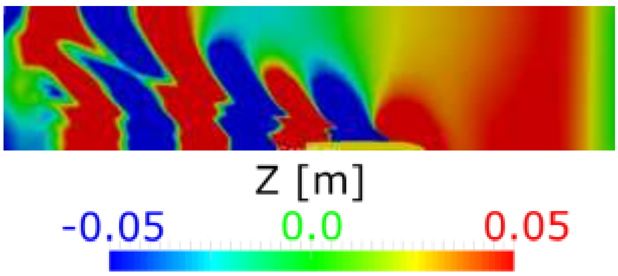

(b, 14000 iterations)

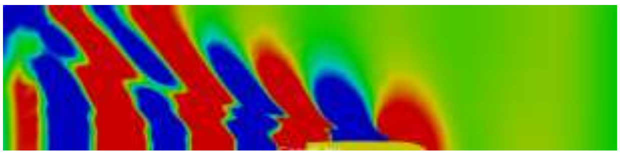

(c, 33000 iterations)

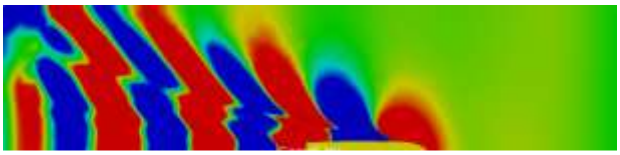

(d, 55000 iterations)

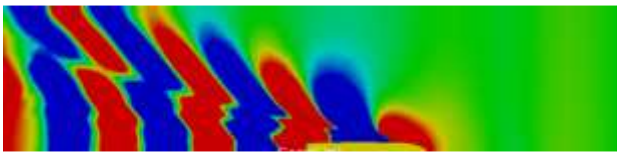

(e, 64000 iterations)

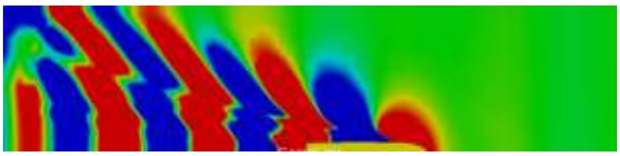

(f, 75000 iterations)

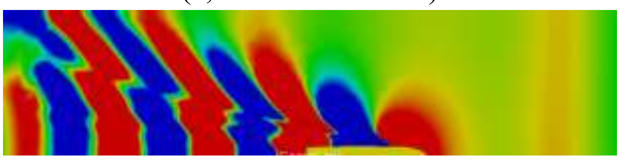

(g, 79000 iterations)

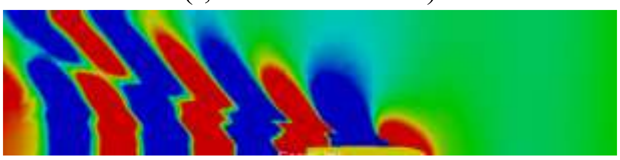

(h, 88000 iterations)

Figure 41: analysis for Hull 15 at $F_r = 0.350$ based on ASUP set-up; $R_{T_{M\_CFD}}$ iterations history with crests and trough (a), wave pattern and the free surface analysis at different iterations: 14000 (a), 33000 (b), 55000 (c), 64000 (d), 75000 (e), 79000 (f) and 88000 (g).

With the respect to three different section longitudinal planes positioned at $Y = 0\ [m]$, $Y = 2.4\ [m]$ and $Y = 4.8\ [m]$, as reported by Figure 42a, the wave cuts analysis has run. Based on Figure 42b, where both a trough condition (registered at 20000 iterations) and a crest one (registered at 99000 iterations) have been identified, the first analysis on the results from the three different plane sections accounts for a decrease for the wave as Y increases, as expected and displayed by Figure 42c (results for crest, 20000 iterations) and Figure 42d (results for trough, 99000 iterations).

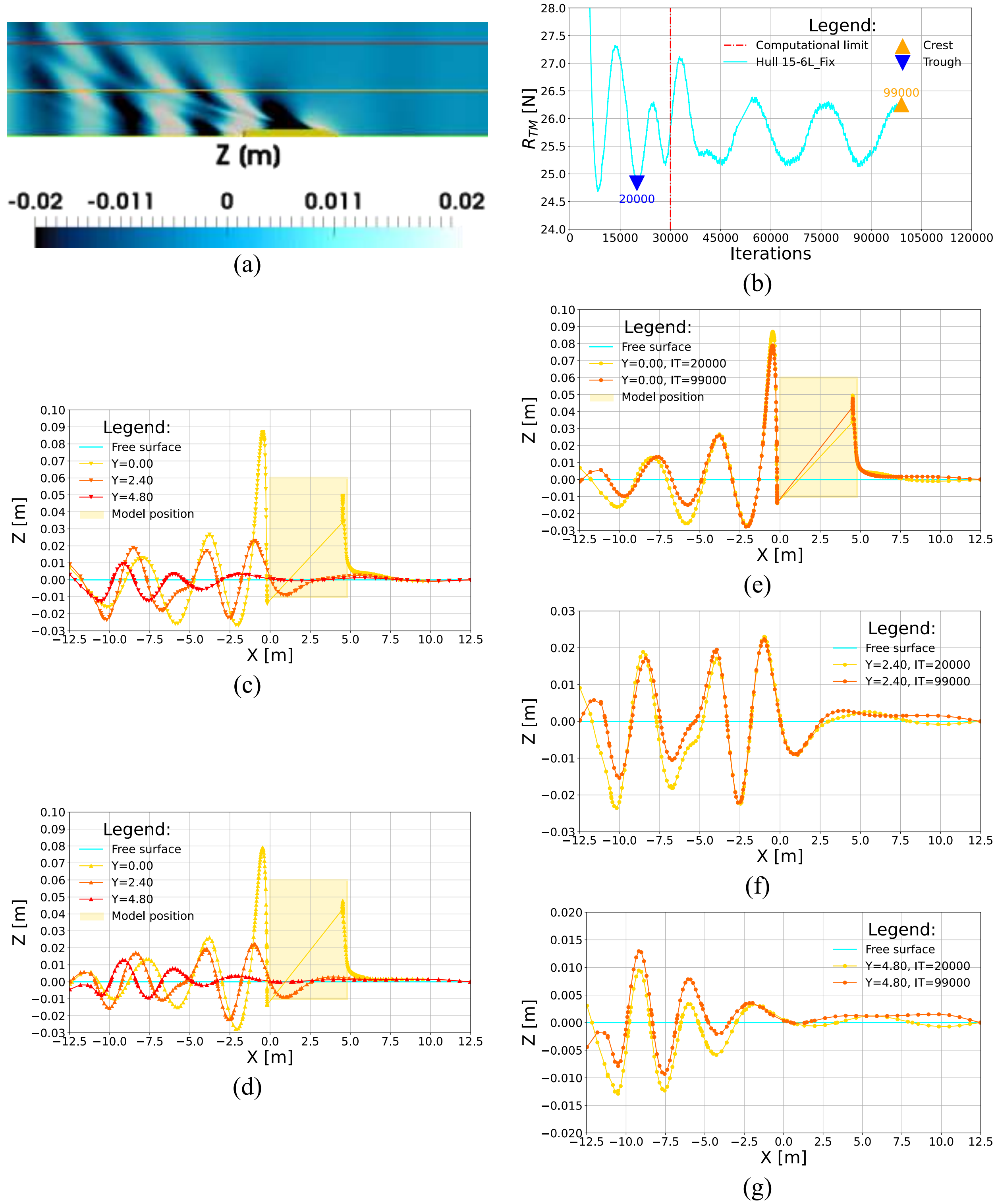

Figure 42: wave-cuts analysis based on ASUP set-up for Hull 15 at $F_r = 0.350$; free-surface with the traces for 3 wave cuts (a), $R_{T_{M\_CFD}}$ iterations history with crests and trough (b), wave-cuts at 20000 iterations (c), wave-cuts at 99000 iterations (d), comparisons for wave-cuts at fixed position and varying the iterations data (e), (f) and (g). The ship position is defined for $0 \leq x \leq 4.865$ [m] with $y = 0$ [m].

While, considering the peak for the wave close to the bow for the model (corresponding to $X = 4.865\ m$ and for Y$= 0\ m$) the results differ a little, but this difference leads to a greater modification in the wave pattern following the model; indeed, the height for the peaks differs by 10%, as displayed on Figure 42e. Moreover, considering Figure 42f and Figure 42g, it is possible to appreciate the wave in the region between the hull and the inlet which is forced to reach the boundary value at the border for the domain. Another confirm that this waves-system has physical implications for the hull resistance, can be obtained by considering the pressure iteration history for a point below the free-surface. Indeed, as reported by Figure 43a, three probes have been installed inside the computational domain as follows: $P_1 \equiv (5.25, 0, -0.05)$, $P_2 \equiv (8.00, 0, -0.05)$ and $P_3 \equiv (12.00, 0, -0.05)$. To better appreciate the variations, the pressure has been computed with the hydrostatical component, as reported by equation (115):

$$P_{\rho gz} = P - \rho gz \left[\frac{N}{m^2}\right] \tag{115}$$

where, z represents the probe depth. The results exhibit a variation across the iterations, a decrease for the difference height moving far from the hull and similar trace with the respect to the $R_{T_{M\_CFD}}$ but shifted, as reported by Figure 43b.

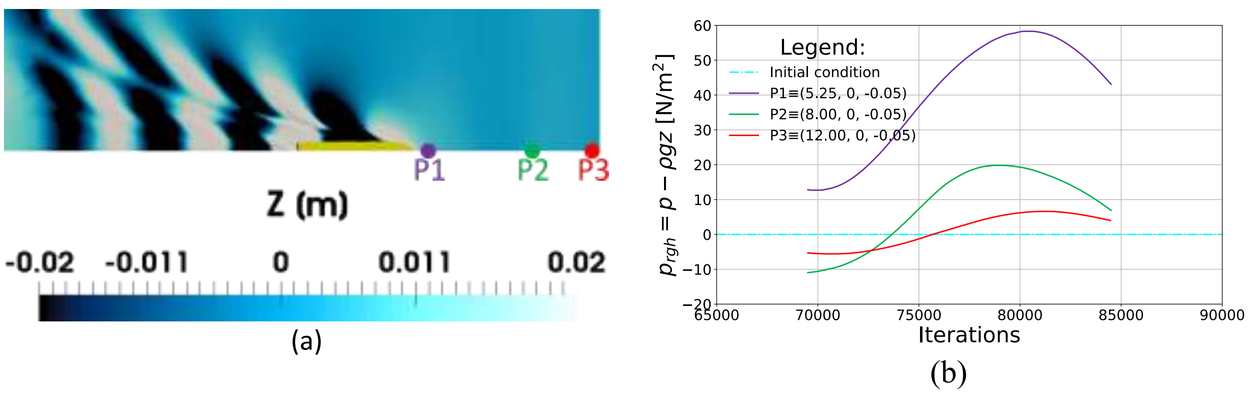

Figure 43: probe analysis based on ASUP set-up for Hull 15 at $F_r = 0.350$; probe positioning (a), pressure iterations history for each single probe (b).

This analysis gives the evidence that the hull interacts effectively with the wave system and there is a fluctuation inside the domain in a region where the perturbation was unexpected. Therefore, other investigations are required to find the numerical set-up that runs as prescribed. In order to find the numerical set-up that performs as prescribed, investigations among the domain and the refinements have been performed, considering the trim as fixed to reduce any possible issues connected to the numerical noise. The dimensions for the domain have been systematically changed in order to run the simulations. This choice has been considered as more robust, when compared with the numerical dumping approach. Indeed, the dumping approach proposed by the OpenFOAM suite (version 8) was evaluated; however, proper functionality was not achieved, likely due to limitations in its implementation by the author.

With the respect to the domain, it is possible to appreciate the changes for the inlet, the outlet and the side for the domain referred to ASUP set-up for Hull 15-06L_FIX, as numerically reported by Table 17. Indeed, when comparing the ASUP set-up, which data are in bolt and underlined, it is possible to appreciate the differences considering the bold data. Considering the changing for the domain dimensions, the simulations display the trends reported in Figure 44a. The variations are displayed as follows: standard ASUP dimensions Figure 44b, outlet variation Figure 44c, side variation Figure 44d, combined inlet and outlet variation Figure 44e and combined inlet, outlet and side variation Figure 44f.

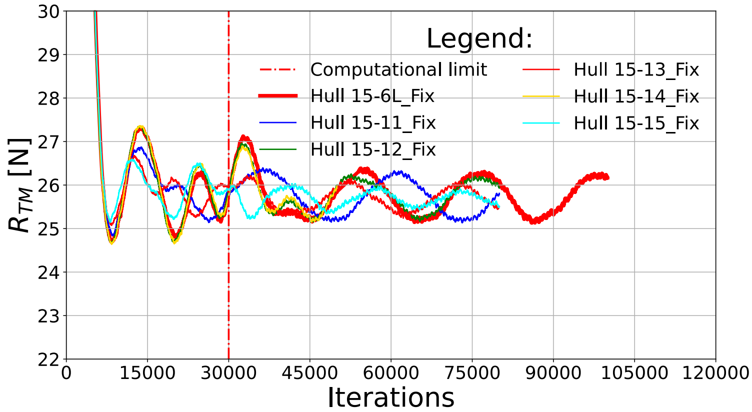

(a)

(b)

(c)

(d)

(e)

(f)

Figure 44: domain dimension variations for Hull 15 at $F_r = 0.350$*;* $R_{T_{M\_CFD}}$ *iterations history (a), standard ASUP dimensions (b), outlet variation (c), side variation (d), combined inlet and outlet variation (e) and combined inlet, outlet and side variation (f).*

Each one of the variations leads to a difference in result; among them, the most relevant one is connected to the increase for the lateral dimension, where a decrease in oscillations is displayed (15-15_FIX).

Table 17: numerical set-up for Hull 15 ($F_r = 0.350$), domain dimension variations analysis.

Hull ID(3)(4)	DOMAIN(1)							ITERATIONS	FIX TRIM & SINKAGE	NOTES
	Cells(2)	Ref.	X			Y(2)	Z			
			X	X_{INLET}	X_{OUTLET}					
15-06L_FIX	**0.807**	**STD**	**STD**	**STD**	**STD**	**STD**	**STD**	**100000**	**Y**	**LTS**
15-11_FIX	0.808	STD	**+36%**	**+75%**	STD	STD	STD	80000	Y	LTS
15-12_FIX	0.846	STD	**+36%**	STD	**+75%**	STD	STD	80000	Y	LTS
15-13_FIX	0.827	STD	**+36%**	**+75%**	STD	**110%**	STD	80000	Y	LTS
15-14_FIX	0.889	STD	**+75%**	STD	**153%**	STD	STD	50000	Y	LTS
15-15_FIX	0.829	STD	STD	STD	STD	**215%**	STD	80000	Y	LTS

(1) Where "STD" is present, it is referred to the dimension reported in Table 12.
(2) Millions of cells referred to half domain, based on the symmetry condition.
(3) Bolt data display the variations.
(4) Bolt and underlined data display the reference case.

Another study can be performed on the grid size. Based on the parametric refinement defined for the ASUP case, and considering the dimension for the bigger cell in the far field, it is possible to change this value and get a new grid with an increased/decreased number of cells but with the same refinement ratio. The numerical value and differences are displayed in Table 18.

Table 18: numerical set-up for Hull 15 ($F_r = 0.350$), grid size analysis.

Hull ID(3)	DOMAIN(1)							ITERATIONS	FIX TRIM & SINKAGE	NOTES
	Cells(2)	Ref.	X			Y(2)	Z			
			X	X_{INLET}	X_{OUTLET}					
15-06L_FIX	**0.807**	**STD**	**STD**	**STD**	**STD**	**STD**	**STD**	**100000**	**Y**	**LTS**
15-19_FIX	**1.298**	STD	STD	STD	STD	STD	STD	50000	Y	LTS
15-21_FIX	**1.960**	STD	STD	STD	STD	STD	STD	50000	Y	LTS
15-22_FIX	**0.491**	STD	STD	STD	STD	STD	STD	80000	Y	LTS

(1) Where "STD" is present, it is referred to the dimension reported in Table 12.
(2) Millions of cells referred to half domain, based on the symmetry condition.
(3) Bolt data display the variations.

While, considering the results from these new groups of set-ups, it is possible to assess that a greater excursion among the peaks is achieved without any particular difference for the mean value, as reported by Figure 45a; the bigger difference consists in the computational effort required to run the finer simulations. With the respect to the central symmetry plane, a comparison among the very fine, fine and coarse meshes is reported in Figure 45c, Figure 45d and Figure 45e, respectively.

With the respect to the refinements, a study about the influence for the free-surface description has been performed. The numerical data for this group of simulations are reported in Table 19. The results from these simulations exhibit a reduction for the excursion across the peaks but a not negligible increase for the computational effort is required but it is negligible when comparing the standard lateral dimension for the domain with the increased one, as reported in Figure 46a. The effects for the mesh refinement are displayed in Figure 46b and Figure 46c. Therefore, even if the surface discretization leads to a reduction for the oscillations, it is not computationally affordable.

Table 19: numerical set-up for Hull 15 ($F_r = 0.350$), free-surface refinements analysis.

Hull ID(3)	DOMAIN(1)							ITERATIONS	FIX TRIM & SINKAGE	NOTES
	Cells(2)	Ref.	X			Y(2)	Z			
			X	X_{INLET}	X_{OUTLET}					
15-06L_FIX	0.807	STD	STD	STD	STD	STD	STD	100000	Y	LTS
15-10_FIX	2.059	WL	STD	STD	STD	STD	STD	80000	Y	LTS
15-16_FIX	2.088	WL	STD	STD	STD	215%	STD	80000	Y	LTS

(1) Where "STD" is present, it is referred to the dimension reported in Table 12.
(2) Millions of cells referred to half domain, based on the symmetry condition.
(3) Bolt data display the variations.

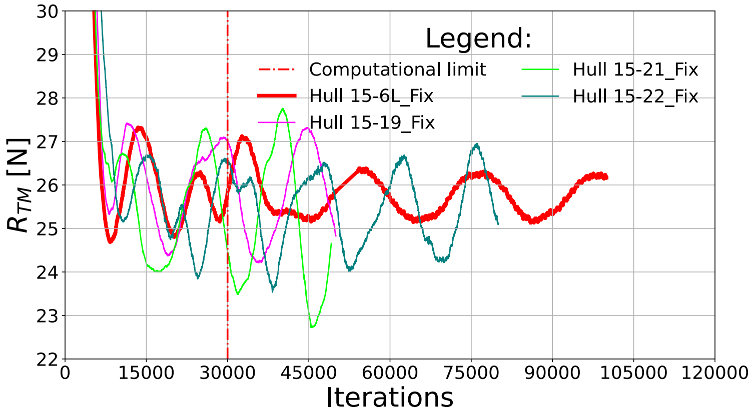

(a)

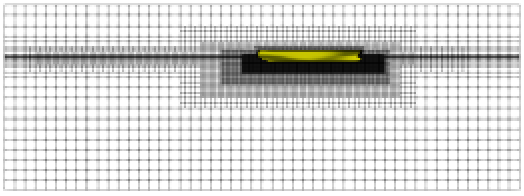

(b)

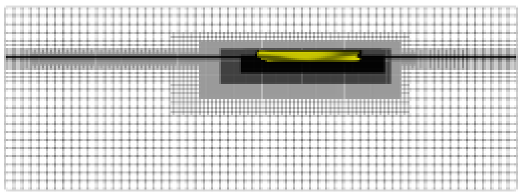

(c)

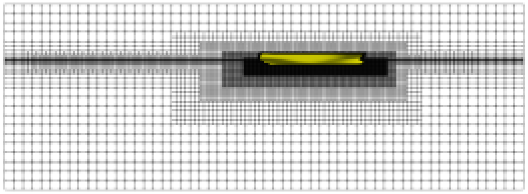

(d)

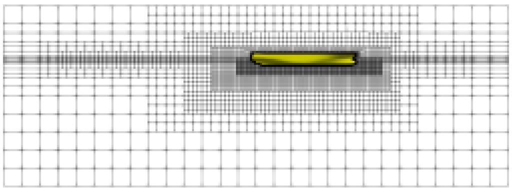

(e)

Figure 45: domain grid size variations for Hull 15 at $F_r = 0.350$; R_{TM_CFD} iterations history (a), ASUP mesh (b), very fine mesh (c), fine mesh (d) and coarse mesh (e).

Finally, it is possible to consider the type of solver. The ASUP set-up implements a steady solver, but among the openFOAM environment, an unsteady configuration can be used to run the simulations, as displayed by Table 20.

Table 20: numerical set-up for Hull 15 ($F_r = 0.350$), solver analysis.

Hull ID(3)	DOMAIN(1)							ITERATIONS(4)	FIX TRIM & SINKAGE	NOTES
	Cells(2)	Ref.	X			Y(2)	Z			
			X	X_{INLET}	X_{OUTLET}					
15-06L_FIX	**0.807**	**STD**	**STD**	**STD**	**STD**	**STD**	**STD**	**67480**	**Y**	**LTS**
15-17_FIX	0.806	STD	STD	STD	STD	STD	STD	60s	**Y**	**Unsteady**

(1) Where "STD" is present, it is referred to the dimension reported in Table 12.
(2) Millions of cells referred to half domain, based on the symmetry condition.
(3) Bolt data display the variations.

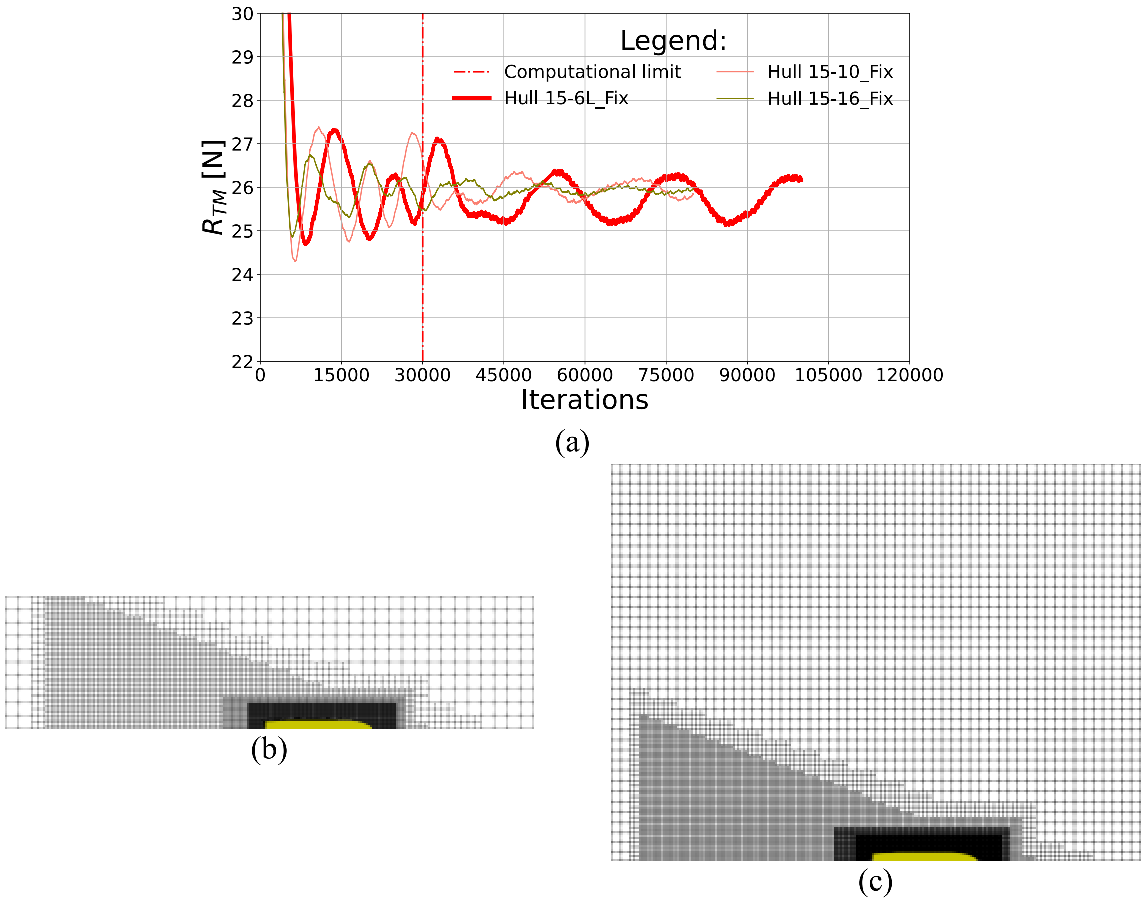

Figure 46: free-surface discretization for Hull 15 at $F_r = 0.350$; $R_{T_M\_CFD}$ iterations history (a), ASUP mesh (b) and finer mesh (c).

To compare the $R_{T_M\_CFD}$ iterations history, as displayed by Figure 40, with the $R_{T_M\_CFD}$ time history, as reported by Figure 47a, the computational time has been considered as the key parameter to get results from the two different approaches; indeed, the physical time of 79 hours is considered. In this period, the LTS model performed 67840 iterations, while the unsteady solver reaches 65s of simulations. Moreover, running 30000 iterations for a LTS simulation corresponds to a 35.12s of unsteady simulations (on the available workstation), and therefore, this limit represents the acceptable computational limit to assess if the unsteady solver performs as request. Additionally, in this time the flow sails more than 3 times the virtual towing tank length, being 10.29s the time to run a single tank. These issues are graphically represented by Figure 47b. The results from this analysis lead to a substantial equivalence for the solver.

Finally, considering the dynamical attitude for the model, the numerical domain size, the grid refinements and the solver, a reviewed set-up has been identified. This new set-up, later on named as Bravo set-up (BSUP), consists in an ASUP with the following differences: 26000 iterations with 4 equilibrium checks (respectively at 2000, 7000, 12000 and 17000 iterations), an increased anisotropic refinement for the free-surface reaching a mean value of 1.0M cells for the half domain, a three times bigger domain with the respect to the lateral dimension. The selected measures conform to the ITTC requirements, as prescribed by the "Practical Guidelines for Ship Resistance CFD" [112].

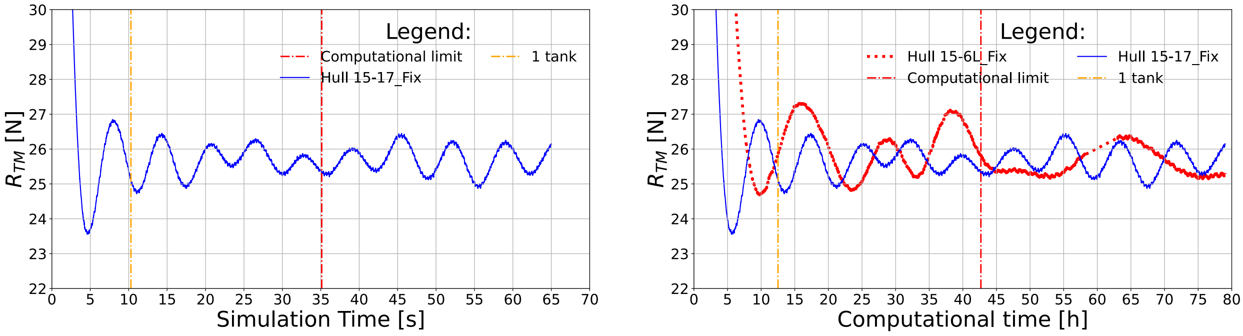

(a) (b)

Figure 47: solver analysis for Hull 15 at $F_r = 0.350$*;* $R_{T_{M\_CFD}}$ *time history (a),* $R_{T_{M\_CFD}}$ *time history compared with the ASUP configuration based on computational time (b).*

More in details, the prescribed size for the domain "should be taken sufficiently large" and, as a general rule of thumb, the upstream, the down-stream and the lateral boundaries should be at a distance equivalent to one model length with the respect to it. As an illustrative example, Figure 48 shows a graphical comparison among the size for the computational domain prescribed by ITTC guidance (orange features) and the one implemented in current research (green features) for Hull 20 (yellow color), which length among the perpendiculars is 7.27m.

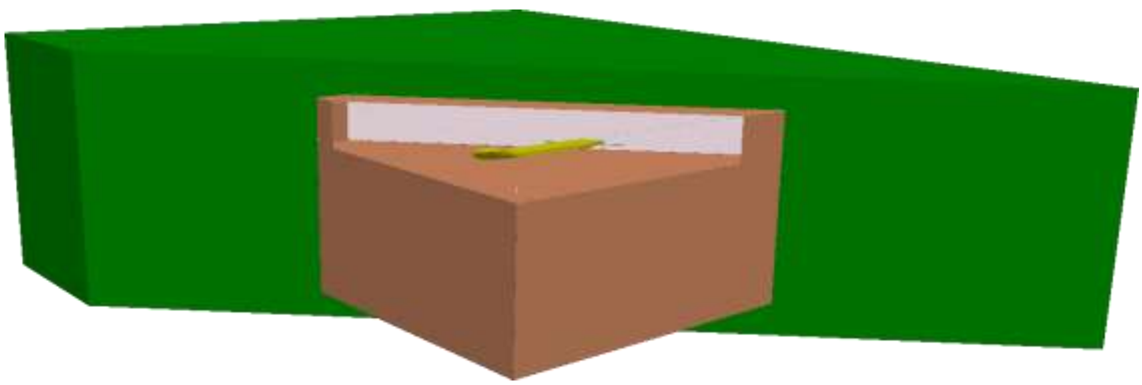

Figure 48: comparisons among the ITTC suggested dimension for the computational domain (orange features) and the one implemented in current work (green features) for the model Hull 20.

More in details, as reported in Table 21 with the respect to Hull 20, it is possible to appreciate the actual correspondence between the selected dimensions and those prescribed by the ITTC; indeed, considering the dimension along the three axes, the mean value for the ITTC domain dimensions is within the range of three times and half smaller than the value obtained from the numerical domain implemented in this research. Finally, in order to get a complete situational awareness about the dimensions for the domain compared with the model dimension (Hull 20, yellow in color), a detailed view describing the ITTC suggested one (orange features) and the implemented one (blue features for water and cyan for air), is reported in Figure 49a; while, considering Figure 49b Figure 49c and

Figure 49d, comparative views are available with the respect to the transversal, the longitudinal and the half-breadth planes, respectively.

Table 21: ITTC suggested computational domain size compared with the current research one for Hull 20.

Boundary distance	Value [m]		Times Model length [adim]	
	ITTC	Research	ITTC	Research
Upstream	14,60	18,20	2,0	2,5
Down-stream	7,45	18,20	1,0	2,5
Lateral	7,35	27,66	1,0	3,8
Top(*)	2,21	3,64	0,3	0,5
Bottom	7,35	9,46	1,0	1,3
Domain_X	22,05	36,39	3,0	5,0
Domain_Y	14,70	55,32	2,0	7,6
Domain_Z	9,56	13,10	1,3	1,8

(*) Dimension not directly available from ITTC guidance but considered as the minimum one required to perform simulations.

In order to conclude the BSUP analysis, the following three different plane sections are displayed with the respect to Hull 20: the water plane (Figure 50a), the longitudinal (Figure 50b) and the transversal (Figure 50c). These section planes are intended to deal with the mesh description for the defined numerical set-up addressing the domain discretization. Once the BSUP has been defined, it was tested for several hulls. As reported by Figure 51, BSUP performs properly in some cases, but sometimes it requires more than 26000 iterations to reach the convergence criteria, and therefore other investigations are required in order to define a numerical set-up which performs as requests.

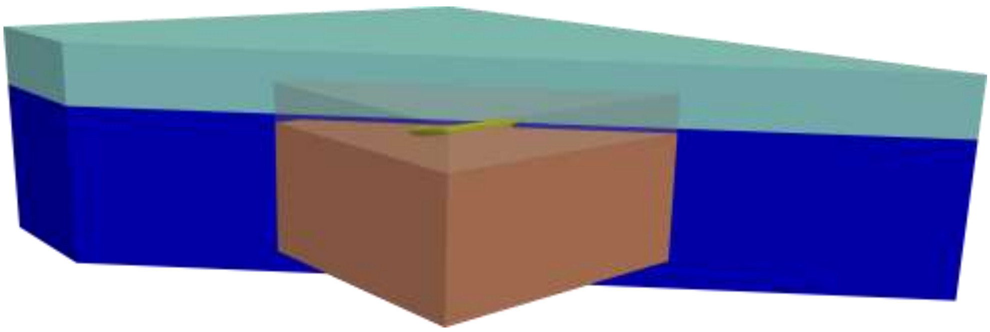

(a)

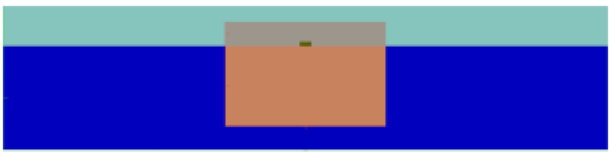

(b)

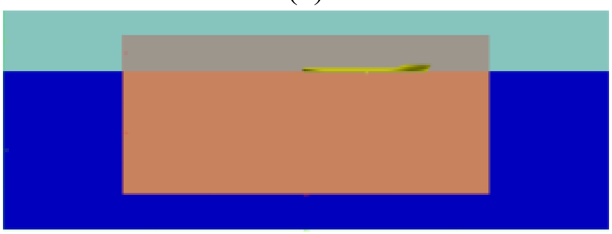

(c)

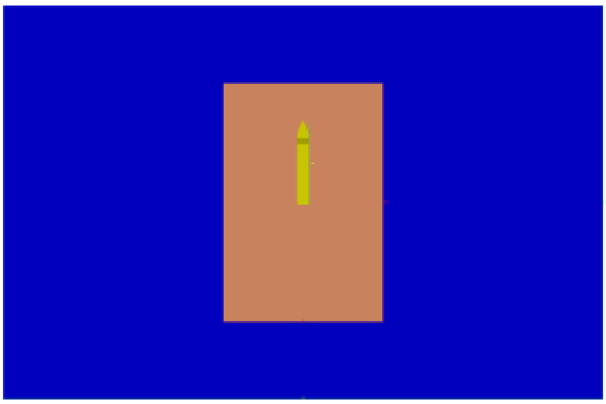

(d)

Figure 49: schematic representations (a) about the differences among the ITTC suggested dimension for the computational domain (orange features) and the one implemented in current work (blue and cyan), general view for transversal plane (b), longitudinal plane (c) and half-breadth plane (d).

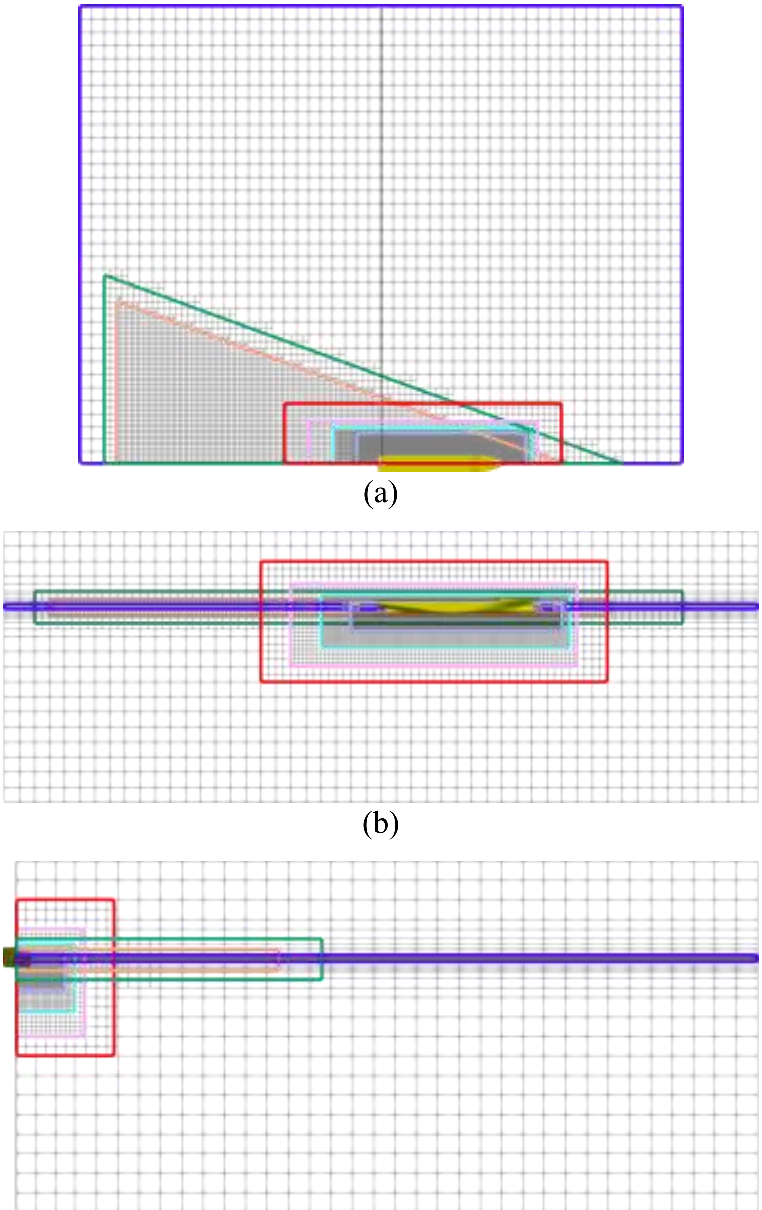

(a)

(b)

(c)

Figure 50: BSUP domain for Hull 20; water plane section (Figure 50a), longitudinal section (Figure 50b) and transversal section (Figure 50c).

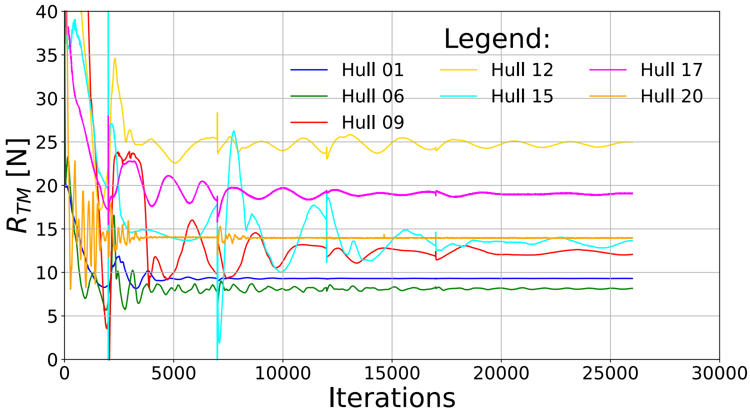

Figure 51: BSUP comparison for different hulls.

3.3 Pressure-velocity issue

Based on the study conducted in order to identify the BSUP set-up, it was possible to assess that the free surface description assumes a crucial role in the simulation. Therefore, an investigation about the numerical algorithm to solve the pressure–velocity coupled issue has been performed. When using a local time stepping (LTS) approach, in the OpenFOAM environment the merged PISO-SIMPLE algorithm (PIMPLE) accounts for the advantages arising from the Pressure-Implicit with Splitting of Operators (PISO) and the Semi-Implicit Method for Pressure-Linked Equations (SIMPLE) algorithms, leading the simulation to reach a convergent result in a lower time. This numerical tool exhibits the opportunity to customize its set-up inside the configuration file named "fvSolution". The configurable parameters are listed inside Figure 52.

```
PIMPLE
{
   momentumPredictor
   nOuterCorrectors
   nCorrectors
   nNonOrthogonalCorrectors
   maxCo
   maxAlphaCo
   rDeltaTSmoothingCoeff
   rDeltaTDampingCoeff
   nAlphaSpreadIter
   nAlphaSweepIter
   maxDeltaT
}
```

Figure 52: set-up parameters of the PIMPLE algorithm.

Among all the possibilities, a systematic variation has been performed on the parameters. These variations have been accomplished considering three values for the Courant number for the domain $\max(\mathrm{C_O})$, three for the free surface $\max[(\mathrm{C_O})_{\mathrm{FS}}]$, three for the smoothing coefficients (Δt_S), and three for the damping one (Δt_D). As reported in Table 22, a total number of 9 set-up has been evaluated for Hull 11 to further diversify the study through another hull geometry and to assess whether it operates as intended. These parameters are considered as the key parameters to get a simulation running in the prescribed time without losing accuracy. Before describing the analysis, a comparison among the results obtained from all the simulations for one speed has run. This analysis has run adhering to the methodology implemented by the ITTC resistance committee to assess the outliers for the experimental test [114]. Indeed, each variation for the PIMPLE set-up leads to a different value for the advance resistance; all the values have been compared by considering the mean and its double standard deviation to assess the presence for outliers. Only the case Hull 11-BSUP_03 exceeds twice the standard deviation, and it may represent an outlier. Once the mean value, the double and the triple standard deviations have been evaluated without the result from Hull 11-BSUP_03, it is possible to identify this value as an outlier.

Table 22: PIMPLE, numerical variation for the parameters.

HULL ID	$\max(C_O)$	$\max[(C_O)_{FS}]$	Δt_S	Δt_D
11-BSUP_00[(1)]	5	2	0,05	0,5
11-BSUP_01	2	1	0,025	0,25
11-BSUP_02	2	1	0,05	0,5
11-BSUP_03	2	1	0,7	0,7
11-BSUP_04	5	2	0,025	0,25
11-BSUP_05	5	2	0,05	0,5
11-BSUP_06	5	2	0,1	0,1
11-BSUP_07	10	5	0,025	0,25
11-BSUP_08	10	5	0,05	0,5
11-BSUP_09	10	5	0,1	0,1

[(1)] BSUP_00 represents the standard numerical set-up for the BSUP configuration.

Although an outlier is present, the analysis can still be considered invariant with respect to the choice for the set-up, since the results display close values with a very narrow standard deviation (0.8% with the respect to the experimental value for the resistance). Therefore, this analysis leads the opportunity to change the parameters without losing the desired accuracy. Figure 53a displays the results for R_{T_M} varying the setup; the red star represents the result for the original set-up (later on defined as Hull 11-BSUP_00), the blue dots the simulations results changing the set-up, the red dashed-dotted line the mean and the green horizontal lines the double and triple standard deviations; while Figure 53b, represents the same data with the procedure to identify the outliers.

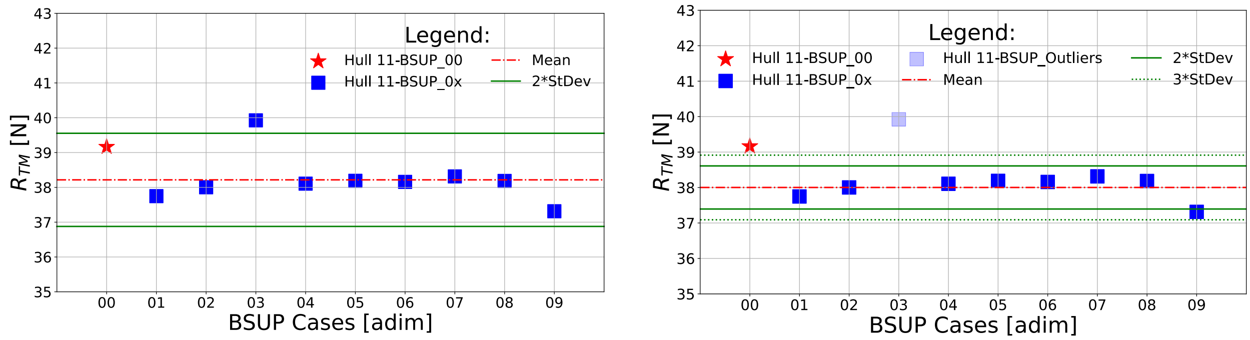

(a) (b)

Figure 53: advance resistance $R_{T_{M\_CFD}}$ results changing the BSUP configuration (a) and outlier detection(b).

Once it has been demonstrated the equivalence for the set-up with the respect to the results, the iterations history analysis can run. As shown by Figure 54a, Hull 11-BSUP_00 exhibits the necessity to run over 30000 iterations to reach a trend, and therefore, it is not computationally affordable. The trace for Hull 11-BSUP_00 is displayed in all the plots of Figure 54 through a red line. The analysis of the 9 set-ups can be performed considering as fixed the Courant values and varying the coefficients or vice versa. When considering as fixed the values for Courant, the three cases analyzed exhibit the following two main features: a decrease for the iterations to reach the convergence when Δt_S, Δt_D

coefficients increase and a reduction for the R_{T_M} as the Courant increase, as reported in Figure 54b, Figure 54c and Figure 54d.

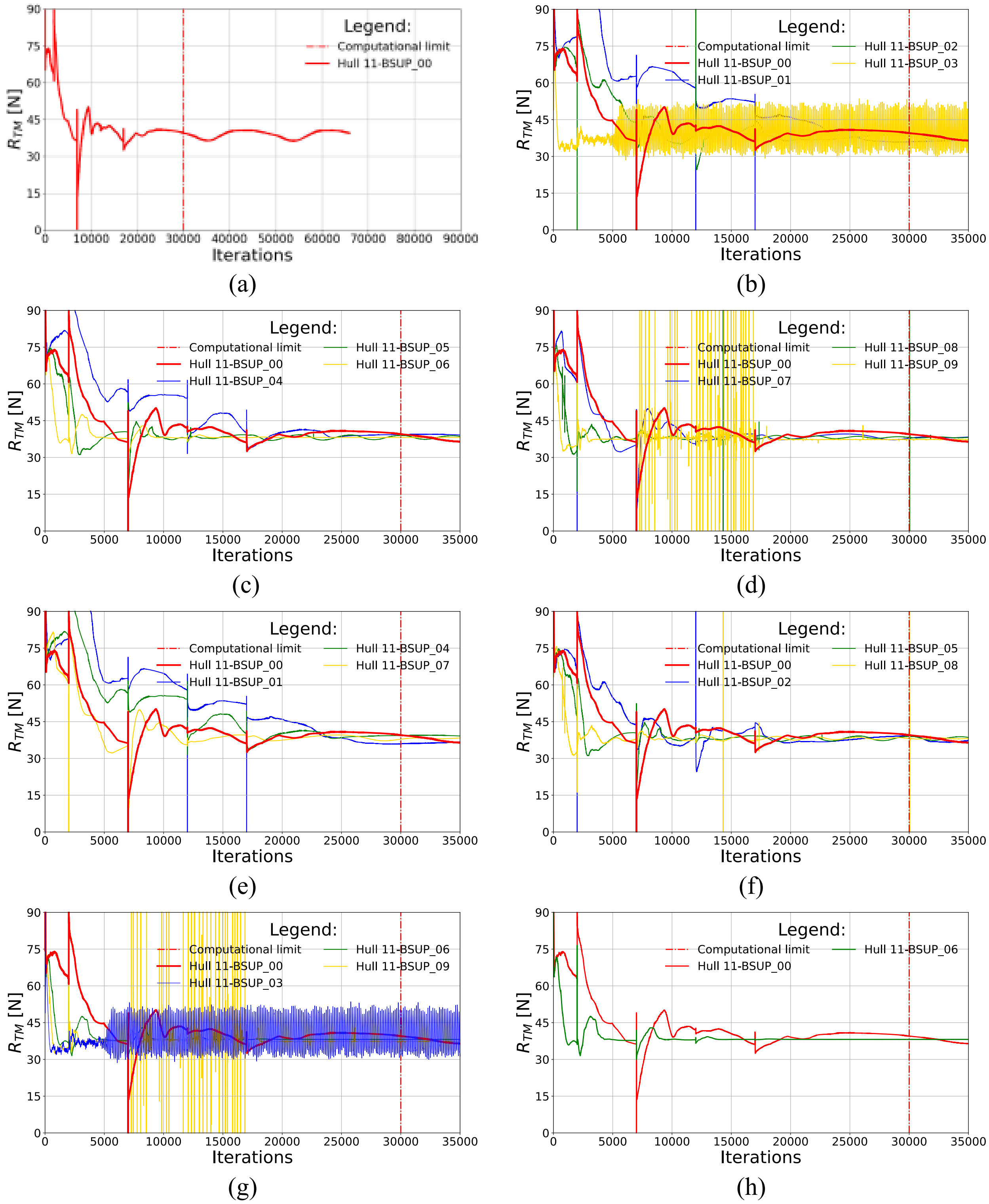

Figure 54: comparisons among the iterations history for the advance resistance $R_{T_{M\_CFD}}$; Hull 11-BSUP_00 (a), fixed C_O varying the Smoothing- Damping coefficients (b), (c), (d), varying C_O fixed the Smoothing-Damping coefficients (e), (f), (g) and comparison among Hull 11-BSUP_00 versus 11-BSUP_06 (h).

It means that, if the Courant number increase and the smoothing-damping coefficients follows, the simulation can reach the convergence in a fewer number of iterations, if compared with the original case; moreover, if the coefficients are increased, a sort of noise affects the iterations history. This last finding can be observed considering as fixed the values for the coefficients and varying the Courant values, as reported by Figure 54e, Figure 54f and Figure 54g. Therefore, Hull 11_BSUP-06 represents the best compromise among accuracy and stability when compared with all the test cases considered. A comparison among the iteration history for Hull 11_BSUP-00 and Hull 11_BSUP-06 demonstrates how this last numerical set-up works properly in less than 30000, as reported in Figure 54h. This new set-up, later on named as Charlie set-up (CSUP), consist in an BSUP with the following differences: maximum Courant number for the domain $\max(\mathrm{C_O}) = 5$, maximum Courant number for the free surface $\max[(\mathrm{C_O})_{\mathrm{FS}}]$=2, and smoothing-damping coefficients $\Delta t_S = \Delta t_D = 0.1$.

3.4 Turbulence models

Moving from a CSUP, a comparison among the turbulence model has run. Among the available ones in the OpenFOAM environment, the $k - \omega\ SST$ (Shear Stress Transport, "kOmegaSST") and the "realizableKE" have been compared. Both of the methods use a two equations model; the first one combines the $k - \omega$ model next to the wall and a $k - \varepsilon$ one in the free-stream region, while the second method should be less accurate, as reported by Halim et al. [116], but it is said to have great robustness, as reported by Ansys guide [117]. Considering the experimental results for another hull (Hull 16) to further diversify the geometries considered in the numerical set-up calibration, a comparison among the two turbulence models has run considering the numerical results obtained. To get these differences and considering the same mesh solved with different turbulent models, the advance resistance has been evaluated for 6 different speeds and scaled on the respective one from the experimental campaign; the cases and the results are reported in Table 23.

Table 23: CSUP, $k - \varepsilon$ and $k - \omega\ SST$ cases.

HULL ID	F_r [%]	$\frac{R_{TM\_k-\epsilon}}{R_{TM_{EFD}}} - 1$ [%]	$\frac{R_{TM_{k-\omega}}}{R_{TM_{EFD}}} - 1$ [%]
16-CSUP_00	0.079	14.28%	5.54%
16-CSUP_01	0.111	2.85%	1.28%
16-CSUP_02	0.142	0.43%	-2.36%
16-CSUP_03	0.174	-1.15%	-4.35%
16-CSUP_04	0.253	4.59%	3.76%
16-CSUP_05	0.348	4.32%	1.36%
Mean	-	4.22%	0.87%

To clearly identify any possible trend, the results from Table 23 as displayed by Figure 55, where the blue dots represent the $R_{T_{M\_CFD}}$ evaluated by the $k - \omega\ SST$ turbulence model and the cyan markers the ones for $k - \varepsilon$. It is possible to assess that both models follow the same generical trend with respect to the velocity variations, although a vertical shifting can be observed between them. Additionally, among the two models, a clear superiority of one over the other does not emerge from results. A detailed comparison between the simulation results of the $k - \varepsilon$ turbulence model and those of the experimental ones (represented by the horizontal line for $y = 0$) shows a greater deviation in the $F_r < 0.1$ and $F_r > 0.25$ ranges; the results are comparable to those form the in the $k - \omega\ SST$ model in the range $0.1 \leq F_r \leq 0.25$ and are, overall, in reasonable agreement.

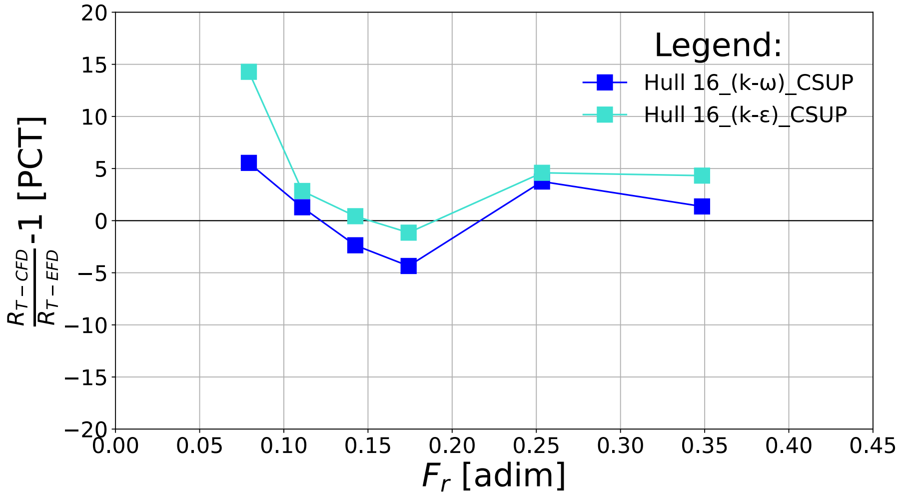

Figure 55: comparisons among turbulence models for the advance resistance $R_{T_M\_CFD}$ varying the speed.

Finally, with the respect to these last findings, the $k - \omega\ SST$ turbulence model has been implemented in the CSUP. This new set-up, later on defined as DSUP, represents the final numerical set-up used to perform all the simulations.

Adhering to the SPTM, in Chapter 4, the procedure to run the comparisons is going to be described. The DSUP represents the numerical set-up implemented to run all the simulations in order to get results and later on to account for any conclusion with the respect to the question "how precise is a Computational Fluid Dynamics (CFD) calculation when compared with an Experimental Fluid Dynamics (EFD) result?".

4 Repository of EFD and CFD results.

When considering EFD results and CFD calculations, and in the perspective of providing a substantiated and methodologically grounded answer to the question: "how precise is a CFD calculation when compared with results deriving from the towing tank experiences", three kinds of approaches can be listed. In the first one, named as "Single comparison" (SPTO), the calculations arising from one numerical set-up are compared with the EFD measurements. In this sense, it is just possible to evaluate if an overestimation or an underestimation has occurred when comparing the data obtained by the two approaches. Moving to the second approach, identified as "workshop type approach", early defined as MPTO, several numerical set-ups versus one single (or few) hull EFD result are compared and this is the typical approach used by the numerical workshops, as the Lucy Ashton one [37]. Indeed, several participants submit their works by using their best practices, trying to assess the quantities of interest required by the workshop organizers. Therefore, usually the scatter in results is analyzed to assess the mean differences, for the hull test case (or few cases) when dealing with the results for resistance, dynamical attitudes for the models, wave-cuts along with the pressures on some particular features. While, the last approach, referred to as "One numerical set-up versus many EFD results", early defined as SPTM, is conceived with the primary objective of employing one single parametrical numerical set-up as a comprehensive analytical framework, designed to systematically identify, examine, and interpret the full spectrum of differences observed among all the results for the hulls tested.

Among the three approaches, in this work the SPTM approach has been taken into account. As a matter of fact, once the parametrical numerical set-up has been defined, it has been possible to apply it on several kinds of hulls for each one of them, both the geometries and the experimental data were available. Indeed, a dedicated and conceptually coherent framework has been devised. This framework constitutes the structural environment within which all the simulations have been developed, systematized, and interrelated, thereby ensuring uniformity of approach and analytical robustness throughout the investigations. Therefore, the framework was organized as a structured workflow, beginning with the research for the experimental data along with the geometries for the ship to be tested and culminating in the population of the comparative database. In the repository all the data deriving from the comparisons are stored. The procedure run through the following intermediate steps: hull identification, 3D model generation, mesh customization and performing the simulations along with the individual post-processing analysis. This approach, beyond distinguishing the differences among EFD and CFD, is theoretically capable of identifying several additional aspects related to its characteristics. In fact, given that various types of hulls are considered in the comparison, the differences can be correlated with specific elements of interest; among them the following comparisons reveal the most significant variations between differences and speed, differences and the configuration for the in towing tank test and lastly, differences connected with geometrical parameter like scale factor or model length and hydrodynamical ratios (like L_{WL}/B_{WL} and B_{WL}/T_M). Finally, the results deriving from 142 different simulations for a total number of 22 hulls, tested at different speeds will be stored inside the comparative repository.

In order to enhance the clarity and immediate recognizability of each hull among all the others, the present research adopts a coherent numerical-color-coding logic. More in details, each hull is assigned a clear and consistently maintained color and number association, ensuring that each color unequivocally refers to the same element throughout the analysis. These visual associations are represented in Figure 56, where it is possible to find the correspondence.

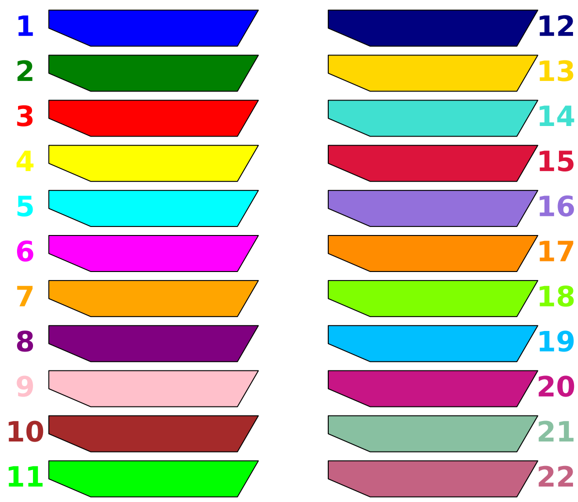

Figure 56: graphical symbology (numerical and color-coding) for the hulls tested.

Indeed, in the radar plot of Figure 57, it is possible to get a general overview about the simulations; specifically, each radius represents one single hull and the sector areas represent the total number of the simulations performed (along with a number to quickly identify their value), with an average value of 6.45 simulations for each hull (red dashed line). In order to ensure a representative comparison, the number of the simulations performed for each hull was changed considering the lengths, the speeds and the main hydrodynamical parameters.

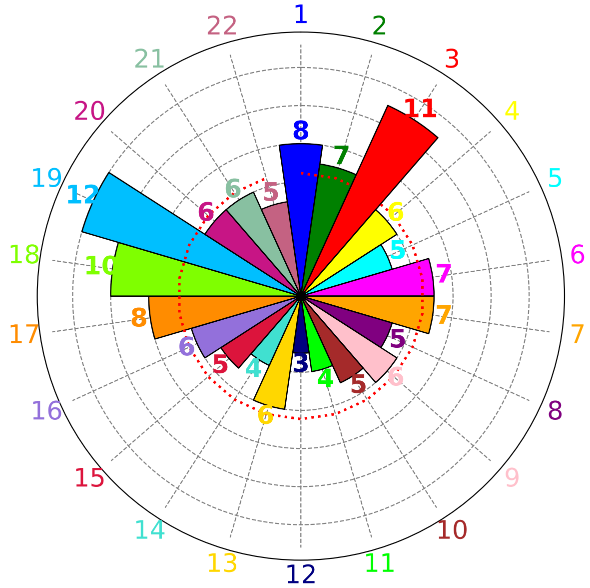

Figure 57: number of simulations varying the speed for each hull tested.

4.1 The available experimental database

By looking at the available benchmark for CFD, as reported in the ITTC benchmark-repository [56], the total number of the cases to be tested is small, sometimes old and difficult to be found with the respect of the geometries and the experimental data. Whereas, at the University of Genova, more than 200 experimental tests have been found inside a collection of ancient volumes. Experiments inside the volumes mainly come from the experiences performed inside two different towing tanks, which are La Spezia and the old Roma, respectively. Among all the available cases, where both the geometries and the experimental data were available, those were selected in order to achieve the most heterogeneous group of comparisons (with the respect of hull shapes, speeds, dimensions and general characteristics) to perform a detailed post-processing analysis on the differences obtained. Even if Genova university database collects both old fashion hull shapes and some relatively modern hull, its great amount of data has been considered an important opportunity to test CFD capability to predict the EFD results which, moreover, have been regarded as benchmarks. Among all the available hulls, 16 have been used to apply the numerical set-up and perform all the CFD calculations. In order to overcome the potential limitations associated with the use of outdated hull shapes, additional modern shapes were also investigated, considering the one listed in the I.T.T.C. benchmark-repository [56], where the link for both the geometries and the experimental results is available. Among them, the following hulls have been selected: KVLCC2, DTC, KCS, JBC (ballast and full load conditions) and DTMB. Accordingly, in Table 24 the main characteristics for the hulls tested are reported. Moreover, both the symbols and the nomenclature of the dimensions and results follow the conventions established by the I.T.T.C. Symbols and Terminology list [118].

Table 24: Main characteristics of the updated database.

Model characteristics	Symbol	Values			UNIT
		Minimum	Maximum	Mean	
Length between perpendiculars	L_{PP}	3,4671	7,2785	5,1588	m
Length, overall submerged	L_{OS}	3,7426	7,3288	5,2654	m
Length of waterline	L_{WL}	3,6074	7,3288	5,2458	m
Maximum moulded Breadth at design WL	B_{WL}	0,651	1,2688	0,8443	m
Draught at forward perpendicular	T_F	0,1804	0,455	0,2576	m
Draught at midship	$T_M = (T_A + T_F)/2$	0,185	0,455	0,2619	m
Draught at aft perpendicular	T_A	0,185	0,455	0,2662	m
Displacement volume	∇	0,2314	3,2724	0,8086	m^3
Area of wetted surface	S	2,63	13,0128	5,2899	m^2
Ratio L/B	L_{WL}/B_{WL}	3,4566	7,6283	6,26	-
Ratio B/T	B_{WL}/T_M	2,4098	5,2234	3,3143	-
Block coefficient	$C_B = \nabla/LBT$	0,4008	0,8441	0,563	-
Froude's length coefficient, or length-displacement ratio	$M^C = \nabla^{1/3}$	4,7149	7,825	6,1555	-
Scale ratio	$\lambda = L_s/L_M$	5	59,4043	25,6778	-
Area of water-plane	A_W	2,0746	8,009	3,526	m^2
Longitudinal centre of flotation	L_{CF}, X_{CF}	1,6801	3,7433	2,5817	m
Longitudinal centre of buoyancy	L_{CB}, X_{CB}	1,5196	3,6886	2,4799	m

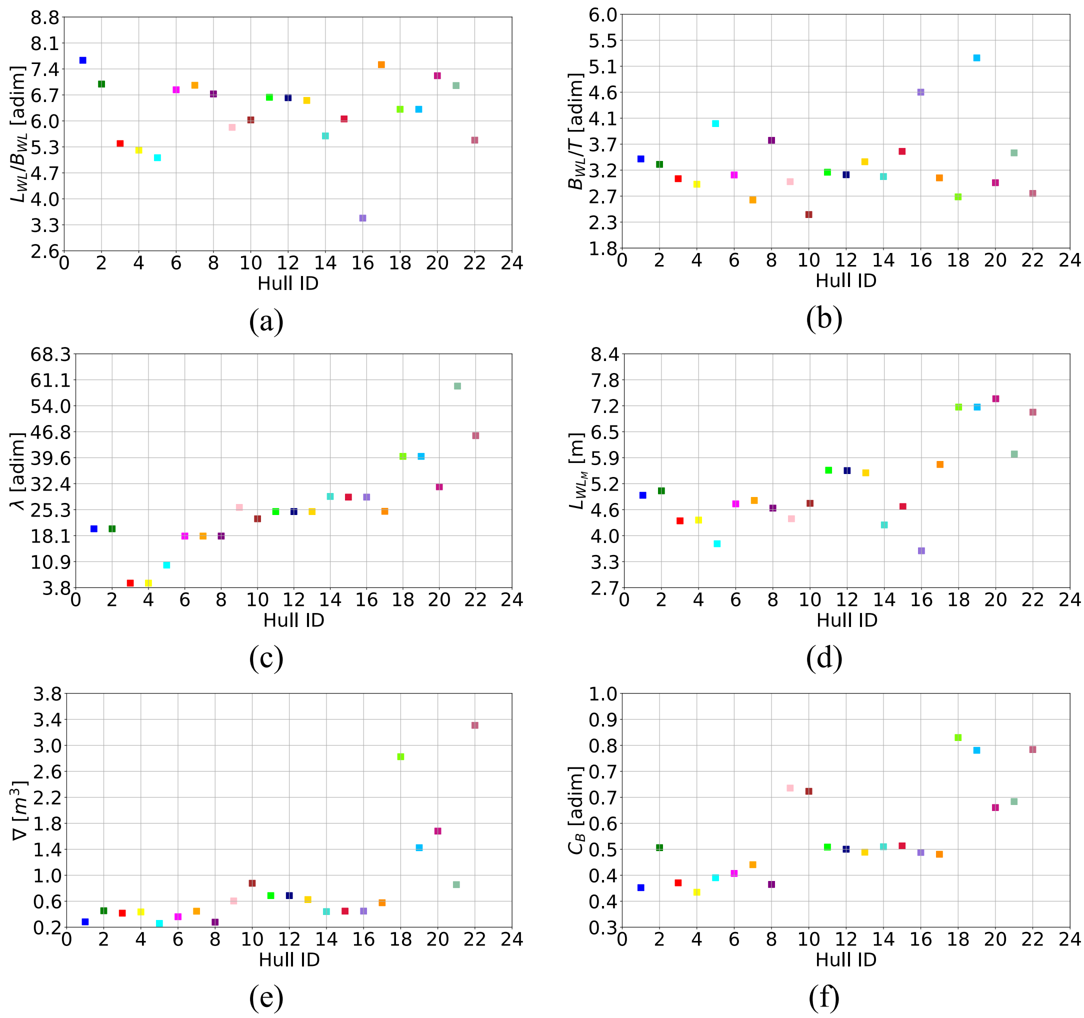

Figure 58: representation about ratio L_{WL}/B_{WL} (a), ratio B_{WL}/T (b), scale factor (c), model length (d), volume of hull (e) and coefficient of block (f) versus each hull tested, represented by one single color.

Finally, 22 different hulls have been tested and among them 16 comes from Genova database and the other 6 has been taken among the I.T.T.C. benchmark-repository. Considering each selected hull as a single color marker (which remains the same for each representation), Figure 58 shows the variations about the ratio L_{WL}/B_{WL} (a), the ratio B_{WL}/T (b), the scale factor (c), the model length (d), the volume of hull (e) and the block coefficients (f) versus the hulls; moreover, the graphical data were employed to verify that the representative sample of the hulls exhibited an adequate degree of dispersion, thereby ensuring the heterogeneity of the initial dataset.

4.2 Workflow description

By starting from an empty repository, a new comparative repository must be generated, where both the outputs of the simulations and the experimental data are stored. To replicate the same approach for all simulations, a workflow has been defined, as illustrated in Figure 59. In the following sub-paragraphs, a description about each item is going to be provided.

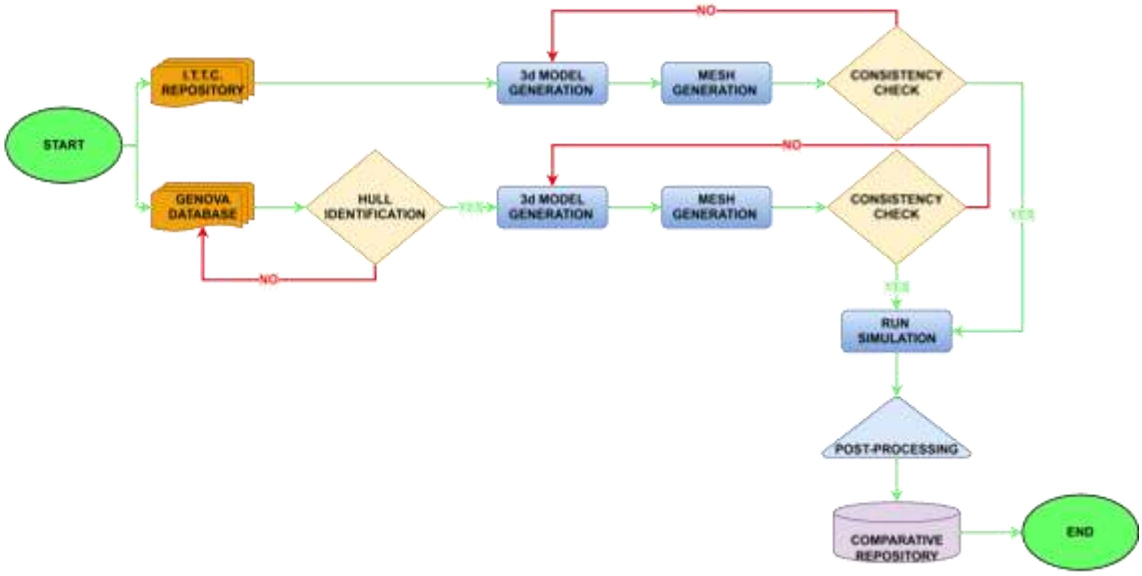

Figure 59: workflow representation.

4.2.1 Hull identification

Before testing a new hull, it is essential to first analyze and select the parent hull based on specific characteristics. Several parameters can be used to describe a generical hull; among the many possibilities in this multi-dimensional space for the choice, a selection process for relevant parameters has been conducted. Specifically, the following items have been identified as key parameters for consideration:

- Model length (L_{LW}): as reported in Guo et al. [119], the dimension of the model length can directly affect the resistance prediction. As suggested by I.T.T.C. Ship Models Procedure 7.5-

01-01-01 [62], the model should be simultaneously “as large as possible” to overcome, or at least to reduce, possible situations where the model operates under conditions different from the ship and small enough to avoid the interaction with the walls of the tank (blockage effect). Ended, the criterion used to choose among all the available parent hulls deals with the greater variation as possible for the model length to perform the simulations.

- Ratio L_{WL}/B_{WL}: as reported in Le et al. [120], this ratio has a direct impact on the ship resistance; more in details, if the ratio increase, the resistance decrease. Furthermore, the study suggests that variations in the ratio exert a stronger influence on pressure resistance coefficient than on frictional one. Moreover, as reported in Sessa’s PhD thesis [121], this ratio has a direct impact on ship stability and maneuverability and its range of variation is between 3.0 and 9.5. Consequently, based on these considerations, hulls with highly heterogeneous ratios were selected so as to maximize the variability within the test sample.
- Ratio B_{WL}/T_M: it is an important parameter when considering wave resistance, as reported by Petersson [122]; an increase in the ratio results in a higher value for the wave resistance. Moreover, as reported in Sessa’s PhD thesis [121], this ratio has a direct impact on ship stability and on the drift resistance; its range of variation is between 2.0 and 4.5. Also in this case, hulls selection was made with the attempt to diversify this ratio as much as possible in order to obtain a sample that is as varied as possible.
- Scale Factor ($\lambda = L_s/L_M$): when dealing with the scale effects on ship resistance components, as reported in the work of Dogrul et al. [123], the scale effects can influence the residual resistance coefficient for the ship. This aspect leads to consider even the scale ratio as a key parameter when defining the hull to be tested.
- Non-dimensional speed (F_r): when considering a towing tank experiment, the dependence of the oscillatory behavior on the Froude number, the acceleration rate, and the acceleration smoothing profile has been analyzed by Doctors [124]. During the test, the amplitude for the oscillations arising in the supposed steady-state phase are connected with the speed; thus, it can be argued that the speed influences directly the resistance. To account for the effects of the variation for the Froude number and, in completely compliance with I.T.T.C. recommendations for the Resistance Test (7.5-02-02-01) [69], the non-dimensional speeds values were selected to guarantee a heterogeneous sample, which could then be used for subsequent simulations.

The range of variation observed for the model length, Ratio L_{WL}/B_{WL}, Ratio B_{WL}/T_M, Scale Factor and the non-dimensional speed are displayed in Table 25.

Table 25: variation among the parameters considered for the selection of the hulls within the databases.

Parameters	Symbol	Value Ratio		UNIT
		Min	Max	
Model length	L_{WL}	3,6074	7,3288	[m]
Ratio L/B	L_{WL}/B_{WL}	3,4566	7,6283	[adim]
Ratio B/T	B_{WL}/T_M	2,4098	5,2234	[adim]
Scale factor	λ	5,0000	59,4043	[adim]
Ship speed	F_r	0.0500	0.4160	[adim]

4.2.2 3D model generation

Once the hull to be tested has been defined, it is possible to move at the 3D geometry generation step. The output of this phase consists in preparing a STereoLithography (STL) file with triangular mesh objects, describing the geometry of the hull to be tested. As described in the study on "Ship Hull Resistance Calculations Using CFD Methods" of Voxakis [125], the file format consists in a list of triangles, each one characterized by three vertices and a unit vector normal to the face (ordered by the right-hand rule, counterclockwise); in Figure 60 a view from a script for a single triangle is shown.

```
solid cube
 facet normal 0.0 0.0 -1.0
  outer loop
   vertex 0 0 0
   vertex 0 1 0
   vertex 1 0 0
  endloop
 endfacet
 ...
endsolid cube
```

Figure 60: ASHII representation for a triangular surface in STL format.

This approach leads to describe a complex 3D geometry through unstructured planar triangular surfaces. As reported in Leirmo et al. [126], when a prismatic surface (P_ORIG) is modelled with this approach, a new surface is obtained (C), but differences among them, P_ORIG and P_ORIG_STL respectively, cannot be listed. As reported in the graphical representation of Figure 61, a unit-length cube (as representative example for P_ORIG) is shown along with the same surface described by triangles; in each image the triangle with a vertex in the point (1, 0, 1) and with a side parallel to the unit vector $\hat{\imath}$, being $\vec{\imath} = (1,0,0)$ is painted in yellow along with its red outward normal. More in details, considering the refinement to get the P_ORIG_STL surface moving from the prismatic one (P_ORIG), Figure 61a shows a P_ORIG_STL surface composed by $3 \cdot 2^2$ triangular surfaces (equal to the minimum numbers of surfaces necessary to describe the initial surface, P_ORIG), while in Figure 61b-d this number moves from $3 \cdot 2^3$, $3 \cdot 2^4$ and $3 \cdot 2^5$, respectively.

While, considering a curved surface (C_CURV), and considering the re-described surface (C_CURV_STL), differences occur. The number of triangles used to model the C_STL surface is directly connected with the difference among the original surface and the reconstructed one; indeed, as the number of triangles increase, the differences tend to decrease.

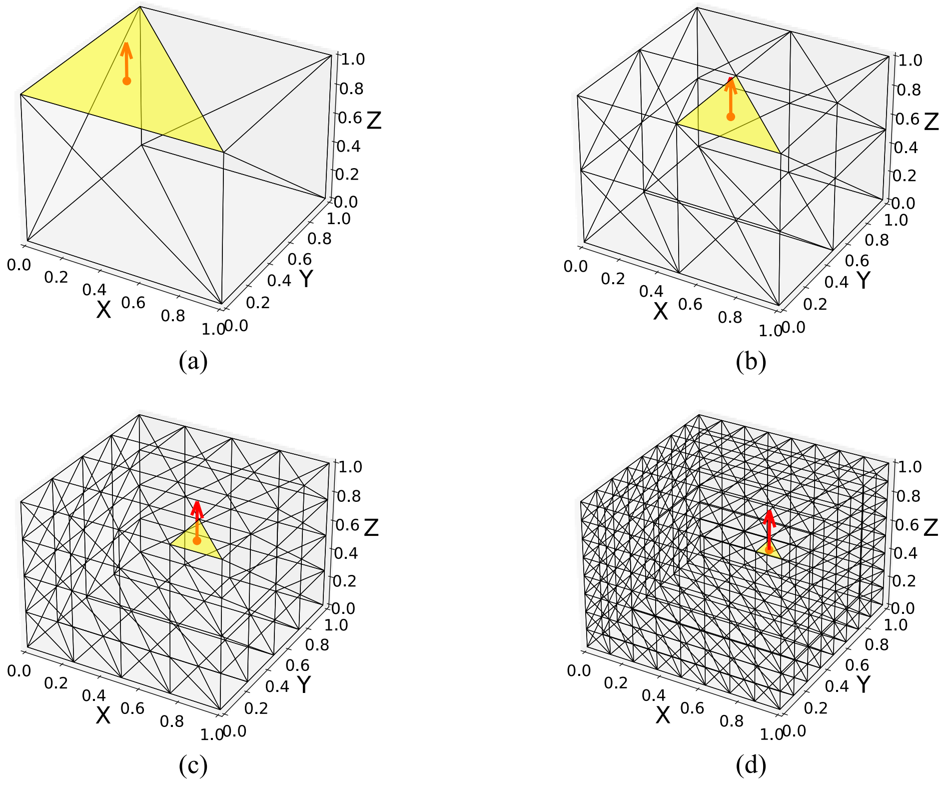

Figure 61: STereoLithography representation of a cube varying the number of triangles for each surface; $3 \cdot 2^2$ *triangles (a),* $3 \cdot 2^3$ *triangles (b),* $3 \cdot 2^4$ *triangles (c),* $3 \cdot 2^5$ *triangles (d).*

As an illustrative case, a model of a sphere of unit diameter, as shown in Figure 62, can be used to demonstrate the type and the order of magnitude about the differences among the surfaces C_CURV and C_CURV_STL.

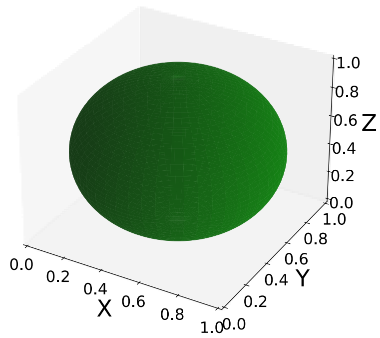

Figure 62: sphere of unit diameter.

Even in this case, the curved surface C_CURV, can be approximately described through a number of triangular planar surfaces to get the C_CURV_STL surface and the approximation improves as the number of triangles increase. Indeed, considering the sphere of unit diameter and one triangle (blue in shape with its red outward normal) it possible to attest how the tessellation influences the precision for the C_CURV_STL. Furthermore, when 32 triangles are used to model the C_CURV surface (Figure 63a) the shape for C_CURV_STL surface is very far from a sphere. While, using a higher number of triangles, for instance 72 (Figure 63b), 128 (Figure 63c), 200 (Figure 63d), 288 (Figure

63e), 392 Figure 63f), 43808 Figure 63g) and 80000 (Figure 63b), it possible to graphically assess how the new C_CURV_STL surface is close to the original one.

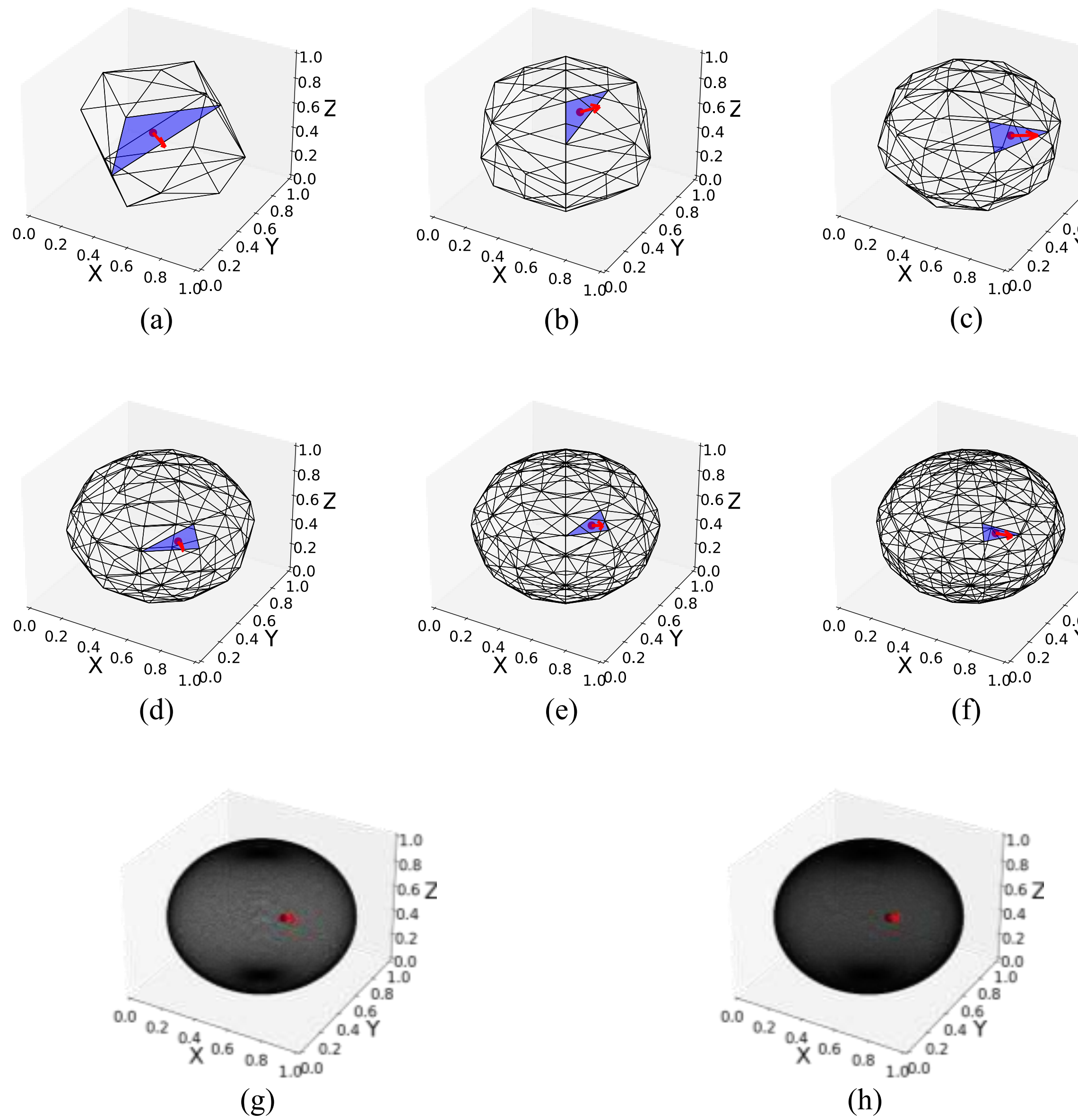

Figure 63: STereoLithography representation for the surface of the sphere of unit diameter varying the number of triangles, moving from 32 (a), 72 (b), 128 (c), 200 (d), 288 (e), 392 (f), 43808 (g) to 80000 (h) triangular new surfaces.

In order to quantify this difference, it possible to use an XY plane passing at Z=0.5 height (the unity-length sphere centre), to cut the two surfaces, C_CURV_STL and C_CURV_STL respectively, and consider their traces. Notably, considering the combined representation on the first quadrant for the above mentioned plane along with the two traces, it can be firmly stated how the number of triangular surfaces moving from 32 (Figure 64a), 72 (Figure 64b), 128 (Figure 64c), 200 (Figure 64d), 288 (Figure 64e), 392 (Figure 64f), 43808 (Figure 64g) and 80000 (Figure 64h) directly influence the approximation when a curved surface has to be modelled.

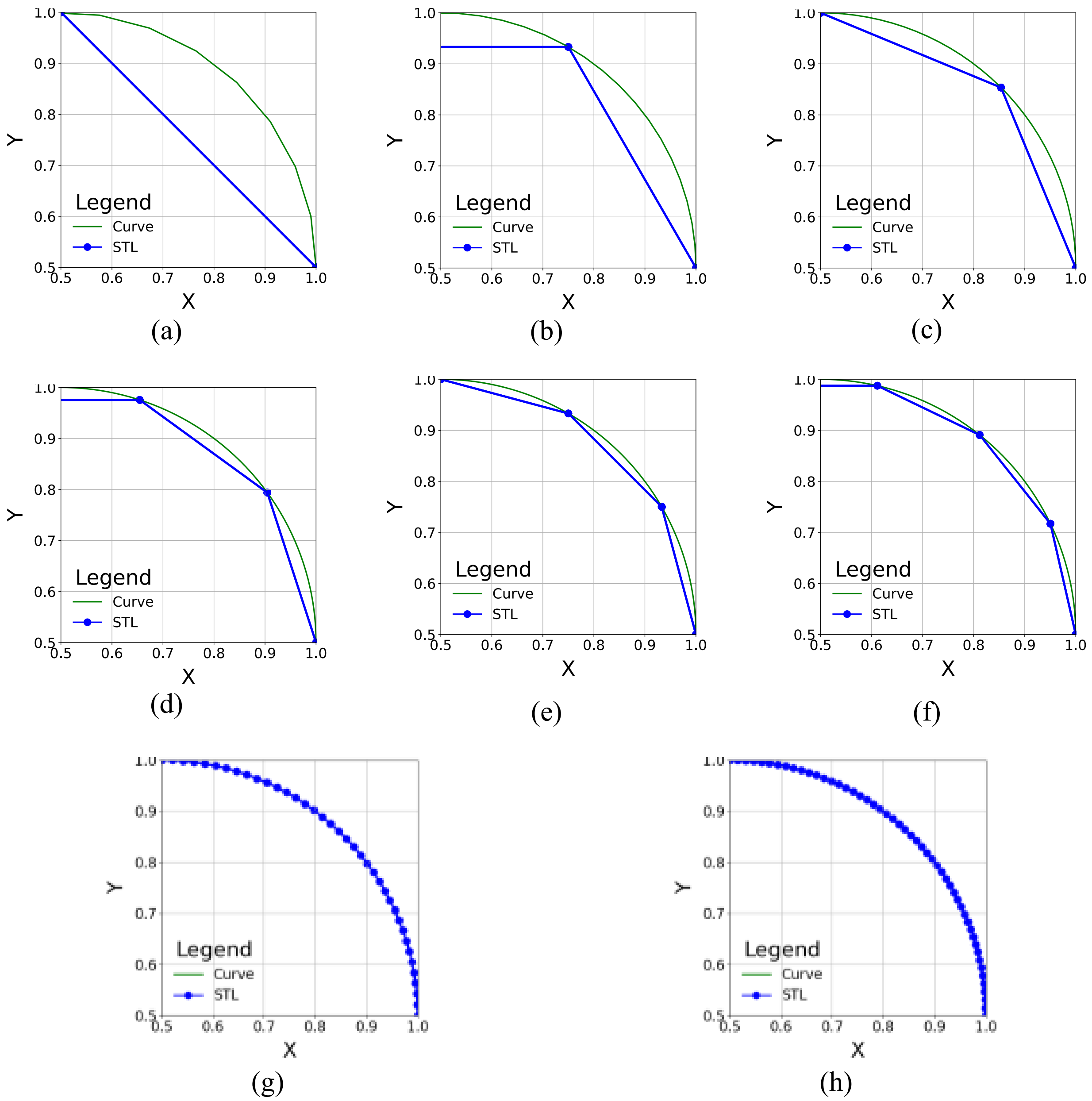

Figure 64: differences among surfaces on the plane XY passing through the sphere of unit diameter centre varying the number of triangles 32 (a), 72 (b), 128 (c), 200 (d), 288 (e), 392 (f), 43808 (g), 80000 (h) to describe the C_CURV_STL surface.

Moreover, with the respect of the two surfaces on the XY plane, it is possible to compare mathematically the results for the value of the area of the circumference with a unit diameter, as reported in equation (116), and the value for the area from the polygonal trace from the STL representation.

$$Area = \frac{\pi D^2}{4} = 0.785\ [u^2] \qquad (116)$$

Indeed, based on the analysis of Figure 65a, the value of 0.785 can be considered asymptotic, while considering Figure 65b the decay rate can be observed, which tends to zero when an infinite number of triangles is used.

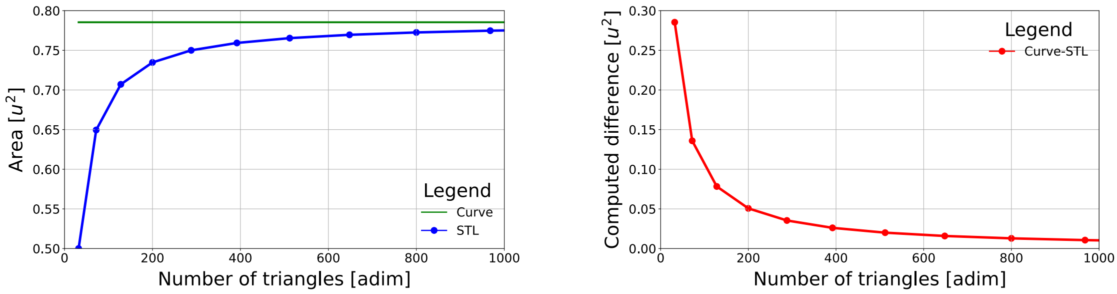

(a) (b)

Figure 65: comparison among a unity-diameter circumference and the trace of STL surface on the plane XY passing at Z=0.5, value of areas (a) and difference among areas (b).

4.2.3 Mesh generation

As described in the numerical set-up Chapter, with the respect to the length of the model to be tested, the mesh has been generated with the same parametrical set-up for each simulation performed. Therefore, a new ".stl" representation about the geometry for the hull to be tested has been prepared inside the openFOAM environment.

4.2.4 Consistency check

Moving from the ".stl" representation about the to be tested and considering the 3D geometry generated in the mesh phase, a detailed analysis has to be performed on this new geometry to guarantee the expected degree of accuracy, when compared with the experimental data. Indeed, as reported in Lakatoš et al [108], the shape for the hull can lead to differences in results. Hence, considering Figure 66a where the 3D geometry of Hull 20 is reported along with 3 different plane sections, positioned at $L_{PP} = 0$ (red trace), $L_{PP} = 10$ (green trace) and $L_{PP} = 20$ (blue trace) respectively, it possible to attest the differences among the original ".stl" and the remeshed one. Indeed, looking at Figure 66b, where the details about all the traces for the plane sections are shown, it is possible to consider a couple of them, generated by the section plane at $L_{PP} = 0$ and $L_{PP} = 20$; as shown in Figure 66c and Figure 66d, differences among the two geometries can be observed. More specifically, considering Figure 66e and Figure 66f, two points characterized by high curvature were considered as representative examples to emphasize the differences between the two traces; in the first case the difference is 0.0045m while in the second one the difference is 0.0158m in ship scale dimension. This, considering the model scale, leads to differences on the order of one and four micrometer, respectively.

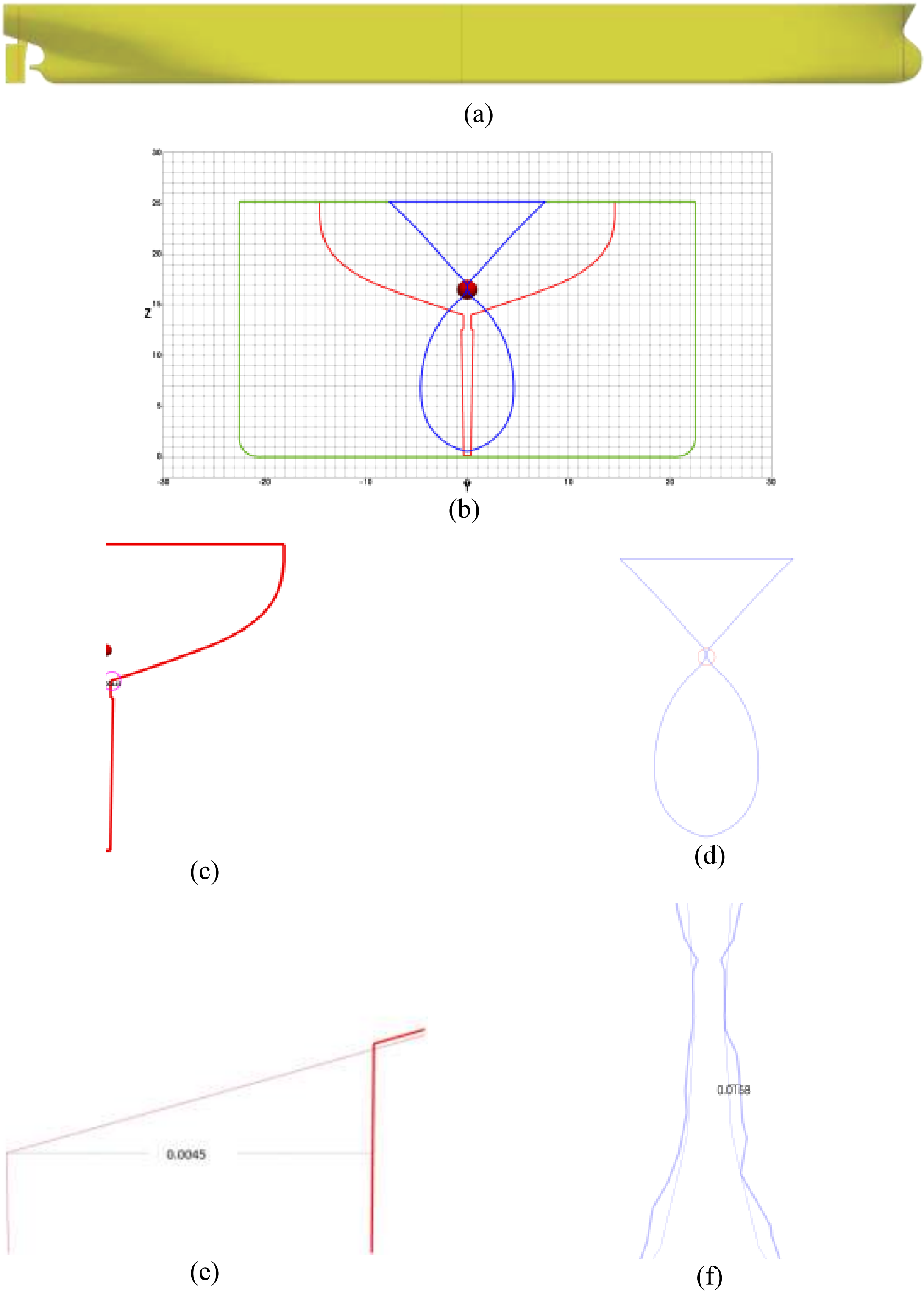

Figure 66: ".stl" original file compared with the meshed one (full scale dimensions). Traces for the plane sections at $L_{PP} = 0$ (red), 10 (green), 20 (blue) for hull 20 (a), details on the transversal traces for the plane sections (b), plane section at $L_{PP} = 0$ (c) and its details (e), plane section at $L_{PP} = 20$ (d) and its details (f).

Nevertheless, in order to account for this possible discrepancy, an in house developed tool has been used to work on ".stl" geometries. The tool's results are directly compared with the experimental data to verify the accuracy and reliability of the geometry to be tested. In the workflow, this phase is referred to as the "consistency check" and different kinds of evaluation are performed in this section. Among the checks, the most important is the volume one; indeed, the volume for the model hull in towing tank is compared with the one from the meshed hull at the same condition, as reported in (117) and if the value remains below 0,5%, the test is deemed to be successful otherwise further investigations about the father 3D geometry has to be performed.

$$\left(\frac{(\nabla_{CFD})_M}{(\nabla_{EFD})_M} - 1\right) = \begin{cases} \leq \mp 0.5\%, & satisfied \\ > \mp 0.5\%, & not\ satisfied \end{cases} \tag{117}$$

This "pass-no pass" check ensure the correctness for the hull volume implemented in CFD simulation with the experimental one, and therefore the equivalence among the force in the Z-direction at time 0 and the hull displacement. Once the initial control has been successfully passed, additional analysis is required in accordance with the same procedure. Each one of them is characterized by a "looser acceptance criteria", with the pass/fail threshold defined as 1%. More precisely, as reported in equations (118)-(124), the ratios among the waterplane area, the longitudinal position for the centre of flotation, the longitudinal position for the centre of buoyancy, the wetted surface area, the L/B ratio, the B/T ratio and the coefficient of block have been respectively investigated when experimental data were available.

$$\frac{\left(A_{WL\_CFD}\right)_M}{\left(A_{WL\_EFD}\right)_M} = \begin{cases} \leq \mp 1\%, & satisfied \\ > \mp 1\%, & not\ satisfied \end{cases} \tag{118}$$

$$\frac{\left(X_{F\_CFD}\right)_M}{\left(X_{F\_EFD}\right)_M} = \begin{cases} \leq \mp 1\%, & satisfied \\ > \mp 1\%, & not\ satisfied \end{cases} \tag{119}$$

$$\frac{(B_{CFD})_M}{(B_{EFD})_M} = \begin{cases} \leq \mp 1\%, & satisfied \\ > \mp 1\%, & not\ satisfied \end{cases} \tag{120}$$

$$\frac{(S_{CFD})_M}{(S_{EFD})_M} = \begin{cases} \leq \mp 1\%, & satisfied \\ > \mp 1\%, & not\ satisfied \end{cases} \tag{121}$$

$$\frac{\left(L_{WL\_CFD}/B_{WL\_CFD}\right)_M}{\left(L_{WL\_EFD}/B_{WL\_EFD}\right)_M} = \begin{cases} \leq \mp 1\%, & satisfied \\ > \mp 1\%, & not\ satisfied \end{cases} \tag{122}$$

$$\frac{\left(B_{WL\_CFD}/T_{M\_CFD}\right)_M}{\left(B_{WL\_CFD}/T_{M\_EFD}\right)_M} = \begin{cases} \leq \mp 1\%, & satisfied \\ > \mp 1\%, & not\ satisfied \end{cases} \tag{123}$$

$$\frac{\left(\nabla_{CFD}/(LBT)_{CFD}\right)_M}{\left(\nabla_{EFD}/(LBT)_{EFD}\right)_M} = \begin{cases} \leq \mp 1\%, & satisfied \\ > \mp 1\%, & not\ satisfied \end{cases} \tag{124}$$

Considering Hull 19 as an example, and running the in house developed code for both its original ".slt" and the remeshed one, and comparing them with the experimental data, results obtained are in agreement with all the criteria previously cited. The numerical results from this analysis are shown in Table 26.

Table 26: consistency checks and parameters with the respect to Hull 19.

Parameters	Values			Values Ratio		Compliance criterion
	EXP	STL1	STL2	STL2/STL1	STL2/EXP	
$\frac{(\nabla_{CFD})_M}{(\nabla_{EFD})_M} - 1$	89222.800	89226.300	89211.100	-0.02%	-0.01%	$\leq \mp 0.5$ pass
$\frac{(A_{WL\_CFD})_M}{(A_{WL\_EFD})_M} - 1$	-	10922.800	10922.800	0.00%	-	N.A.
$\frac{(X_{F\_CFD})_M}{(X_{F\_EFD})_M} - 1$	-	147.544	147.543	0.00%	-	N.A.
$\frac{(X_{B\_CFD})_M}{(X_{B\_CFD})_M} - 1$	-	144.260	144.258	0.00%	-	N.A.
$\frac{(S_{CFD})_M}{(S_{EFD})_M} - 1$	15005.100	14958.400	14954.800	-0.02%	-0.34%	$\leq \mp 1$ pass
$\frac{\left(L_{WL\_CFD}/B_{WL\_CFD}\right)_M}{\left(L_{WL\_EFD}/B_{WL\_EFD}\right)_M} - 1$	6.3333	6.3034	6.3034	0.00%	-0.47%	$\leq \mp 1$ Pass
$\frac{\left(B_{WL\_CFD}/T_{M\_CFD}\right)_M}{\left(B_{WL\_CFD}/T_{M\_EFD}\right)_M} - 1$	5.2234	5.2234	5.2234	0.00%	0.00%	$\leq \mp 1$ pass
$\frac{\left(\nabla_{CFD}/(LBT)_{CFD}\right)_M}{\left(\nabla_{EFD}/(LBT)_{EFD}\right)_M} - 1$	0.8075	0.8114	0.8113	-0.02%	0.46%	$\leq \mp 1$ pass

The Table 27 displays data concerning the application of the consistency check to Hull 20 case, as an additional illustrative example. Although the dynamical attitudes of a displacement ship are less crucial than those of a planing boat for the advance resistance evaluation, a focus for the centre of gravity (CG) position needs to be executed. In the cases considered, the experimental data for CG weren't always available but the initial trim was known. Therefore, all the simulations were performed considering $L_{CG} \equiv L_{CB}$ to guarantee the initial attitude. While, being the vertical position for CG unknown, it has been assumed equal to the buoyancy one.

Table 27: consistency checks and parameters with the respect to Hull 20.

Parameters	Values			Values Ratio		Compliance criterion
	EXP	STL1	STL2	STL2/STL1	STL2/EXP	
$\frac{(\nabla_{CFD})_M}{(\nabla_{EFD})_M} - 1$	52030	51980.1	52015.9	0.069%	-0.027%	$\leq \mp 0.5$ pass
$\frac{(A_{WL\_CFD})_M}{(A_{WL\_EFD})_M} - 1$	-	6149.44	6149.68	0.004%	-	N.A.
$\frac{(X_{F\_CFD})_M}{(X_{F\_EFD})_M} - 1$	-	101.96	101.956	-0.004%	-	N.A.
$\frac{(X_{B\_CFD})_M}{(X_{B\_CFD})_M} - 1$	-	111.597	111.517	-0.072%	-	N.A.
$\frac{(S_{CFD})_M}{(S_{EFD})_M} - 1$	9539	9537.21	9555.03	0.187%	0.168%	$\leq \mp 1$ pass
$\frac{\left(L_{WL\_CFD}/B_{WL\_CFD}\right)_M}{\left(L_{WL\_EFD}/B_{WL\_EFD}\right)_M} - 1$	7.2205	7.2113	7.2467	0.492%	0.364%	$\leq \mp 1$ Pass
$\frac{\left(B_{WL\_CFD}/T_{M\_CFD}\right)_M}{\left(B_{WL\_CFD}/T_{M\_EFD}\right)_M} - 1$	2.9815	2.9838	2.9838	0.00%	0.079%	$\leq \mp 1$ pass
$\frac{\left(\nabla_{CFD}/(LBT)_{CFD}\right)_M}{\left(\nabla_{EFD}/(LBT)_{EFD}\right)_M} - 1$	0.6435	0.6426	0.6399	-0.420%	-0.552%	$\leq \mp 1$ pass

4.2.5 Run the simulation

Once the "Consistency check" has been successfully passed, the simulation can run. As defined in the numerical set-up Chapter, the best practices are used to perform all the simulations with a standardized (and parametrical) common set-up with the respect to the physical description of the problem along with the numerical one. Each individual simulation required a dedicated allocation of computational resources. Considering the large number of simulations involved, the cumulative demand on computational capacity proved to be non-negligible and it isn't feasible to execute on a typical desktop computer. In particular, the computational resources employed for the execution of simulations, provided by Genova university, are detailed in Figure 1 (the resources HPC3 and HPC4 were provisioned at a subsequent stage), thereby offering a comprehensive overview of the computing effort required for this phase of the study.

Regarding the expected duration of the current phase, it represents the most time-consuming stage within the entire proposed workflow, when compared to all other phases. In accordance with the hardware specifications and computational constraints outlined in Table 28, the total wall-clock time required to perform a single simulation (involving approximately 1.2 M computational cells) is estimated to be on the order of 30 hours, when executed under standard workload conditions. This estimate accounts for the typical resource allocation and operating environment considered in the present study.

Table 28: HPC characteristics.

Parameters	Workstation1	Workstation2	HPC1	HPC2
Socket(s)	2	2	2	2
Core(s) per socket	6	6	12	12
Thread(s) per core	2	2	2	2
CPU(s)	12	12	24	24
Model name	Intel® Xeon® CPU E5-2640 0 @ 2.50 GHz	Intel® Xeon® CPU E5-2640 0 @ 2.50 GHz	Intel® Xeon® CPU E5-2680 v3 @ 2.50 GHz	Intel® Xeon® CPU E5-2680 v3 @ 2.50 GHz
CPU max	3000 MHz	3000 MHz	3300 MHz	3300 MHz
CPU min	1200 MHz	1200 MHz	1200 MHz	1200 MHz
Memory	32 MB	32 MB	64 MB	64 MB
HDD	1TB	1TB	500 GB	500 GB

4.2.6 Post-processing analysis

Once the simulation has run, its raw data (inside the OpenFOAM environment) are stored across several files, split into different directories within the case folder. This outcome represents the driver data for the post-processing analysis. This analysis can be divided into two layers: the assurance of correct interpretation for the physical problem and its numerical evaluation. In the first case, the objective is to verify whether the simulation has accurately captured the physical description of the case tested through the graphical interpretation for hydrodynamic attitudes and numerical conditions, running inside ParaView graphical visualization interface. Considering as an example the results for Hull 17 ($F_r = 0.39$), these main features are described through the submerged hull (Figure 67a), the relative pressure[4] among the hull (Figure 67b), the wall shear stress (Figure 67c), the flux around the hull (Figure 67d) and the wave patterns (Figure 67e-h). Furthermore, to provide greater assurance regarding the consistency of the result for the wave field of the simulation because of its importance for high speed resistance, wave-cuts are analyzed, and their graphical results are considered as pas-no pass check; an example for this analysis, considering four different transversal slices (at frames 0, 7, 14, 20 respectively) among the domain for Hull 17 ($F_r = 0.39$), is shown in Figure 68. Considering the graph, it is possible to graphically validate the behaviour for the wave pattern and moving on. While, in the numerical evaluation set, the relevant physical quantities are numerically evaluated. For this type of study, considering the available experimental data, the main parameters investigated are the advance resistance and its frictional component along with the dynamic attitude for the ship (considering the only two degrees of freedom for sinkage and trim). With the respect to the resistance evaluation, the history of the forces is stored inside an openFOAM output file; indeed, for each iteration (by using a LTS model), the three component for the pressure and viscous forces along with the moments, computed with reference to the Center of Rotation (CofR, belonging to the XY plane at Z=0, being this quote the trace for the water plane at velocity equal to zero), are reported.

[4] The relative pressure is the pressure without the effect connected with the gravity force. It better describes the phenomena around the hull and can be calculated through $p_{rgh} = p - \rho g \cdot h \; [N/m^2]$.

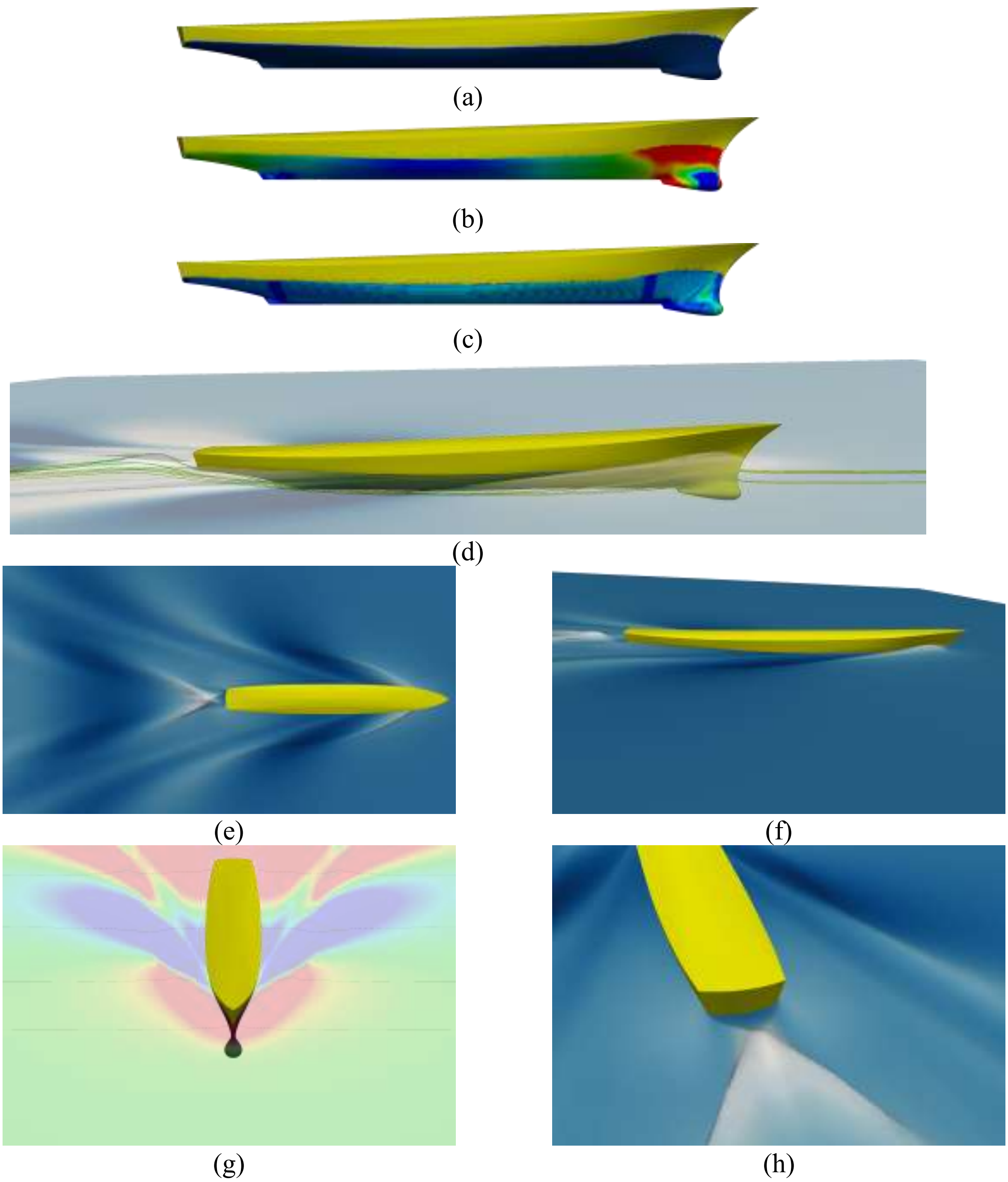

Figure 67: hydrodynamic attitudes and numerical condition for Hull 17 ($F_r = 0.39$); submerged hull (a), C_P (b), wall shear stress (c), the flux (d) and wave patterns (e-h).

Among all the available components, the projection on X axis (line of intersection between the water and symmetry planes) has been considered to evaluate the total advance resistance $\left(R_{T_M}\right)$ through the sum of each contribution arising from viscous $\left(F_{X\_V_M}\right)$ and pressure $\left(F_{X\_P_M}\right)$ components, as reported in (125):

$$R_{T_M} = F_{X_M} = F_{X\_P_M} + F_{X\_V_M} = \sum_S f_{X\_P_M} dA + \sum_S f_{X\_V_M} dA \ [N] \tag{125}$$

where, $f_{X\_P_M}$ and $f_{X\_P_M}$ represent the horizontal contributions for every surface that belongs to the hull for the viscous and the pressure forces, respectively. Considering just half hull due to the imposed symmetry condition for the simulation, the results for a couple of hulls are shown as representative examples for a noisy and a noise-free force signal. Specifically, Hull 1 ($F_r = 0.258$) corresponds to a noisy force signal, as reported in Figure 69a, whereas Hull 17 ($F_r = 0.158$) corresponds to a noise-free one, as shown in Figure 69b. Furthermore, Figure 69 illustrates the three resistance values $\left(R_{T_M}, F_{X\_P_M}, F_{X\_V_M}\right)$ across the iterations; in each graph a yellow box indicates the steady state region and all this period has been used to evaluate the representative value for each quantity. Moreover, considering Figure 69a, noise among the signals can be observed. This is something expected and confirmed by different studies, among which the following can be listed: Gilkeson et al. [127] and Bozzo et al. [128].

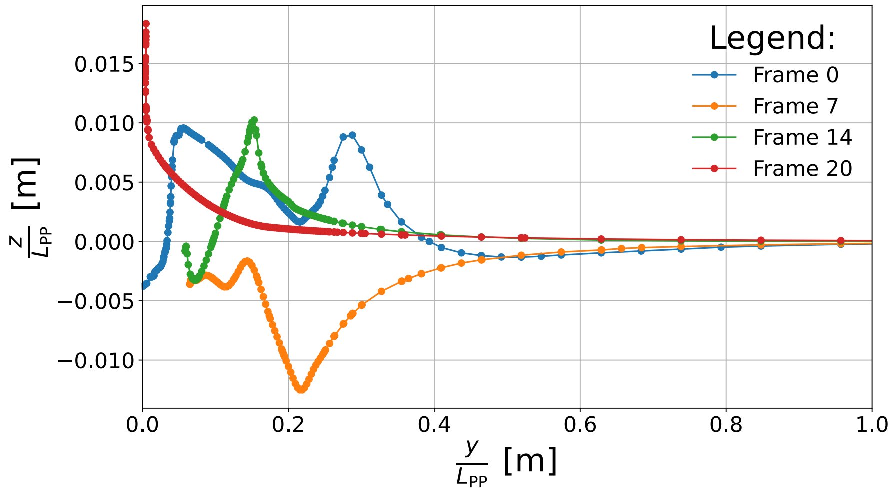

Figure 68: transversal wave-cuts Hull 17 (F_r = 0.39) at frames 0, 7, 14, 20 respectively.

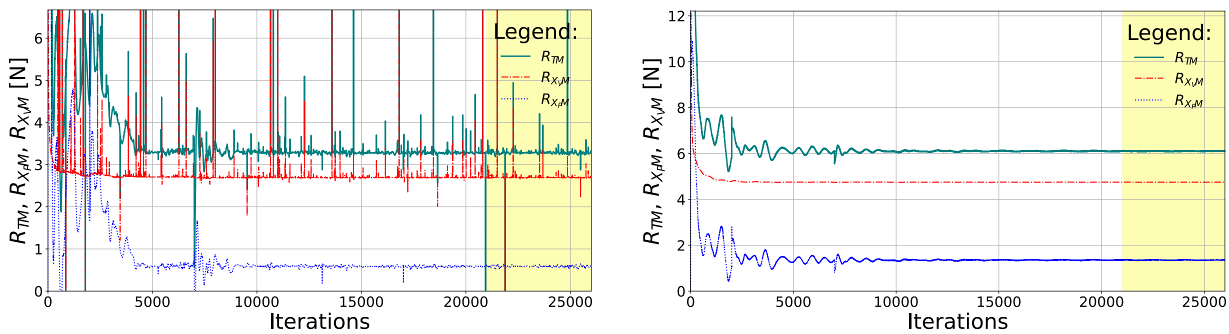

(a) (b)

Figure 69: advance resistance components for Hull 1 (a) and Hull 17 (b), tested at $F_r = 0.258$ and $F_r = 0.158$, respectively.

Indeed, when dealing with unstructured meshes, the presence of spikes in the history for the signals, especially when employing high number of cells, can be found. Therefore, a low-pass filter has been designed to handle the possible presence of noise and to prevent it from adversely influence the real trace of the signal considered. Considering the two cases listed, the outcomes resulting from the application of the filter (considering always just half hull) are reported in Figure 70a and Figure 70b, respectively. It is possible to assess the quality of the filter by looking at the raw signal (R_{TM}), its filtered one (R_{TM_FILT}) both of them scaled on a mean value $(R_{TM\_FILT_{MEAN}})$ evaluated in the steady state region among the iterations. Indeed, the peaks in the raw signal (R_{TM}) doesn't influence the general behavior of the filtered resistance (R_{TM_FILT}), represented by the black lines.

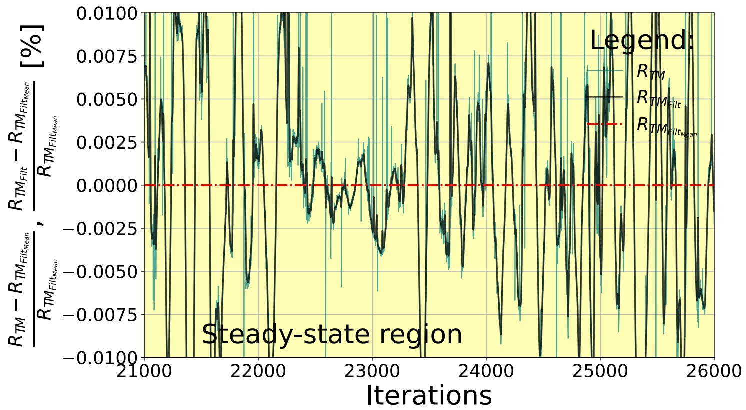

(a)

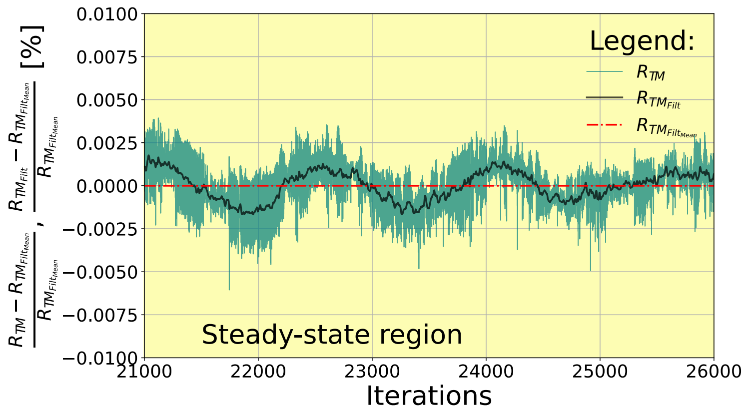

(b)

Figure 70: advance resistance filtered signals for Hull 1 (a) and Hull 17 (b), tested at $F_r = 0.258$ *and* $F_r = 0.158$*, respectively.*

With the respect to the other components stored inside an openFOAM output file, their contributions have been investigated for the verification about the displacements and the longitudinal trimming moment (MTL). More in details, considering the displacement (Δ), the contributions arising from viscous $(F_{Z\_V_M})$ and pressure $(F_{Z\_P_M})$ vertical components have been used, as reported in (126):

$$\Delta_M = F_{Z_M} = F_{Z\_P_M} + F_{Z\_V_M} = \sum_S f_{Z\_P_M} dA + \sum_S f_{Z\_V_M} dA \ [N] \tag{126}$$

where, $f_{Z\_P_M}$ and $f_{Z\_P_M}$ represent the vertical contributions for every surface that belongs to the hull for the viscous and the pressure forces, respectively. Considering just half hall due to the imposed symmetry condition for the simulation, a couple of examples, one for Hull 1 ($F_r = 0.258$) and one for Hull 17 ($F_r = 0.158$), are reported in Figure 71a and Figure 71b, respectively, where the three values $\left(F_{Z_M}, F_{Z\_P_M}, F_{Z\_V_M}\right)$ are representing among the iterations; in each graph a yellow box indicates the steady state region and all this period has been used to evaluate the representative value for each quantity.

Considering Figure 71a, some spikes among the signals can be observed, even if very smaller compared with the one obtained for the R_{TM}, reported in Figure 69a. In addition, it is possible to assess how negligible the viscous component is and a similar behavior is likewise observed in Figure 71b.

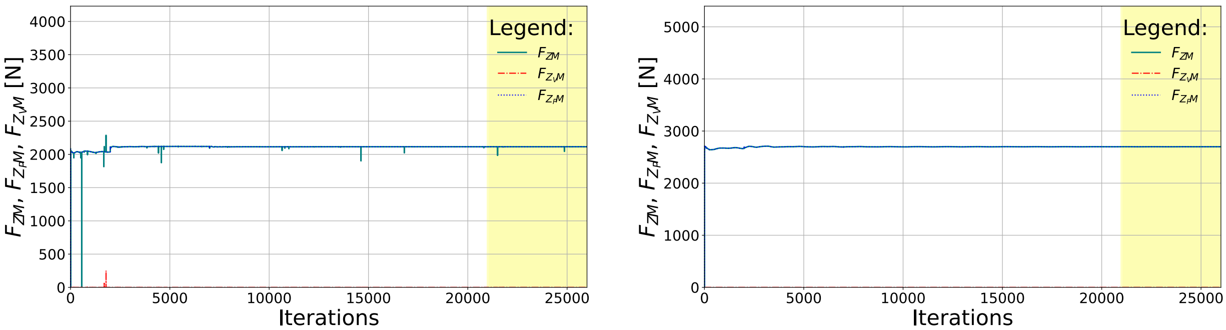

(a) (b)

Figure 71: forces vertical components for Hull 1 (a) and Hull 17 (b), tested at $F_r = 0.258$ *and* $F_r = 0.158$*, respectively.*

By filtering the signals, the results (considering always just half hull) are shown in Figure 72a and Figure 72b, demonstrating again the properly set-up for the filter because its proper functioning is confirmed by the fact that, where present, spikes are not considered. Indeed, when considering the raw signal (F_{ZM}) and its filtered one $\left(F_{ZM\_FILT}\right)$, both of them scaled on a mean value $\left(F_{ZM\_FILT_{MEAN}}\right)$ evaluated in the steady state region, the filtered signal is very close to the original one.

While, considering MTL, the moment about Y has been considered. Indeed, the pitching moment acting on the hull with respect to the CofR is given by (127):

$$MLT_M = M_{Y_M} = M_{Y_{P_M}} + M_{Y_{V_M}} = \sum_S (r - CofR) x f_{z\_P_M} dA + \sum_S (r - CofR) x f_{z\_V_M} dA \ [Nm] \quad (127)$$

where, $CofR$ represents the centre of rotation, r the centroid for i-th cell; while, $f_{Z\_P_M}$ and $f_{Z\_P_M}$ represent the vertical contributions for every surface that belongs to the hull for the viscous and the pressure forces, respectively. By convention, MTL is taken as positive when it results in a downward immersion of the stern.

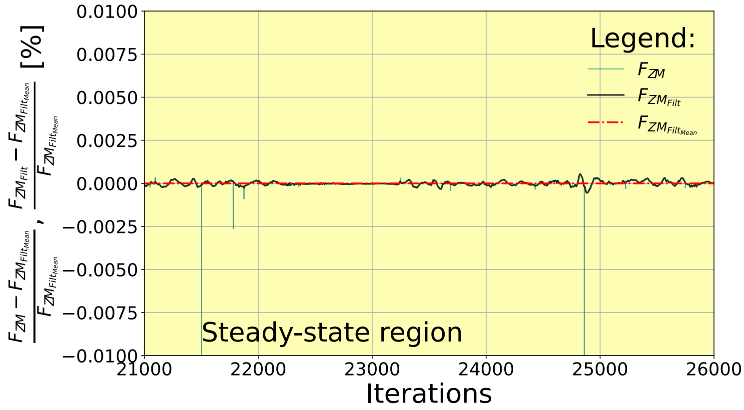

(a)

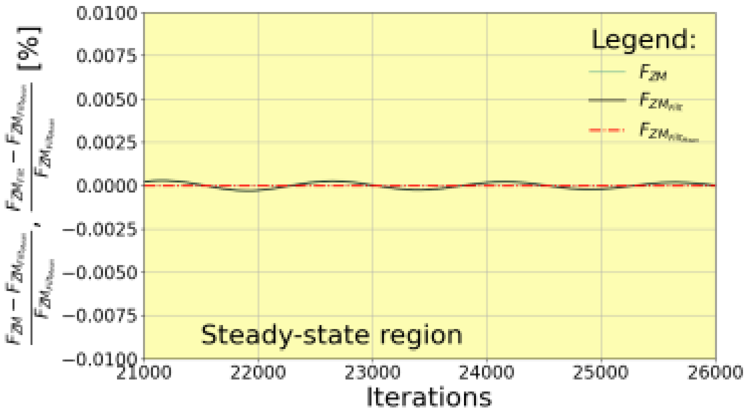

(b)

Figure 72: forces vertical components filtered signals for Hull 1 (a) and Hull 17 (b), tested at $F_r = 0.258$ *and* $F_r = 0.158$*, respectively.*

Considering just half hull due to the imposed symmetry condition for the simulation, a couple of examples, one for Hull 1 ($F_r = 0.258$) and one for Hull 17 ($F_r = 0.158$) are reported in Figure 73a and Figure 73b, respectively, where the three values $\left(M_{Y_M}, M_{Y\_P_M}, M_{Y\_V_M}\right)$ are representing among the iterations; in each graph a yellow box indicates the steady state region and all this period has been used to evaluate the representative value for each quantity. While, considering Figure 73a, noise among the signals can be observed, even if very smaller compared with the one obtained for the R_{TM}, reported in Figure 69a. In addition, it is possible to assess even in this case, how negligible the viscous component is whit the respect to MLT. By filtering the signals, the results (considering always just half hull) are shown in Figure 74a and Figure 74b, demonstrating again the properly set-up for the filter because its proper functioning is confirmed by the fact that spikes are not considered where present; when considering the raw signal (M_{YM}) and its filtered one $\left(M_{YM\_FILT}\right)$, both scaled on a mean value $\left(M_{YM\_FILT_{MEAN}}\right)$ evaluated in the steady state region among the iterations, even in this last case the filtered signal is very close to the original one.

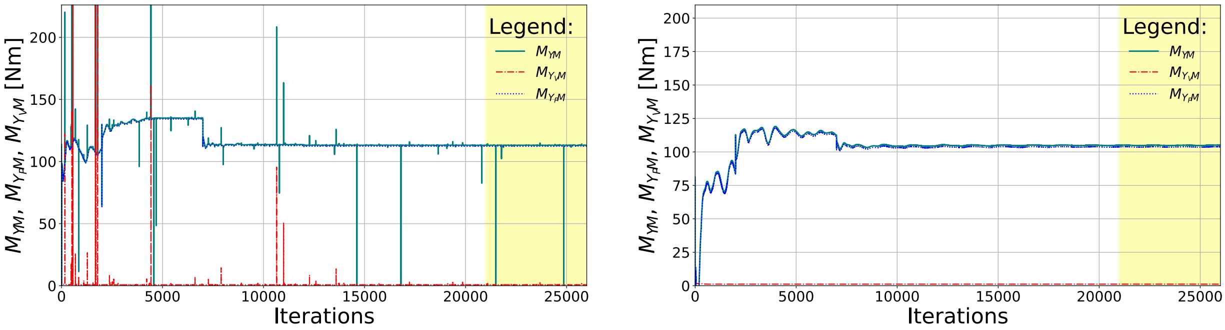

(a) (b)

Figure 73: MTL components for Hull 1 (a) and Hull 17 (b), tested at $F_r = 0.258$ *and* $F_r = 0.158$*, respectively.*

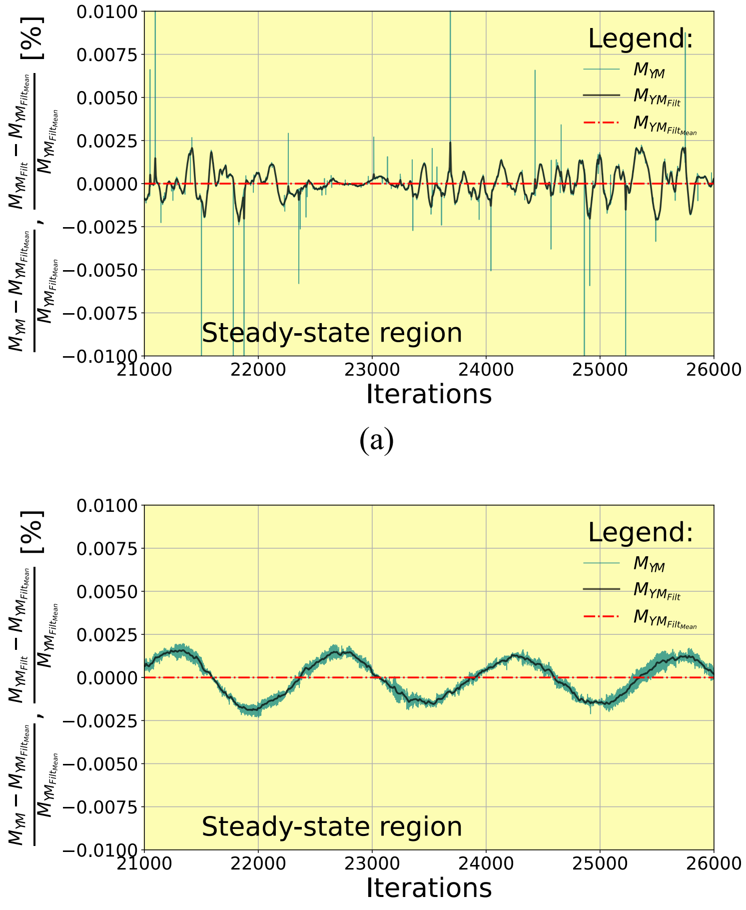

(a)

(b)

Figure 74: MTL components filtered signals for Hull 1 (a) and Hull 17 (b), tested at $F_r = 0.258$ *and* $F_r = 0.158$*, respectively.*

Finally, considering the dynamic attitude for the hull, during the simulation the MLT is evaluated four times and its values are compared with the longitudinal righting moment, as reported in (128); if a difference occurs, a new trim is defined and the model hull is forced to change its trim and to move on to the simulation.

$$MLT_M = M_{Y_{P_M}} + M_{Y_{V_M}} \cong \Delta(\overline{GM_L})\, sin(\vartheta) = \Delta(\overline{KM}_L - \overline{KG})\, sin(\vartheta) = M_L \tag{128}$$

Considering as example Hull 1 ($F_r = 0.258$) and by applying the above exposed procedure, it is possible to assess the value for the trim and the sinkage among the variation for the iterations, as reported in Figure 75a and Figure 75b respectively.

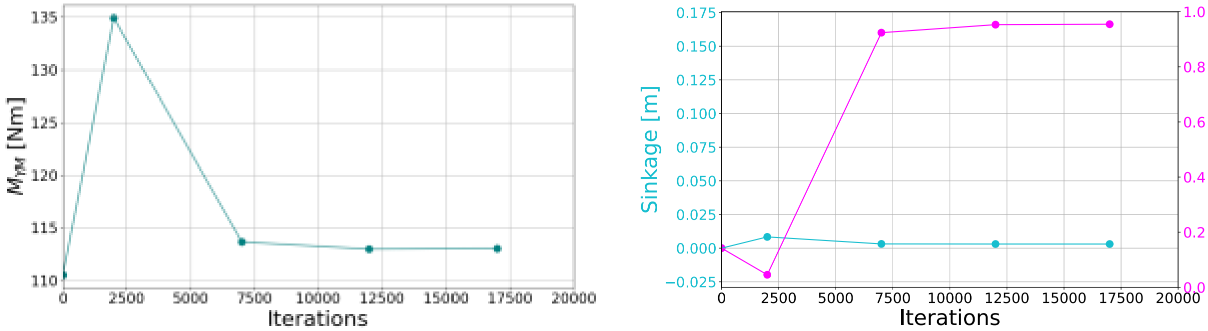

(a) (b)

Figure 75: MTL (a) and sinkage along with trim (b) for Hull 1 tested at $F_r = 0.258$.

Indeed, after a first initial peak (first check-point at 2000 iterations), the values always tend to a stable value; this final value is the one to be considered. Similar conclusions can be obtained through the analysis of Figure 76a and Figure 76b, representative of another test case, the Hull 17 ($F_r = 0.158$) one.

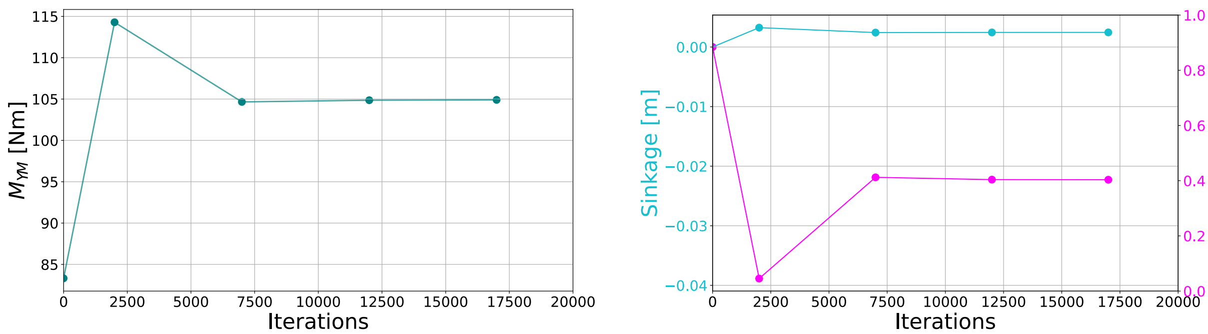

(a) (b)

Figure 76: MTL (a) and sinkage along with trim (b) for Hull 17 tested at $F_r = 0.158$.

Once the post-processing step is concluded, it is possible to move along the procedure to the following step.

In this stage of the procedure, a condition was achieved whereby all simulations had been successfully executed, and all results generated through the post-processing activities were systematically consolidated within an appropriately designed repository. Therefore, this step is the end of the procedure and its main feature deals with the comparative repository; as shown in Chapter 5, this repository has been investigated looking for correlations and for the evaluation of the precision obtained by a CFD calculation when compared with a result from a towing tank experiment.

This page is intentionally left blank

5 Data analysis

The comparisonal repository has been illustrated in Chapter 4. Indeed, once the data from all the simulations has been stored inside this repository, it is possible to analyze them in order to try to find and answer to the question "how precise is a Computational Fluid Dynamics (CFD) calculation when compared with an Experimental Fluid Dynamics (EFD) result?". By comparing the data, differences are predictable; therefore, in current Chapter different kinds of analysis will be performed about these expected differences in order to get an answer to the initial question and try to find any possible correlation among the hull (shapes, speed, configuration, scale) and the differences themselves. A broad spectrum of methodological strategies may be utilized to perform the data analysis. More in details, three kinds of analysis have been analyzed: the first one consists on the raw differences analysis, the second is based on the hull test configuration (bare or fully appended) and the last one considers the differences combine with the main hydrodynamic parameters.

Bases on "Numerical Uncertainty Assessment Direct Approach" (later on identified as NUADA), the results obtained from the comparisonal database are compared and a statistical analysis can be performed on them in order to derive the behaviour for the system. While, as further on described, the academic way to account for the Uncertainty Assessment can be spilt into the verification and the validation phases. With the respect to the numerical uncertainty evaluation in the verification phase, the theoretical approach can be identified as "Numerical Uncertainty Assessment Procedural Approach" (NUAPA). In NUAPA, the available theoretical approaches are used to identify the numerical uncertainty based on a generical simulation, where different parameters change to identify the system's sensitivity to them. The numerical uncertainty assessment experienced through NUAPA has to be combined with the experimental one to get the uncertainty assessment for that case.

While, considering the case when a propeller (o more) is mounted at the stern of a ship, a mutual interaction between the propeller and the hull occurs. To account for this kind of domain, and in the perspective of delivering a fully complete answer to the question about the precision of a CFD calculation when compared with an experimental result, a detailed analysis of the self-propulsion from both the numerical and the experimental points of views will be presented in Chapter 6, encompassing all relevant aspects of the phenomena. Indeed, without implementing the propeller in the CFD domain, which requires a non-negligible computational effort and considering the robustness about the virtual disk theory, a simplified approach to define the interaction among hull and the effect for the propeller thrust and torque has been investigated.

For the sake of completeness, in order to enhance the clarity and immediate recognizability of each hull among all the others, present Chapter adopts the same coherent numerical-color-coding logic, as exposed in Chapter 4.

5.1 Data analysis

In this section, the analysis on the data is presented; all the approaches utilized are described with figures and results with the attempt to define the first assessment for the differences in results among EFD and CFD. In the framework of this research, the main activity deals with the systematic identification of the differences between EFD and CFD, with the advance resistance for the model hull assumed as key parameter. Indeed, as numerically reported by equation (129), it is possible to assess, for each simulation performed and compared with the experimental result, the specific differential contribution associated with it.

$$\Delta R_{T_M} = \left(\frac{R_{TM_{CFD}}}{R_{TM_{EFD}}} - 1\right) \begin{cases} < \ 0\ \%, & CFD\ underestimate \\ = \ 0\ \% & No\ difference \\ > \ 0\%, & CFD\ overestimate \end{cases} \quad [\%] \tag{129}$$

where, $R_{T_M\_EFD}$ and $R_{T_M\_CFD}$ represent the towing tank experimental result and the numerical one, respectively.

5.1.1 Raw data

Inside the comparisonal repository, the calculations obtained through the simulations and the experimental test results have been stored. The first attempt to deal with this data consists in considering the data in the way "as is"; in fact, taking into account for all the differences registered for the total advance resistance value, it is possible to look at them with the attempt to get a general behavior. Therefore, considering all the comparisons represented by dots (whose colors follow the general convention about the hull identification) as function of the speed variation (expressed nondimensionally by Froude's number), it is possible to get the representation reported in Figure 77 for a total amount of 142 samples.

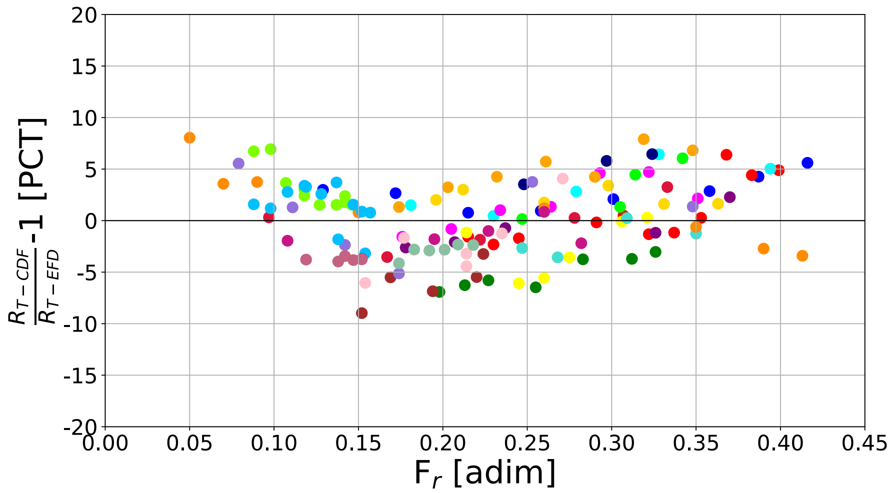

Figure 77: raw data results, each colour represents one hull and each bullet a single comparison.

A preliminary inspection reveals two main features: considering the first one, the data scatter doesn't exceed the upper limit for the model speed ($F_r = 0.45$), as recommended by ITTC with the resistance test procedure 7.5-02-02-01 [69]; while, considering the second one, all the differences don't exceed the value of $\pm 10\%$. A secondary analysis can be performed by applying the concepts of mean and standard deviation. As reported by Diez et al. [129], when dealing with the mean, sometimes even called average, the centre of the distribution for the data can be obtained; indeed, considering (130), this value can be computed by the sum of all the differences recorded divided by the total number of comparisons:

$$\overline{\Delta R}_{T_M} = \frac{\sum_{i=1}^{n}\left[\frac{\left(R_{TM_{CFD}}\right)_i}{\left(R_{TM_{EFD}}\right)_i} - 1\right]}{\sum_{i=1}^{n}(comparison)_i}\ [\%] \tag{130}$$

While, if the general trend for the data with the respect to its mean value is the target, we are dealing with the standard deviation. Indeed, considering the deviation (131) as the distance among the ΔR_{TM_i} and $\overline{\Delta R}_{T_M}$,

$$\Delta R_{TM_i} - \overline{\Delta R}_{T_M}\ [\%] \tag{131}$$

and considering all the occurrences, by applying (132) it is possible to get the variance, σ^2.

$$\sigma^2 = \frac{\sum_{i=1}^{n}\left(\Delta R_{TM_i} - \overline{\Delta R}_{T_M}\right)}{\left[\sum_{i=1}^{n}(comparison)_i - 1\right]}\ [\%] \tag{132}$$

Performing the square root for the variance, the standard deviation, σ,is obtained (133).

$$\sigma = \sqrt{\frac{\sum_{i=1}^{n}\left(\Delta R_{TM_i} - \overline{\Delta R}_{TM}\right)}{\left[\sum_{i=1}^{n}(comparison)_i - 1\right]}}\ [\%] \tag{133}$$

Moreover, as defined by Chen [130], Gaussian distribution is one of the most important tools to adopt when dealing with statistical analysis. The shape for the Probability Density Function (PDF) can be obtained by (134),

$$PDF = \frac{1}{\sigma\sqrt{2\pi}} e^{-\frac{(x-\mu)^2}{2\sigma^2}}\ with\ x\ \in\ \mathbb{R} \tag{134}$$

where, μ represent the mean from the observations and σ its standard deviation. Figure 78, shows a generical example about the PDF. Furthermore, it is possible to appreciate that in the range of $-\sigma \leq \left(\overline{\Delta R}_{T_M}\right) \leq +\sigma$, the probability to get the value is 68% c.a. (green region), while in the range of $-2\sigma \leq \left(\overline{\Delta R}_{T_M}\right) \leq +2\sigma$ the probability grows to 95% c.a. (yellow region) and finally in the range of $-3\sigma \leq \left(\overline{\Delta R}_{T_M}\right) \leq +3\sigma$ it reaches the value of 99.7% c.a. (red region).

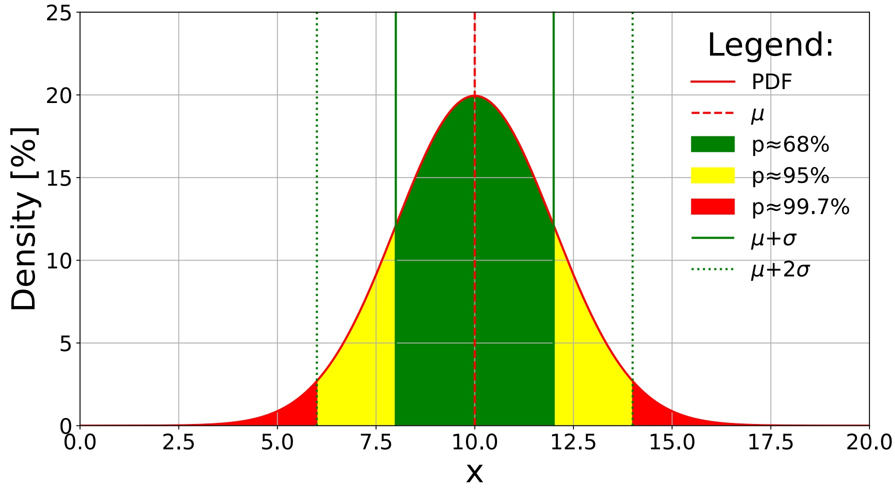

Figure 78: Gaussian distribution properties.

Considering the raw data, by looking at the difference with or without their own sign and at the mobile mean, three analyses be respectively performed.

5.1.1.1 Differences with sign

With the respect to the mean value $\left(\overline{\Delta R}_{T_M}\right)$ and the standard deviation (σ) for the raw data and by applying the exposed theory, it is possible to assess how the CFD calculations differ from the EFD results. Two kinds of representations can be listed to characterize the raw data through the statistical indexes $\left(\overline{\Delta R}_{T_M},\ \sigma\right)$. Indeed, in the first attempt a graphical representation for the statistical indexes across the raw data fields can be argued, as reported in Figure 79.

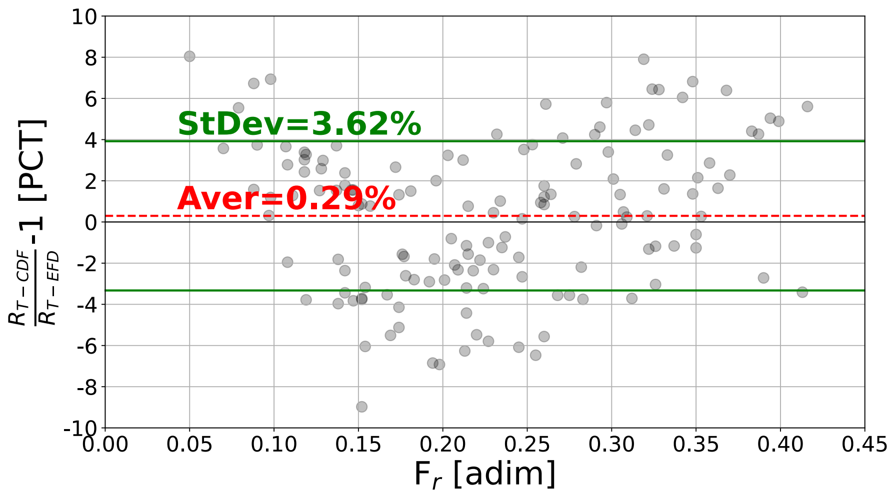

Figure 79: differences among EFD and CFD raw data considered together with mean and standard deviation.

An initial result can be inferred from this approach; indeed, considering the variations for the speed, the mean difference obtained from the comparison gives a value of 0.29% along with a standard deviation of 3.62%. Indeed, this behavior can be explained by the quite well-balanced overestimations and underestimations as a rule of thumb. Moving on the second representation, as shown in Figure 80, it can be appreciated how far the differences are with the respect to the mean value when considering a normalized PDF. A second consideration can be well-defined with the respect to the differences recorded; indeed, about the 70% of them lies within the range $\overline{\Delta R}_{T_M} \pm \sigma$ and therefore, when comparing a single numerical result with an experimental one, the probability to get a difference in the range $\pm 3.62\%$ is 65% (93 samples in the range on 142 total).

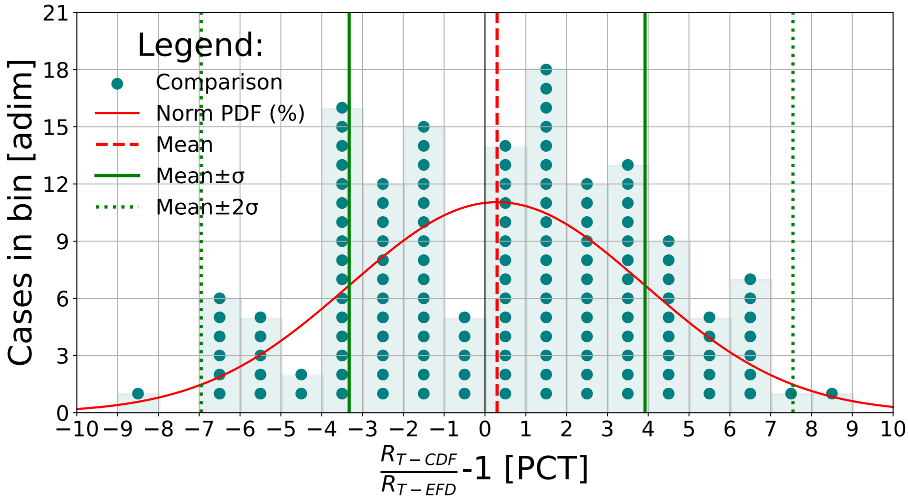

Figure 80: PDF from the differences among EFD and CFD raw data analysis.

5.1.1.2 Differences without sign

Another way to process the raw data consists in the evaluation for the mean value $\left(\overline{\Delta R}_{T_M}\right)$ and the standard deviation (σ), considering the module of each difference achieved $\left(\left|\Delta R_{T_M}\right|_i\right)$. Indeed, by following the same procedure outlined for "Differences with sign", the graphical representation shown in Figure 81 can be obtained.

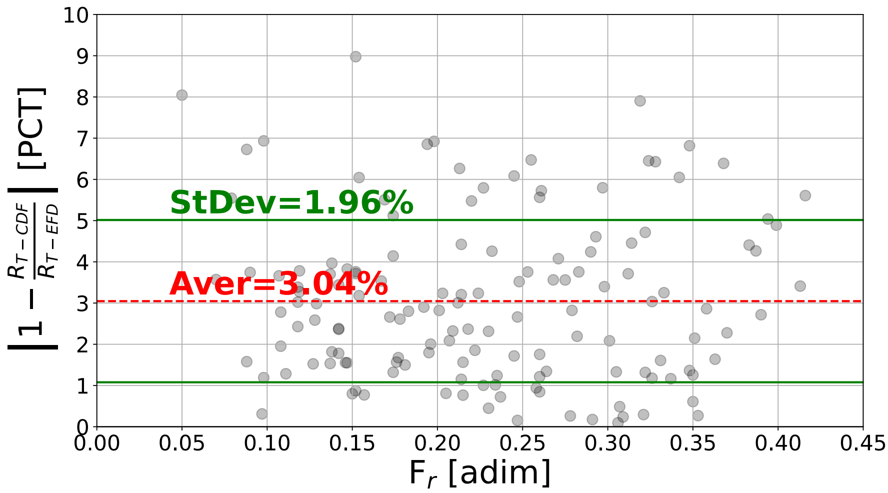

Figure 81: module of the differences among EFD and CFD raw data considered together with mean and standard deviation.

Therefore, by varying the speed it follows that the mean value for $\left(\overline{|\Delta R_{T_M}|}\right)$ is evaluated in 3.04% and the one for the standard deviation (σ) in 1.96%. Additionally, by considering Figure 82, it is possible to assess that about the 70% of the dots (representative for the differences registered) lies within the range $\overline{|\Delta R_{T_M}|} \pm \sigma$ and therefore, when comparing a single numerical result with an experimental one, the probability to get a difference in the range $(|3.04| \pm 1.96)\%$ is 67% (95 samples in the range on 142 total).

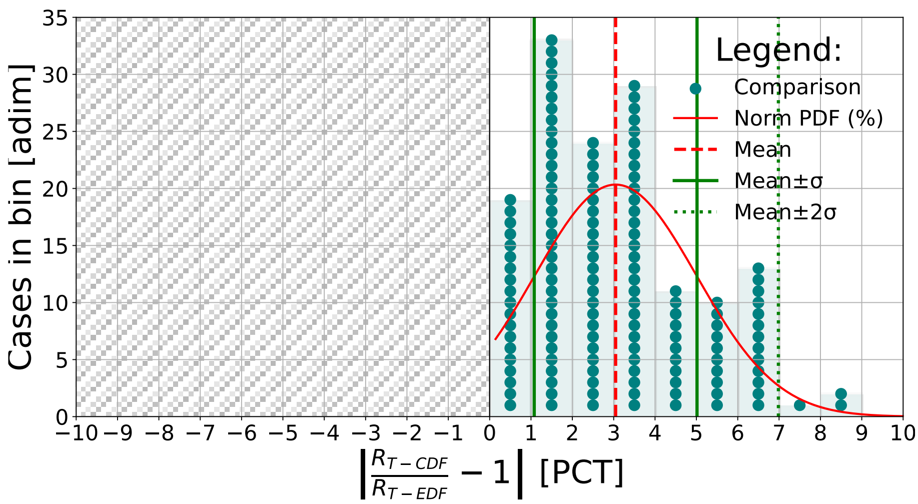

Figure 82: PDF from the module of the differences among EFD and CFD raw data analysis.

The same raw data can be addressed by considering the cumulative frequency, as displayed in Figure 83. With the respect to the considering the module of each difference achieved $|\Delta R_{T_M}|$, the cumulative distribution function allows the determination of the following results:

- a difference below 2.81% has been achieved in 50.0% of the cases, as reported by the blue area in Figure 83;
- a difference below 3.04% has been achieved in 55.3% of the cases, when considering the range 0% ÷ 3.04% (specifically for maximum differences below the average value), as reported by the red field, named “AVG”, in Figure 83;
- a difference below 5.00% has been achieved in 82.0% of the cases, when considering the range 0% ÷ 5.00% (specifically for maximum differences below the average value plus the standard deviation), as reported by the green field, named “AVG+StDev”, in Figure 83.

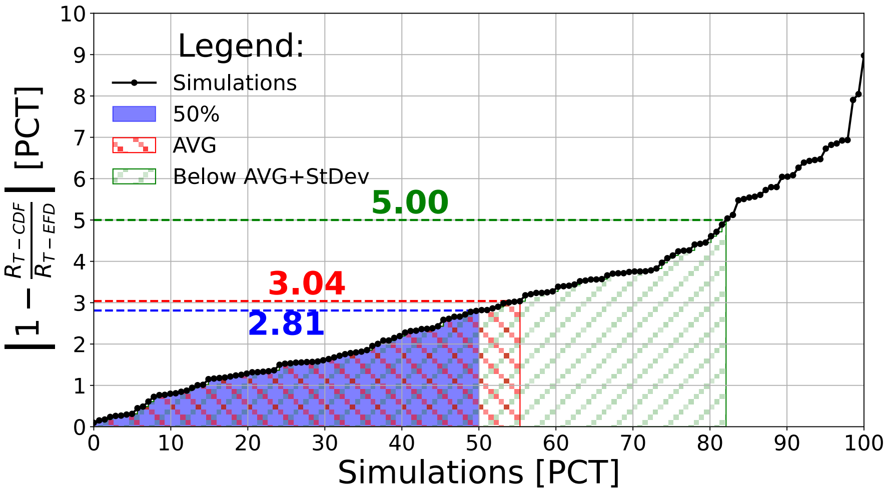

Figure 83: cumulative frequency from the module of the differences among EFD and CFD raw data analysis.

Based on these findings, it is possible to observe than the difference exceeds 5.0% in only 18% of the cases considered; therefore, it indicates a direct influence for the outliers on the mean value, while a limited impact of the difference for the recurrence is achieved.

5.1.1.3 Mobile mean

Finally, in the order to look for any possible correlation among the speed and the differences, the data discrete binning method can perform well in this scattered case. Considering the available data, they are arranged such that no particular gap is observed, therefore the continuous binning method for discrete data can properly fit in this case without the need for other methods, as the one proposed by Prieto Curiel et al. [131]. Therefore, the range across the minimum and the maximum value of the speed range ($0.05 \leq F_r \leq 0.416$) has been divided into bins; indeed, considering one bin, the mean and the standard deviation have been computed by considering all the samples inside it and the same activity has been performed for all the other ranges. By considering Figure 84a, once the means (red square) and the standard deviations (red horizontal line segments) have been evaluated for each bin (whose total number is ten and the shape is given by the brown and white boxes), it is possible to define their behavior by changing the speed, as shown by the dashed red line.

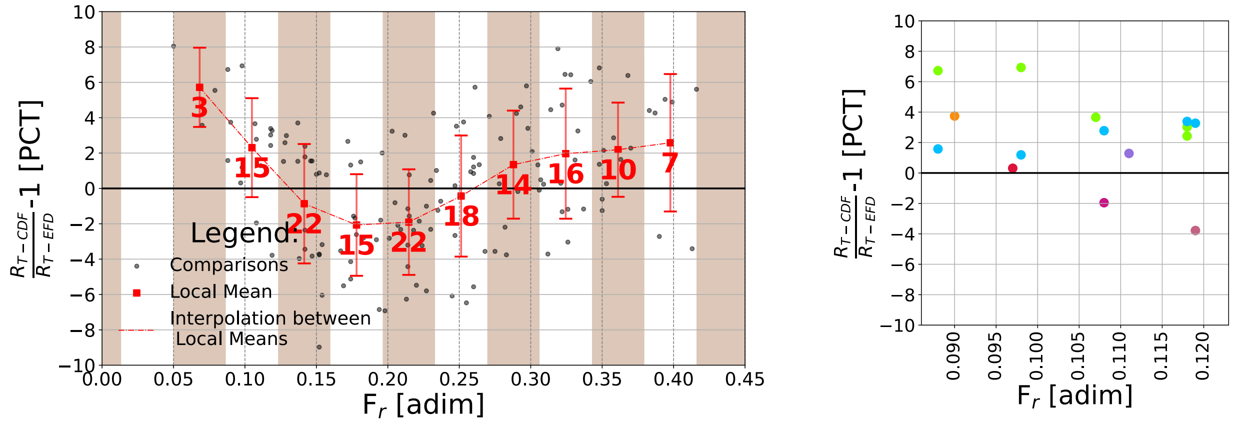

(a) (b)

Figure 84: mobile mean method applied on raw data of the differences among EFD and CFD (a), detail for $0.086 \leq F_r \leq 0.123$ *(b).*

In view of the whole speed range, detailed considerations are needed when the Froude's number is lower than 0.125. Indeed, to be sure that a representative sample is considered, a minimum number of five results per bin has been used as a binary (pass/no pass) decision threshold therefore, the case with just 3 samples ($0.050 \leq F_r \leq 0.086$) have to be neglected. Moreover, considering the detail reported in Figure 84b, two-thirds data for the case made by 15 samples ($0.086 \leq F_r \leq 0.123$) comes from one single model hull (tested into two different configurations, Hull 18 and Hull 19, respectively) and therefore, this data-generation mode may introduce issues tied to the individual model hull, potentially biasing the overall trend interpretation and for this reason it has established to neglect them too. Moreover, among this range of variation for the speed, the wave pattern isn't yet well established; the study of Jeong et al. [132] shows that for a $F_r = 0.15$ no clear wave is observed and this consideration can be found even for the two hulls 17 and 18, when tested at $F_r = 0.090$ and $F_r = 0.117$. More in details, Figure 85a and Figure 85b show a representation for the free surfaces of the two hulls with the same scale colors; while, in Figure 85c and Figure 85d respectively, the "pseudo" wave-patterns (3 different transversal cuts) are shown for the two hulls. These wave-cuts have been generated by cutting the free surface with different plane sections; more in details, the three different values for the longitudinal position (based on frame 0, 10 and 20) have been considered as plane sections and the cells centroids where the "alpha-value" is 0.5 (half cell full of water and the remaining part of air) have been considered as the trace for the free surface. Based on the waves heights, whose maximum values (0.0353m and 0.0134m, respectively) are always registered next to the bow (frame 20), it is possible to demonstrate that the main contribution for the advance resistance arises from the frictional components; moreover, by considering the experimental procedures some bayas effects can grow among the data obtained by the instrumentation tools, which have to be calibrated even for the higher speed.

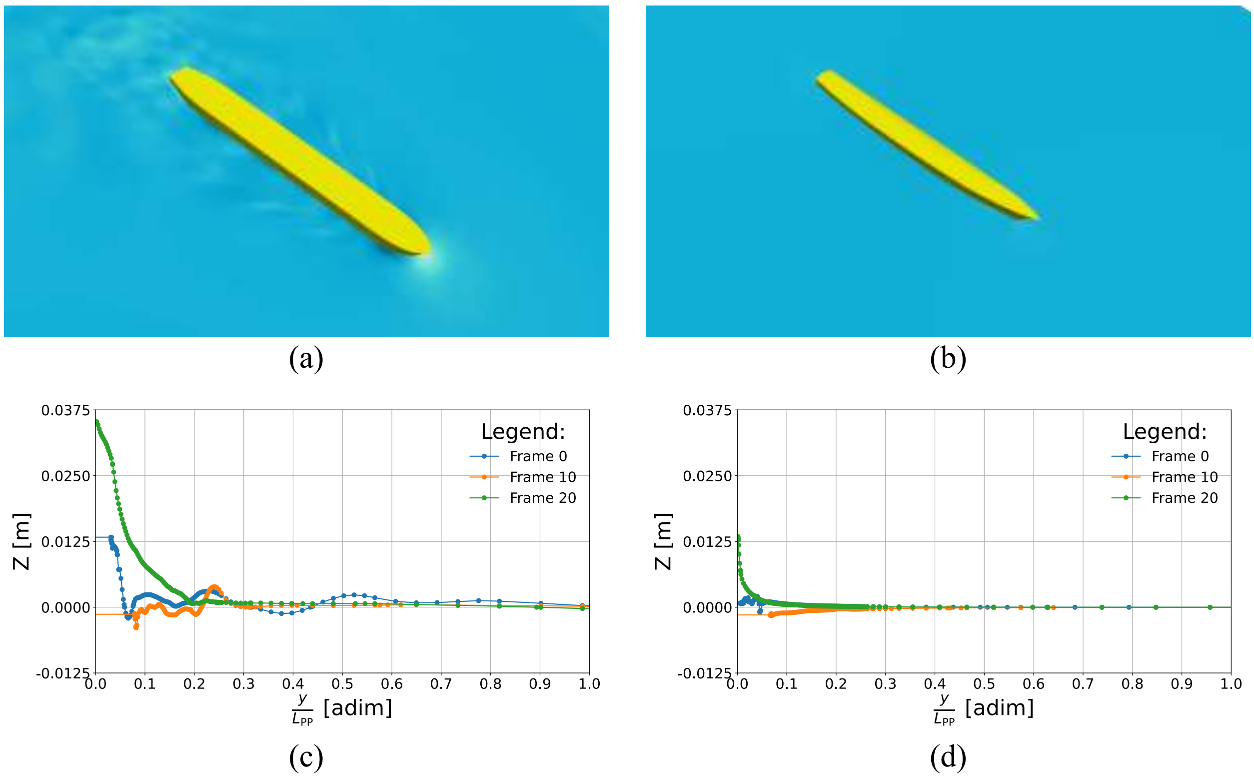

Figure 85: wave patterns on the free surface for hull 17 at $F_r = 0.090$ *(a) and hull 18 at* $F_r = 0.117$ *(b); wave-cuts (frame 0, 10 and 20) for hull 17 at* $F_r = 0.090$ *(c) and hull 18 at* $F_r = 0.117$ *(d).*

As a result, by considering the range $0.123 \leq F_r \leq 0.416$ as the new dataset, it is possible to apply the moving average mean approach in order to find any possible trend. The number of bins to divide the speed range needs to be defined for a detailed analysis. By changing the number of bins (for all the speed range analyzed $0.05 \leq F_r \leq 0.416$ and considering just the one in the new range, $0.123 \leq F_r \leq 0.416$), the results may change because of the possible lack of data in someone of them or different clusterizations. To get a reliable subdivision, different tests have been performed; indeed, the number of bins tested was varied, taking values of 5, 10, 15, 20, 25, 30. For each value, it is possible to see a graphical representation in Figure 86a-f. The findings of this study indicate that a correlation among the differences along with the speed variations exists; indeed, the results from CFD calculations tend to underestimate experimental prevision performed by EFD when the speed is low while, this trend appears to reverse when the speed increase. As demonstrated by the points where the trend (red lines) intersects the x-axis (traces highlighted by blue pentagons) in Figure 86a-f, the speed and the trend reversal can be defined. By considering Figure 87, it is possible to appreciate how the number of bins affect the evaluation for the speed at the inversion point; indeed, by considering all point obtained it is possible to calculate the mean value as the value representative for the researched point, which is quantify by the non-dimensional speed of 0.266.

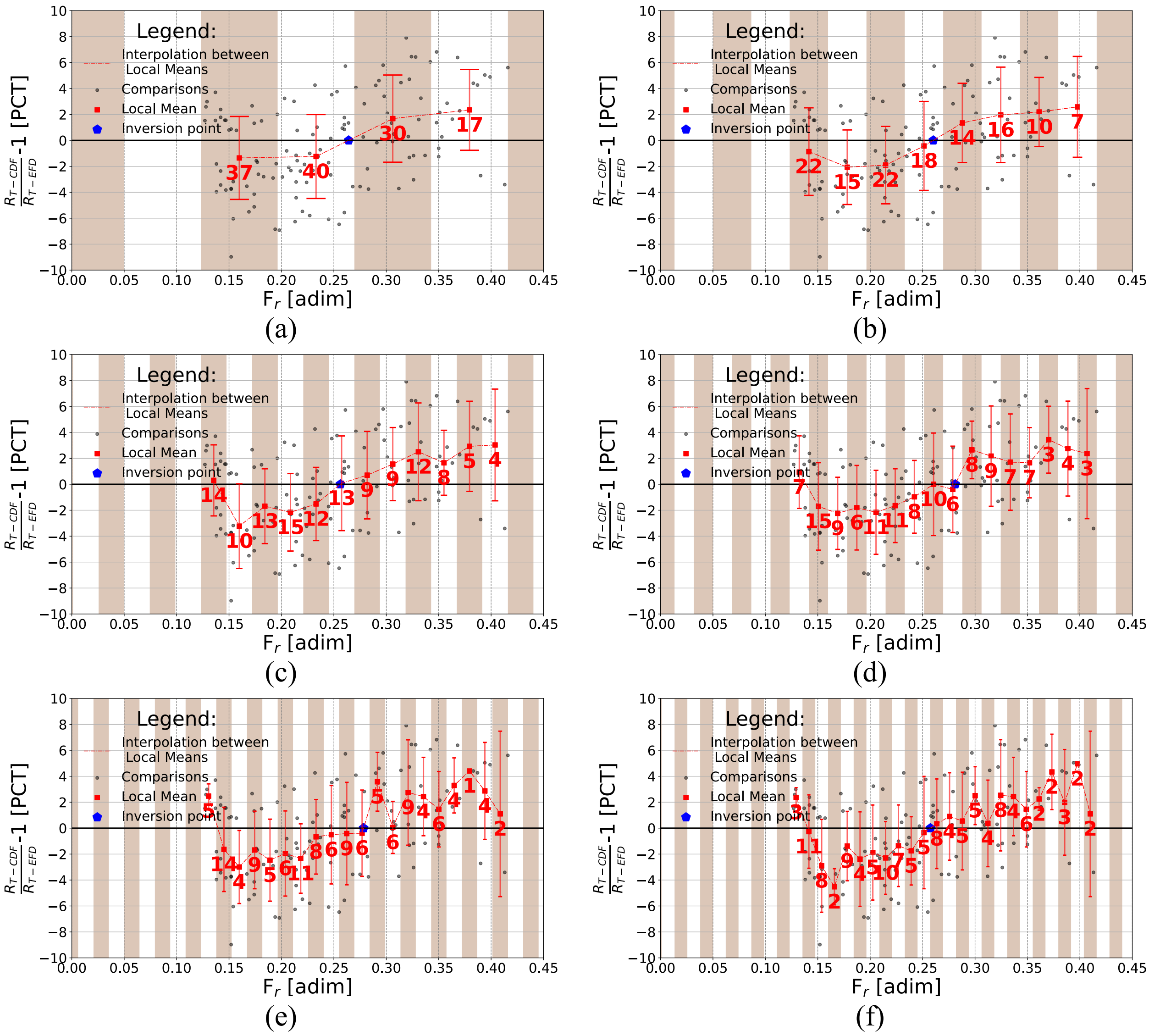

Figure 86: speed range clusterizations by means of bins; 5 bins (a), 10 bins (b), 15 bins (c), 20 bins (d), 25 bins (e) and 30 bins (f).

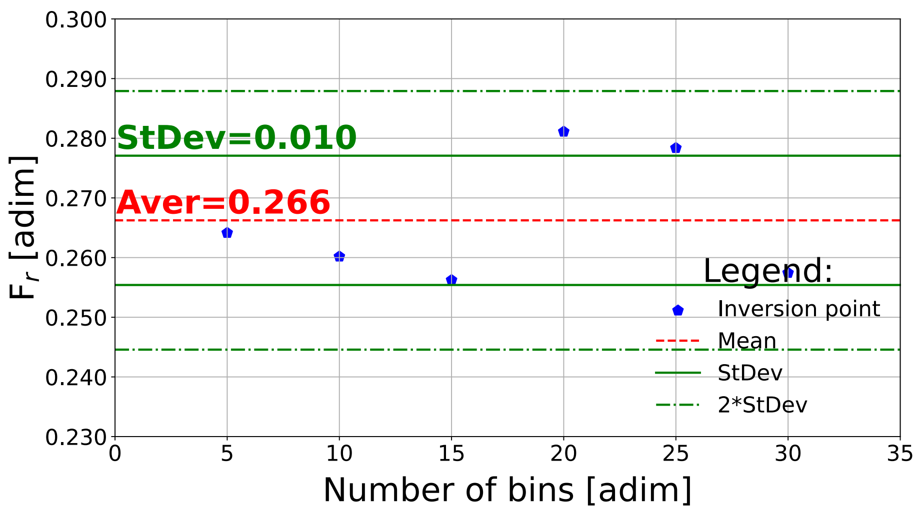

Figure 87: values for the inversion points by varying the number of bins.

Among all the representations analyzed, the 10 bins subdivision is the selected one because it represents the best compromise among samples for bins and precision (given by the number of bins itself), and when comparing EFD results with CFD calculations, the value of $F_r = 0.266$ was chosen as the representative value for the inversion among underestimations and overestimations.

Another way to assess this correlation among differences and speed can be defined by applying another statistical approach. Indeed, as reported in Gignac's et al. works [133], where details on Pearson's correlations factor (r) are shown, it is possible to numerically assess the magnitude of a correlation, based on the value of factor r_{xy}. More in details, considering two variables x and y, the mathematical formulation for the coefficient is reported in equation (135):

$$r_{xy} = \frac{\sigma_{xy}}{\sigma_x \sigma_y}, -1 \leq r \leq 1[adim] \quad (135)$$

where, σ_{xy} represents the covariance and σ_x, σ_y the standard deviations for x and y. As shown in Figure 88, the value for the coefficient has to be in the range ± 1; if the value for the $r > 0$, correlation is said to be positive (red dots and trace), otherwise if $r < 0$ negative (green dots and trace) and if $r = 0$ (blue dots and trace) the variables are said to be uncorrelated; three other values assume a particular importance for the coefficient: indeed, if $r \leq 0.1$, the recommended correlation is small, if $r \cong 0.3$, is medium and lastly, if $r \geq 0.5$, the correlation is large.

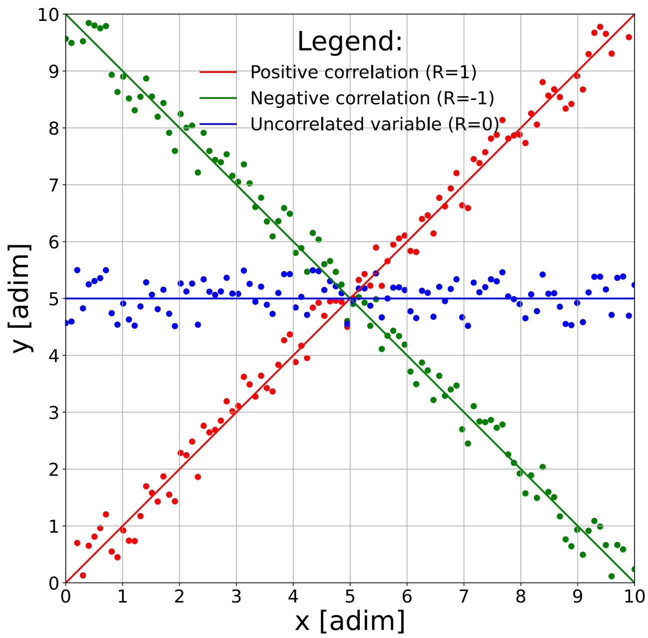

Figure 88: Pearson correlation index.

Considering the range $0.123 \leq F_r \leq 0.416$, and by applying Pearson's theory, it is possible to assess a value of 0.406 for the r coefficient, as reported in Figure 89:

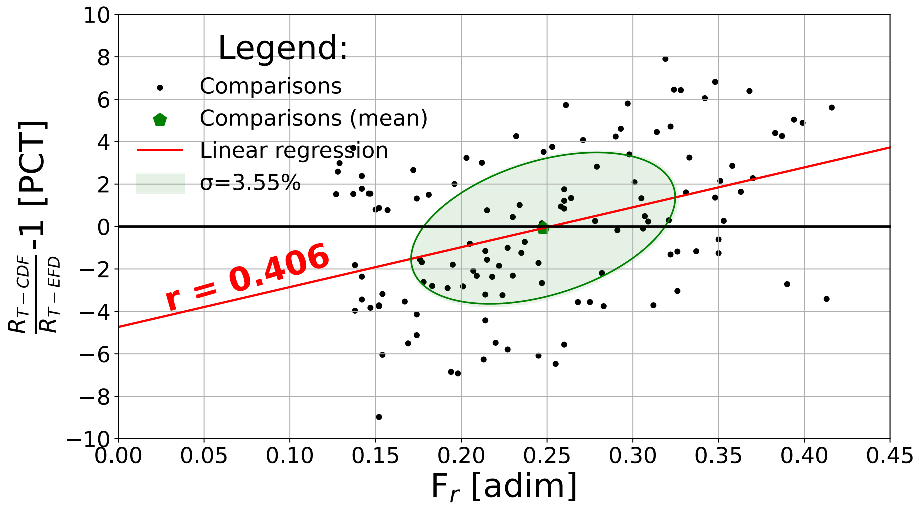

Figure 89: Pearson correlation index applied on speed range raw data.

where, the centre among the comparison distribution is represented by a green pentagon on the linear regression red line surrounded by a green ellipse representing the correlation strength via the major-to-minor axis ratio. The value of 0.406 mathematically confirms a quite large correlation among the results and the speed range, as visually inferred from the analysis.

Something more can be found according to the trend observed. Considering the results obtained from the Gothenburg 2010 workshop [31], it is possible to perform a comparison between these results and those obtained by this research. Indeed, in 2010 several participants submitted their work with the respect to three different hulls (DTMB 5415, KVLCC2 and KCS) and the results have been summarized by considering equation (136):

$$\left(\overline{\Delta R}_{T_M}\right)_{CASE} = \left[\frac{R_{TM_{EFD}} - \dfrac{\sum_{i=1}^{n}\left(R_{TM_{CFD}}\right)_i}{n_{partecipants}}}{R_{TM_{EFD}}}\right]_{CASE} \begin{cases} < \ 0\,\%;\ CFD\ underest. \\ = \ 0\,\%;\ No\ difference \\ > \ 0\%,;\ CFD\ overest. \end{cases} [\%] \qquad (136)$$

where, for each hull tested a mean value $\left(\overline{\Delta R}_{T_M}\right)_{CASE}$ has been obtained by considering the percentual difference among the experimental result $\left(R_{TM_{EFD}}\right)$ and the mean value arising from all the numerical simulations $\left(\sum_{i=1}^{n}\left(R_{TM_{CFD}}\right)_i / n_{partecipants}\right)$. Moreover, the mean value of the accuracy obtainable for each case $\left(\overline{\Delta R}_{T_M}\right)$ is evaluated in -0.1% with a standard deviation of 2.1%. Therefore, as reported in Figure 90, where the red squares with dashed line represents the here obtained mobile means from this research along with the other lines which connect the results from the different hulls tested by the participants to the workshop (green stars for DTMB 5415, orange triangles for KVLCC2 and fuchsia circles for KCS), a common behavior among trends can be observed along with close value for the inversion speed.

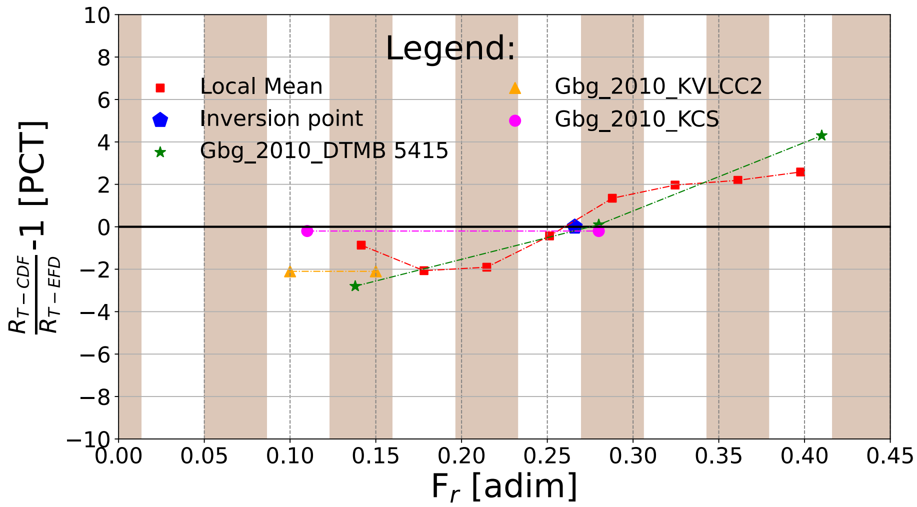

Figure 90: comparison among current research trend and Gothenburg workshop.

This last finding, attests how current research is compliant with the results obtained by other CFD community with the respect to three different features: the accuracy obtained by CFD are closer (-0.1% for workshop and 0.29% for current work) along with the standard deviations (2.1% and 3.62%, respectively), the general trend for the differences connected with the variations for the speed is similar and lastly, the speed at which the transition from underestimations to overestimations occurs is assessed to be in the range $F_r = 0.26 \div 0.27$.

Therefore, once achieved this result, it is possible to move on with the other type of approaches to look for any possible correlation with confidence in the reliability of the obtained data.

5.1.2 Test condition

The data inside the comparisonal repository can be post-processed with a second approach. Indeed, by considering the registered differences among EFD and CFD with the respect to the total advance resistance, it is possible to have a look at the differences registered for each hull to extract some conclusions. By applying the color convention, the registered differences varying the speed for the 22 hulls tested can be globally reported as in Figure 91. It can be observed that the general trend among underestimations and overestimations is globally confirmed, except for hull 17; indeed, its speed variation is the higher among all the hull tested and some particular phenomena may have occurred in the regions near the extremes. A similar representation can be obtained from grouping of the data considering the hulls on x-axis and the differences registered on y-axis. Therefore, in order to get a generical overview abouts the comparisonal results, they are plotted adhering to the color map and split based on the hulls subdivision (22 different hulls), as reported by Figure 92.

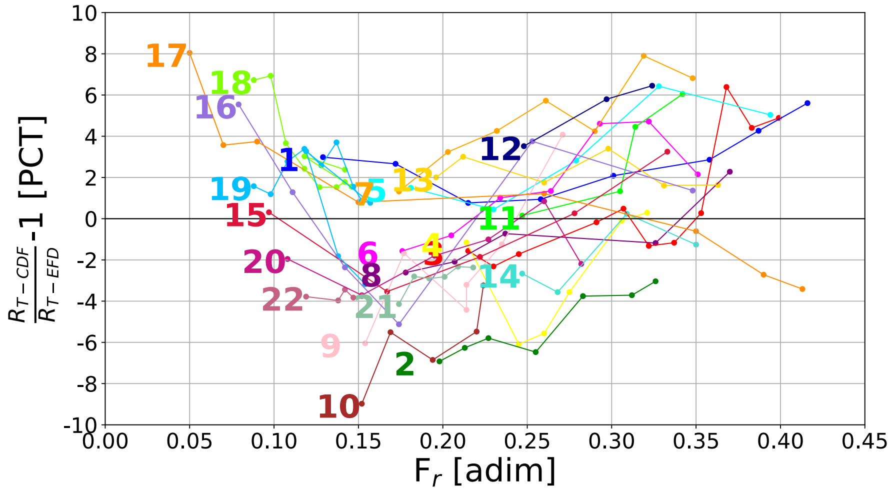

Figure 91: resistance curves of differences among EFD and CFD, each colour represents one hull, each bullet a single comparison and each hull is identified by its code.

Further statistical analysis can be performed on the data grouped by families of hull; indeed, it is possible to assess the mean and the standard deviation for each family and finally, the global mean and its standard deviation for all the categories, as shown in Figure 93a. This kind of approach leads to define that the mean difference is 0.14% with a standard deviation of 2.14% and considers each result.

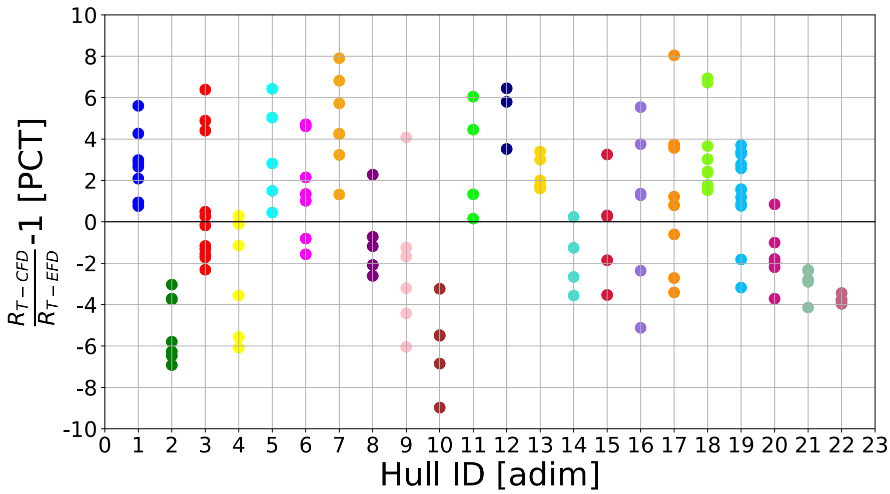

Figure 92: raw data advance resistance differences among EFD and CFD, grouped by hulls.

While, considering the value for the differences registered at the maximum speed for the resistance curve for each single hull $(R_{T-EFD})_{MAX}$, it is possible to scale the results on this value in order to define the differences with the respect to the most representative prediction (with the respect to power prediction); indeed, as shown in Figure 93b, it is possible to evaluate the mean value and the standard deviation, quantified in 0.18% and 1.41%, respectively. These values are smaller compared to the initial candidates and demonstrate how the results can be scattered with the respect to one single prediction.

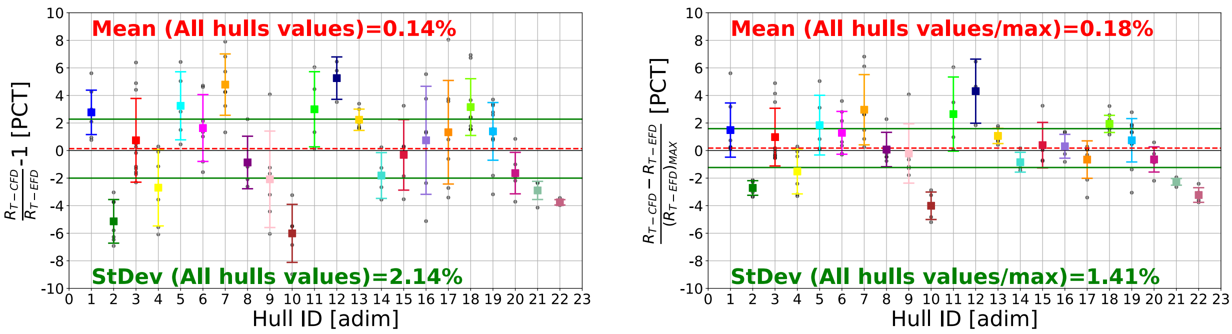

(a) (b)

Figure 93: statistical analysis of the raw data advance resistance differences among EFD and CFD, grouped by hulls (a) along with data scaled on the difference registered for the maximum speed for each hull (b).

Among the family represented by all the hulls and by considering the configuration for the hulls when tested in the towing tanks, two more sub-families can be found: the bare and the fully appended hull configurations, respectively. Indeed, by sharing the data as reported in Figure 93a, it is possible to get a detailed overview among configurations for the bare (Figure 94a) and the fully appended (Figure 94b) hulls.

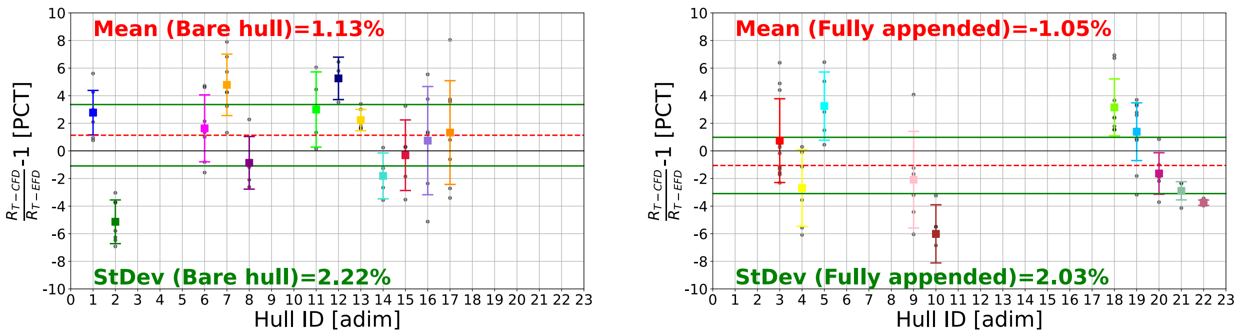

(a) (b)

Figure 94: statistical analysis of the raw data advance resistance differences among EFD and CFD, grouped by hull and divided in two configurations: bare (a) and fully appended (b).

These new representations lead to define that the mean value of the differences changes when the configuration for the test changes (difference for the bare hull 1.13% and -1.05% for the fully appended); moreover, both the standard deviations for results are smaller (bare hull 2.22% and 2.03% for the fully appended) than 3.62%, as defined in the raw data analysis.

Based on the findings form the analysis about the test condition, a result can be obtained, as follows. The raw data analysis accounts for a higher value for the standard deviation (3.62%), if compared with the standard deviation value obtained from all the cases considered in the test condition analysis (2.14% the higher one). Moreover, considering the results for each hull, Figure 93a, Figure 94a and Figure 94b display differences that usually belong or to the positive field or to the negative one; while, considering Figure 93b, it can be observed that the greater differences arise from the lower speed comparisons. Based on these findings, it can be argued the presence for a systematical error. Therefore, considering on hull, if a calibration is performed for one speed, all the other results for the resistance curve can be updated, and finally a smaller difference can be observed.

5.1.3 Analysis of the hull parameters influence

In this last statistical analysis based on the comparative repository, a correlation among different hydrodynamical parameters and the differences recorded has been investigated; indeed, the correlation among the differences with the respect to the length for the model tested, its scale, the ratio length over beam, the ratio beam over draft and finally the block coefficient are going to be analyzed in this section. These investigations are the typical field of application where the Pearson's theory can be applied in order to find any possible correlation. Indeed, the following representations are structured moving from the raw data analysis of the differences versus each single hydrodynamical parameter and can be split in two different visualizations. In this sub-paragraph, the figure on the left-side shows the samples (black dots) based on the hull (represented by colored square and each one of them has its own colored number to identify the hull family based on the convention for colors) along with a green pentagon centered in the hull family's distribution enclosed to a green ellipse representing the correlation strength via the major-to-minor axis ratio of the hull families; therefore, the more the ellipse tends to collapse to a line, the more correlated the data are. While, the figure on the right-side shows all the data from the speed range (black dots) and evaluates the linear regression (red line) along with the Pearson's coefficient; even in this representation is shown a green pentagon as the centre for the samples, surrounded by a green ellipse representing the correlation strength via the major-to-minor axis ratio of the hull families.

5.1.3.1 Model length (L_{PP}).

This section considers the differences registered between the CFD calculations and the EFD results by changing the model length. Considering Figure 95a, a visual inspection on the data suggests that it isn't possible do define a cluster for the dots, meaning that a correlation cannot be found. This consideration can be numerically confirmed by the Person's coefficient indeed, given that its value is very close to zero ($r = 0.04$), the variables are uncorrelated and the linear regression is practically a horizontal line, as reported in Figure 95b.

5.1.3.2 Scale Factor ($\lambda = L_S/L_M$).

In this representation the scale factor for all the hull tested has been evaluated and considered as the hydrodynamical parameter to take into account for dealing with the differences among EFD results and CFD calculations. By applying the procedure exposed for this section, two kinds of representations have been considered, as shown in Figure 96a and Figure 96b. In this case, as no correlation is visually observed and the Person's coefficient is evaluated in a number close to zero ($r = -0.094$), it isn't possible to assess any possible correlation.

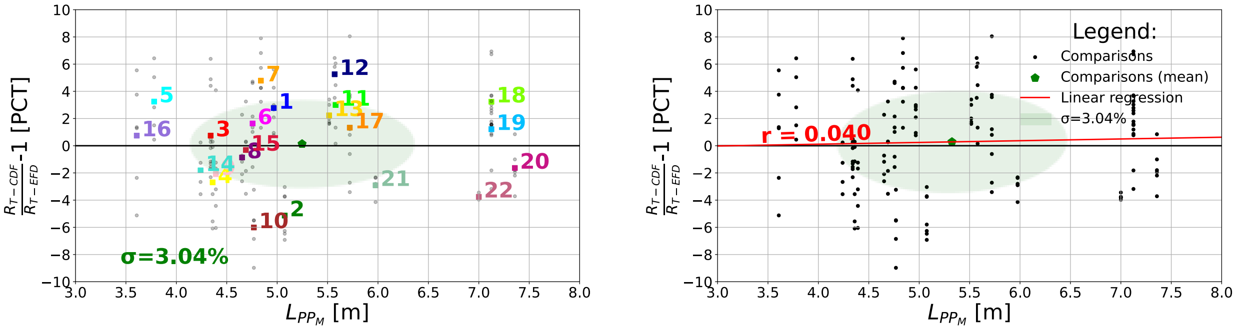

(a) (b)

Figure 95: differences among EFD and CFD with the respect to the model length, L_{pp}; families of hull (a) and correlation analysis (b).

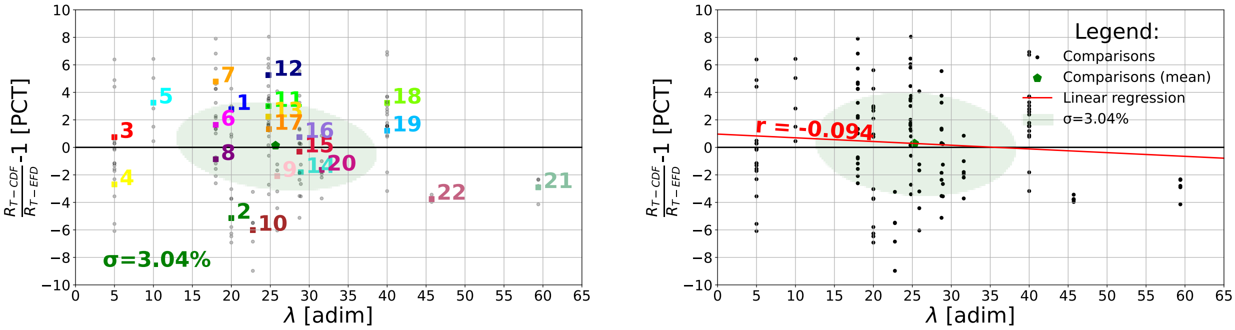

(a) (b)

Figure 96: differences among EFD and CFD with the respect to the scale factor, $\boldsymbol{\lambda}$; families of hull (a) and correlation analysis (b).

5.1.3.3 Ratio (L_{WL}/B_{WL}).

In this case, the differences among CFD and EFD versus the ratio L_{WL}/B_{WL} have been considered. By performing a visual inspection on the data, as presented in Figure 97a, nothing in particular can be said about the correlation because of a scattered region without any particular trend. While, by performing the Pearson's analysis, a small correlation can be observed because of the value of -0.094 for its coefficient, as reported in Figure 97b.

5.1.3.4 Ratio (B_{WL}/T_M).

In this new case, the ratio among the bean and the draft has been used to correlate the differences among EFD calculations and the CFD results. Similarly with the ratio length on beam, it is not possible to find any particular clusterizations for the data field, as shown in Figure 98a, but a small correlation among the data can be discovered, based on the value for the Pierson's coefficient ($r = 0.113$), as reported in Figure 98b.

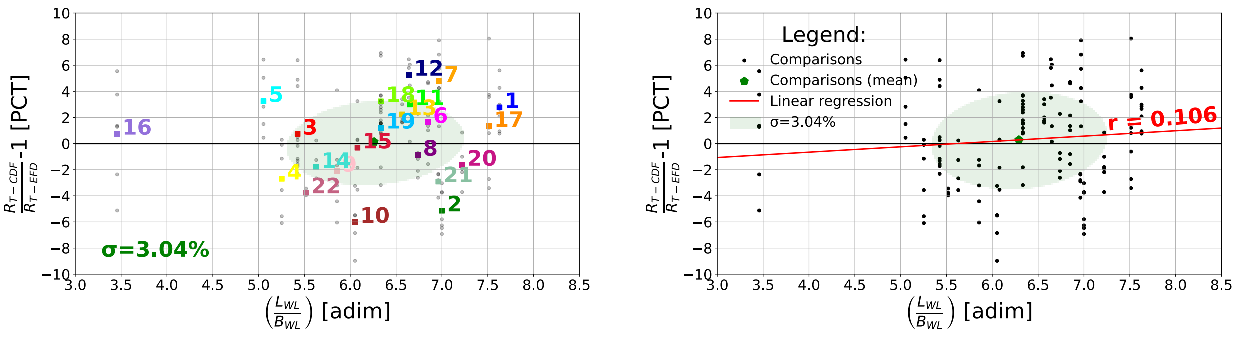

(a) (b)

Figure 97: differences among EFD and CFD with the respect to the ratio L_{WL}/B_{WL} ; families of hull (a) and correlation analysis (b).

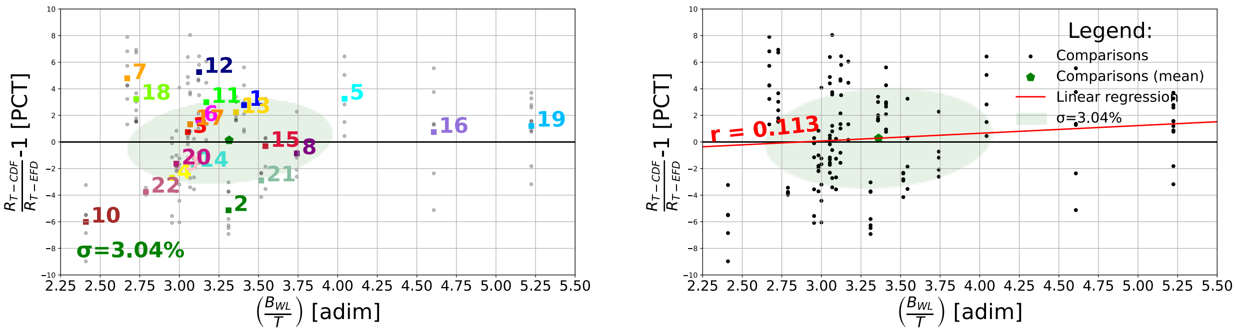

(a) (b)

Figure 98: differences among EFD and CFD with the respect to the ratio B_{WL}/T_M ; families of hull (a) and correlation analysis (b).

5.1.3.5 Block coefficient ($C_B = \nabla/LBT$).

With the respect to the block coefficient, and as reported in Figure 99a, the hulls tested appear clustered into 3 main family, the first one in the range $0.4 \leq C_B \leq 0.55$, the second in range $0.64 \leq C_B \leq 0.69$ and the last one in range $0.8 \leq C_B \leq 0.84$. Indeed, as reported in Figure 99b, it is possible to evaluate always a value for the Pierson's coefficient and its values (-0.055, -0.269, and 0.525, respectively) show a medium anticorrelation for the range $0.64 \leq C_B \leq 0.69$ and a large correlation for the range $0.8 \leq C_B \leq 0.84$. While, considering all the data inside the selected speed range, a small correlation has been found based on Pierson's coefficient ($r = 0.128$), as reported in Figure 99c. This last representation is considered the most representative one because of the higher number of samples considered.

Therefore, the analysis of the differences among EFD results and CFD calculations versus the hydrodynamical parameters gives three small correlations, based on Pierson's coefficients; indeed, by considering the ratio (L_{WL}/B_{WL}), the ratio (B_{WL}/T_M) and the block coefficient, the values obtained are -0.094, 0.113 and 0.128, respectively.

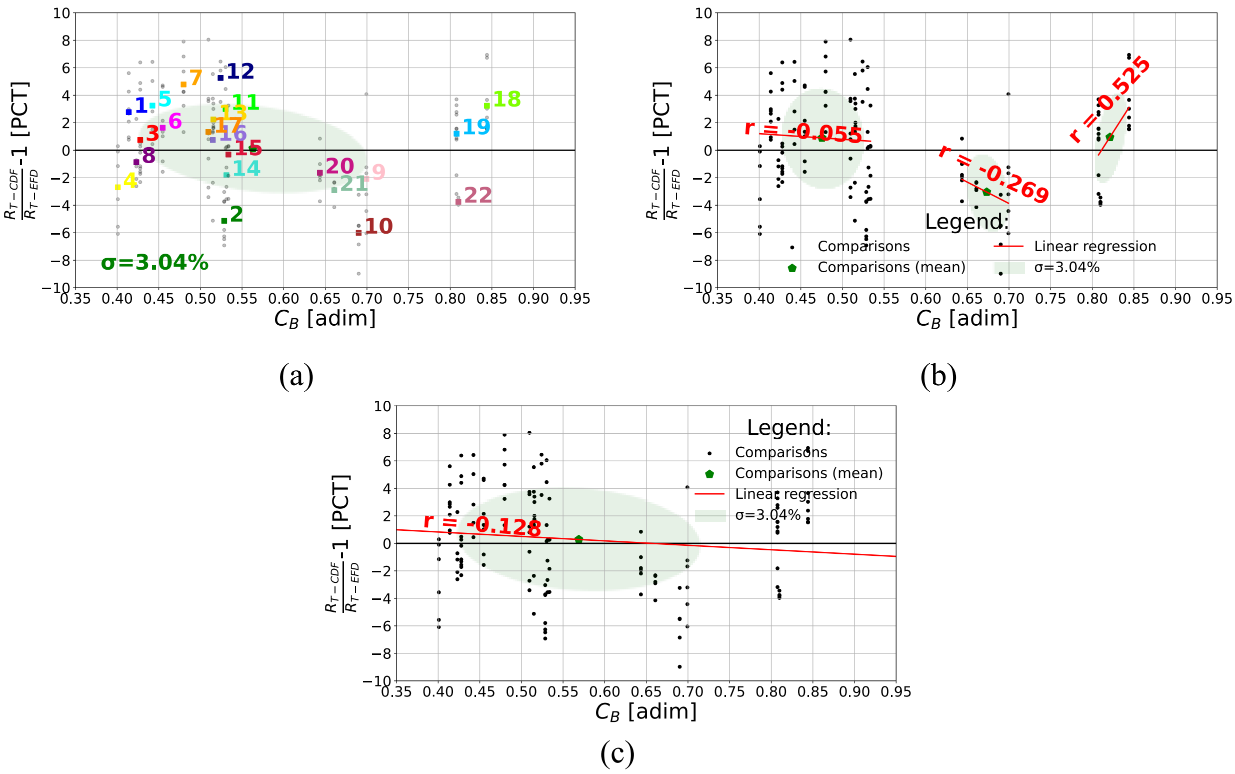

Figure 99: differences among EFD and CFD with the respect to the block coefficient, C_B; families of hull (a) and correlation analysis (b).

5.1.4 Data analysis conclusions

Based on the raw data analysis for the differences among the total advance resistance values, a mean difference among CFD calculations and EFD results has been quantified in 0.29% with a standard deviation of 3.62%, while considering the absolute difference, its mean value has been evaluated in 3.04% with a standard deviation of 1.96%. More in details, it has been demonstrated that if a blind simulation is carried out, in 50% of cases, the percentual difference with the EFD results doesn't exceed the 2.81 value, and in 80% of cases, the same difference is lower than 5%.

While, based on the analysis for the differences among the total advance resistance considering each single hull, it has been demonstrated a lower scatter in results, if compared with the raw data ones. This lower scatter can be quantified considering the standard deviation based on the 22 hulls; indeed, this standard deviation has been quantified in 2.14%, which is 40% smaller than the one from the raw data analysis. This analysis can lead to a conclusion that, if the numerical set-up can be calibrated for one speed, the resistance curve can follow the same calibration obtaining a lower difference with the experimental data.

Moreover, a weak but measurable trend among the speed variations and the differences among CFD calculations and EFD results has been found; indeed, when the Froude's number is lower than 0.266, the CFD tends to underestimate the value obtained by EFD tests while for higher speed, the trend shows an opposite pattern. Once these results have been assessed, the uncertainty analysis will be presented to get a general overview about the results.

Therefore, based on NUADA approach and considering the results from the raw data analysis (later on identified as "COMparisonal DataBase", COMPDB), the obtained value of the expected difference among a CFD calculation and the EFD result lays within the range $\pm(3 \div 5)\%$.

5.2 Uncertainty assessment

In the field of metrology, as reported by Kučera et al. and D'Agostini [134][135], who cited the definition from ISO "Guide to the Expression of uncertainty in measurement" [136], the word uncertainty (U) can be defined as "a parameter associated with the results of a measurement, that characterizes the dispersion of the values that could reasonably be attributed to the measurand". A simple but effective definition to identify the concept of uncertainty can be found in the recommended procedure 7.5-02-01-01, "Guide to the Expression of Uncertainty in Experimental Hydrodynamics" edited by ITTC [103]; indeed, according to which the term "uncertainty means doubt" and "therefore in its broadest sense…omissis…means a doubt about the validity of the results of that measurement". These concepts pertain to both the EFD and CFD, as detailed in current paragraph. Considering the field of the experimental towing tank tests, once an EFD test has been performed, a result is found and if the test is repeated, the results will be different from the first one obtained. As described in the recommended procedure 7.5-02-02-02, "General Guideline for Uncertainty Analysis in Resistance Tests" edited by ITTC [137], the uncertainty in results can be obtained starting from the sum of several contributions affecting the model geometry, the test installation, the instruments calibration and the measure of the quantity of interests (like the resistance, the carriage speed) and moving on the propagation for the errors. The composed uncertainty deriving from all these sources of uncertainties is known as the experimental uncertainty (U_D). Something similar can be observed even in the numerical towing tank experience; indeed, the geometry for the hull to be tested is towed inside a two phases computational domain (air and water) and data from the field are considered. In this case, the uncertainty (U_S) represents the value to be evaluated in order to get a result with the 95% of confidence and incorporates errors and uncertainties deriving from both the numerical resolution for the equations and the model applied to describe the physical phenomena.

When dealing with the numerical part of the uncertainty, we are speaking about the verification procedures, which target involves defining the value for U_{SN}. With the respect to the numerical uncertainty, as reported by Wilson et al. [138], Lakatoš et al. [108] and Sorrentino et al. [139], among all the contributions, the most relevant one is the discretization error (U_G); therefore, in equation (137) a simplify but still accurately way to account for the numerical uncertainty, U_{SN}, is shown:

$$U_{SN} = \sqrt{U_G^2 + U_T^2 + U_I^2 + U_P^2} \cong \sqrt{U_G^2} \tag{137}$$

Based on this assumption, it is possible to perform the convergence study to evaluate U_{SN}. In light of Richardson's Extrapolation (RE), according to which it is possible to increase the numerical precision based on the power series expansion moving from few discrete points, all methodologies currently available differ with respect to how the coefficients for RE are evaluated, but share the same approach to perform the convergence study. Therefore, in this type of study a single parameter is modified (grid size), while the others remain unchanged and the results obtained are processed to define the type of convergence (which can be arranged in the following categories: monotonic, oscillatory convergence, oscillatory divergence and divergence) and lead the researcher to choose among the available methodologies. More in details, the convergence study for the grid refinement for a 3D scenario can be expressed as reported in equation (138):

$$r_k = \sqrt[3]{\frac{\Delta X_k}{\Delta X_{k-1}}} \cong \sqrt[3]{\frac{N_1}{N_2}} \tag{138}$$

where, N_1 represents the total number of cells for a finer mesh and N_2 the number for a coarser one. The academic debate is still open with the respect to the "correct" value for the refinement ratio parameter; indeed, this parameter has to be great enough to avoid noise in result and meantime computationally affordable. With the respect to r_k, and according to the literary review based on Wilson et al. [138], its minimum value is $\sqrt[4]{2}$ and the reported maximum is 2 (in some way the suggested one). Based on this refinement's theory, at least three simulations are required to implement the theory proposed by Celik et al. [51] and Stern et al. [50], while a minimum number of four simulations are required for Eça and Hoekstra's methodology [53].

Finally, once the numerically uncertainty has been evaluated, it is possible to deal with the uncertainty modelling errors (U_{SM}) and therefore, move on the validation field.

In following paragraphs, considering the total advance resistance for a model hull $\left(\Delta R_{T_M}\right)$, as calculated by equation (3), different V&V procedures are applied on test cases in order to address in an in-depth analysis about the dependency among the numerical uncertainty (U_{SN}) and the speed variation, along with a comparison on the available theoretical approaches combined with their main strength and weakness. Indeed, three different parts consist in the uncertainty assessment: creation of data (EFD test and CFD calculations), verification (estimation for the numerical uncertainty, U_{SN}) and finally the validation (comparison among EFD and CFD to assess the modelling errors, U_V).

5.2.1 The case studies

To assess the numerical uncertainty, two model hulls have been used as case-studies and identified through the names of Hull_A and Hull_B, respectively; their main characteristics are reported in Table 29. To better identify the two different hulls across the research, a code color has been implemented; indeed, Hull_A will be always represented by fuchsia markers while Hull_B by green markers. These models have been tested at different speeds (respectively three and four) and Hull_B has been tested in different configurations (free or fix trim and sinkage).

Table 29: Hull_A and Hull_B main characteristics.

Dimension for model hull	Symbol	HULL_A	HULL_B	UNIT
Length of waterline	L_{WL}	5.5794	3.6074	m
Maximum moulded breadth at design WL	B_{WL}	0.8390	0.7715	m
Draught at midship	T_M	0.2650	0.2830	m
Displacement volume	∇	0.6585	0.4208	m^3
Area of wetted surface	S	4.9238	3.2950	m^2
Ratio L/B	L_{WL}/B_{WL}	6.6314	4.6755	-
Ratio B/T	B_{WL}/T_M	3.1662	2.7260	-
Block coefficient	$C_B = \nabla/LBT$	0.5309	0.5342	-
Scale ratio	$\lambda = L_s/L_M$	24.763	28.750	-
Froude number	$F_r = V/\sqrt{gL}$	0.27 ÷ 0.34	0.22 ÷ 0.34	-

Indeed, since the results showed a scatter for the value of the total advance resistance for a model hull, the simulations performed in fix sinkage and trim configuration were implemented for Hull_B to assess any possible correlation among the dynamic attitude for the model and the differences registered. These last simulations have been identified through pentagonal markers with green borders and with surfaces. For each condition several simulations have been performed by varying the number of cells for a total of 72 simulations, following the pattern described in Table 30.

Table 30: simulations pattern for Verification analysis. The number of cells is referred to half domain.

Case_ID	F_r [-]	Nr. Cells * 10^6 [adim]	$0.5\frac{\Delta R_{T\_CFD}}{R_{T\_EFD}}$ [%]	Nr. Simulations [adim]
Hull_A-1	0.276	0.7 ÷ 4.0	2.30	7
Hull_A-2	0.314	0.7 ÷ 2.9	2.27	6
Hull_A-3	0.342	0.7 ÷ 4.0	1.99	7
Hull_B-1	0.158	0.9 ÷ 2.9	0.60	7
Hull_B-2	0.222	0.7 ÷ 4.0	1.18	9
Hull_B-3	0.285	0.9 ÷ 5.0	1.22	8
Hull_B-3*	0.285 (*)	0.9 ÷ 4.8	1.82	7
Hull_B-4	0.348	0.9 ÷ 5.0	1.26	8
Hull_B-4*	0.348 (*)	0.6 ÷ 9.7	1.67	13

(*) Simulations performed in fix trim and sinkage configuration.

The results are presented in Figure 100, where the triangular markers represent the simulation-based calculations for the free sinkage and trim configuration, the pentagonal ones represent the simulation-based calculations for the fix trim and sinkage configuration; the horizontal line represents the trace for the experimental result (not directly reported but seen as "% difference"). In accordance with the color legend for the two hulls, the numbers (which position is close to the markers identifying the simulations performed with the finer meshes) give the trackability for the case under investigation. Based on the results summarized in Table 30, a preliminary analysis of the differences observed with varying speed suggests the presence of a trend; indeed, considering Hull_A the differences tend to decrease with the increase of the speed, while Hull_B shows an opposite trend.

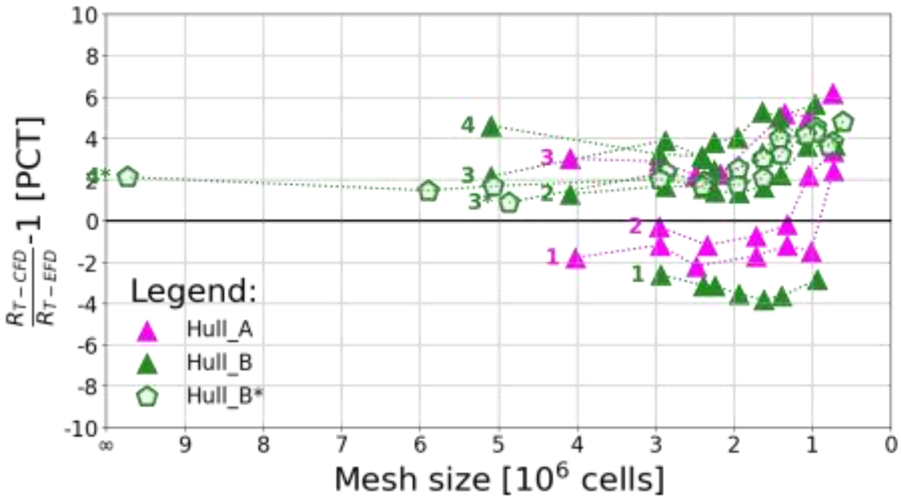

Figure 100: mesh independence analysis for the percentual difference between EFD and CFD with the respect to the advance resistance in free trim-sinkage configuration for Hull_A and Hull_B, and fix trim-sinkage configuration for Hull_B.*

The observed trend in one case seems not entirely compliant with the one defined in paragraph 5.2.1, but the differences are very small and the data registered falls inside the field defined by the mean value more/less its standard deviation. Therefore, the observed trends can be assumed as compliant with the founding of the paragraph 2. This raw data will be analyzed in the following sections.

Once all the 72 simulations have run, it is possible to perform the grid sensitivity analysis. The results for all the simulations are available in Annex 2, where all the results have been reported and split according to the case identification. Each figure accounts for the difference among the EFD and the CFD results in y-axis versus the x-axis, where the mesh refinement ratio is reported and assessed through equation (139). Moreover, a second scale is available for x-axis to get the information about the number of cells (referred to half domain because of the symmetry condition) used to perform each simulation.

$$r_{(k,k+1)} = \frac{h_k}{h_{k+1}} = \sqrt[3]{\frac{h_k}{h_{k+1}}} \tag{139}$$

where, subscript "k" indicates a finer mesh compared with the "$k+1$". This index assumes the value of 1 for the fine mesh and increases as the meshes became coarser.

Among all the cases, two of them has been considered as representative; indeed, the cases are Hull_B-3 and Hull_B-4, respectively. The results from 8 mesh refinements are available in both cases, as reported in Figure 101a and Figure 101b.

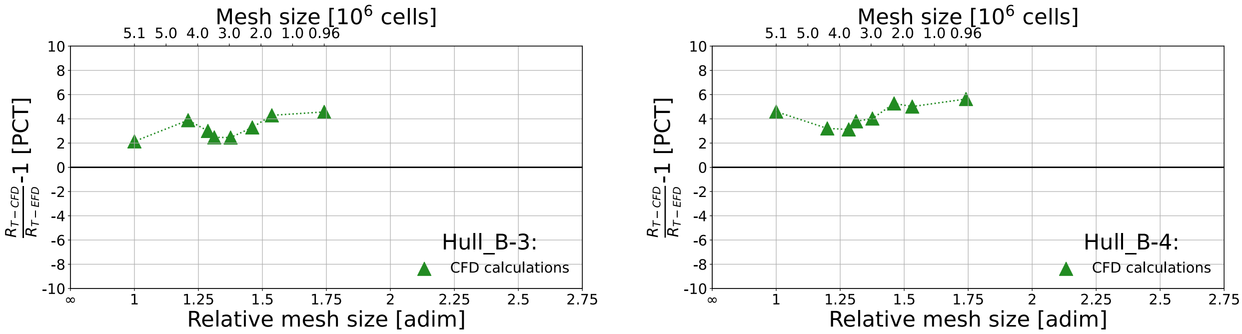

(a) (b)

Figure 101: mesh independence analysis for the percentual difference between EFD and CFD with the respect to the advance resistance in free trim-sinkage configuration for Hull_B-3, tested at $F_r = 0.285$ *(a) and Hull_B-4, tested at* $F_r = 0.348$ *(b).*

Considering Figure 101a, the scattered results are not compliant with the expected asymptotic range where the results are expected to get closer to an asymptotic value as the meshes became finer and the same non-asymptotic range is present in Figure 101b, too. Based on these results, a noise in results has been discovered, and investigated as follows. Given that the advance resistance for hull is connected with the trim and the sinkage, a possible explanation for the registered noise can be related to the dynamical attitude for the simulations, performed in free trim-sinkage configuration. Therefore, other simulations have been performed in fix trim-sinkage configuration for the two initial cases, to assess if the dynamical attitude has an impact on the mesh independence analysis. Two new sets of comparisons are available for Hull_B-3* (7 simulations) and Hull_B-4* (13 simulations), respectively; indeed, the simulations have run in fix trim and sinkage configuration with their initial guess values coming from the finer simulation for the case Hull_B-3 and Hull_B-4, respectively. The graphical results are reported in Figure 102a for Hull_B-3 and Figure 102b for Hull_B-4.

Even in these cases, the results analysis accounts for a non- asymptotic trend because of the presence for scattered results. Indeed, the noise may be connected with the kind of mesh (unstructured) rather than the dynamical attitude for the model; this trend is similar to the convergence issue defined in the numerical set-up evaluation (see Chapter 3). If the data for the same speed are plotted together, a new representation is available to assess a possible difference. Therefore, the comparisons for both the free and the fix trim-sinkage configurations for a $F_r = 0.285$ and $F_r = 0.348$ are plotted in Figure 103a and in Figure 103b, respectively. Firstly, considering Figure 103a, a vertical shifting among triangular marker (free trim-sinkage, Hull_B-3) and the pentagonal one (fix trim-sinkage, Hull_B-3*) can be observed along with a similar general trend; finally, considering Figure 103b, the same conclusions are confirmed across the marker (free trim-sinkage, Hull_B-4 and fix trim-sinkage, Hull_B-4*).

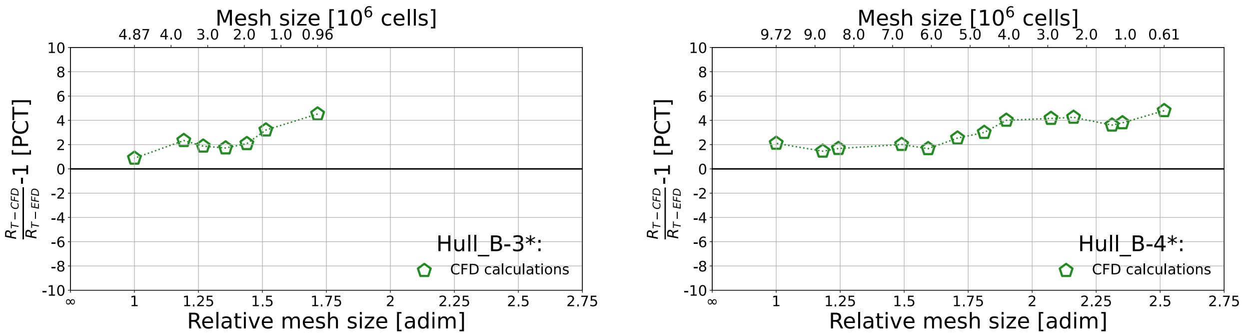

(a) (b)

Figure 102: mesh independence analysis for the percentual difference between EFD and CFD with the respect to the advance resistance in fix trim-sinkage configuration for Hull_B-3, tested at* $F_r = 0.285$ *(a) and Hull_B-4*, tested at* $F_r = 0.348$ *(b).*

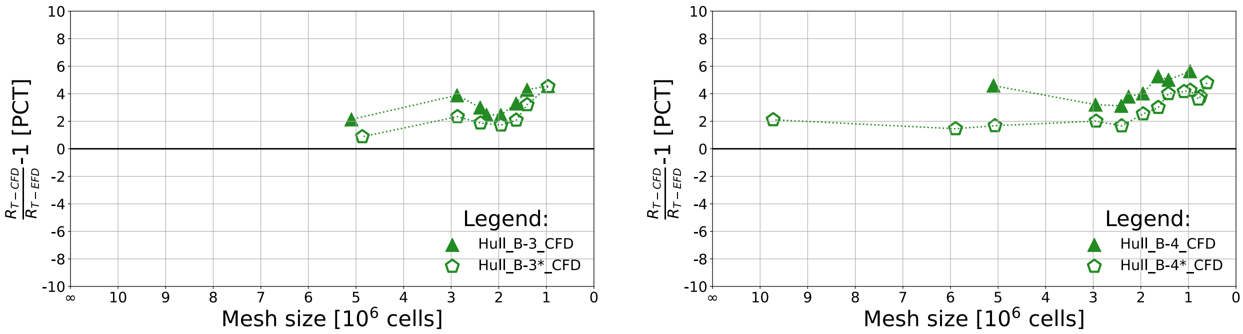

(a) (b)

Figure 103: mesh independence analysis, comparison with the respect to the advance resistance in both free and fix trim-sinkage configuration for both Hull_B-3 and Hull_B-3, tested at* $F_r = 0.285$ *(a) and both Hull_B-4 and Hull_B-4*, tested at* $F_r = 0.348$ *(b).*

5.2.2 Verification

With the respect to the numerical uncertainty estimation (U_{SN}), the available methodologies can be divided in two families: the first one requires at least a number of three results to run while, for the second one, a minimum number of four is mandatory. Considering as "test case" the results obtained for "Hull_B-4*", a number of thirteen solutions are available ($S = 13$), which is more than the minimum requirements of three and four. Hence, by applying equation (140)[140], and considering the case with 3 solutions ($m = 3$) and the one with five solutions ($m = 5$), it is possible to evaluate all the combinations in 286 and 1287, respectively.

$$n = \frac{S!}{m! * (S-m)!} \tag{140}$$

Considering as available data the results from the speed and the configuration criterion (free and fix), a number of nine clusters has been obtained across the 72 simulations and the number of comparisons for each group ranges from six toward thirteen cases, as reported in Table 30. These numbers lead the floor open to investigate, compare and apply different kinds of theoretical approaches in order to evaluate the numerical uncertainty (U_{SN}). Therefore, in this sub-paragraph the results from Hull_B-3* and Hull_B-4* are considered as test case database, and different analyses are described in order to identify the advantages along with the disadvantages arising from the implementation of the available different methodologies.

5.2.2.1 First analysis, "user-defined" parameters

In the first analysis, the numerical uncertainty assessment has run considering as entry data all the solutions to perform the study with Eça and Hoekstra's methodology and a triplet of results (from the finer, the medium, and the coarsest meshes) to run the other three approaches proposed by Celik, Stern, Xing and Stern.

With the respect to Hull_B-3*, all the methodologies have been applied and the results obtained are reported in Table 31, considering all the results and the one obtained for the triplet 4.8-1.9-0.9 millions cells (ratio of 2.52 and 2.11). The data analysis shows that the effective order of accuracy coefficient, p, displays different values as the methodology change, except for Eça and Hoekstra's approach where the value is the same of the theoretical one ($p_{th} = 2$). Speaking about the numerical uncertainty, U_{SN}, the evaluated data show differences; these result from both the kind of approach and the type of correction for the result (for the chosen methodology can be listed four different kinks of corrections: F_S, C_k, $F_S(P)$ and 3 factors). From this data, Celik and Stern formulations lead to similar values with the respect to the numerical uncertainty, while Xing-Stern and Eça-Hoekstra yield similar values among themselves, but differ from the others (the maximum value differs from the minimum one by a factor of 23,6 times). Considering the percentage difference among the extrapolated values as the last index to consider to analyze this first analysis, a good agreement among all the methodologies has been found; indeed, the maximum difference reach the value of 1.76% and all the values are close to the experimental one (that for this configuration is the value 0%).

Moving on the case represented by Hull_B-4*, which results have been stored inside Table 32, it is possible to perform a similar analysis. Indeed, the effective order of accuracy coefficient, p, displays a similar behavior, when compared with the one obtained for Hull_B-3*; while, the extrapolated value maximum difference exhibits a value of 1.32% but remains close to the experimental value. Finally, the results for the numerical uncertainty show a greater scatter when compared with the previous case; indeed, in this case the maximum difference is 9.76% but the smaller evaluation differs from the higher by a factor of 196 times. By this first analysis it seems that the scattered results displayed in Figure 102a for Hull_B-3 and Figure 102b for Hull_B-4, can generate noise to properly assess the uncertainty; indeed, a higher value has always been registered when considering all the data. Based on the findings from this first analysis, it is possible to conclude that the extrapolated values do not differ when the theoretical approach changes; while, among all the available approaches, the Eça-Hoekstra one accounts for the higher value for the uncertainty estimation.

*Table 31: first analysis, mesh independence analysis (4.8M, 1.9M, 0.9M for half domain) with different methodologies for Hull_B-3**.

ID	Symbol [UNIT]	Methodology			
		Celik	**Stern (2001)**	**Stern (ITTC)**	**Eça et al.[1] (2014)**
Constant refinement	-	NO	NO	NO	NO
Order of accuracy (th)	p_{th} [-]	2	2	2	2
Convergence Index	R [-]	0.303	0.303	0.303	-
Order of accuracy (eff)	p_{eff} [-]	5.558	3.035	3.922	2.000
Extrapolated value Vs EFD	φ_{extr} [%]	0.685%	0.319%	-0.160%	-1.078%
Approx. Extrap. Relative error	ε_{extr}^{21} [N /// %]	0.002 0.19%	-	-	-
Grid Convergence Index	GCI_{fine}^{21}	0.002 **0.24%**	-	-	-
Uncertainty Correct (C_k)	$U_{SN_C}(C_k)$ [N /// %]	-	0.087 0.39%	-	-
Uncertainty Correct (F_s)	$U_{SN_C}(F_s)$ [N /// %]	-	0.025 **0.11%**	-	-
Uncertainty Correct ($F_s(P)$)	$U_{SN_C}(F_s(P))$ [N /// %]	-	-	1.128 **5.04%**	-
Uncertainty Correct ($3\ factors$)	$U_{SN}(\dots)$ [N /// %]	-	-	-	1.270 **5.67%**

[1] All the solutions have been considered to run the methodology.

*Table 32: first analysis, mesh independence analysis (9.7M, 1.9M, 0.6M for half domain) with different methodologies for Hull_B-4**.

ID	Symbol [UNIT]	Methodology			
		Celik	**Stern (2001)**	**Stern (ITTC)**	**Eça et al.[1] (2014)**
Constant refinement	-	NO	NO	NO	NO
Order of accuracy (th)	p_{th} [-]	2	2	2	2
Convergence Index	R [-]	0.190	0.190	0.190	-
Order of accuracy (eff)	p_{eff} [-]	4.544	2.437	3.102	1.820
Extrapolated value Vs EFD	φ_{extr} [%]	2.067%	1.948%	1.777%	0.745%
Approx. Extrap. Relative error	ε_{extr}^{21} [N /// %]	0.000 0.04%	-	-	-
Grid Convergence Index	GCI_{fine}^{21}	0.001 **0.05%**	-	-	-
Uncertainty Correct (C_k)	$U_{SN_C}(C_k)$ [N /// %]	-	0.052 0.10%	-	-
Uncertainty Correct (F_s)	$U_{SN_C}(F_s)$ [N /// %]	-	0.039 **0.08%**	-	-
Uncertainty Correct ($F_s(P)$)	$U_{SN_C}(F_s(P))$ [N /// %]	-	-	1.155 **2.32%**	
Uncertainty Correct ($3\ factors$)	$U_{SN}(\dots)$ [N /// %]	-	-	-	4.891 **9.81%**

[1] All the solutions have been considered to run the methodology.

5.2.2.2 Analysis of uncertainty in Eça and Hoekstra's method

The first analysis displays that the numerical uncertainty values, experienced through Eça and Hoekstra's approach, exceed the one expected by considering the uncertainty bounding approach, as proposed by equation (87). Indeed, the bounding approach accounts for an uncertainty of 1.82% for Hull_B-3* and a value of 1.67% for Hull_B-4*. As previously defined, Eça and Hoekstra's methodology accounts for a number of solutions greater than four without a theoretical limit; the noise among results directly affects the numerical uncertainty assessment. Therefore, in the second analysis, the Eça-Hoekstra approach is considered in order to define a procedure able to manage the noise in results without affecting the uncertainty assessment. Indeed, as reported in Figure 100 and detailed in the in Annex 2, all the cases show a scatter distribution among solutions when the mesh independence analysis is performed; therefore, the regression functions generated are directly affected by this variability. Based on the analysis for the dynamic attitude for the hull on the results, it appears that this numerical noise can be directly connected with the generation of the meshes for the cases studied and subsequently accounting for variations in sinkage and trim. Indeed, the implementation for an unstructured mesh refinement approach may introduce numerical noise, potentially masking the variation of the mesh refinement, along with an influence on the value for the numerical uncertainty. A possible way to address this issue is to perform a custom procedure which try to mitigate the effects for the noise in the numerical uncertainty assessment, as explained in the following.

Firstly, considering the least squares analysis as the most widely used methodology because of its ability to create a "best fit" curve through the data, as reported by Ostertagová [141], it is possible to fit on the plane R_{TM} versus mesh refinements a the second order function to minimize the differences among data in the Least Squares Method (LSM) way, as reported in equation (141), where R_{TM}, a and b represents the unknown coefficients.

$$R_{TM} = R_{TM_i} + ar^b \qquad (141)$$

Secondly, once the curve has been generated, a statistical analysis can be performed on both the data and the curve. Indeed, it is possible to evaluate the standard deviation (σ) for the data by considering the distance from each point and the curve with the respect to the R_{TM}.

Thirdly, based on the value for the standard deviation, it is possible to identify two different regions. The first one, the so called "green zone", is a symmetric interval centered on the fit curve and shifted by an amount of $\pm\sigma$ by the centre; while, the second one, defined as "red zone", is everything outside the "green zone". Based on the two regions, it is possible to evaluate each entry data; indeed, if a point lays in the "green zone", it is considered as representative point; otherwise, if it lays in the "red zone", the outlier condition occurs and the point is considered as noise dependent and can be neglected.

Fourthly and finally, once the points which lay in the "green zone" have been identified, a new group of results is available. This new group of samples can be analyzed in order to define the numerical uncertainty for that case.

The described procedure has been applied on Hull_B-4*, as test case to assess the numerical uncertainty and compare the result with the one obtained by first step procedure. Indeed, considering all the 13 available comparisons, it is possible to define the curve fit and the standard deviation (which value has been evaluated in 25.11%), and identify the "red" and "green" regions. As reported in Figure 104, it is possible to see all the comparisons, represented by stars (which color represents the relative mesh size, being 1 the finer one and 2.52 the coarser), the curve fit (green dashed line), coincident with the trace of the bisector and finally the green-red regions.

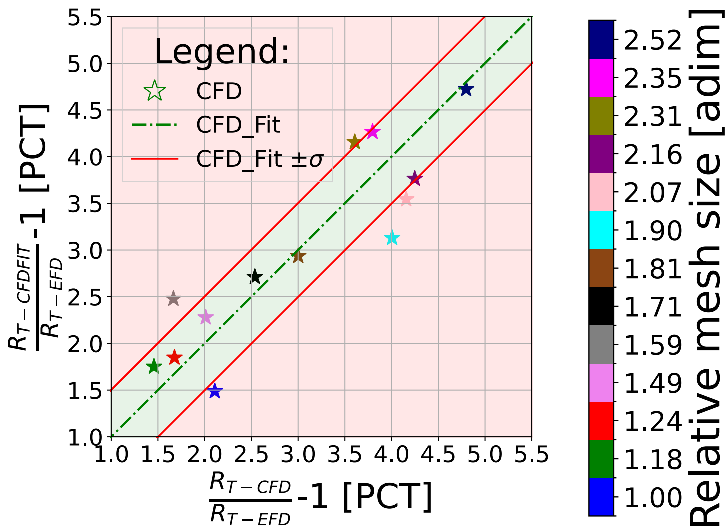

Figure 104: mesh independence analysis for Hull_B-4 with the curve fit and the green and red regions.*

Out of the 13 comparisons, 8 are located in the green zone and 5 in the red one and so considered as outliers; therefore, the new sub-set of data is composed by 8 samples and these samples can be used to perform the verification analysis to get the numerical uncertainty assessment. In Figure 105, a comparison among the initial fit curve (Hull_B-4*, red marker and dashed red line) and the one obtained for the new dataset (Hull_B-4*_Filtered, green markers and dashed green line) are visible, moreover it is possible to appreciate how the value for the uncertainty evaluated for the finer mesh in both the dataset changes. Indeed, the numerical uncertainty value is 3.53% for Hull_B-4*_Filtered and the comparison among this new value with the one calculated for Hull_B-4* (9.81%) shows a decrease by half; while, with the respect to the extrapolated value, φ_{extr}, the registered difference is equal to 0.62%. Another kind of comparison can be carried out by considering the approach shown for the three solution methodologies when an oscillatory convergence among results has been achieved; indeed, as reported in equation (142), in this case the numerical uncertainty cannot be evaluate but just bounded it by the mean value among the higher and minimum values for the comparisons among the resistance of advance. When this approach is applied to Hull_B-4* and Hull_B-4*_Filtered cases, it yields the same value of 1.67%.

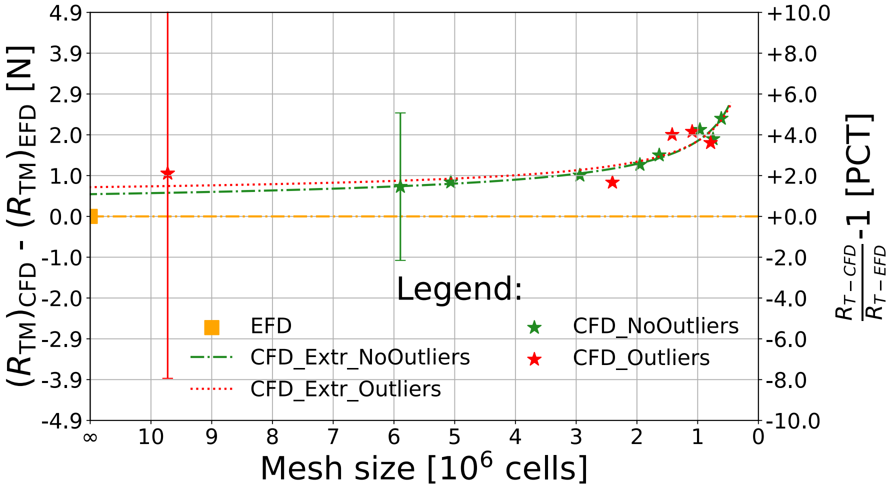

Figure 105: mesh independence analysis on raw data for Hull_B-4 with outliers (red markers and curve) and on filtered data for Hull_B-4*_Filtered, (green markers and curve).*

$$U_{SN} = \frac{1}{2}\left[\left(\frac{R_{T-CFD}}{R_{T-EFD}} - 1\right)_{MAX} - \left(\frac{R_{T-CFD}}{R_{T-EFD}} - 1\right)_{MIN}\right] [\%] \quad (142)$$

Therefore, the value for U_{SN} evaluated for the case Hull_B-4*_Filtered (3.53%) is close to the one obtained by bounding the uncertainty in the range reported in equation (142) and it means that this procedure in some way may account for the numerical noise in results when the numerical uncertainty has to be evaluated through Eça and Hoekstra's approach.

For the sake of completeness this approach may appear not fully consistent from a theoretical point of view; indeed, the procedure can neglect the points which lay in the red zone irrespective of their mesh size and it means that even the results for a finer mesh can be neglected. Despite this, the procedure is deemed correct, since the numerical noise can affect all the solution while disregarding the mesh size. The results obtained from this approach are summarized in Table 33. A comparison with the first procedure exhibits a reduction in the numerical uncertainty estimation. Additionally, the analysis for the extrapolated values experiences a percentual reduction (representing a closer agreement with respect to the experimental results).

This second analysis accounts for the Eça-Hoekstra approach with the attempt to define the numerical uncertainty based on a procedure able to reduce the noise effects in results. The application of the procedure led to an uncertainty estimation which is lower than the initial one and close to the one obtained by NUADA approach.

*Table 33: analysis of uncertainty in Eça and Hoekstra's method (numerical noise), mesh independence analysis for Hull_B-4*_Filtered (fix trim-sinkage configuration, filtered data).*

ID	**Symbol [UNIT]**	**Methodology Eça et al.[1] (2014)**
Constant refinement	-	NO
Order of accuracy (th)	p_{th} [-]	2
Convergence Index	R [-]	-
Order of accuracy (eff)	p_{eff} [-]	1.640
Extrapolated value Vs EFD	φ_{extr} [%]	0.125% **(0.745%)** [2]
Approx. Extrap. Relative error	ε_{extr}^{21} [N /// %]	-
Grid Convergence Index	GCI_{fine}^{21}	-
Uncertainty Correct (C_k)	$U_{SN_C}(C_k)$ [N /// %]	-
Uncertainty Correct (F_s)	$U_{SN_C}(F_s)$ [N /// %]	-
Uncertainty Correct ($F_s(P)$)	$U_{SN_C}(F_s(P))$ [N /// %]	
Uncertainty Correct ($3\ factors$)	$U_{SN}(\ldots)$ [N /// %]	1.749 3.53% **(9.81%)** [2]

[1] All the solutions have been considered to run the methodology.
[2] The parenthesized bolt data from the first analysis and are the same of Table 32.

5.2.2.3 Application for three solutions methods

Based on the availability for multiple datasets, it is possible to consider different criteria to choose the results. Specifically, rather than sampling considering the results for the finer, the medium and coarser meshes, a fixed refinement factor can be adopted to define the cases. Among all the possible values to choose, the one proposed by Celik [51] has been considered in this analysis. Therefore, the value of 1.3 has been considered as the constant reference refinement factor for the three solutions methodologies. Performing this activity on the case Hull_B-4*, where is possible to get the maximum number of combinations, three possible clouds of results can be sorted as: Triplet_1 (9.7, 5.0 and 2.4 million cells for half domain, ratio of 1.24 and 1.28), Triplet_2 (2.4, 1.0 and 0.6 million cells for half domain, ratio of 1.30 and 1.21) and Triplet_3 (5.0, 2.4 and 1.0 4 million cells for half domain, ratio of 1.28 and 1.30). Considering Triplet_1 and Triplet_2, the mesh independence analysis shows a value for the convergence index, R, higher than zero (respectively 38.2 and 3.8); indeed, being the convergence indexes higher than zero, divergence condition occurs in both cases. Therefore, for Triplet_1 and Triplet_2 nothing can be said from a theoretical point of view about the numerical uncertainty. While, with the respect to Triplet_3, the value for the convergence index gives the negative value of -0.005 and therefore, the numerical uncertainty cannot be evaluated but just bounded among the value of 1.24% normalized on the EFD. The calculations for these cases are reported in Table 34.

Table 34: application for three solutions methods, mesh independence analysis for Hull_B-4, Triplet_1,2,3.*

ID	Symbol [UNIT]	CASES		
		1	2	3
Nr. Cells Fine	N_1	9,725	2,403	5,064
Nr. Cells Normal	N_2	5,064	1,091	2,403
Nr. Cells Coarse	N_3	2,403	0,611	1,091
Output value Fine	$\hat{S}_1$	49,856	49,640	49,646
Output value Normal	$\hat{S}_2$	49,646	50,857	49,640
Output value Coarse	$\hat{S}_3$	49,640	51,169	50,857
Grid Refinement Factor	$r_{21} = \frac{N_2}{N_1}$	1,243	1,301	1,282
Grid Refinement Factor	$r_{32} = \frac{N_3}{N_2}$	1,282	1,213	1,301
Difference of estimation	$\varepsilon_{21} = \hat{S}_2 - \hat{S}_1$	-0,210	1,216	-0,006
Difference of estimation	$\varepsilon_{32} = \hat{S}_3 - \hat{S}_2$	-0,006	0,313	1,216
Convergence Index	$R = \frac{\varepsilon_{21}}{\varepsilon_{32}}$	38,251	3,890	-0,005
Type of convergence	-	Divergence	Divergence	Oscillatory
Normalized Bounded Uncertainty	$U_{SN} = \frac{\hat{S}_{UP} - \hat{S}_{LO}}{2 * \hat{S}_{EFD}}$	-	-	1.24%

Moving on the second test case, Hull_B-3*, it is possible to define one triplet of solution compliant with the value close to 1.3 for the grid refinement factor (Triplet_4: 4.8, 2.3 and 0.9 million cells for half domain, ratio of 1.26 and 1.35). In this case a monotonic convergence occurs, as the value of R is 0.37 and the numerical uncertainty can be evaluated even with the three solutions methodologies. Considering the results obtained, as shown in Table 35, these confirm the observations already highlighted after the application of first approach methodology, being the values for the numerical uncertainty clusterable into the low (Celik, Stern) and in the high (other approaches) uncertainty groups.

Based on the findings from this third analysis, it is possible to conclude that if a three solutions approach is used, it is not always possible to assess the numerical uncertainty; indeed, it is not always true that the results obey to the analytical form consistent with a monotonically convergent function.

5.2.2.4 Robustness of the uncertainty evaluation

With the respect to the numerical uncertainty assessment, the analysis one, two and three show the main differences for the results among the theoretical approaches; moreover, in some case not all the proposed procedures are able to find a value for U_{SN}. The shown lack of results addresses an important role with the respect to the robustness of the methodology. In this sub-paragraph, an analysis about the robustness of the available theoretical approaches is described. To better define how the proposed methodologies can be considered robust and effective, another kind of analysis has been carried out.

Considering Hull_B-4* as test case because of its number of comparisons (a total number of 13), it is possible to cluster the results based on both the number of samples to consider and the relative size for the meshes.

Table 35: application for three solutions methods, mesh independence analysis for Hull_B-3 (Triplet_4: 4.8, 2.3 and 0.9 million cells for half domain).*

ID	Symbol [UNIT]	Methodology		
		Celik	**Stern (2001)**	**Stern (ITTC)**
Constant refinement	-	NO	NO	NO
Order of accuracy (th)	p_{th} [-]	2	2	2
Convergence Index	R [-]	0.377	0.377	0.377
Order of accuracy (eff)	p_{eff} [-]	2.700	5.129	4.104
Extrapolated value Vs EFD	φ_{extr} [%]	−0.230%	0.459%	−0.707%
Approx. Extrap. Relative error	ε_{extr}^{21} [N /// %]	0.011 1.11%	-	-
Grid Convergence Index	GCI_{fine}^{21}	0.014 **1.37%**	-	-
Uncertainty Correct (C_k)	$U_{SN_C}(C_k)$ [N /// %]	-	0.176 0.79%	-
Uncertainty Correct (F_s)	$U_{SN_C}(F_s)$ [N /// %]	-	0.011 **0.05%**	-
Uncertainty Correct ($F_s(P)$)	$U_{SN_C}(F_s(P))$ [N /// %]	-	-	1.326 **5.92%**

[1] All the solutions have been considered to run the methodology.

By considering the number of samples equal to three and with a relative size bigger than 1.2 for a total of 40 combinations, the cluster for the three solutions methodology has been identified; while, Eça-Hoekstra's cluster is composed by 20 combinations of 5 solutions. A detailed representation about the data subdivision is available in Figure 106 where, on x-axis all the cases have been reported, on y-axis the relative mesh size is displayed (indeed each group of data reports the value 1, based on the third root of the h_i to h_{i+1} ratio, but h_i changes for each family) along with the circles which identify the mesh size for each result; the details for three solutions and five solutions clusters are shown in Figure 106a and Figure 106b, respectively.

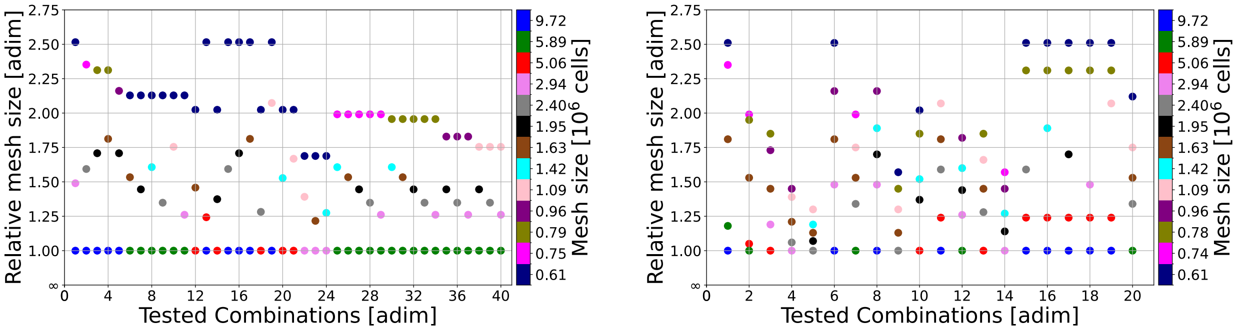

(a) (b)

Figure 106: cases identification for mesh independence analysis on Hull_B-4 case; three (a) and five (b) solution.*

Once the datasets are available, the uncertainty analysis has been performed on each one of them with all the proposed methodologies. Later on, with the respect to the resistance for the model hull, the results have been investigated in order to first assess the robustness of each approach and second, their effectiveness by considering the order of accuracy, p_{eff}, the numerical uncertainty, U_{SN}, and the extrapolated value, φ_{extr}.

With the respect to the robustness to evaluate the numerical uncertainty, results for the three solutions methodologies shows an applicability rate of 22/40 cases (55%) and 20/20 (100%) for Eça-Hoekstra's one. This is a direct consequence for the convergence criteria; indeed, only when a monotonic convergence is achieved, the three solutions methodologies can perform; the results about the types of convergence are stored inside Table 36.

Table 36: type of convergence for three solution methodology on 40 cases.

Type of convergence	Range [-]	Cases [adim]	Cases [%]
Monotonic convergence	$0 < R < 1$	22	55,0%
Oscillatory convergence	$-1 < R < 0$	5	12,5%
Monotonic divergence	$R > 1$	2	5,0%
Oscillatory divergence	$R < -1$	11	27,5%

Moving on the second layer of analysis, in order to identify any possible correlation or trend and following the data discrete binning method for scattered results, a new representation has been considered; indeed, the x-axis (representative for p_{eff}, U_{SN} and φ_{extr}) has been divided into bins to account for the occurrences varying the range while, on y-axis the number of occurrences has been plotted and normalized on the total number of samples. Moreover, to better appreciate the differences among all the theoretical approaches, the results for the three solutions methodologies are plotted next to the Eça-Hoekstra's ones and colors have a code to properly identify each theory, as follows: light green for Stern, brown for Celik and blue for Eça-Hoekstra.

The first coefficient analyzed is the extrapolated value. As reported in Figure 107, the x-axis has been scaled on the experimental value to directly identify the differences among the various approaches (the value zero on the graphs represents 0% difference with the respect to the experimental data) and their results dispersion. With the respect to the three solutions methodology, bins distributions exhibit a peak close when $\varphi_{extr} \cong 2\%$ and some result has a difference higher than 10% when compared with the experimental value, as reported in Figure 107a. While, moving on Eça-Hoekstra's cases, results are similar with the ones for the three solutions methodology but exhibit a higher peak (40%) close to $\varphi_{extr} \cong 2\%$ along with a lower dispersion among the results, as shown in Figure 107b. Moreover, with the respect to the value obtained with all the solutions ($\varphi_{extr} \cong 0.745\%$ for Hull_B-4* case, 13 solutions), which is reported in the graph through a red line, the difference registered is small and close to 1%.

The second parameter analyzed is the order of accuracy. Considering Figure 108a, results don't exhibit a cluster close to the theoretical order of accuracy (which value is 2 and it is represented by a vertical orange line) and nothing in particular can be defined because of the presence of a data sample dispersed uniformly in the range $(0 \div 10)$. With the respect to Eça-Hoekstra's cases, all the cases are in the range $(0 \div 2.02)$ with a peak of 50% when $p = 2$, as reported in Figure 108b.

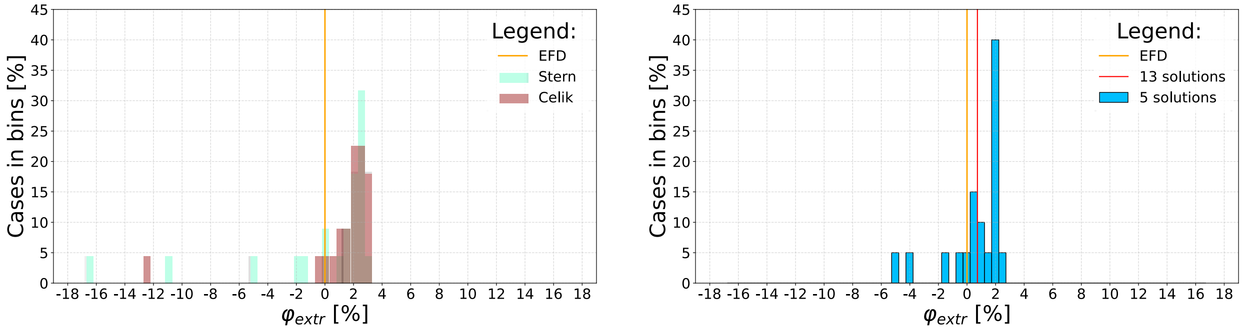

(a) (b)

Figure 107: binning method approach to assess the extrapolated values, three solution methodologies (a) and Eça-Hoekstra's one (b).

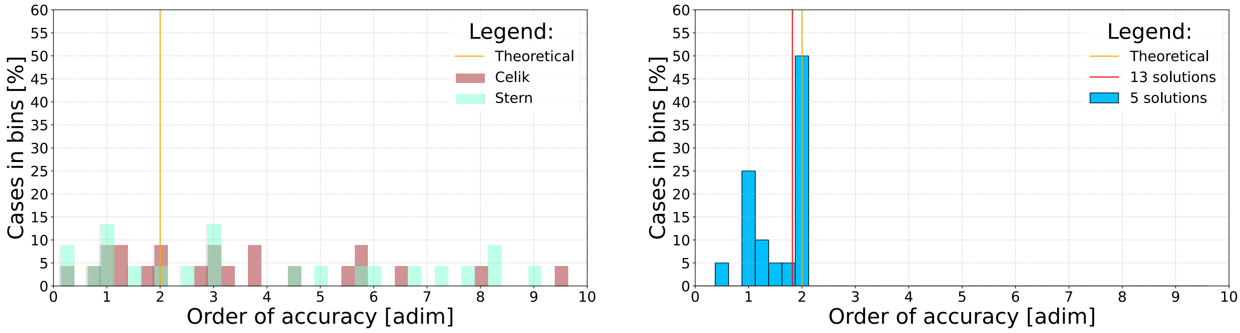

(a) (b)

Figure 108: binning method approach to assess the order of accuracy, three solution methodologies (a) and Eça-Hoekstra's one (b).

The last parameter to be analyzed is the numerical uncertainty. With the respect to the three solutions methodology, as reported in Figure 109a, most of the solutions exhibit a value for the uncertainty less than 3% with a peak value of 70% for an uncertainty estimation below the value of 1%; very few cases report a value higher than 10%. When considering Eça-Hoekstra's cases, the uncertainty estimation is less than 8% (85% of cases) and there is a higher value (25% of samples) for the estimation in the range $(0 \div 1)\%$, as reported in Figure 109b.

Therefore, by comparing the three solutions cases (40) with Eça-Hoekstra's ones (20), two important features can be fixed: firstly, with the respect to the numerical uncertainty evaluation, Eça-Hoekstra's methodology performs always; while, the other approaches lead to a result in 55% of the available cases; secondly, the value for the order of accuracy has a great scatter for the three solutions approaches without an appreciable impact to the extrapolated value; whereas, in the other case the values for the order of accuracy are inside a narrow range $(0.5 \leq p \leq 2)$. This trend needs more investigations, as follows.

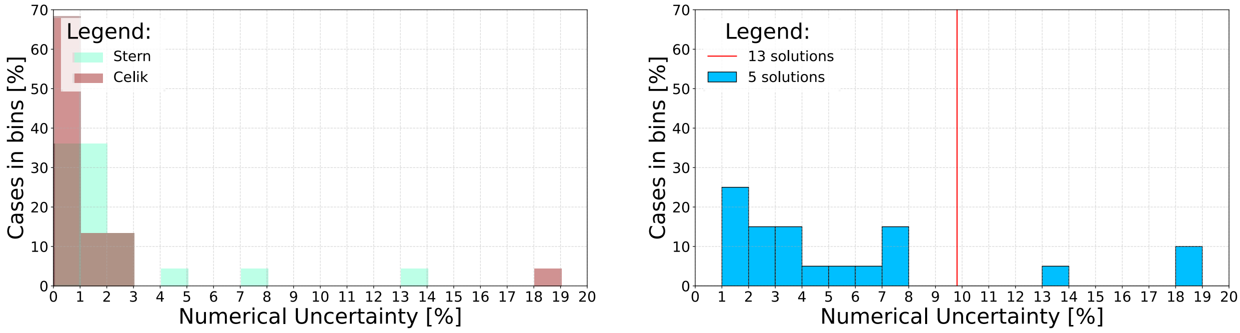

(a) (b)

Figure 109: binning method approach to assess the numerical uncertainty, three solution methodologies (a) and Eça-Hoekstra's one (b).

A statistically investigation can run in order to better describe the phenomena. Indeed, by considering the scattered distribution for the coefficient p , as shown in Figure 110, it is possible to characterize this distribution with the mean-standard deviation approach or by the Median Absolute Deviation about the median (MAD) one. It is important to implement both the theoretical approaches in order to get a general description for the phenomena. Indeed, in equation (143) from Rousseeuw et al. [142], MAD represents a robust and fast way to estimate the scale for the phenomena considered:

$$MAD_n = b \cdot med_i \left| x_i - med_j(x_j) \right| \tag{143}$$

where, x_J represents the j-th case, $med_j(x_j)$ the median for all the cases, med_i stands for the median assessed for $\left|x_i - med_j(x_j)\right|$, and finally b represents a coefficient, usually defined as 1.4826.

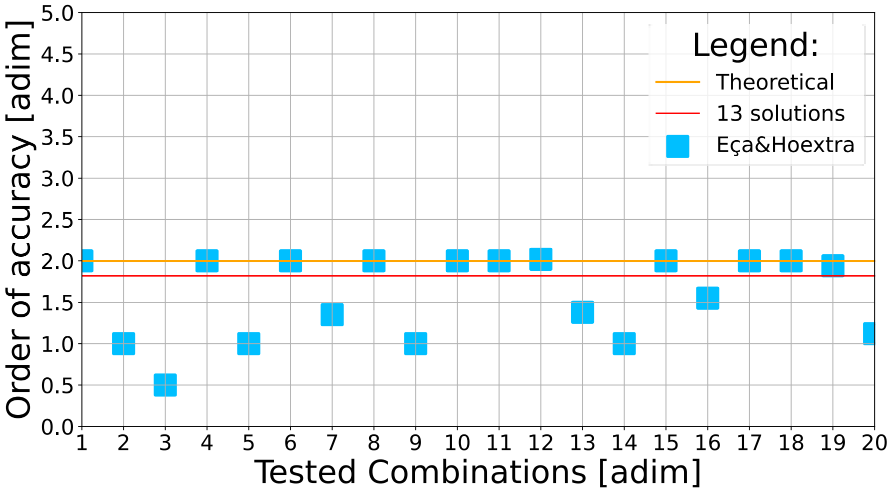

Figure 110: order of accuracy for Eça-Hoekstra's methodology applied on 20 cases.

Once the theoretical approaches have been defined it is possible to move the application and later on to the results analysis. Therefore, considering the results, by comparing the mean value (1.593) and the standard deviation (0.498) for the dataset, as shown in Figure 111a, with the median (1.970) and its MAD (0.059), as reported in Figure 111b, it is possible to appreciate how the change of statistical approach leads to different conclusions. Indeed, the number on samples inside the interval $|p - Median| \leq MAD_n$ (range 0.118) is evaluated in 11 (representing 50%) while, the one inside the interval $|p - Mean| \leq \sigma$ (range 0.996) is 15 (representing 68%). These data lead to evaluate the density of sampling (Φ) for the observations[5]; indeed, the value of 93.2 is the characteristic one for the median approach and 15.0 for the mean one. This peak in density explains the higher density of samples lying in the range $(0 \div 4)\%$ for the uncertainty estimations. As a result, a connection among the order of accuracy and the numerical uncertainty estimation has been found; so, a way to account for this connection has to be exploited.

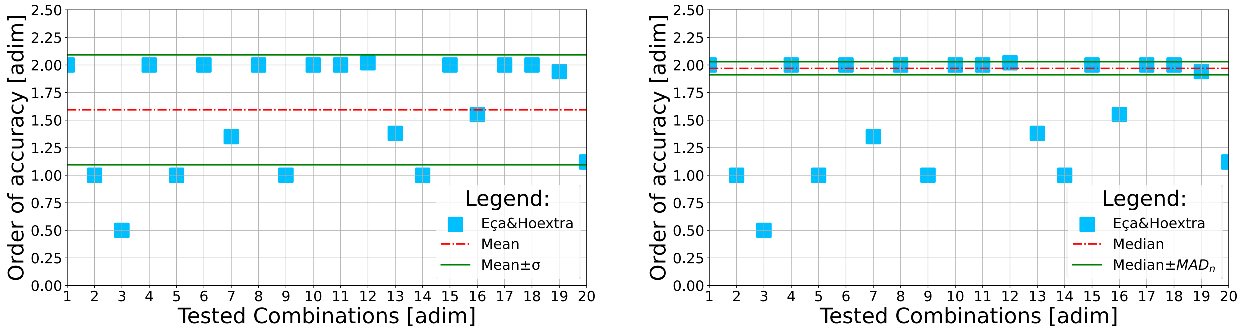

(a) (b)

Figure 111: statistical analysis on the order of accuracy for Eça-Hoekstra's methodology applied on 20 cases, mean and standard deviation (a) and median and MAD_n (b).

With the respect to the value for the numerical uncertainty estimation performed with Eça-Hoekstra's methodology applied on 20 cases, as shown in Figure 112a, it is possible to compare the results with the ones obtained for the order of accuracy (Figure 110). This comparison accounts for an increase for the uncertainty estimation, as the order of accuracy deviates from the theoretical one ($P_{th} = 2$), as displayed in Figure 112b. This relation is particularly evident for cases 3 and 5; indeed, when p assumes the values of 0.5 and 1.0, the values for the numerical uncertainty has been evaluated in 18.99% and 18.74%, respectively. Based on the foregoing, moving from the 20 cases database, it is possible to cluster it by the order of accuracy coefficient; indeed, considering only the cases where p falls in the narrow range of 1.5 to 2, it is possible to perform a statistical analysis on this reduced database (with the respect to U_{SN} and φ_{extr}), represented by 11 cases. The results obtained are shown in Figure 113a-c. With the respect to the φ_{extr} coefficient, as shown in Figure 113a, results exhibit a peak of about 70% in a range close to the one obtained by considering all the cases (case Hull_B-4*, 13 solutions represented as a red vertical line).

[5] The density of observation can be evaluated as $\Phi = {}^{Nr.samples}/_{Range}$.

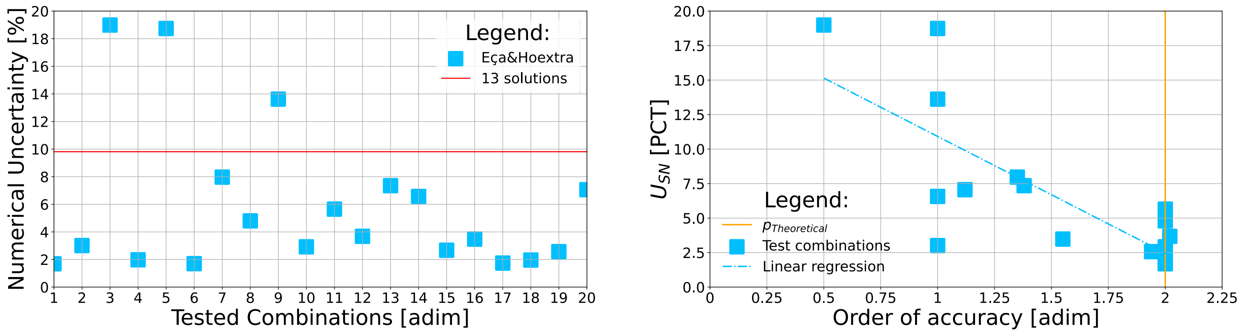

(a) (b)

Figure 112: 20 cases application for the Eça-Hoekstra's methodology; numerical uncertainty assessment (a), p and U_{SN} correlation analysis (b).

When considering the order of accuracy, the values presented in Figure 113b are in agreement with the initial condition for this last test case, indeed a peak higher than 80% is present for a value of p equal to the theoretical one ($p_{th} = 2$). Finally, considering the numerical uncertainty assessment, results exhibit a lower value when compared with all the 20 cases, but all the samples lay on the range $(0 < U_{SN} \leq 6)\%$ with a probability of to assess a value for the numerical uncertainty lower than 3% for 60% of the cases, as reported in Figure 113c.

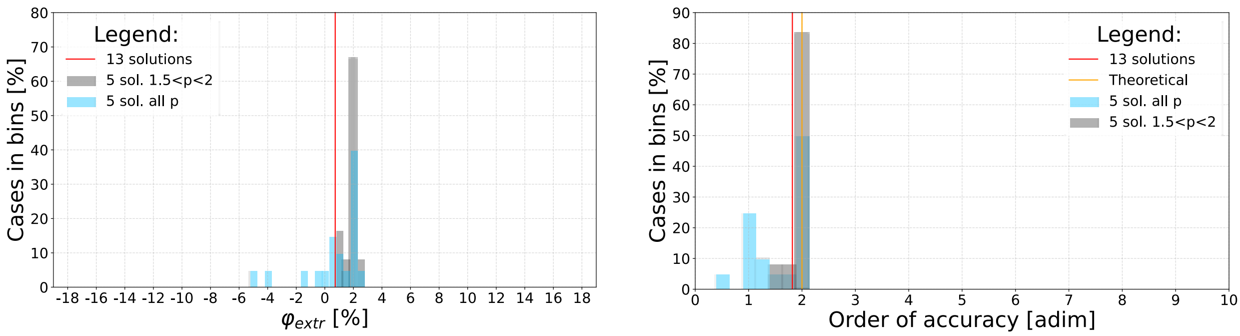

(a) (b)

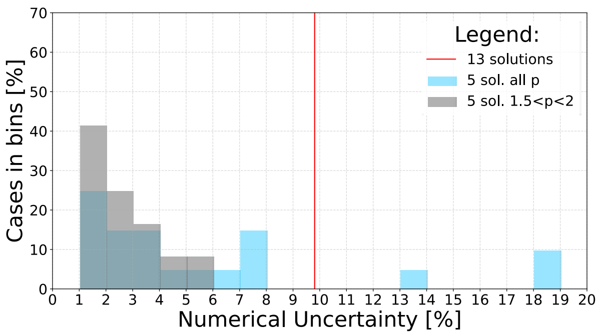

(c)

Figure 113: statistical analysis on φ_{extr} (a), p (b) and U_{SN} (c) for Eça-Hoekstra's methodology applied on 11 samples showing p in range of 1.5 to 2.

Based on the results obtained by the robustness analysis, it can be derived that Eça-Hoekstra's methodology always performs, while the approaches to three solutions lead to a result in only 55%

of the considered cases. Moreover, with the respect to the Eça-Hoekstra's methodology, an anti-correlation among the order of accuracy and the uncertainty estimation has been found as follows: if the order of accuracy is far from the theoretical one, the value for the uncertainty estimation increases, requiring further analysis.

5.2.2.5 Noise-aware numerical procedure

In order to define the numerical uncertainty with the attempt to get a value without the noise influence, it is possible to derive a general application for the Eça and Hoekstra's approach, based on the results arising from the four previous analyses. Indeed, when at least four simulations have run, and the results are available, the order of accuracy can be evaluated, as prescribed by the procedure. Considering the extrapolated value, it can be always considered as accurate enough. Differently, considering the numerical uncertainty estimation, if the p value lays in the range from 1.5 to 2, it can be considered as a reliable estimation. Otherwise, if p assumes values far from the theoretical one, another simulation should be carried out and a new order of accuracy can be addressed. If this new value lays in the prescribed range $(1.5 \leq p \leq 2)$, the value for the numerical uncertainty can be considered as representative for a reliable estimation; while, if the p value lays outside the prescribed range, another simulation should be performed. The procedure can be iterated with the only limitation given by the computational effort potentially required.

In the following, it is provided an example to validate the proposed procedure. Among the available data, the 5 solutions case 3 has been considered as the test case to run the proposed procedure. Based on Eça and Hoekstra's approach, the initial value for the numerical uncertainty estimation was quantified in 18.99% and the order of accuracy $(p_{INITIAL})$ provided a value of 0.5. Adhering to the iterative procedure, another simulation is required to move to the following procedural step; among the available solutions, the coarse one has been considered. Based on Eça and Hoekstra's methodology, the new order of accuracy $(p_{1\_IT} = 1.05)$ exhibits a value outside the prescribed range, and therefore, another iteration is required. In the second iteration, the 1.4M cells result has been considered to run Eça and Hoekstra's approach with 7 solutions. The second iteration accounts for $p_{2\_IT} = 2.00$ and $U_{SN} = 3.88\%$. Based on p_{2_IT} value, it is possible to consider a low numerical noise influence on the data, and therefore, the numerical uncertainty value can be qualified as a representative value. Moreover, U_{SN} value is close to the one obtained by bounding the uncertainty, as reported in equation (142). All cases considered are displayed in Figure 114a, adhering to the following code colors: black circles for the results, red circles for the 5 solutions initial case, green circles for the 6 solutions implemented in the first iteration and finally the blue circles for the 7 solutions implemented in the second iteration. While, Figure 114b, Figure 114c and Figure 114d show the numerical uncertainties recorded for the initial case, the first and the second iterations, respectively.

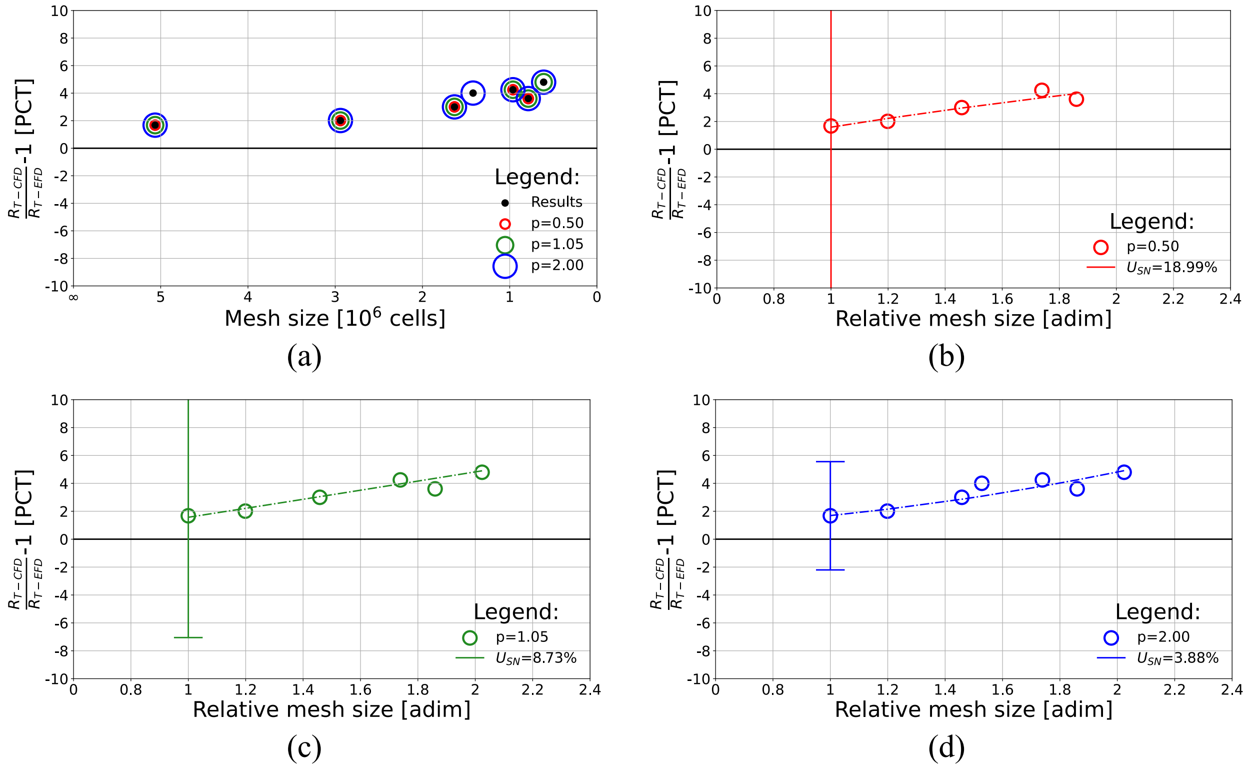

Figure 114: the numerical procedure application on Hull_B-4. Representation for the cases considered (a), red circles for the U_{SN} assessment in the initial case (b), green circles for U_{SN} assessment in the first iteration case (c) and blue circles for U_{SN} assessment in the second iteration case (d).*

5.2.2.6 Verification considerations

NUAPA approach deals with the numerical uncertainty estimation based on different theoretical approaches. By taking into account all the formulation for the verification together with the bounding approach, different results have been obtained. A study about these differences has run in order to identify the robustness of the methodology, the value for the uncertainty estimation and the extrapolated values. More in details, based on the available data four analysis have been performed as follows:

- in the first analysis, all the data have been considered to run the four solutions approach and the results from the finer, the coarser and the one in the middle mesh refinements have been considered to run the three solutions approaches;
- in second analysis, the influence of noise in results for the four solutions approach has been investigated;
- in third analysis, a quite constant and suggest value for the mesh refinement factor has been considered to choose the triplets of result to run approaches to three solutions;

- in fourth analysis, several combinations among the results have been considered to run all the theoretical approaches in order to get the numerical uncertainty assessment and to define their robustness.

Based on the findings from these analyses, the four solutions approach reaches a success rate of 100%, while approaches to three solutions perform in 55% of the cases considered. With the respect to the numerical uncertainty estimations, the noise influences the results for the four solutions approaches and a correlation among the order of accuracy and the numerical uncertainty assessment has been found. More in details, four solutions approach exhibits the tendency to overestimate the numerical uncertainty, when compared with both approaches to three solutions and the bounding uncertainty approach. This overestimation can be partially reduced through the proposed numerical procedure, which, as shown by the results, is able to partially mitigate the noise influence for the uncertainty estimation.

Finally, among all the available approaches, Eça-Hoekstra accounts for the higher reliability when four solutions are available. When considering U_{SN} and the "All Hulls" available data (later on identified as AH, and composed by 72 simulations), the four solutions approach accounts for a mean value of 6.65%, when all the simulations performed are considered. If the proposed procedure is considered, the value for the numerical uncertainty is closer to the one from the bounding approach.

5.2.3 Validation

Once the numerical uncertainty assessment value has been defined using NUAPA approach, it is possible to move to the verification issue in order to get the uncertainty assessment, as later on described.

From a theoretical point of view, if the value for the experimental uncertainty (U_D) is not available, it is not possible to perform this kind of analysis. In this work, the values for U_D aren't available and therefore it is non possible to achieve a full verification analysis. Nonetheless, in order to try to overcame this lack of knowledge, it is possible to consider the variation among the data obtained by different towing tank, testing the same model hulls (exactly the same physical objects) at different speed, as a way to account for a similar order of magnitude for the experimental uncertainty. Indeed, in the view of the "Final Report and Recommendations to the 28th ITTC" held in Wuxi (2017) [115], it is possible to draw the data and define an experimental uncertainty surrogate as described above. Indeed, the results for the total resistance coefficient (C_{TM}) of a model hull $\left(DTMB\ 5415, L_{PP\_M} = 3.078\ m\right)$, tested at three different speeds are plotted in Figure 115a, where x-axis represents F_r, the y-axis the percentage difference for each single test with the respect to the mean value obtained for that speed and its standard deviation (each dot represents a single experiment). While, Figure 115b shows the results in the same representation for the equivalent hull but with a larger scale $\left(DTMB\ 5415, L_{PP\_M} = 5.720\ m\right)$.

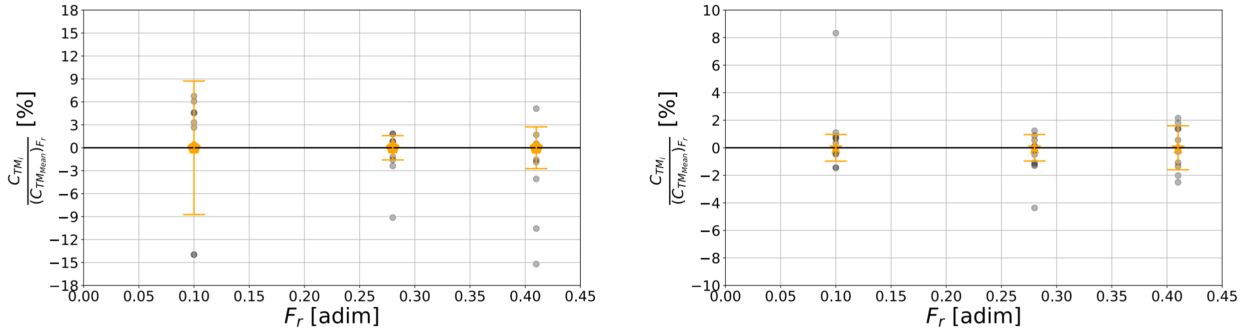

(a) (b)

Figure 115: statistical analysis on towing tank test for model hull DTMB 5415 small (a) and large(b).

By considering these data, it is possible to define how the results change when either the speed or the scale changes, or both jointly. More in details, the greater dispersion is registered for lower speed of the small model ($\sigma_{F_{r\_0.1}} = 8.73\%$), while the scale seems to have a smaller effect on C_{TM} for the two higher speeds; indeed, results exhibit a trend which can be considered as a raw way to account for the value of U_V, as reported in Figure 116.

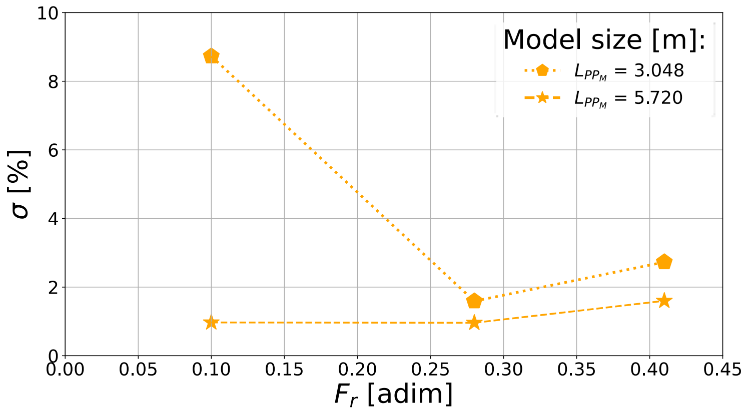

Figure 116: standard deviation for the statistical analysis on towing tank test for model hull DTMB 5415 small (labelled with pentagons) and large (labelled with stars).

Indeed, the unknown experimental uncertainty of another hull can be derived from the distribution of the standard deviation obtained from the two hull models (small and large). Therefore, performing a first linear interpolation among the speed (being available the data only for three speeds, $F_r = 0.10, 0.28, 0.41$) and a second one among the length for the models, it is possible to assess the value for the standard deviation by this bounding approach. This assessment can be mathematically obtained for each speed and each length among the boundary represented by the experimental values. This procedure has been implemented for the two model hulls tested for the numerical uncertainty assessment; the results have been plotted in Figure 117a for the model Hull_B-3* ($F_r = 0.285$) and in Figure 117b for the model Hull_B-4* ($F_r = 0.348$), where the dashed green lines represent the interpolation among the experimental data and the squares exhibit the interpolation for the speed. Finally, the results for the experimental uncertainty, U_D, are represented by the value of 1.53% for the slower hull and 2.04% for the faster one.

The same evaluation can be performed even for COMPDB. In this case, 22 different hulls have been tested at different speeds; therefore, in order to apply the procedure with the attempt to define U_D, the model length and the speed have been defined as follows. Firstly, the length considered has been evaluated through the its mean value among the hulls, and the same approach has been implemented with the respect to the speed. Finally, the following two values have been found: $F_{r\_\overline{\text{COMPDB}}} = 0.229$ and $L_{PP\_\overline{\text{COMPDB}}} = 5.35\ m$. Based on these values, the derived experimental uncertainty has been evaluated in 1.32%.

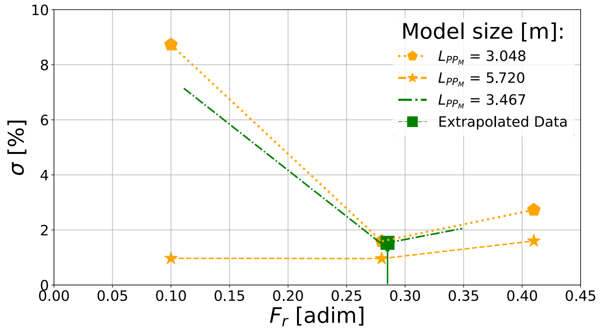

(a)

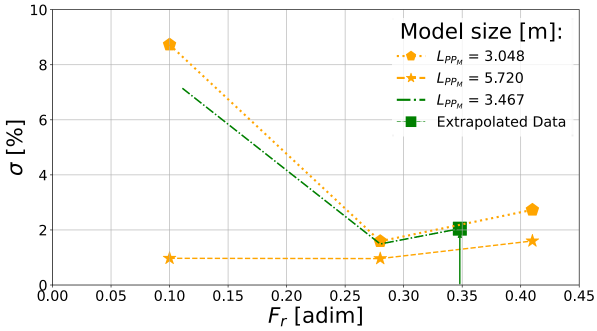

(b)

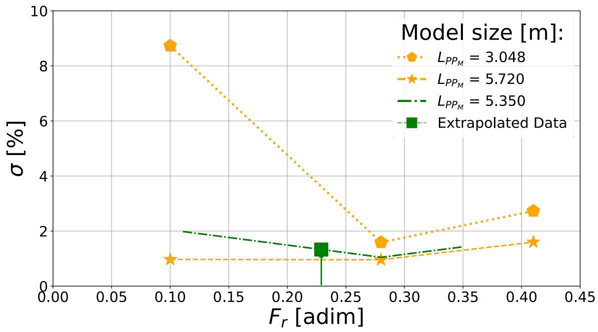

(c)

*Figure 117: surrogate for the experimental uncertainty evaluated for Hull_B-3** ($F_r = 0.285$) *and Hull_B-4** ($F_r = 0.348$)*, cases (a) and (b), respectively and for COMPDB case (c).*

5.2.4 Accuracy for a CFD calculation

Once both the Verification and the Validation have run, the uncertainty assessment is completely achieved. In order to define the level of validation, the values for the numerical uncertainty (U_{SN}), the experimental (U_D) and the requested (U_{REQD}) have to be compared.

The results from the numerical uncertainty (U_{SN}) assessed through NUAPA approach, combined with results for the experimental uncertainty (U_D) and the validation one (U_V), are summarized in Table 37. With the respect to the requested uncertainty (U_{REQD}), its value is not considered in this study. Indeed, its value is directly connected with the design aim and does not provide any further characterization about the uncertainty estimation, but only declare if the value obtained can be considered as affordable in that design.

Table 37: results from verification and validation.

Test Case	$\|E\|$	U_{SN}	U_D	U_V
All Hull	0.20%	6.65%	(1.53÷2.04) %	(6.82÷6.95) %
Hull_B-4*_Filt	0.12%	2.29%	2.04%	3.06%

For the cases considered, a fully validation occurs. Indeed, considering the 6 cases listed in Table 11, the first one ($|E| < U_V$) has been achieved in all the cases considered.

With the respect to the question "how precise is a CFD calculation", the following considerations can be listed, based on the findings from both the data analysis and the uncertainty assessment. From a theoretical point of view, the NUAPA approach has to be used and the experimental uncertainty represents a mandatory input data. Considering current research, the value for the uncertainty assessment lays across the 5%. While, considering the results from all the simulations performed, if a blind CFD simulation has run to define the pure towing resistance, a mean absolute difference with the EFD results of 3.04% has been registered and 82% of cases exhibit difference lower than 5%. These results can be considered as representative for the NUADA. Therefore, based on the two different described approaches, similar results have been obtained.

6 Model self-propulsion, experimental and numerical results

When a new ship has to be design, with the respect to the power estimation, three main issues have to be considered, as follows: the hull, the propeller (what follows can be true for cases with a single or multiple propellers) and the interaction among them. As established, when a generical hull is towed, the interaction among the hull and the water generates a pressure field along it with a boundary layer, where the velocity vector changes its module and direction. Similar characteristics can be also observed for the same hull in self-propulsion test, but in this case the interaction among the propeller and the hull has to be addressed. Indeed, the propeller operating in the aft part of the ship, where the flux is affected by the hull shapes, performs differently when compared with the open water condition. Moreover, the propeller operating in the aft region of the ship (where the inflow is affected by the presence for the hull and the struts) exhibits different performances compared with the open-water conditions, where an undisturbed flux characterize the inflow region for the propeller; additionally, even the hull is affected by the propeller suction and an increase for the resistance is achieved.

All these considerations have to be addressed; the self-propulsion test accounts for an experimental or numerical procedure to assess the propulsion coefficients like wake fraction $(1-w)$ and the thrust deduction $(1-t)$ to define the mutual interaction among the hull and the propeller (or propellers). These coefficients are the ones used to identify the propeller (or propellers) operational parameters and the interaction among the propeller and the hull. The self-propulsion experimental procedure can be addressed through the ITTC procedure for the “Propulsion/Bollard Pull Test” 7.5-02-03-01.1 [143]. While, the numerical procedure for the same experience can be issued by three different approaches: firstly, both the propeller (or propellers) and the ship geometries have to be physically modelled, secondly the body force method inside the domain can replace the propeller (or propellers), and finally a viscous/potential coupled method can be used to implement the geometries for the propeller and to compute the forces by means of a BEM approach.

These approaches lead to a different computational effort; indeed, if the propeller has to be modelled, a higher number of cells is required when compared with the body force, which represents the faster approach among the proposed ones. As further on described, and following the results from Jasak et al. [35], among the available theoretical approaches, the actuator disk one has been selected to model the propeller effects in the self-propulsion experience. This choice can reduce the computational effort to perform several simulations for different hulls to define a repository to store the results, as previously done for the resistance test. Moreover, this simplified strategy enables a saving in computational effort along with a limited loss of accuracy as proposed by Gokce et al. [144].

In current paragraph, after the description for the virtual disk theory, the results from the self-propulsion numerical experience for one test hull are given. These experiences have been performed considering different kinds of numerical set-up; each one of them has been tested in order to define the better compromise among the physical description for the problem, the accuracy and the computational effort. More in details, with the respect to the Hull 19 (the JBC hull, which is considered one of the most famous benchmarks in the CFD applications), five different types of numerical set-up have been considered to run all the simulations, as follows:

- resistance test (free trim and sinkage with the free surface) for half hull (Resistance Test – Symmetry, RT-S), resistance test (free trim and sinkage with the free surface) for all hull (Resistance Test – No Symmetry, RT-NS). The RT-S set-up is exactly the one defined by DSUP (with an additional refinement across the propeller position), whereas the RT-NS corresponds to a DSUP set-up with an identical mesh discretization replicated symmetrically with respect to the symmetry plane (with an additional refinement across the propeller position). These simulations are requested to proceed through the self-propulsion experiences.
- self-propulsion (free trim and sinkage with the free surface) with virtual disk no torque and half hull (Self Propulsion - No Torque Symmetry, SP-NTS). This set-up accounts for the less computational effort, which is roughly the same requested by the RT-S one. Based on the torque absence, it has been tested in order to try to get results with the less computational effort;
- self-propulsion (free trim and sinkage with the free surface) with virtual disk no torque and all hull (Self Propulsion - No Torque No Symmetry, SP-NTNS). This set-up accounts for a computational effort in a similar manner to the RT-NS one. It has been tested in order to try to get results about the torque effects on the results;
- self-propulsion (free trim and sinkage with the free surface) with virtual disk with torque and all hull (Self Propulsion - Torque No Symmetry, SP-TNS). The torque value can be obtained by considering the open water curves, since the ratio among the K_T and K_Q coefficients (as

later on described) is quite constant varying the advance coefficient. These last approaches account for a computational effort which is similar to the RT-NS one; nevertheless, they provide the most accurate physical description among the other proposed numerical set-up and are considered as numerical benchmarks to assess the precision for the other set-up.

Moreover, for each one the tested cases, the mesh sensitivity analysis has been developed to assess the effects of the spatial discretization. This is a key aspect of the analysis; indeed, as defined for the uncertainty assessment (see Chapter 5), when the mesh depending analysis runs the numerical noise can influence the findings from that analysis. To deal with this noise, and in order to avoid its influence in the results, it is mandatory to perform both the pure towing and the self-propulsion tests with the same grid refinement.

Based on these characterizations, current section deals with the assessment for a numerical set-up to run all the self-propulsion experiences with a sustainable computational effort and in accordance with the desired level of accuracy, while remaining consistent with the target for this research; the results and considerations performed for a single propeller can be applied even in cases where two or more propellers are present. Once the set-up has been defined, a repository containing both the EFD results and the CFD calculations can be generated, enabling further analyses of the differences between these two approaches to define the self-propulsion test.

6.1 Actuator disk theory

One of the first theories to define the propeller effects inside the fluid was the actuator disk theory developed by Froude in 1889 [145]. This approach is founded on the change in momentum and the following hypothesis are considered: the friction in the fluid is neglected, the propeller is modelled through an actuator disk which gives the same propeller trust (without any rotational component), seen as a constant acceleration all over the disk surface, and lastly, the inflow and the outflow regions are located at an infinite distance far from the disk, respectively.

The propeller load coefficient (C_T) can be assessed through the actuator disk theory; the physical formulation for this non-dimensional coefficient is reported in equation (144), as follows:

$$C_T = \frac{T}{\frac{1}{2}\rho\left(\frac{\pi D^2}{4}\right)V^2}\ [adim] \tag{144}$$

where, D and T represent the propeller diameter and thrust, respectively, while V stands for the undisturbed flow speed. Therefore, the C_T coefficient represents the non-dimensional thrust T from the propeller.

Based on the coefficient, it is possible to define the mean flow velocity at the propeller disk (V_D) through equation (145), as follows:

$$V_D = V(1+a)\ [m/s] \tag{145}$$

where, a represent the increase for the speed, even called as induced velocity, and can be evaluated as reported by equation (146), as follows:

$$a = \frac{1}{2}\left(1 - \sqrt{1 + C_T}\right)\ [adim] \tag{146}$$

Based on this finding, it is possible to define a mathematical function to link the induct velocity to the propeller load coefficient, which, thereby, depends on the inflow velocity. This is a theoretical approach used to connect the thrust with the speed in the propeller disk area. In following paragraphs, the velocity within the propeller disk position is assessed based on the virtual disk approach, founded on the body force method, wherein the value for the thrust is applied in the computational domain at the propeller region to define the resulting flow field.

6.2 Numerical self-propulsion with virtual disk

In this paragraph, the procedure to define the self-propulsion coefficients (i.e. wake fraction and thrust deduction) is presented.
When the hull runs under the effects of a propeller, an increase in the drag resistance is experienced by the hull. The thrust deduction factor $(1-t)$ can be evaluated as reported by equation (147):

$$(1-t) = \frac{R_T - F_D}{T}\ [adim] \tag{147}$$

where, R_T represents the towing drag and F_D (or SFC) is the Skin Friction Correction; this correction can be experienced through the ITTC procedure 7.5-02-03-01.1 [143], as reported by equation (148):

$$F_D = \frac{1}{2}\rho_M V_M^2 S_M [C_{FM} - (C_{FS} + \Delta C_F + C_A)]\ [N] \tag{148}$$

where, the ΔC_F represents the Roughness allowance. It can be experienced through the ITTC procedure 7.5-03-03-01 [146], as reported by equation (149):

$$\Delta C_F = 0.044\left[\left(\frac{k_S}{L_{WL}}\right)^{\frac{1}{3}} - 10 \cdot (R_e)^{-\frac{1}{3}}\right] + 1.25 \cdot 10^{-4}\ [adim] \tag{149}$$

where, k_S stands for the hull surface roughness and can be fixed at the ITTC recommended value $k_S = 150 \cdot 10^{-6}\ [m]$, if no experimental evaluation is available.

The wake fraction coefficient $(1-w)$ represents the mean velocity field (V_A), evaluated in the propeller plane during the self-propulsion experience. This coefficient can be experienced as reported by equation (150):

$$(1-w) = \frac{V_A}{V_S}\ [adim] \tag{150}$$

where, V_S stands for the ship speed. The coefficient $(1-\mathrm{w})$ evaluated through this procedure differs from the one experienced by the pure towing tank test; this difference is directly connected with the interaction among the hull and the propeller. Moreover, the propeller working behind the hull represents an additional challenge to be addressed because of the presence for a non-uniform inflow; indeed, when comparing the results obtained by the self-propulsion experience with the one characterized by an average flow, the functioning for the propeller is not perfectly equivalent, as reported by Gaggero et al. [147]. To account for this discrepancy, the relative rotation efficiency coefficient (η_R) is used. This coefficient can be experienced through the ITTC procedure 7.5-03-03-01 [146], as reported by equation (151):

$$\eta_R = \frac{K_{Q,OW}}{K_Q} = \frac{K_T}{K_{T,OW}}\ [adim] \tag{151}$$

where, $\mathrm{K_{Q,OW}}$, $\mathrm{K}_{T,\mathrm{OW}}$ represent the torque and the thrust coefficients experienced through the open-water test, respectively, and $\mathrm{K_Q}$, K_T the same coefficients defined through the self-propulsion experience. The interaction among the hull and the propeller can be experienced even through the hull efficiency (η_H), as reported by equation (152):

$$\eta_H = \frac{R_T \cdot V}{T \cdot V_A} = \frac{1-t}{1-w_T}\ [adim] \tag{152}$$

Once the open water (η_O), the hull (η_H) and relative rotation (η_R) efficiencies have been experienced, it is possible to compute the behind hull (η_B) and the propulsive (η_D) efficiencies, respectively define by equations (153), (154):

$$\eta_B = \eta_R \eta_O\ [adim] \tag{153}$$

$$\eta_D = \eta_B \eta_H\ [adim] \tag{154}$$

With the respect to the numerical evaluation for wake fraction and the thrust deduction coefficients, their values can be defined through a Four STeps Procedure (FSTP), developed as reported by Figure 118.

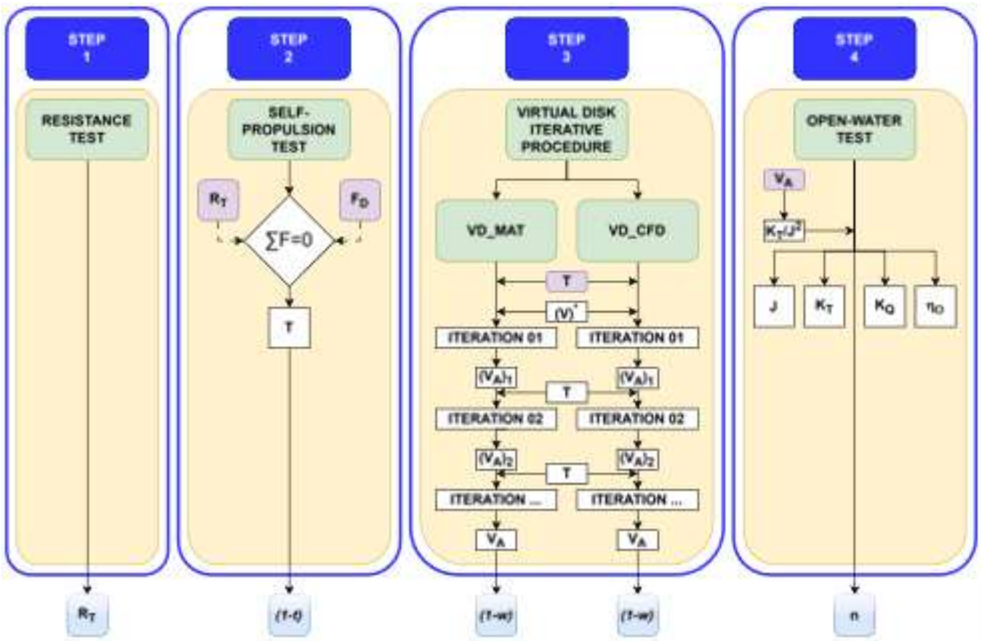

Figure 118: FSTP flow-chart, numerical self-propulsion procedure.

<u>*FSTP Step1*</u>

A pure towing simulation has to be performed in order to assess the R_T value, based on DSUP numerical set-up, but with a particular refinement. Indeed, a pair of cylindrical refinements across the propeller region must be designed in accordance with the characteristics described in FSTP Step 2.

<u>*FSTP Step 2*</u>

Based on the force equilibrium, considering the findings from the step 1 and once the Skin Friction Correction has been evaluated, it is possible to perform another simulation in a self-propulsion configuration to compute the thrust value, and therefore the thrust deduction, as stated by equation (147). Indeed, at each iteration, the recorded value for the model advance resistance, corrected by the Skin Friction Correction as reported by equation (148), has to be compared with the momentum sources from the actuator disk (analogous considerations can be exerted to the torque, if considered). As the equilibrium is obtained, it is possible to assess the thrust value, and therefore, the thrust deduction factor $(1 - t)$. Considering the numerical virtual disk, the propeller effects are replaced by volumetric body forces laying in the same place where the propeller works. Because of the absence for the propeller geometries, it is not required a specific topology for the mesh to model the blades, but a cylindrical refinement region has to be design. As reported in Figure 119a, this region is positioned across the propeller position and the following two different cylindrical refinements lay inside it: the first (dark blue) is positioned across the virtual disk place (the traces for the volumes where the forces acting in the domain are represented by red spheres) and the second one (light blue) in the remaining part, as depicted by Figure 119b. More in details, considering the reference mesh, these two refinements present a hierarchical higher resolution, as distance from the virtual disk place decrease, as displayed by Figure 119c. These refinements are the same of the ones implemented in FSTP Step 1 to eliminate possible variations in results induced by a mesh refinement change. The force acting in the volumes inside the virtual disk region have to be known before the simulation, or alternatively, they can be assessed through the equilibrium condition in the simulation itself. As reported by Villa et al. [148], the values for the forces do not depend on any flow solution and a steady state solution to the problem is expected.

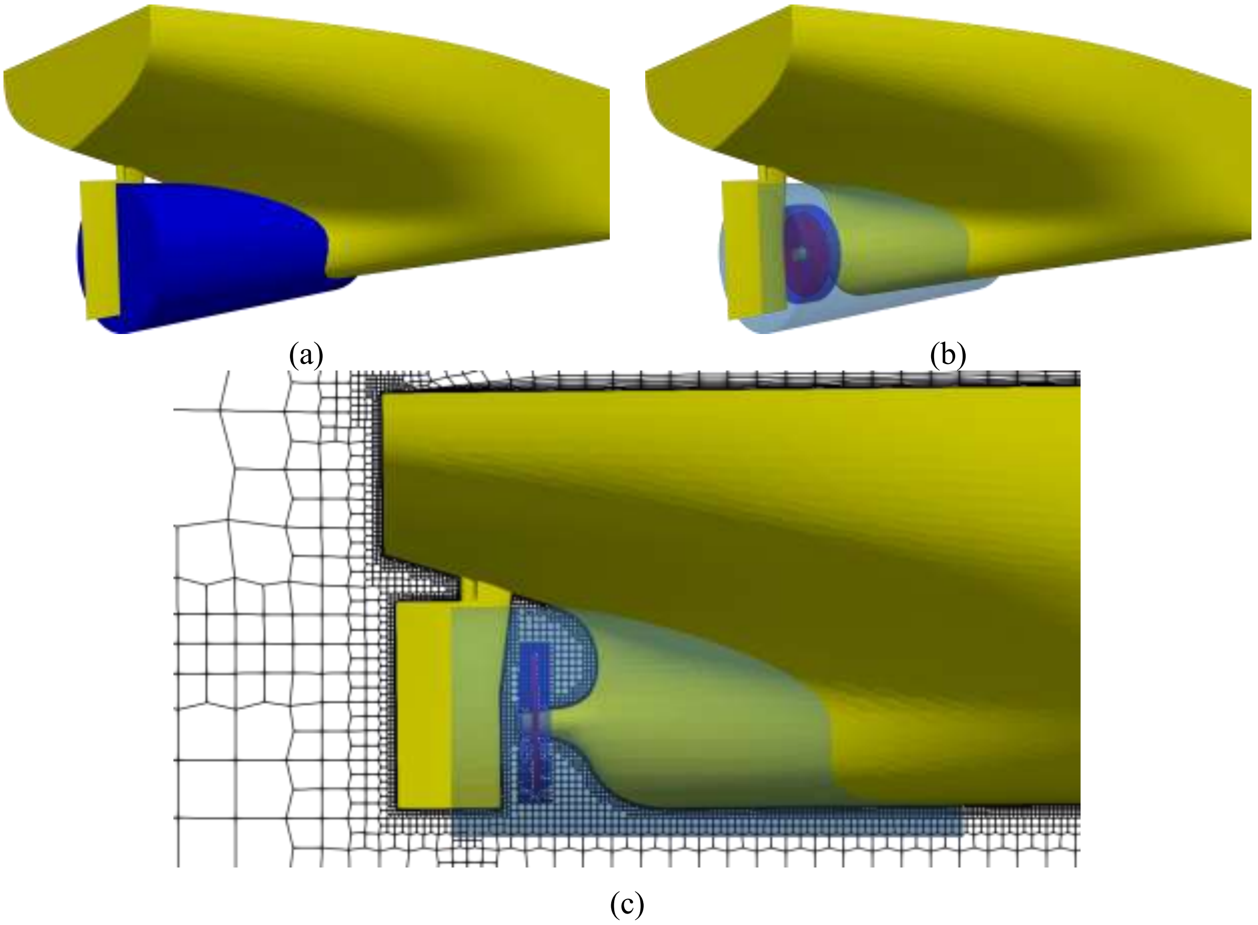

Figure 119: self-propulsion mesh for Hull 19, refinement across the propeller position (a) with its details (b) and the mesh resolution on the longitudinal plane (c).

<u>*FSTP Step 3*</u>

In the towing tank self-propulsion experimental procedure, the model runs at fixed speed, where the propeller revolution rate is varied until the longitudinal equilibrium between the hull resistance and the propeller thrust is obtained, and therefore, it is possible to compute directly the revolution rate (n). While, with the respect to the wake fraction, an iterative procedure has to run to deal with the self-inducted speed for the propeller.

The advance coefficient (J), defined as reported by equation (155):

$$J = \frac{V_a}{nD} \; [adim] \tag{155}$$

can be experienced through the interpolation procedure based on both the open-water curve for that propeller, and the thrust coefficient (K_T), as defined by equation (156):

$$K_T = \frac{T}{\frac{1}{2}\rho n^2 D^4} \; [adim] \tag{156}$$

In this kind of non-dimensional representation, the torque coefficient (K_Q) and the propeller open-water efficiency (η_O) can be addressed as reported by equation (157) and (158), respectively:

$$K_Q = \frac{Q}{\frac{1}{2}\rho n^2 D^5} \; [adim] \tag{157}$$

$$\eta_O = \frac{J}{2 \cdot \pi} \cdot \frac{K_T}{K_Q} \; [adim] \tag{158}$$

With the respect to the numerical procedure to perform a self-propulsion test with the virtual disk approach, an iterative procedure is required as the revolution rate for the propeller is unknown. This iterative procedure accounts for the wave fraction evaluation and can be exerted in two different ways, as follows: by applying the virtual disk theory (Virtual Disk Mathematical, later on called as VD_MAT being based on the pure actuator disk theory) or by considering a new type of simulation where the body force method is implemented inside a new computational domain where only the body forces act (Virtual Disk CFD, later on called as VD_CFD). Both of the models use as first guess parameter the model advance speed $(V)^*$ to perform the first iteration, where all the parameters to let the equations (145), (146), and (147) working are known from the previous steps. In the second step, the guess value is replaced by the $(V_A)_1$, which coincides with the speed computed inside the disk (V_D), as reported by equation (146), and considering again the value for the thrust a new value for the speed inside the disk can be evaluated and considered as the guess value for the following iteration, and so on for the other iterations. In less than six iterations, it is possible to define the wake fraction $(1 - w)$. With the respect to the advance speed, and based on SP-NTS case with 3.756M cells, Figure 120 displays how fast both the virtual disk theory (red plot and markers) and the CFD virtual disk (blue plot and markers) rapidly converge compared with the experimental value.

FSTP Step 4

Once the thrust deduction and the wake fraction coefficients are known, it is possible to move to the last step in order to define the revolution rate for the propeller. In this case, the open-water curves are used but an auxiliary variable (K_T/J^2), as defined by equation (159), has to be defined in order to overcame the lack of the knowledge about the revolution rate.

$$\frac{K_T}{J^2} = \frac{T}{\frac{1}{2}\rho V_A^2 D^2} \; [adim] \tag{159}$$

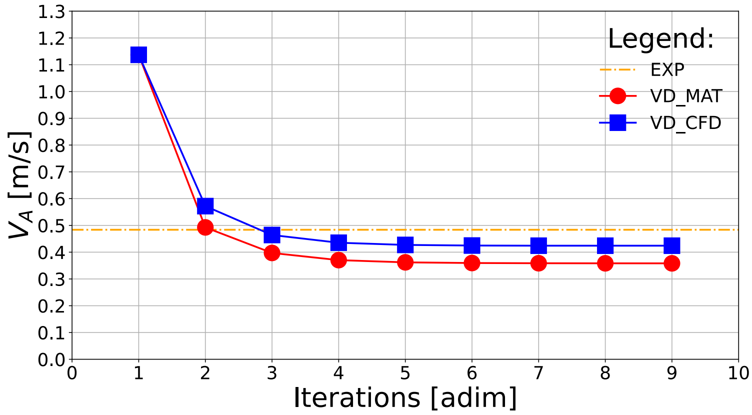

Figure 120: advance speed evaluation through the virtual disk theory for SP-NTS case with 3.756M cells.

Once this variable has been computed, it is possible to define the intersection among this variable and the thrust coefficient from the open water curves, as reported by Figure 121a with the respect to the propeller for Hull 19, as example. Based on the intersection, it is possible to define a vertical line corresponding to the equilibrium advance coefficient (J_{EQ}) and to compute the remaining coefficients $(K_Q,\ \eta_O)$ from the open-water curves, as reported by Figure 121b.

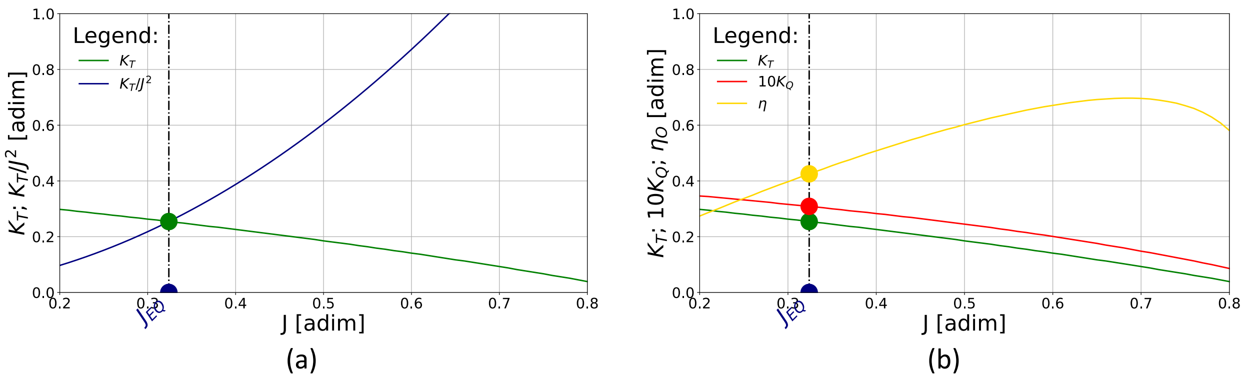

Figure 121: propeller open water curves for Hull 19; thrust coefficient and auxiliary variable (a) and all open-water parameters (b).

Finally, considering equation (155), it is possible to define the revolution rate for the propeller.

6.3 Test-cases and results

The numerical self-propulsion study has run for one speed of Hull 19. This study has been performed considering different approaches to assess the wake fraction and the thrust deduction coefficients and finally the revolution rate for the propeller. In this scenario, Table 38 summarizes the pure towing numerical experiences (RT-S, RT-NS). Each one of the simulations has its own alphanumeric identifier; indeed, the last part of the labels employes an alphabetical convention, moving from the coarser mesh (identified with "_A") to the finer one (which is represented by the letter closest to the "Z"). More in details, the "Symmetry" column identifies the domain characteristic for the simulations.

Table 38: towing cases.

Case ID	Cell [M]	Relative Size	Symmetry
RT-S_A	1.014	2.440	Y
RT-S_B	1.608	2.092	Y
RT-S_C	2.600	1.782	Y
RT-S_D	4.860	1.447	Y
RT-S_E	6.252	1.330	Y
RT-S_F	7.512	1.251	Y
RT-S_G	14.722	1.000	Y
RT-NS_A	1.014	1.949	N
RT-NS_B	1.609	1.671	N
RT-NS_C	2.601	1.424	N
RT-NS_D	4.861	1.156	N
RT-NS_E	6.253	1.063	N
RT-NS_F	7.508	1.000	N

With the respect to the self-propulsion cases (SP-NTS, SP-NTNS, SP-TNS), Table 39 describes all the tested configuration, as follows: the "Thrust", "Torque" and "Symmetry" columns define the numerical set-up variations, while the other columns define both the mesh refinement and the labelling convention (as implemented in Table 38 cases). For the purpose of technical transparency, in cases where the symmetry condition is enforced, the torque is assumed to be identically zero in order to ensure the physical consistency and correctness of the problem formulation.

Table 39: self-propulsion cases.

Case ID	Cell [M]	Relative Size	Thrust	Torque	Symmetry
SP-NTS_A	1.014	2.440	Y	N	Y
SP-NTS_B	1.608	2.092	Y	N	Y
SP-NTS_C	2.406	1.829	Y	N	Y
SP-NTS_D	4.860	1.447	Y	N	Y
SP-NTS_E	6.252	1.330	Y	N	Y
SP-NTS_F	7.512	1.251	Y	N	Y
SP-NTS_G	14.722	1.000	Y	N	Y
SP-TNS_A	1.014	1.834	Y	Y	N
SP-TNS_B	1.690	1.547	Y	Y	N
SP-TNS_C	2.601	1.340	Y	Y	N
SP-TNS_D	4.861	1.088	Y	Y	N
SP-TNS_E	6.253	1.000	Y	Y	N
SP-NTNS_A	1.014	1.949	Y	N	N
SP-NTNS_B	1.609	1.671	Y	N	N
SP-NTNS_C	2.601	1.424	Y	N	N
SP-NTNS_D	4.861	1.156	Y	N	N
SP-NTNS_E	6.253	1.063	Y	N	N
SP-NTNS_F	7.508	1.000	Y	N	N

All these simulations have run considering the mesh variation and the type of numerical approach to describe the numerical set-up for the virtual disk. Moreover, as described for the uncertainty assessment (see Chapter 5), changing the mesh, the result can change and therefore, in order to achieve a properly defined comparisonal environment, the simulations have run with the same different mesh refinements.

A first comparison can be defined based on the simulations for the FSTP Step1. As reported by ITTC guideline 7.5-03-02-04 [112], even if the symmetry condition reduces the grid size by half, it is recommended to run simulations with all the domain. In this phase, a comparison among the same simulation has run considering the symmetry condition (RT-S) and later on neglecting it (RT-NS). Considering the ΔR_T value as defined by equation (160), it is possible to plot the results obtained for RT-S and RT-NS conditions and compare them.

$$\Delta R_T = \frac{R_{T-CFD}}{R_{T-EFD}} - 1\ [\%] \tag{160}$$

As plotted in Figure 122a, the half-filled circular markers stand for the RT-S results, while the filled ones represent the RT-NS results; a general common trend can be identified, and this can be considered as the trace for the numerical noise which affects both the conditions in the same manner. This noise can be properly identified through the difference among the results, as reported by equation (161):

$$(\Delta R_{TM})_{CFD} = (\Delta R_{TM})_{RT-S} - (\Delta R_{TM})_{RT-NS}\ [N] \tag{161}$$

Indeed, by considering the variation varying the mesh size, it is possible to identify a variation among the results within the range ±2% of the experimental value, as reported by Figure 122b. This range is compliant with the scatter in results experienced in the mesh sensitivity analysis performed in the uncertainty analysis.

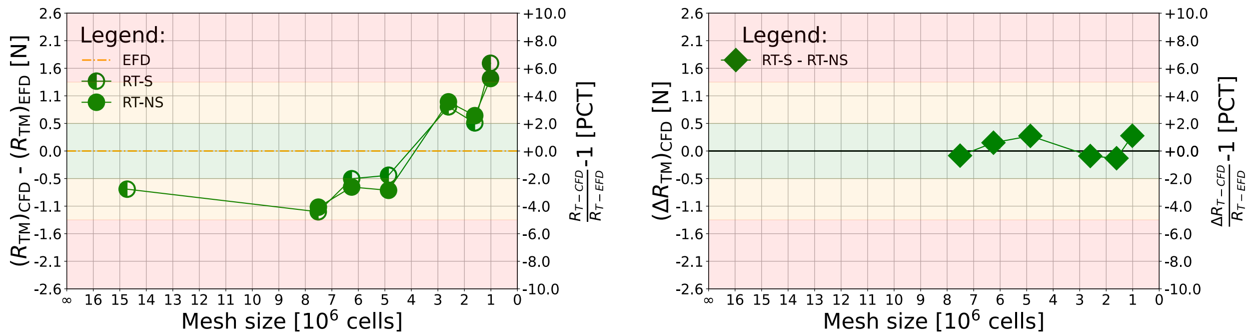

(a) (b)

Figure 122: mesh sensitivity analysis for RT-S (half-circle marker) and RT-NS (solid-circle marker) cases (a) along with the differences among them (b).

Therefore, an equivalence in results has been established with the respect to the symmetry condition applied to assess the advance resistance; moreover, since the mesh dimension is exactly the half, the computational effort decreases as the symmetry condition is implemented. Another important issue to be considered is the mesh refinement. In the FSTP procedure, the hull has to be tested into two different conditions: pure towing and self-propulsion. In order to get comparable results, the mesh has to be exactly the same for both the simulations; indeed, the numerical set-up is the one defined in

Chapter 2, but an additional refinement has been implemented as reported in FSTP Step 2, and applied in both the simulations.

Secondly, three different conditions for the virtual disk have been investigated to define if it is possible to get an accurate enough result with a lower computational effort; among them, the SP-NTS requires the lowest computational effort; indeed, theoretically, it is approximately half that of the other two, which presents practically the same computational effort. For SP-NTS, the absence for the torque it is mandatory and if the results return comparable values, it is possible to consider this set-up as the one to run all the simulations. As reported by FSTP Step 2, the output from this phase consists in the thrust deduction factor estimation considering equation (147), where the R_T value represents the towing drag and it comes from the FSTP Step 1. Based on findings for the mesh sensitivity analysis for the pure towing, it is important to define the $(1-t)$ value based on the same mesh characteristic in order to replicate the same noise for the mesh. As an example, considering the RT-S and SP-NTS cases, it is possible to assess the $\Delta(1-t)$, as defined by equation (162):

$$\Delta(1-t) = \frac{(1-t)_{CFD}}{(1-t)_{EFD}} - 1 = \frac{\frac{R_T - F_D}{T}}{(1-t)_{EFD}} - 1 \; [\%] \tag{162}$$

Based on the different numerical available set-up for the self-propulsion experience (SP-NTS, SP-NTNS, SP-TNS), it is possible to account for different ways to get the $1-t$ values. Indeed, if the same F_D value can be addressed as reported in equation (148), a reference R_T value cannot be addressed. More in details, if the mesh changes, the results vary accordingly and therefore, among all the available combinations of the pure towing and the self-propulsion it has to be considered only the corresponding one. In this scenario, when considering the R_T values from the RT-S simulations with the T values from SP-NTS, 7x7 different combinations can be addressed, as reported in Table 40. Among the available combinations, only the boldface ones and laying on the descend diagonal are representative of a fair comparison under same mesh condition.

Table 40: SP-NTS case, evaluation for the thrust deduction factor.

		T							
		SP-NTS_A	**SP-NTS_B**	**SP-NTS_C**	**SP-NTS_D**	**SP-NTS_E**	**SP-NTS_F**	**SP-NTS_G**	
R_T	**RT-S_A**	**-4.00%**	-5.91%	-0.59%	8.25%	8.54%	13.24%	11.96%	
	RT-S_B	-10.83%	**-12.60%**	-7.66%	0.56%	0.83%	5.19%	4.00%	
	RT-S_C	-8.99%	-10.80%	**-5.76%**	2.63%	2.90%	7.35%	6.14%	
	RT-S_D	-16.82%	-18.47%	-13.86%	**-6.20%**	-5.95%	-1.88%	-2.99%	
	RT-S_E	-17.22%	-18.86%	-14.28%	-6.65%	**-6.40%**	-2.36%	-3.46%	
	RT-S_F	-21.01%	-22.57%	-18.20%	-10.92%	-10.68%	**-6.82%**	-7.87%	
	RT-S_G	-18.41%	-20.03%	-15.51%	-8.00%	-7.75%	-3.76%	**-4.85%**	
		1.014	1.608	2.406	4.860	6.252	7.512	14.722	**M. Cells**

When considering a RT-NS pure towing test, the same considerations also apply to the SP-NTNS and SP-TNS cases, and the differences recorded on a case-by-case basis with the respect to the experimental value can be plotted as reported by Figure 123.

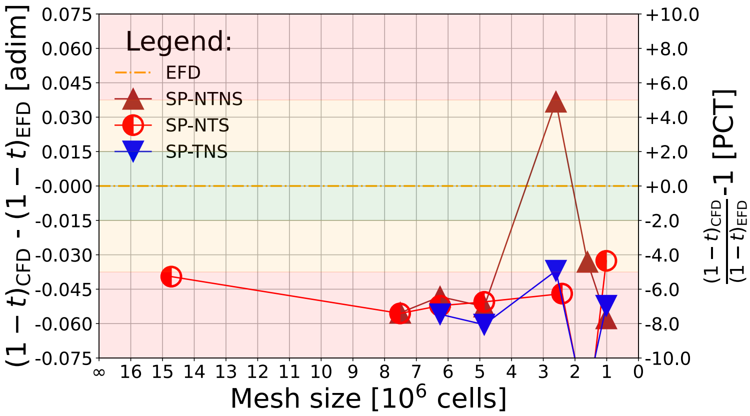

Figure 123: thrust deduction factor based on SP-NTS, SP-NTNS and SP-TNS cases.

When comparing the same mesh discretization in the pure towing and in the self-propulsion tests, the numerical noise vanishes. Except for two cases with a total number of cells lower than 2 million cells for all the numerical domain, all the thrust deduction factor results lay in the range $-8\% \div +5\%$ of the experimental value and except for one case, the CFD tends to underestimate the $(1-t)$ value, when compared with the experimental value. With the respect to the Figure 124, and considering the SP-TNS_E case, a representation about the flow field can be obtained; more in details, Figure 124a gives the 3D general overview (without the free-surface to better appreciate the streamlines) and Figure 124b the longitudinal section for the case.

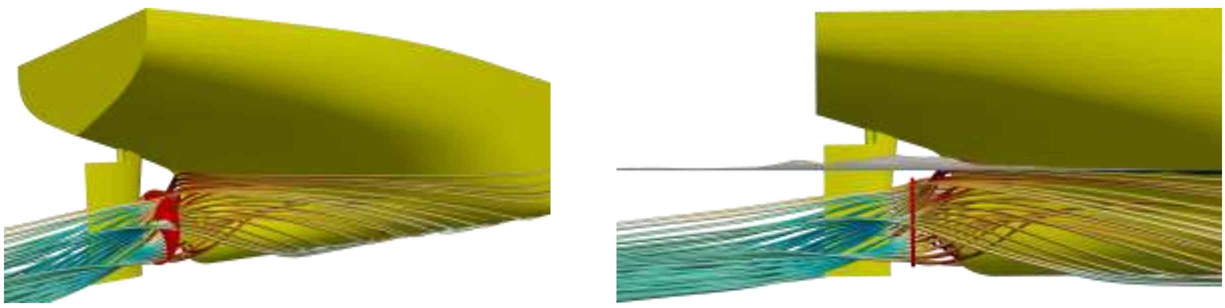

(a) (b)

Figure 124: SP-TNS_E case 3D view without the free surface to better describe the streamlines (a) and a longitudinal section with the free surface and the streamlines (b).

When dealing with the wake fraction, it is possible to assess its value based on two different procedures, as detailed in FSTP Step 3. Among the two procedures, the numerical one (VD_CFD) has been selected. This procedure has run for four different cases, as follows: SP-NTS_F, SP-TNS_C, SP-TNS_E and SP-NTNS_F. For each one of the cases, identified by both the case and the number of cells in the meshes, 6 different simulations have been performed. By considering both the thrust value obtained by the FSTP Step 2 and the advance speed the SP-TNS_E case, it is possible to move

to FSTP Step 3. With the advance speed value form the SP-TNS_E case considered as the guess velocity $(V)^*$ for the virtual disk, the first iteration can run in order to define the advance velocity $(V_A)_1$ to be used as the candidate velocity for the second iteration. The first iteration results are plotted inside Figure 125. All the images exhibit a representation for the speed based on colormap scale coherent with the Figure 125a; the streamlines representation Figure 125(HistoryIT---a), the longitudinal Figure 125(HistoryIT---b) and the transversal velocity Figure 125(HistoryIT---c) fields are displayed changing the "---" value based on the following step-iterations: 0 (initial), 20, 40, 80, 200 and 500 (final, where the convergence for the simulation has been achieved).
The simulation has run for a total number of iterations equal to 500-time steps; within this range, the convergence has been achieved. In order to define if the convergence occurs, it is possible to consider the advance resistance (R_T) offered by the shaft line, expressed in dimensionless form as given by (163):

$$\frac{(R_T)}{(R_T)_{MEAN}} - 1\ [\%] \tag{163}$$

where, the $(R_T)_{MEAN}$ represents the mean value evaluated within the range $200 \div 500$ iterations.
Once the first iteration has run, it is possible to define the $(V_A)_1$ value, and therefore, to move to the second iteration. Therefore, $(V_A)_1$ is used as the candidate for the iteration 2, and another simulation can run with the same numerical set-up by updating the initial velocity accordingly; this iterative procedure can run for the third, fourth, fifth, and so on simulations. Figure 126 displays the results obtained for all the iterations; more in details, the velocity streamlines are reported in the figures identified by "(Iteration---a)", whereas the longitudinal "(Iteration---b)" and the transversal velocity "(Iteration---c)" fields are displayed changing the "---" value based on the following iteration number. At the end of the last iteration, it is possible to identify the advance velocity, and therefore, the wake fraction for the self-propulsion numerical experience. With the respect to the SP-NTS_F, SP-TNS_C, SP-TNS_E and SP-NTNS_F cases, the results obtained for both the wake fraction (considering both the body force method, as experienced through the VD_CFD approach, and the actuator disk method, as experienced through the VD_MAT approach, considered as a literature-based reference solution used solely for comparison purposes) and the thrust deduction factors are summarized in Table 41.
When these differences are plotted together, possible correlations among results and observed trends can be investigated. With the respect to the four cases, and considering the differences from the experimental values for both the propulsion coefficients $\Delta(1-t)$, $\Delta(1-w)_{VD\_MAT}$, $\Delta(1-w)_{VD\_CFD}$ and the advance speed $\Delta(V_A)_{VD\_MAT}$, $\Delta(V_A)_{VD\_CFD}$, it is possible to get the results displayed by Figure 127.

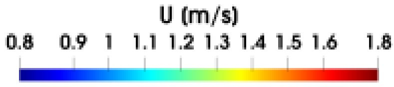

(a)

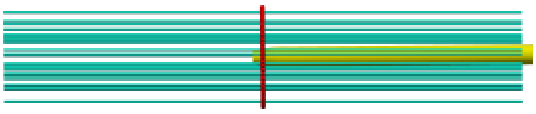

(HistoryIT0a)

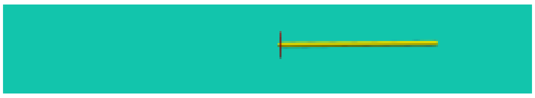

(HistoryIT0b)

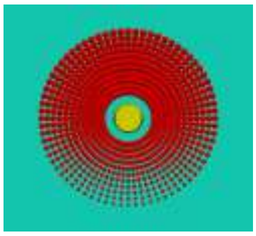

(HistoryIT0c)

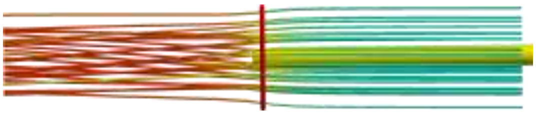

(HistoryIT20a)

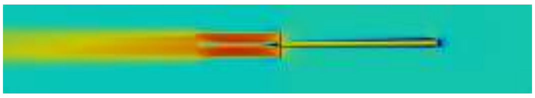

(HistoryIT20b)

(HistoryIT20c)

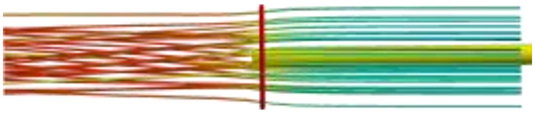

(HistoryIT40a)

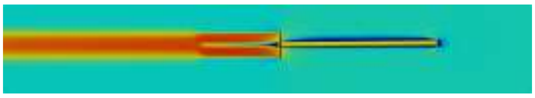

(HistoryIT40b)

(HistoryIT40c)

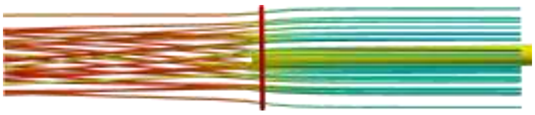

(HistoryIT80a)

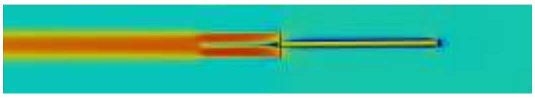

(HistoryIT80b)

(HistoryIT80c)

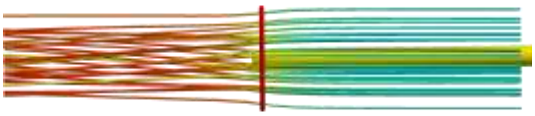

(HistoryIT200a)

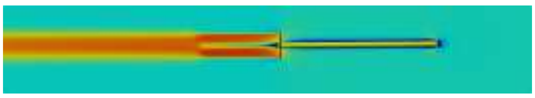

(HistoryIT200b)

(HistoryIT200c)

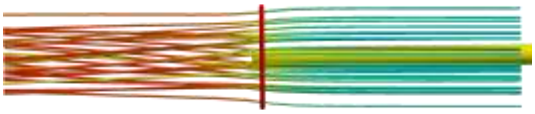

(HistoryIT500a)

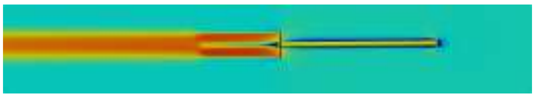

(HistoryIT500b)

(HistoryIT500c)

Figure 125: FSTP Step 3 iteration 1, wake fraction evaluation for SP-TNS_E case with a virtual disk (represented by the red dots) applied on the shaft line (yellow axis); velocity field scale (a), longitudinal stream lines representation (HistoryIT---a), longitudinal velocity field (HistoryIT---b) and transversal section representing the velocity field (HistoryIT---c).

(a)

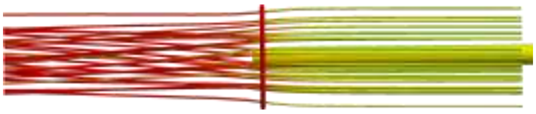

(Iteration1a)

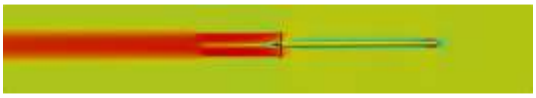

(Iteration1b)

(Iteration1c)

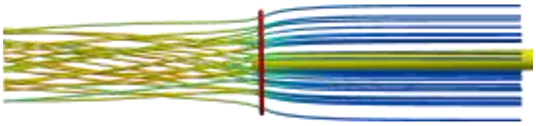

(Iteration2a)

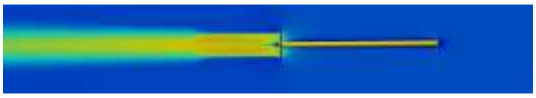

(Iteration2b)

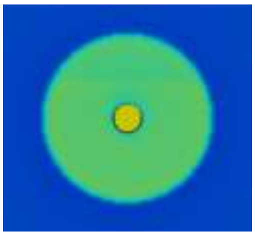

(Iteration2c)

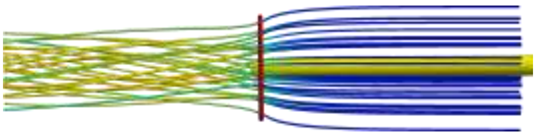

(Iteration3a)

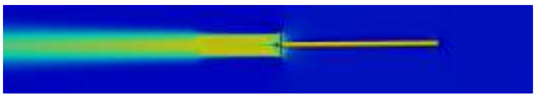

(Iteration3b)

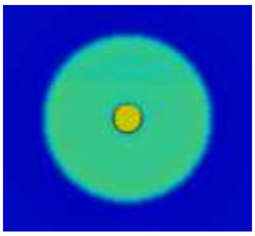

(Iteration3c)

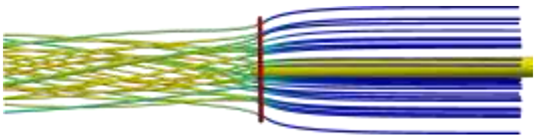

(Iteration4a)

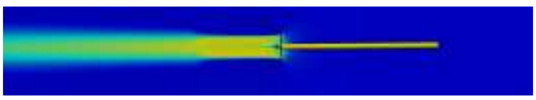

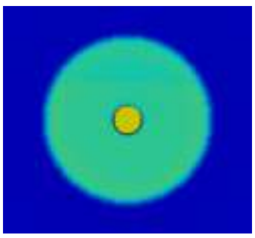

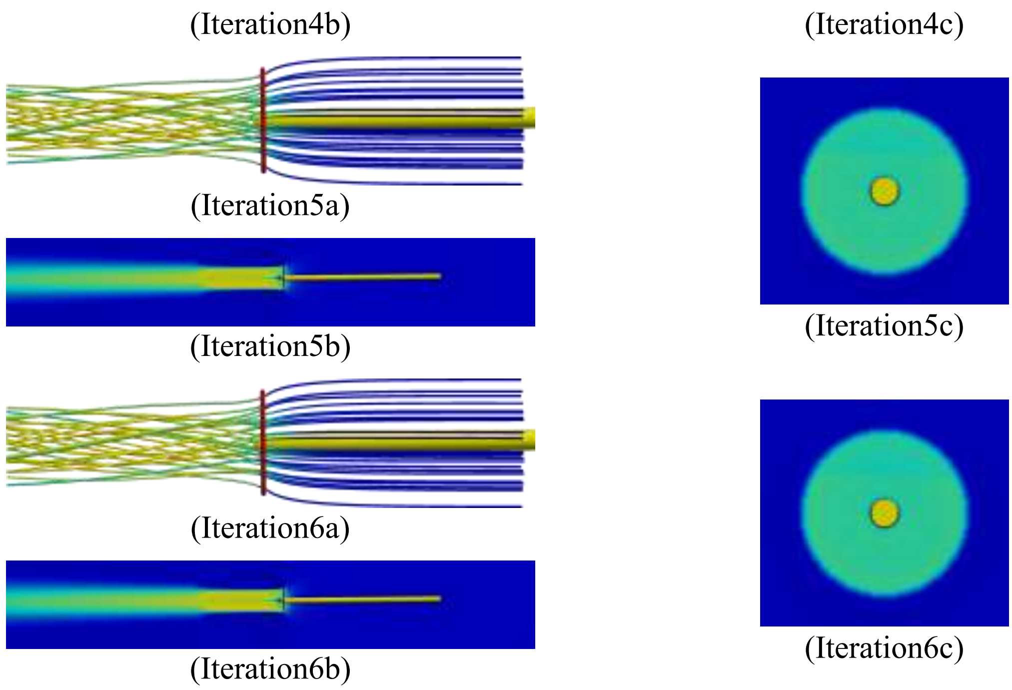

Figure 126: FSTP Step 3 iterations form 1 to 6, wake fraction evaluation for SP-TNS_E case with a virtual disk (represented by the red dots) applied on the shaft line (yellow axis); velocity field scale (a), longitudinal stream lines representation (Iteration ---a), longitudinal velocity field (Iteration ---b) and transversal section representing the velocity field (Iteration ---c).

These data allow the following conclusions: when the numerical set-up has changed among the three proposed, the thrust deduction factor exhibits a low scatter in results and therefore the proposed numerical set-up can be considered as equivalent. By contrast, when considering the wake fraction (and therefore the advance speed) a scatter in result is observed, reaching up to twice the value, but a clear trend hasn't identified. Additionally, the VD_MAT approach shows a larger deviation from the experimental data than the VD_CFD one, and by considering the mean difference with the experimental value, the values of -13.88% and -11.04% have been experienced, respectively. This means that a mean difference of 2.84% has been recorded among the two approaches.

Nevertheless, based on the findings from FSTP Step 3, it is possible to move to the last step of the FSTP in order to identify the revolution rate for the propeller. Adhering to the FSTP Step 4, the auxiliary variable (K_T/J^2) has been introduced, as defined by equation (159), in order to identify the value for the equilibrium advance coefficient $\left(J_{EQ}\right)$ on the open-water curves. Later on, the values for K_T, K_Q and η_O coefficients have been experienced. Moreover, based on equation (155), it is possible to evaluate the revolution rate. With the respect to the four cases analyzed, the recorded differences from the open-water parameters have been summarized in Figure 128. Even in this case, the VD_CFD approach results in a lower deviation from the experimental value than the VD_MAT method. Additionally, among the tested numerical set-up, the SP-NTNS_F one experienced always the lower deviation from the experimental value and a clear trend hasn't been identified.

Table 41: numerical self-propulsion experience, results for the propulsion coefficients.

Case ID	Cell [M]	$\frac{(1-t)_{CFD}}{(1-t)_{EFD}}-1$ [%]	$\frac{(1-w)_{VD\_MAT}}{(1-w)_{EFD}}-1$ [%]	$\frac{(1-w)_{VD\_CFD}}{(1-w)_{EFD}}-1$ [%]
SP-NTS_F	7.512	-6,78%	-10,33%	-7,05%
SP-TNS_C	2.601	-4,54%	-10,91%	-8,24%
SP-TNS_E	6.253	-6,86%	-18,40%	-16,46%
SP-NTNS_F	7.508	-6,82%	-15,89%	-12,43%

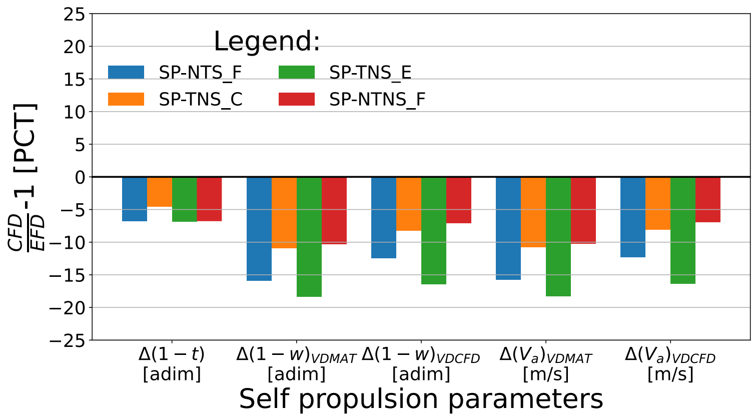

Figure 127: PSTP Step 3, results for both the propulsion coefficients $\Delta(1-t)$, $\Delta(1-w)_{VD\_MAT}$, $\Delta(1-w)_{VD\_CFD}$ and the advance speed $\Delta(V_A)_{VD\_MAT}$, $\Delta(V_A)_{VD\_CFD}$.

While, as reported by Figure 129, when the revolution rate has been considered a smaller difference occurs by comparing the numerical with the experimental data. Even in this case similar considerations can be derivate from the VD_MAT approach and the VD_CFD except for the SP-TNS_C case; in this particular case, the cell count (2.6M) is halved compared to the other cases (the cells are at least 6.2M), and therefore it may indicate a lack of accuracy for the solution.

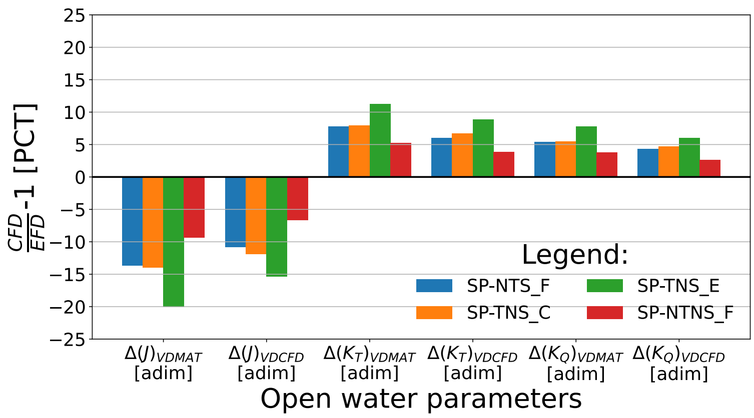

Figure 128: PSTP Step 4, results for open water parameters.

Moreover, considering the VD_CFD approach and the results from the SP-NTS_F, SP-TNS_E and SP-NTNS_F approaches, it can be established that all results fall within the range $\pm 2\%$ of the experimental value; while the SP-TNS_C case gives the higher difference, but this difference (4.33%) may be connected with a discretization issue and the results is considered as an outlier when compared with the other results.

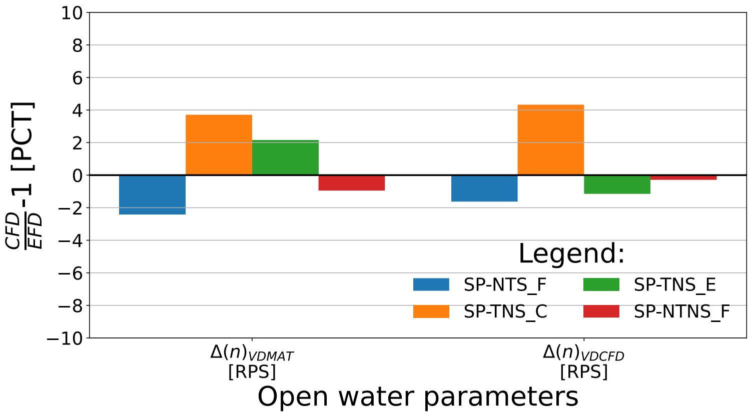

Figure 129: PSTP Step 4, revolution rate for the propeller.

Therefore, the revolution rate analysis shows only marginal variations across the considered numerical set-up, provided that a suitable discretization is used.

6.4 Self-propulsion conclusions

The propulsion coefficients can be experienced through the experimental approach and the numerical one. This first analysis about the numerical self-propulsion demonstrates the opportunity to assess the value for the propulsion coefficients. A numerical procedure based on 4 points was developed and it is referred to as FSTP; more in details this procedure requires a pure towing test and a self-propulsion experience to assess the thrust deduction factor, later on an iterative procedure based on a particular set-up it allows the wake fraction knowledge to be acquired and finally based on the open-water curves the revolution rate can be experienced. Several simulations have been performed considering three different set-ups as, follows: SP-NTS, SP-TNS and SP-NTNS. Based on the results from these simulations, the following conclusions can be argued:

- discretization of both the domain and the propeller position is crucial; if the discretization is row, results cannot be considered as reliable;
- with the respect to the thrust deduction factor, by changing the numerical set-up a small difference in results has been recorded;
- the VD_MAT approach differs from the VD_CFD by a factor close to 3%; furthermore, VD_CFD approach is closer to the experimental data;
- even if numerical results for the wake fraction coefficient differs more than 10% with the experimental value, the evaluation for the propeller revolution rate lays within the range of ±2% of the experimental value for all the numerical approaches.

Therefore, given the small discrepancies recorded, it is possible to conclude that the numerical self-propulsion can be experienced through the SP-NTS approach. Based on this numerical set-up, later on considered as the reference numerical-set for the self-propulsion issue, further investigation can be carried out considering several types of hulls tested at different speed. Once all the results are available, it will be possible to perform a statistical study about the differences among the numerical results compared with the experimental ones, in order to define any possible correlation among the propulsion coefficient and the speed, the type of vessel and the hydrodynamical parameters, similarly to the pure towing comparisonal analysis.

7 Conclusions

In the second half of last century, the first computer displayed a new kind of technology. Following the increase for the computational capabilities, the Computational Fluid Dynamics (CFD) has progressively gained ground and reliability in many research fields, encompassed the naval architecture one. Over the years the CFD scientific community members defined procedures and codes able to assess the dynamical attitude for a ship and model, replicating the EFD experiences. In order to define if the numerical results were close to experimental ones, different workshop have been organized to firstly compare the different numerical approaches, and later on to compare their results along with the confidence for the results obtained. With the respect to the ways to assess the precision for a calculation, three kinds of approaches have been identified, as follows: *Single Participant To One* (SPTO), *Multiple Participants To One* (MPTO) and *Single Participant To Multiple* (SPTM). Except for the SPTO, which is something used case by case, the MPTO is the typical approach exerted by workshops, while the SPTM is the one implemented in current research. Both the MPTO and SPTM approaches try to give an answer to the question "how precise is a CFD calculation when compared with a EFD experience" but in two different ways. Indeed, several participants submit their works for a few models to be tested in the MPTO approach, while in SPTM one a single numerical set-up has been used to study different hulls tested at different speed.

In order to define the numerical set-up to subsequently perform all the simulations for the SPTM approach, three main driving factors have been considered: the type of code, the precision and the computational cost. The open-source code OpenFOAM has been used in the pre-processing and in the solving phases along with the Paraview suite for the post processing analysis; while, considering the precision, a number of cells close to 2 million for the domain has been assumed adequate to guarantee simulation results consistent with the requested level of accuracy, and finally, based on the available computational resources, 30000 iterations have been considered as the computational limit to achieve the convergence for the simulations. Based on these considerations, a finite volume method with cells centered variables performing for a multiphase physic for two fluids (air and water) considered as immiscible and isothermal has been used inside a numerical domain discretized by unstructured mesh. The volume of fluid approach has been used to model the interface among the two fluids along with a quasi-steady approach. Considering the OpenFOAM environment, the following utilities has been used to generate an unstructured mesh: cfMesh and blockMesh; while, in the solve multiphase flow, the interFOAM solver with the Local Time Step (LTS) option have been used. Moreover, in order to define the dynamical attitude for the model with the respect to the trim and sinkage, a mesh morphing approach has been considered in correspondence of four different check-points; the dynamical and statical buoyancy are compared with the displacement and the new configuration is evaluated for each one the check points. The domain dimensions have been used to customize this numerical set-up because of the presence of a dependency among the noise in signal history with the domain dimensions. Based on this finding, the domain size has been selected, and later on the compliance with the ITTC requirements was demonstrated. More in details, when comparing the defined dimensions with the ITTC ones, the length along the x, y, z axis was found to be 1.66, 3.80, 1.38 times greater, respectively.

In order to define a repository, where the CFD calculations are stored and benchmarked against the EFD results, a workflow procedure has been identified and defined trough the following steps: hull identification, 3D model generation, mesh generation, consistency check, simulation, post processing analysis and data storage. Each point for the procedure represents a pass-no-pass issue to be sure to get a representative repository to carry on further statistical investigations. More in details, the hull identification represents a guarantee that a sufficiently diversified geometries and speed field to perform the comparisons are defined; additionally, to be sure that the described geometries properly represent the physical one, the consistency check enables the same test condition between EFD and CFD. Finally, the data storage phase represents the main core in current research. Indeed, only if a greater enough number of comparisons is available, the statistical analysis can lead to some results.

In current research, 22 different hulls have been tested at different speed; a total number of 142 comparisonal results have been implemented in the statistical and correlational analysis in order to define the precision for CFD calculations, when compared with EFD results. Three types of analysis have been performed, as follows: raw data, test condition and the analysis of the hull parameters influence. Based on these kinds of analysis, the following results have been identified:

- With the respect to the mean value $\left(\overline{\Delta R_{T_M}}\right)$ and the standard deviation (σ) for the raw data, it is possible to assess how the CFD calculations differ from the EFD results. Indeed, considering the variations with signs for the speed, the mean difference obtained from the comparison gives a value of 0.29% along with a standard deviation of 3.62%. Therefore, this means that probability for a CFD calculations to underestimate or overestimate an EFD result is the same, and globally the difference among the two ways to assess the model resistance leads to a difference of ±3.62% in 65% of cases.

- Considering the variations without signs, the mean difference achieved $\left(\overline{\left|\Delta R_{T_M}\right|}\right)$ and its standard deviation (σ) are evaluated in 3.04% and 1.96%, respectively. Therefore, based on this last result, it is possible to get 67% of comparisons in a range lower than 3.04%. Moreover, if the cumulative function is considered, in 50% of the cases the recorded difference does not exceed the 2.81% value and in 82% of cases is within the range $|0 \div 5.00|$%.
- With the respect to the speed variations, a weak trend for the differences has been discovered. Indeed, for the lower speeds, CFD tends to underestimate the EFD results, while considering the higher speed, the opposite tendency has been discovered. By considering the mobile mean approach, the non-dimensional speed corresponding to the shifting from underestimation to overestimation was evaluated to be at $F_r = 0.266$. Based on Pearson's index (0.406), the correlation between differences and speed is quite large and this can lead to a statistical credible relationship.
- When the configuration for the test is considered, nothing remarkable has been found. Indeed, considering the bare and the fully appended configurations, similar results have been achieved.
- When the raw data have been split by the hulls, the statistical analysis accounts for a lower value for the standard deviation compared with the raw data one. In this case, the ΔR_{TM} usually lays only on the overestimation or underestimation fields and the differences recorded among the speed variations are lower than the ones obtained from the raw data analysis. These considerations lead to a possible issue in the 3D generation for the hull geometries.
- With the respect to the analysis of the hull parameters influence like model length, scale factor, ratio length on beam, ratio beam on depth nothing remarkable has been found. While, with the respect to the block coefficient, three clusters in results have been found, and a large positive correlation (Pearsons's coefficient equal to 0.525) has been found, when considering the range $0.8 \leq C_B \leq 0.84$.

It is possible to compare the results from the SPTM with the one form the MPTO approach. Indeed, the finds from this study are in agreement with the Gothenburg 2010 workshop and considering the results from other workshops, similar values are registered.

Each calculation has its own uncertainty, therefore, in order to define how precise is a CFD calculation, the Verification, Validation and Uncertainty assessment $(VVUA)$ has to be performed. The uncertainty assessment (UA) deals with the Verification and the Validation processes, even known as V&V, to account for the numerical and the modelling uncertainty. The Verification phase accounts for the numerical uncertainty assessment (U_{SN}), while the Validation phase combine both the experimental and the numerical uncertainty in order to get UA. With the respect to the numerical uncertainty assessment for a CFD calculation, the "Numerical Uncertainty Assessment Procedural Approach" (NUAPA) represents the theoretical approach to use. In current research, the NUAPA approach has been considered and applied adhering to different theories, evaluated through two different hulls, tested at different speeds and configurations for a total number of 72 simulations. In this scenario, the following sources of numerical uncertainties can be listed: the grid size (U_G, δ_G), the iteration number (U_I, δ_I), time step (U_T, δ_T) and other parameters (U_P, δ_P). Among them, the most important one is the mesh sensitivity analysis. Therefore, changing the mesh size, several simulations has run to get results and to perform the numerical uncertainty assessment through different theoretical approaches. These formulations can be divided into the following two families: three and at least four solutions. Based on the analysis, it is possible summarize the findings as follows:

- Considering 40 different cases, the three-solutions approach led to the numerical uncertainty evaluation in 22 cases (success rate of 55%), since the monotonic convergence condition has to be addressed; while, the four-solutions approach applied on 20 different cases led always to the numerical uncertainty estimation (success rate of 100%). Based on these considerations, it is possible to assess that the four solutions approach demonstrates greater robustness and reliability among NUAPA approaches.
- Based on the findings from the three-solutions approach, once the monotonic convergence was achieved, it is possible to estimate values for U_{SN}. Each of these approaches accounts always for a lower level of uncertainty, when compared with the four solutions one. A possible explanation for this difference can be connected with the type of mesh. Indeed, when an unstructured mesh is used, a numerical noise can be observed. The results used exhibit this noise even when the fix trim and sinkage condition is considered; this is particular evident for the case where 13 different solutions have been considered to get the numerical uncertainty. For that case, the noise among solutions directly affects the uncertainty assessment, which value is higher than the difference among the higher versus the lower values obtained considering all the solutions.
- A possible way to phase with the numerical noise in the solutions has been found with the respect to the four solutions approach. Based on the evaluated order of accuracy (p), it is possible to define if the interpolant function can properly describe the data or if the noise affects its shape and therefore the uncertainty assessment. Indeed, if the order of accuracy lays

in the range $1.5 \div 2$, the four solutions approach can properly account for the numerical uncertainty; otherwise, if the value is out of range, an iterative procedure can be considered and one another simulation (or more than one) has to be performed to define if the new value for the index lays in the prescribed range. This proposed procedure accounts for a success rate of 100% and the results obtained provide a value for the numerical uncertainty estimation close to the one obtained by the three-solutions approaches; however, a higher computational effort is required.

- Considering all the simulations results, it is possible to define a numerical uncertainty mean value by considering the theories from Eça et al., Celik et al. and Stern and Xing; indeed, the following results have been achieved, respectively: 6.65%, 0.39% (GCI) and 2.01%.

Once the numerical uncertainty has been achieved, it is possible to phase with the simulation modeling errors through the Validation issues. To perform this phase, both the numerical and the experimental uncertainty has to be available. In this study the experimental uncertainty wasn't available, and therefore, form a theoretical standpoint, the Validation cannot be achieved. To partially mitigate this lack of knowledge, a surrogate evaluation for the experimental uncertainty has been proposed, based on the available results. These results come from an experimental campaign where the same model has been tested (into two different scales) by different towing tanks in order to assess its resistance for three different speeds [115]. The results exhibit a scatter which can be considered as a surrogate for the global experimental uncertainty.

Based on the findings from this study, a blind CFD simulation accounts for a mean precision of ±3.04%, compared with the EFD result. More specifically, in 50% of the cases, this difference is below 2.81%, and in 82% of cases it lays within 5%. Moreover, this analysis gives the probability to get a difference higher than 5% in 18% of the cases and no result exceeded the value of 10%. The precision for a CFD calculation is not a precise value because of the uncertainty estimation issue. In current research, two different ways have been illustrated to get the UA: the NUADA and the NUAPA. Both of them accounts for similar results with the respect to the uncertainty assessment. Moreover, it has been demonstrated how the theoretical available approaches perform and their limitations. Among them, Eça et al. exhibits the higher reliability displaying a success rate of 100%, but accounts for a higher uncertainty estimation, when compared with the three-solutions approaches. This difference is directly connected to the numerical noise observed in the mesh depending analysis. To partially mitigate this issue, an iterative procedure based on the evaluation for the order of accuracy (p) has been defined. Therefore, based on the finding from the uncertainty assessment analysis, a fully validation for the mean precision value has been achieved.

Another feature to account for is the interaction among hull and propeller/propellers. A first analysis has been presented in current study. Results display that the simplify approach of the virtual disk theory can be implemented in the early phase for the design, being the computational effort required similar to the one required for a simulation. Adhering to the approach implemented in current research for the comparisons among the towing tank experiences and the virtual ones, further investigations need to be performed to create a new comparisonal database for the self-propulsion issue. Once the database is available, it will be possible to perform a reliable statistical analysis to assess any possible trend in results.

Finally, based on the findings for the pure towing resistance evaluation from current research, the possible answer to the question "how precise is a CFD calculation" can be described as follows: in the pure towing resistance evaluation, if a blind CFD simulation has run, a difference of below 5% can be experienced with a confidence on 80%.

Bibliography

[1] US Geological Survey. How much water is there on earth? [Internet]. 2019 Nov (accessed 27.02.2026). Available from: https://www.usgs.gov/water-science-school/science/how-much-water-there-earth#overview;

[2] chimica-online.it. Superficie della terra [Internet]. (accessed 02.02.2026). Available from: https://www.chimica-online.it/astronomia/superficie-della-terra.htm;

[3] Camprubí E, De Leeuw JW, House CH, Raulin F, Russell MJ, Spang A, et al. The emergence of life. Space Sci Rev. 2019 Dec;215(8):56. DOI: 10.1007/s11214-019-0624-8;

[4] Oparin, A.I. (1924) The Origin of Life. Moskovskii rabochii, Moscow. (in Russian);

[5] Pearce BKD, Tupper AS, Pudritz RE, Higgs PG. Constraining the time interval for the origin of life on earth. Astrobiology. 2018 Mar 1;18(3):343–64. DOI:10.1089/ast.2017.1674;

[6] Hublin JJ, Ben-Ncer A, Bailey SE, Freidline SE, Neubauer S, Skinner MM, et al. New fossils from Jebel Irhoud, Morocco and the pan-African origin of Homo sapiens. Nature. 2017 Jun 8;546(7657):289–92. DOI:10.1038/nature22336;

[7] Osipowicz G, Orłowska J, Kuriga J. Experimental archaeology in NCU. 2018 Jan.

[8] Mark S. The earliest sailboats in Egypt and their influence on the development of trade, seafaring in the Red Sea, and State development. Journal of Ancient Egyptian Interconnections. 2013 Feb 28;5:28–37. DOI: 10.2458/azu_jaei_v05i1_mark;

[9] Bettini C. Come progettavano i velieri. Alle origini dell'architettura moderna di navi e yacht. Pisa: Edizioni ETS; 2019. ISBN 978-884675510-0;

[10] Mazari P. Archimedes' Principle Revisited. Journal of Applied Mathematics and Physics. 2017 Apr 27;5:836–43. DOI:10.4236/jamp.2017.54073;

[11] Kontomaris SV, Malamou A. A simple explanation of the classic hydrostatic paradox. Physics Education. 2016 May 24;51:045010. DOI:10.1088/0031-9120/51/4/045010;

[12] Albenga G. NEWCOMEN, Thomas. In: Istituto della Enciclopedia Italiana fondata da Giovanni Treccani [Internet]. (accessed 2026 Feb 3). Available from: https://www.treccani.it/enciclopedia/thomas-newcomen_(Enciclopedia-Italiana)/;

[13] Enciclopedia on line G. Watt, James. In: Istituto della Enciclopedia Italiana fondata da Giovanni Treccani [Internet]. (accessed 2026 Feb 3). Available from: https://www.treccani.it/enciclopedia/james-watt/?search=Watt%2C%20James%2F;

[14] Landes DS. The Unbound Prometheus: technological change and industrial development in western Europe from 1750 to the present. Cambridge University Press; 1969;

[15] Sharma, Singh JB. Evolution of industrial revolutions: a review. IJITEE. 2020 Sep 30;9(11):66–73. DOI: 10.35940/ijitee.I7144.0991120;

[16] Mohajan H. The first industrial revolution: creation of a new global human era. 2019 Oct 18;5:377–87;

[17] Chatterton EK. Steamship and their story. Cassel and Company, LTD; 1910;

[18] Mollat du Jourdin M. Navigazione, Enciclopedia delle scienze sociali (1996). In: Istituto della Enciclopedia Italiana fondata da Giovanni Treccani [Internet]. (accessed 2026 Mar 2). Available from: https://www.treccani.it/enciclopedia/navigazione_(Enciclopedia-delle-scienze-sociali)/;

[19] Oosterveld MWC. Advances in maritime hydrodynamic research during the last century. In: Koninckx C, editor. Proceedings of the International Colloquium 'Industrial Revolutions and the Sea'. Brussels; 1989. p. 153–65;

[20] Pedersen PT. Marine Structures: Future Trends and the Role of Universities. Engineering. 2015 Mar;1(1):131–8. DOI: 10.15302/J-ENG-2015004;

[21] Gotman A. A HISTORY OF SHIP RESISTANCE EVALUATION. Journal of Ocean Technology. 2007;2(1):75–96.

[22] Boccalatte C. La vasca navale della Spezia e la nascita della moderna architettura navale in Italia. In Ufficio Storico della Marina Militare. 2013 Sep;

[23] ITTC. In: History of ITTC [Internet]. (accessed 2026 Feb 3). Available from: https://www.ittc.info/about-ittc/history/;

[24] ITTC. In: ITTC Quality System Manual Recommended Procedures and Guidelines, Register [Internet]. (accessed 2026 Feb 3). Available from: https://www.ittc.info/media/11718/0_0.pdf;

[25] ITTC. In: Facilities [Internet]. (accessed 2026 Feb 3). Available from: https://www.ittc.info/facilities/;

[26] Szeszák BM, Kerékjártó IG, Soltész L, Galambos P. Industrial Revolutions and Automation: Tracing Economic and Social Transformations of Manufacturing. Societies. 2025 Mar 29;15(4):88. DOI: 10.3390/soc15040088;

[27] Copeland BJ, Sommaruga G. The Stored-Program Universal Computer: Did Zuse Anticipate Turing and von Neumann? In: Sommaruga G, Strahm T, editors. Turing’s Revolution: The Impact of His Ideas about Computability. Cham: Springer International Publishing; 2015. p. 43–101. DOI: 10.1007/978-3-319-22156-4_3;

[28] Abramovitch D, Franklin G. A brief history of disk drive control. IEEE Control Systems Magazine. 2002 Jun;22(3):28–42. DOI:10.1109/MCS.2002.1003997;

[29] ANSYS. What is computational fluid dynamics (CFD)? [Internet]. (accessed 2026 Feb 3). Available from: https://www.ansys.com/it-it/simulation-topics/what-is-computational-fluid-dynamics;

[30] Wilson RV. A Review of Computational Ship Hydrodynamics. Chattanooga, TN: SimCenter: National Center for Computational Engineering, University of Tennessee at Chattanooga; 2008;

[31] Larsson L, Stern F, Visonneau M. CFD in Ship Hydrodynamics—Results of the Gothenburg 2010 Workshop. In: Eça L, Oñate E, García-Espinosa J, Kvamsdal T, Bergan P, editors. MARINE 2011, IV International Conference on Computational Methods in Marine Engineering: Selected Papers. Dordrecht: Springer Netherlands; 2013. p. 237–59;

[32] Mousaviraad M, Stern, Yang, Wang J, Sadat H, Bhushan, et al. Computational Ship Hydrodynamics: Nowadays and Way Forward. International Shipbuilding Progress. 2013 Jan 17;60:3–105. DOI: 10.3233/ISP-130090;

[33] von Kerczek CH, Christoph G, Stern F. Further developments of the momentum integral method for ship boundary layers. May 1984: SAI; 1984. p. 38. Report No.: SAI Report #8413046;

[34] Bekhit A. Numerical simulation of the ship hull hydrodynamic performance. Universitatea Dunărea de Jos din Galați. 2023;

[35] Jasak H, Vukčević V, Gatin I, Lalović I. CFD validation and grid sensitivity studies of full scale ship self propulsion. International Journal of Naval Architecture and Ocean Engineering. 2019 Jan 1;11(1):33–43. DOI: 10.1016/j.ijnaoe.2017.12.004;

[36] Ratten V. The post COVID-19 pandemic era: Changes in teaching and learning methods for management educators. The International Journal of Management Education. 2023 Jul 1;21(2):100777. DOI: 10.1016/j.ijme.2023.100777;

[37] Lopes R, Eslamdoost A, Bensow RE, Ponkratov D, Kömpe A, Geremia P, et al. A summary of the Lucy Ashton resistance prediction workshop. Ocean Engineering. 2026 Jan 15;343:122951. DOI: 10.1016/j.oceaneng.2025.122951;

[38] ITTC Specialist Committee on Wake Fields. Final reports and recommendations to the 25th ITTC. In: Proceedings of the 25th International Towing Tank Conference. Vol. II. Fukuoka (Japan); 2008. p. 535–562;

[39] Galilei G. Dialogo sopra i due massimi sistemi del mondo. 1632;

[40] Gauss CF. Theoria motus corporum coelestium in sectionibus conicis solem ambientium. 1809;

[41] Enciclopedia della Matematica. Gauss. In: Istituto della Enciclopedia Italiana fondata da Giovanni Treccani [Internet]. (accessed 2026 Feb 3). Available from: https://www.treccani.it/enciclopedia/gauss_%28Enciclopedia-della-Matematica%29/;

[42] Débarbat S, Quinn T. Les origines du système métrique en France et la Convention du mètre de 1875, qui a ouvert la voie au Système international d'unités et à sa révision de 2018. Comptes Rendus Physique. 2019 Jan 1;20(1):6–21. DOI: 10.1016/j.crhy.2018.12.002;

[43] Fanton JP. A brief history of metrology: past, present, and future. Int J Metrol Qual Eng. 2019;10. DOI: 10.1051/ijmqe/2019005;

[44] Joint Committee for Guides in Metrology (JCGM). JCGM 100:2008 – Evaluation of measurement data: Guide to the expression of uncertainty in measurement. Bureau International des Poids et Mesures (BIPM); 2008. DOI: 10.59161/JCGM100-2008E;

[45] Joint Committee for Guides in Metrology (JCGM). Guide to the expression of uncertainty in measurement — Part 1: Introduction (JCGM GUM-1:2023). Bureau International des Poids et Mesures (BIPM); 2023. DOI: 10.59161/JCGMGUM-1-2023;

[46] ITTC. Uncertainty Analysis in CFD Verification and Validation, Methodology and Procedures (7.5-03-01-01). 2024. (accessed 2026 Feb 4). Available from: https://www.ittc.info/media/11950/75-03-01-01.pdf;

[47] Richardson LF, Gaunt JA. VIII. The deferred approach to the limit. Philosophical Transactions of the Royal Society of London, Series A: Containing Papers of a Mathematical or Physical Character. 1927 Jan 1;226(636–646):299–361. DOI: 10.1098/rsta.1927.0008;

[48] Roache PJ, Ghia KN, White FM. Editorial Policy Statement on the Control of Numerical Accuracy. Journal of Fluids Engineering. 1986 Mar 1;108(1):2–2; DOI: 10.1115/1.3242537;

[49] Groves C, Ilie M, Schallhorn P. Comprehensive Approach to Verification and Validation of CFD Simulations Applied to Backward Facing Step - Application of CFD Uncertainty Analysis. In: 51st AIAA Aerospace Sciences Meeting including the New Horizons Forum and Aerospace Exposition. American Institute of Aeronautics and Astronautics; 2013. DOI: 10.2514/6.2013-258;

[50] Stern F, Wilson RV, Coleman HW, Paterson EG. Comprehensive Approach to Verification and Validation of CFD Simulations—Part 1: Methodology and Procedures. Journal of Fluids Engineering. 2001 Jul 10;123(4):793–802. DOI: 10.1115/1.1412235;

[51] Celik I, Ghia U, Roache PJ, Freitas CJ, Coleman H, Raad PE. Procedure for Estimation and Reporting of Uncertainty Due to Discretization in CFD Applications. Journal of Fluids Engineering. 2008 Jul 22;130(078001). doi:10.1115/1.2960953;

[52] Xing T, Stern F. Factors of Safety for Richardson Extrapolation. 2010. DOI: 10.13140/RG.2.1.2054.8008;

[53] Eça L, Hoekstra M. A procedure for the estimation of the numerical uncertainty of CFD calculations based on grid refinement studies. Journal of Computational Physics. 2014 Apr 1;262:104–30. DOI: 10.1016/j.jcp.2014.01.006;

[54] National Maritime Research Institute. Tokyo 2015: A Workshop on CFD in Ship Hydrodynamics. In Tokyo, Japan: National Maritime Research Institute; 2015. [accessed 2026 Feb 4]. Available from: https://t2015.nmri.go.jp/index.html;

[55] Mancini S. The problem of verification and validation processes of CFD simulations of planing hulls. Napoli, Italy. Università degli Studi di Napoli Federico II, Dipartimento di Ingegneria Industriale. 2015;

[56] ITTC. In: List of benchmarks [Internet]. (accessed 2026 Feb 4). Available from: https://www.ittc.info/media/11250/list-of-benchmarks-2.pdf;

[57] Islam H, Guedes Soares C. Uncertainty analysis in ship resistance prediction using OpenFOAM. Ocean Engineering. 2019 Nov 1;191:105805. DOI: 10.1016/j.oceaneng.2019.02.033;

[58] International Organization for Standardization (ISO). Standard atmosphere 2533:1975; 1975. Available from: https://www.iso.org/standard/7472.html;

[59] ITTC. Fresh Water and Seawater Properties (7.5-02-01-03). 2024 (cited 2026 Feb 6). Available from: https://www.ittc.info/media/11764/75-02-01-03.pdf;

[60] Tupper EC. Introduction to Naval Architecture (Third Edition). Oxford: Butterworth-Heinemann (Elsevier Science Ltd.); 1996;

[61] Lewis EV. Principles of Naval Architecture: Resistance, Propulsion and Vibration (2nd Edition). Jersey City, NJ: The Society of Naval Architects and Marine Engineers; 1988;

[62] ITTC. Ship Models (7.5-01-01-01). 2024 (accessed 2026 Feb 6). Available from: https://www.ittc.info/media/11750/75-01-01-01.pdf;

[63] Bozzo S, Villa D. A Fast Numerical Procedure to Design the Shaftline Struts. 2023. DOI: 10.3233/PMST7;

[64] Olivieri A, Pistani F, Avanzini A, Stern F, Penna R. Towing Tank Experiments of Resistance, Sinkage and Trim, Boundary Layer, Wake, and Free Surface Flow Around a Naval Combatant Insean 2340 Model. 2001 Sep 1;42;

[65] ITTC. 1978 ITTC Performance Prediction Method (7.5-02-03-01.4). 2021 (accessed 2026 Feb 6). Available from: https://www.ittc.info/media/11796/75-02-03-014.pdf;

[66] Annali della Vasca Nazionale per le esperienze di architettura navale in Roma, volume III, istituto poligrafico dello stato MCMXXXIII;

[67] Prohaska CW. A Simple Method for the Evaluation of the Form Factor and Low Speed Wave Resistance. In Tokyo, Japan; 1966;

[68] ITTC. In: Report of the Powering Performance Committee: Review of Research Into Powering Performance of Importance to the ITTC (Hull Roughness). In Madrid, Spain; 1990. p. 262–265;

[69] ITTC. Resistance Test (7.5-02-02-01). 2021 (accessed 2026 Feb 6). Available from: https://www.ittc.info/media/11780/75-02-02-01.pdf;

[70] Molland AF, Turnock SR, Hudson DA. Ship Resistance and Propulsion: Practical Estimation of Ship Propulsive Power. 2nd ed. Cambridge: Cambridge University Press; 2017. DOI: 10.1017/9781316494196;

[71] Tanaka I. Scale Effects on Wake Distribution and Viscous Pressure Resistance of Ships. Journal of the Society of Naval Architects of Japan. 1979;1979:53–60;

[72] Greenshields C, Weller H. Notes on Computational Fluid Dynamics: General Principles. Reading, UK: CFD Direct Ltd; 2022;

[73] Patil D, Kadam S. Basics of computational fluid dynamics: An overview. IOP Conference Series: Earth and Environmental Science. 2023 Jan 1. DOI: 10.1088/1755-1315/1130/1/012042;

[74] Linde F. 3D Modelling of Ship Resistance in Restricted Waterways and Application to an Inland Eco-Driving Prototype. Compiègne, France. Université de Technologie de Compiègne; 2017;

[75] Cao J. MIT OpenCourseWare. Massachusetts Institute of Technology; 2012. Non-Equilibrium Statistical Mechanics. (accessed 2026 Feb 6);

[76] Fefferman C. Existence and smoothness of the Navier-Stokes equation. The Millennium Prize Problems. 2006;

[77] Clay Mathematics Institute. The Millennium Prize Problems. (accessed 2026 Feb 6);

[78] Muzamal M. Simulation of Gas Dispersion in Road Tunnel with Traffic: Computational Fluid Dynamics Simulation using FLUENT and In-house TU Delft Codes. Gothenburg, Sweden. Chalmers University of Technology; 2011;

[79] Layton WJ. The 1877 Boussinesq Conjecture: Turbulent Fluctuations Are Dissipative on the Mean Flow. 2014;

[80] Boussinesq JV. Complément à une étude intitulée « Essai sur la théorie des eaux courantes », et à un mémoire « Sur l'influence des frottements dans les mouvements réguliers des fluides ». Journal de Mathématiques Pures et Appliquées. 1878;

[81] Davidson P, Kaneda Y, Moffatt K, Sreenivasan K. A Voyage Through Turbulence. 2011 Oct 7. DOI:10.1017/CBO9781139018241;

[82] Wilcox DC. Turbulence Modeling for CFD. La Cañada, California, USA: DCW Industries; 1998;

[83] Pena B, Huang L. A review on the turbulence modelling strategy for ship hydrodynamic simulations. Ocean Engineering. 2021 Dec 1;241:110082. DOI: 10.1016/j.oceaneng.2021.110082;

[84] Terziev M, Tezdogan T, Incecik A. Application of eddy-viscosity turbulence models to problems in ship hydrodynamics. Ships and Offshore Structures. 2020 May 27;15(5):511–34. DOI:10.1080/17445302.2019.1661625M;

[85] Launder BE, Spalding DB. The Numerical Computation of Turbulent Flow Computer Methods. Computer Methods in Applied Mechanics and Engineering. 1974 Mar 1;3:269–89. DOI:10.1016/0045-7825(74)90029-2;

[86] Paterson E, Wilson R, Stern F. General-purpose parallel unsteady RANS ship hydrodynamics code: CFDShip-Iowa. 2003 Nov 1;

[87] Dashtimanesh A, Tavakoli S, Kohansal A, Khosravani R, Ghassemzadeh A. Numerical study on a heeled one-stepped boat moving forward in planing regime. Applied Ocean Research. 2020 Mar 1;96:102057. DOI: 10.1016/j.apor.2020.102057;

[88] Day HM. Aerodynamic optimisation of vertical axis wind turbines using Adjoint methods in CFD. University of Sheffield; 2021;

[89] Menter FR. Menter FR. Two-equation eddy-viscosity turbulence models for engineering applications. AIAA Journal. 1994 Aug 1;32(8):1598–605. DOI: 10.2514/3.12149;

[90] Johnson BMC. Computational Fluid Dynamics (CFD) modelling of renewable energy turbine wake interactions. University of Central Lancashire; 2015 May;

[91] Mountain JK. The Lax Equivalence Theorem for linear, inhomogeneous equations in L2 spaces. Journal of Approximation Theory. 1981 Oct. 1;33(2):126–30. DOI: 10.1016/0021-9045(81)90082-4;

[92] Ortigueira MD. Discrete-Time Fractional Difference Calculus: Origins, Evolutions, and New Formalisms. Fractal and Fractional. 2023;7(7):502. DOI: 10.3390/fractalfract7070502;

[93] Turner MJ, Clough RW, Martin HC, Topp LJ. Stiffness and Deflection Analysis of Complex Structures. Journal of the Aeronautical Sciences. 1956 Sep 1;23(9):805–23. DOI: 10.2514/8.3664;

[94] McDonald PW. The Computation of Transonic Flow Through Two-Dimensional Gas Turbine Cascades. In: GT1971. ASME 1971 International Gas Turbine Conference and Products Show; 1971. DOI: 10.1115/71-GT-89;

[95] Harlow FH, Welch JE. Numerical Calculation of Time-Dependent Viscous Incompressible Flow of Fluid with Free Surface. Physics of Fluids. 1965 Dec 1;8(12):2182–9. DOI: 10.1063/1.1761178;

[96] Rider WJ, Kothe DB. Reconstructing Volume Tracking. Journal of Computational Physics. 1998 Apr 10;141(2):112–52. DOI: 10.1006/jcph.1998.5906;

[97] DeBar RB. Fundamentals of the KRAKEN Code. Lawrence Livermore Laboratory; 1974. Report No.: UCIR-760;

[98] Hirt CW, Nichols BD. A Computational Method for Free Surface Hydrodynamics. Journal of Pressure Vessel Technology. 1981 May 1;103(2):136–41. DOI: 10.1115/1.3263378;

[99] Noh WF, Woodward P. SLIC (Simple Line Interface Calculation). Proceedings of the Fifth International Conference on Numerical Methods in Fluid Dynamics June 28 – July 2, 1976 Twente University, Enschede. 1976;

[100] Osher S, Sethian JA. Fronts propagating with curvature-dependent speed: Algorithms based on Hamilton-Jacobi formulations. Journal of Computational Physics. 1988 Nov 1;79(1):12–49. DOI: 10.1016/0021-9991(88)90002-2;

[101] Ferziger J, Peric M. Computational Methods for Fluid Dynamics. 2002;

[102] Zhang F, Zhou Z, Zhang H, Yang X. A new single formula for the law of the wall and its application to wall-modeled large-eddy simulation. European Journal of Mechanics - B/Fluids. 2022 Jul 1;94:350–65. DOI: 10.1016/j.euromechflu.2022.03.013;

[103] ITTC. Guide to the Expression of Uncertainty in Experimental Hydrodynamics (7.5-02-01-01). 2016. (accessed 2026 Feb 6). Available from: https://www.ittc.info/media/11762/75-02-01-01.pdf;

[104] Oberkampf WL, Blottner FG. Issues in computational fluid dynamics code verification and validation. AIAA Journal. 1998;36(5):687–95. doi:10.2514/2.456;

[105] Roache PJ. Verification and Validation in Computational Science and Engineering. Albuquerque, New Mexico: Hermosa Publishers; 1998;

[106] Wilson RV, Stern F, Coleman HW, Paterson EG. Comprehensive Approach to Verification and Validation of CFD Simulations—Part 2: Application for Rans Simulation of a Cargo/Container Ship. Journal of Fluids Engineering. 2001 Jul 10;123(4):803–10. DOI: 10.1115/1.1412236;

[107] Huang S, Jiao J, Guedes Soares C. Uncertainty analyses on the CFD–FEA co-simulations of ship wave loads and whipping responses. Marine Structures. 2022 Mar 1;82:103129. DOI: 10.1016/j.marstruc.2021.103129;

[108] Lakatoš M, Mancini S, Niazmand Bilandi R, Tabri K. Verification and validation of hard-chine hull performance in calm water: Effects of numerical setups and hull configurations. Ocean Engineering. 2025 Jun 15;329:121056. DOI: 10.1016/j.oceaneng.2025.121056;

[109] Ziatdinov R, Atteraya MS, Nabiyev R. The Fifth Industrial Revolution as a Transformative Step towards Society 5.0. Societies. 2024;14(2):19. DOI: 10.3390/soc14020019;

[110] Abidin NZ, Grondin F, Muller P, Sigrist JF. Assessment of hydrodynamic characteristics and computational resources for submarine resistance analysis: A comparative study between CFD Codes with application of the BB2 Submarine. In: 26th Numerical Towing Tank Symposium (NuTTS 2024), University of Duisburg-Essen, Oct 2024;

[111] Villa D, Furcas F, Pralits JO, Vernengo G, Gaggero S. An Effective Mesh Deformation Approach for Hull Shape Design by Optimization. Journal of Marine Science and Engineering. 2021;9(10):1107. DOI:10.3390/jmse9101107;

[112] ITTC. Practical Guidelines for Ship Resistance CFD (7.5-03-02-04). 2021 (accessed 2026 Feb 7). Available from: https://www.ittc.info/media/11960/75-03-02-04.pdf;

[113] ITTC. Practical Guidelines for ship CFD Applications (7.5-03-02-03). 2024 [accessed 2026 Feb 7]. Available from: https://www.ittc.info/media/11958/75-03-02-03.pdf;

[114] Cui DJ, Mak CM, Kwok KCS, Ai ZT. CFD simulation of the effect of an upstream building on the inter-unit dispersion in a multi-story building in two wind directions. Journal of Wind Engineering and Industrial Aerodynamics. 2016 Mar 1; 150:31–41. DOI: 10.1016/j.jweia.2016.01.007;

[115] ITTC. The Resistance Committee. In Wuxi, China: International Towing Tank Conference; 2017. (accessed 2026 Feb 7). Available from: https://www.ittc.info/media/7797/4-resistance-committee.pdf;

[116] Halim M, Nik Mohd NAR, Nasir N, Dahalan N. The Evaluation of k-ε and k-ω Turbulence Models in Modelling Flows and Performance of S-shaped Diffuser. International Journal of Automotive and Mechanical Engineering. 2018 Jun 30; 15:5161–77. DOI: 10.15282/ijame.15.2.2018.2.0399;

[117] ANSYS Inc. ANSYS Help Documentation. (accessed 2026 Feb 7). Available from: https://ansyshelp.ansys.com/public/account/secured?returnurl=/Views/Secured/corp/v242/en/cfx_mod/i1345899.html;

[118] ITTC. Symbols and Terminology List (Version 2024). 2024. (accessed 2026 Feb 7). Available from: https://ittc.info/media/12040/structured-list_2024_l.pdf;

[119] Guo C, Zhong X, Zhao D. Research on Scale Effect of Resistance Components for Full-Formed Ship Based on Large-Scale Model Towing Test. Journal of Marine Science and Engineering. 2023;11(7):1300. DOI: 10.3390/jmse11071300;

[120] Le H, Anh N, Tu T, Ngoc Hoa NT, Ngoc V. Numerical Investigation of Length to Beam Ratio Effects on Ship Resistance Using Ranse Method. Polish Maritime Research. 2023 Apr 19; 30:13–24. DOI: 10.2478/pomr-2023-0002;

[121] Sessa CT. Rappresentazione e Trasformazione delle Carene Navali. Università degli Studi di Napoli Federico II. 2008 Nov 30;

[122] Petersson E. Study of Semi-Empirical Methods for Ship Resistance Calculations. 2020 Jun. Uppsala;

[123] Dogrul A, Song S, Demirel YK. Scale effect on ship resistance components and form factor. Ocean Engineering. 2020 Aug 1; 209:107428. DOI: 10.1016/j.oceaneng.2020.107428;

[124] Doctors LJ, Day A, Clelland D. Unsteady effects during resistance tests on a ship model in a towing tank. Journal of Ship Research. 2008;52(4):263–73. doi:10.5957/JSR.2008.52.4.263;

[125] Voxakis P. Ship hull resistance calculations using CFD methods. 2012 Nov 19;

[126] Leirmo TL, Semeniuta O, Baturynska I, Martinsen K. Extracting shape features from a surface mesh using geometric reasoning. Procedia CIRP. 2020 Jan 1; 93:544–9. DOI: 10.1016/j.procir.2020.02.142;

[127] Gilkeson CA, Toropov VV, Thompson HM, Wilson MCT, Foxley NA, Gaskell PH. Dealing with numerical noise in CFD-based design optimization. Computers & Fluids. 2014 May 1; 94:84–97. DOI: 10.1016/j.compfluid.2014.02.004;

[128] Bozzo S, Villa D, Mancini S. Analyses of Different Approaches for Virtual Towing Tank Uncertainty Assessment. Journal of Marine Science and Engineering. 2025;13(10):1882. DOI: 10.3390/jmse13101882;

[129] Diez DM, Barr CD, Çetinkaya-Rundel M. OpenIntro Statistics. 4th ed. 2019;

[130] Chen S. The Gaussian distribution: Derivation method and its applications in selected examples. Theoretical and Natural Science. 2024 Jun 24; 38:196–202. DOI: 10.54254/2753-8818/38/20240595;

[131] Prieto Curiel R, Cabrera Arnau C, Torres Pinedo M, González Ramírez H, Bishop SR. A continuous binning for discrete, sparse and concentrated observations. MethodsX. 2020 Jan 1; 7:100709. DOI: 10.1016/j.mex.2019.10.020;

[132] *Jeong* UC, Doi Y, Mori KH. Numerical Investigation on the Turbulent and Vortical Flows Beneath the Free Surface Around Struts. In: Twenty-First Symposium on Naval Hydrodynamics;

[133] Gignac GE, Szodorai ET. Effect size guidelines for individual differences researchers. Personality and Individual Differences. 2016 Nov 1; 102:74–8. DOI: 10.1016/j.paid.2016.06.069;

[134] Kučera J, Bode P, Stvpánek V. The 1993 ISO Guide to the Expression of Uncertainty in Measurement Applied to NAA. Journal of Radioanalytical and Nuclear Chemistry. 2000 Jul 1; 245:115–22. DOI: 10.1023/A:1006760726572;

[135] D'Agostini G. Guide to the Expression of Uncertainty in Measurement. 1995 Feb 27;

[136] International Organization for Standardization. Guide to the Expression of Uncertainty in Measurement. Geneva, Switzerland: International Organization for Standardization; 1993;

[137] ITTC. General Guidelines for Uncertainty Analysis in Resistance (7.5-02-02-02). 2021 (accessed 2026 Feb 16). Available from: https://www.ittc.info/media/11786/75-02-02-02.pdf;

[138] Wilson RV, Carrica PM, Stern F. Unsteady RANS method for ship motions with application to roll for a surface combatant. Computers & Fluids. 2006 Jun 1;35(5):501–24. DOI: 10.1016/j.compfluid.2004.12.005;

[139] Sorrentino V, Pigazzini R, De Luca F, Mancini S, Pensa C. Experimental and numerical investigation of air lubrication on a planing hull with Double Interceptor System. Ocean Engineering. 2025 Mar 1; 319:120135. DOI: 10.1016/j.oceaneng.2024.120135;

[140] Levin O. Discrete Mathematics: An Open Introduction. 4th ed. 2020;

[141] Ostertagová E. Modelling using Polynomial Regression. Procedia Engineering. 2012 Jan 1; 48:500–6. DOI: 10.1016/j.proeng.2012.09.545;

[142] Rousseeuw P, Croux C. Alternatives to Median Absolute Deviation. Journal of the American Statistical Association. 1993 Dec 1; 88:1273–83. DOI: 10.1080/01621459.1993.10476408;

[143] ITTC. Propulsion/Bullard Pull Test (7.5-02-03-01.1). 2024 (accessed 2026 Feb 16). Available from: https://www.ittc.info/media/11792/75-02-03-011.pdf;

[144] Gokce M, Kinaci O, Alkan A. Self-propulsion estimations for a bulk carrier. Ships and Offshore Structures. 2019 Oct 13;14:656–63. DOI: 10.1080/17445302.2018.1544108;

[145] Froude RE. On the Part Played in Propulsion by Differences in Fluid Pressure. 1889;

[146] ITTC. Practical Guidelines for Ship self-Propulsion CFD (7.5-03-03-01). 2024 (accessed 2026 Feb 16). Available from: https://www.ittc.info/media/11964/75-03-03-01.pdf;

[147] Gaggero S, Villa D, Viviani M. An Investigation on the Discrepancies Between RANSE and BEM Approaches for the Prediction of Marine Propeller Unsteady Performances in Strongly Non-Homogeneous Wakes. Proceedings of the International Conference on Offshore Mechanics and Arctic Engineering - OMAE. 2014 Jun 8;2. DOI: 10.1115/OMAE2014-23831;

[148] Villa D, Gaggero S, Gaggero T, Tani G, Vernengo G, Viviani M. An efficient and robust approach to predict ship self-propulsion coefficients. Applied Ocean Research. 2019 Nov 1;92:101862. DOI: 10.1016/j.apor.2019.101862.

Annex 1 - Hulls characteristics and data

The subsequent sections present the main features of the hull tested, described through tables, figures and plots. Every hull is represented consistently by the same collection of attributes. More in details, the tables present both the general characteristics for the hull tested and the data evaluated through the experimental campaign and the numerical simulations performed; while, two kinds of plots highlight le difference recorded among EFD and CFD varying the speed and the hull resistance curves represented by the EFD and the CFD approach. Lastly, a longitudinal view representation is available for each hull, and in order to let the reader aware about the differences among them, the scale representation is the same for each hull at model scale.

1. Hull 1.

Table 42: main characteristics for hull 1.

Model characteristics	Symbol	Values	UoM
Length between perpendiculars	L_{PP}	4.9800	m
Length. overall submerged	L_{OS}	4.9660	m
Length of waterline	L_{WL}	4.9660	m
Maximum moulded Breadth at design WL	B_{WL}	0.6510	m
Draught at forward perpendicular	T_F	0.1910	m
Draught at midship	$T_M = (T_A + T_F)/2$	0.1910	m
Draught at aft perpendicular	T_A	0.1910	m
Displacement volume	∇	0.2556	m^3
Area of wetted surface	S	2.9125	m^2
Ratio L/B	L_{WL}/B_{WL}	7.6283	-
Ratio B/T	B_{WL}/T_M	3.4084	-
Block coefficient	$C_B = \nabla/LBT$	0.4139	-
Froude's length coefficient. or length-displacement ratio	$M^C = \nabla^{1/3}$	7.8250	-
Scale ratio	$\lambda = L_s/L_M$	20.0000	-
Area of water-plane	A_W	2.1192	m^2
Longitudinal centre of flotation	L_{CF}, X_{CF}	2.5138	m
Longitudinal centre of buoyancy	L_{CB}, X_{CB}	2.3991	m

Figure 130: model scale longitudinal view for hull 1.

Table 43: towing tank and virtual towing tank results for hull 1.

RUN	Carriage speed		$10^{-3}C_{FM}[-]$		R_{TM} [N]	
	V_M [m/s]	F_r [−]	I.T.T.C. 57	CFD	EFD	CFD
1	0.900	0.129	3.470	3.146	4.315	4.444
2	1.200	0.172	3.291	15.346	7.649	7.853
3	1.500	0.215	3.162	9.822	12.405	12.500
4	1.800	0.258	3.061	6.821	18.437	18.610
5	2.100	0.301	2.980	5.011	26.723	27.280
6	2.500	0.358	2.892	3.536	41.874	43.073
7	2.700	0.387	2.854	3.031	56.486	58.896
8	2.900	0.416	2.820	2.628	75.805	80.056

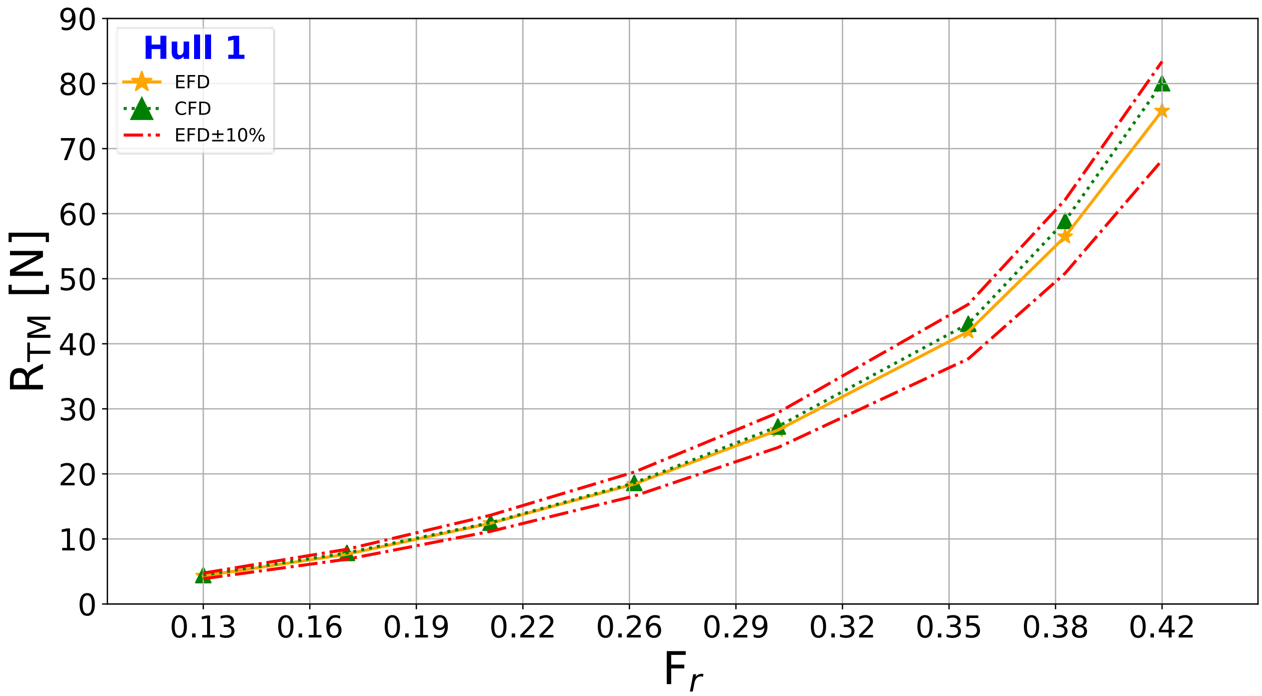

Figure 131: resistance curve, comparisons between EFD results and CFD calculations, varying speed range for the model hull 1.

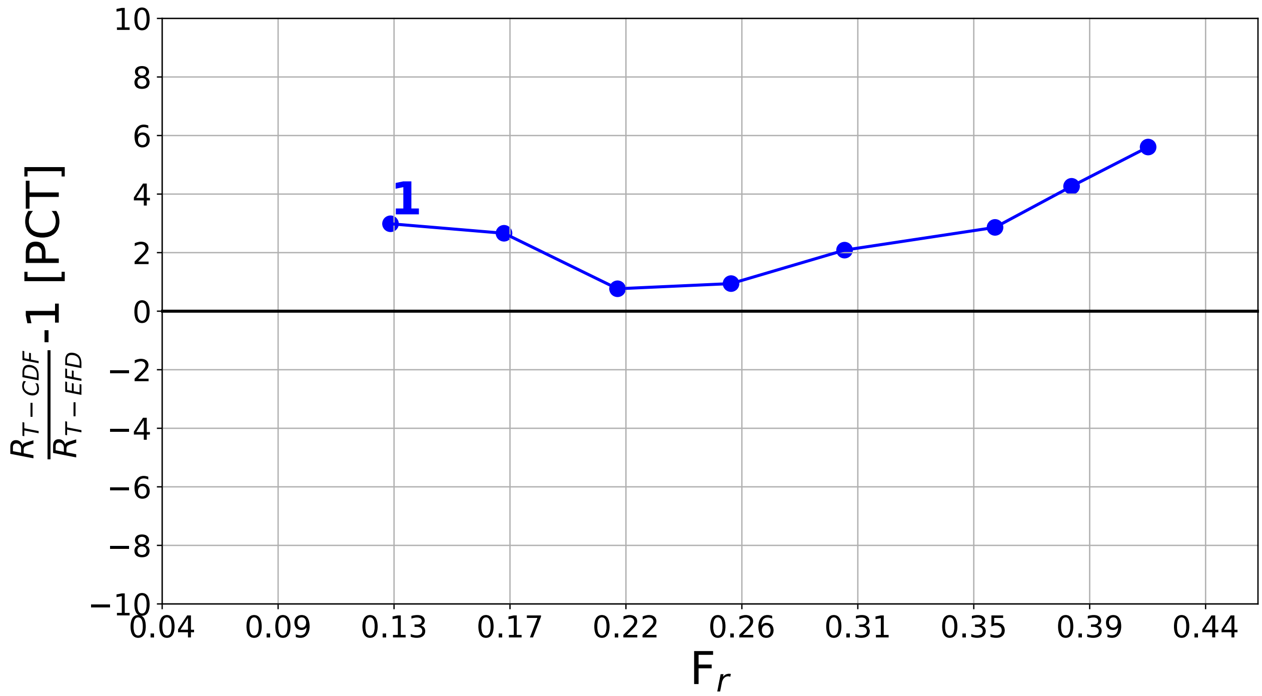

Figure 132: percentual difference between EFD results and CFD calculations, varying speed range for the model 1.

2. Hull 2.

Table 44: main characteristics for hull 2.

Model characteristics	Symbol	Values	UoM
Length between perpendiculars	L_{PP}	4.8650	m
Length, overall submerged	L_{OS}	5.0750	m
Length of waterline	L_{WL}	5.0750	m
Maximum moulded Breadth at design WL	B_{WL}	0.7250	m
Draught at forward perpendicular	T_F	0.2190	m
Draught at midship	$T_M = (T_A + T_F)/2$	0.2190	m
Draught at aft perpendicular	T_A	0.2190	m
Displacement volume	∇	0.4259	m^3
Area of wetted surface	S	3.6075	m^2
Ratio L/B	L_{WL}/B_{WL}	7.0000	-
Ratio B/T	B_{WL}/T_M	3.3105	-
Block coefficient	$C_B = \nabla/LBT$	0.5286	-
Froude's length coefficient, or length-displacement ratio	$M^C = \nabla^{1/3}$	6.7452	-
Scale ratio	$\lambda = L_s/L_M$	20.0000	-
Area of water-plane	A_W	2.5395	m^2
Longitudinal centre of flotation	$L_{CF,} X_{CF}$	2.5039	m
Longitudinal centre of buoyancy	$L_{CB,} X_{CB}$	2.4458	m

Figure 133: model scale longitudinal view for hull 2.

Table 45: towing tank and virtual towing tank results for hull 2.

RUN	**Carriage speed**		$10^{-3} C_{FM} [-]$		R_{TM} [N]	
	V_M [m/s]	F_r [−]	**I.T.T.C. 57**	**CFD**	**EFD**	**CFD**
1	1.400	0.198	3.361	9.005	13.876	12.916
2	1.500	0.213	3.319	7.844	15.789	14.799
3	1.600	0.227	3.280	6.894	17.848	16.814
4	1.800	0.255	3.211	5.447	23.340	21.829
5	2.000	0.283	3.151	4.412	31.381	30.203
6	2.200	0.312	3.098	3.646	40.403	38.904
7	2.300	0.326	3.074	2.889	44.914	43.551

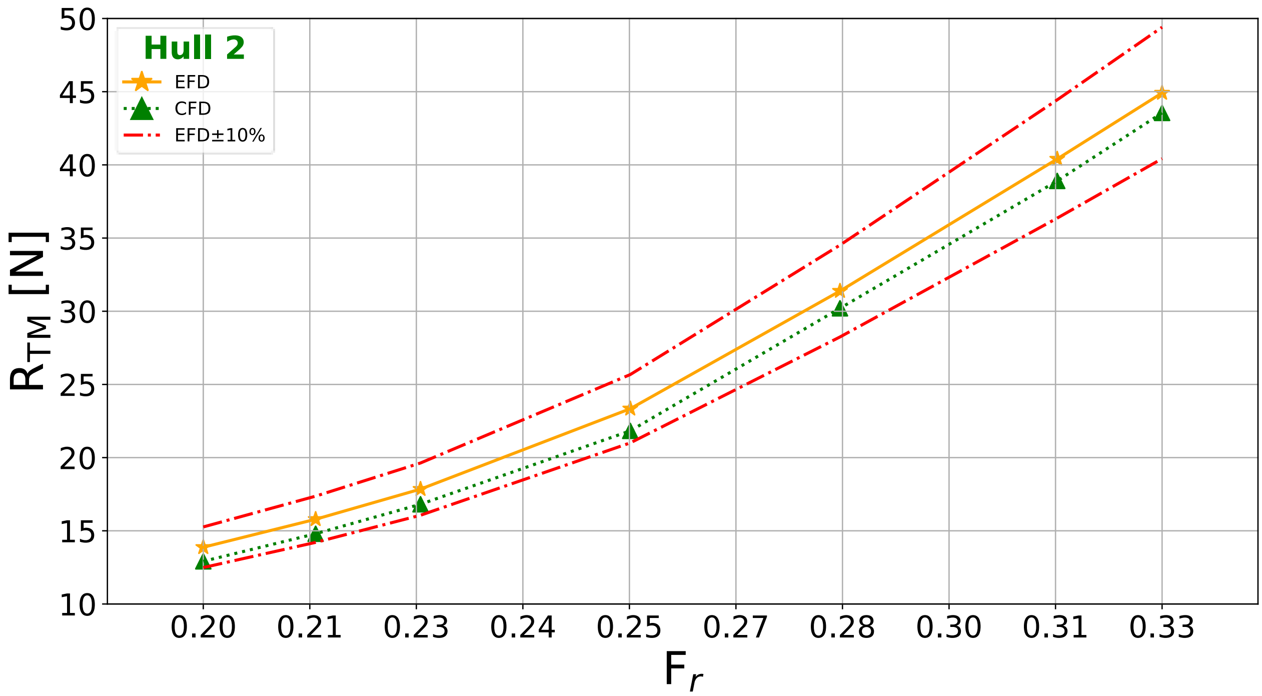

Figure 134: resistance curve, comparisons between EFD results and CFD calculations, varying speed range for the model hull 2.

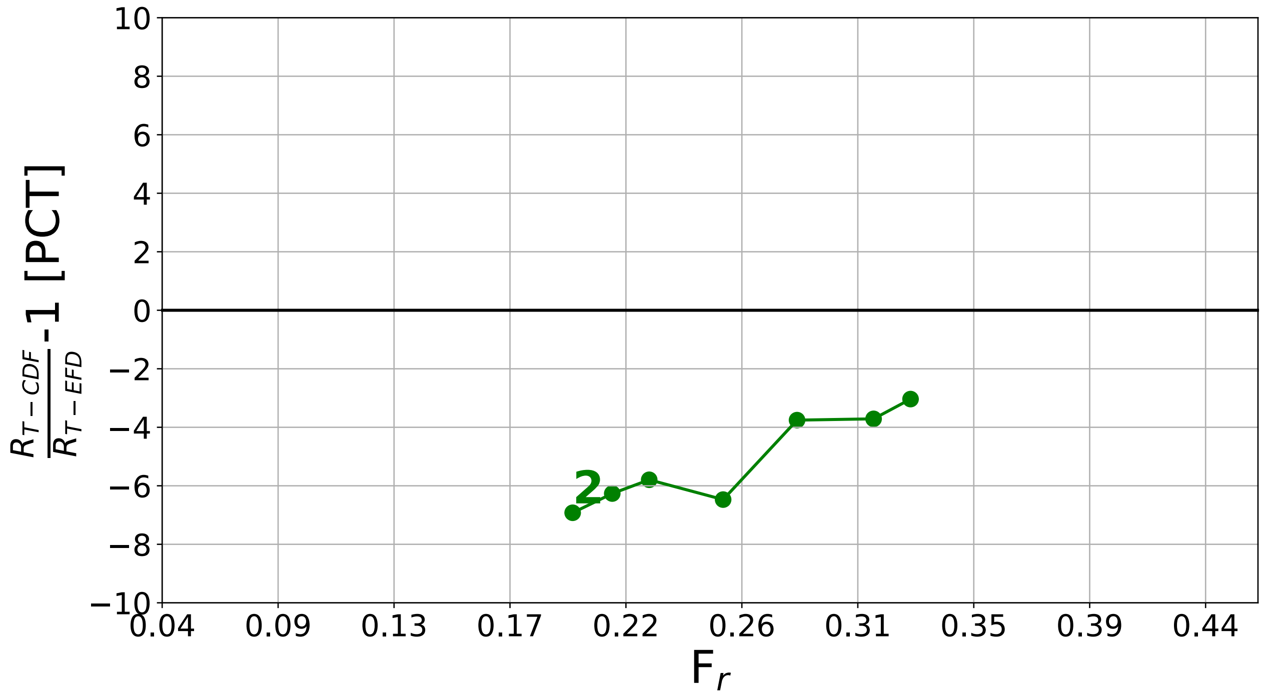

Figure 135: percentual difference between EFD results and CFD calculations, varying speed range for the model 2.

3. Hull 3.

Table 46: main characteristics for hull 3.

Model characteristics	Symbol	Values	UoM
Length between perpendiculars	L_{PP}	4.2000	m
Length, overall submerged	L_{OS}	4.3404	m
Length of waterline	L_{WL}	4.3404	m
Maximum moulded Breadth at design WL	B_{WL}	0.8000	m
Draught at forward perpendicular	T_F	0.2020	m
Draught at midship	$T_M = (T_A + T_F)/2$	0.2620	m
Draught at aft perpendicular	T_A	0.3220	m
Displacement volume	∇	0.3891	m^3
Area of wetted surface	S	3.6990	m^2
Ratio L/B	L_{WL}/B_{WL}	5.4255	-
Ratio B/T	B_{WL}/T_M	3.0534	-
Block coefficient	$C_B = \nabla/LBT$	0.4277	-
Froude's length coefficient, or length-displacement ratio	$M^C = \nabla^{1/3}$	5.9451	-
Scale ratio	$\lambda = L_s/L_M$	5.0000	-
Area of water-plane	A_W	2.5834	m^2
Longitudinal centre of flotation	L_{CF}, X_{CF}	1.9348	m
Longitudinal centre of buoyancy	L_{CB}, X_{CB}	1.8936	m

Figure 136: model scale longitudinal view for hull 3.

Table 47: towing tank and virtual towing tank results for hull 3.

RUN	Carriage speed		$10^{-3} C_{FM} [-]$		R_{TM} [N]	
	V_M [m/s]	F_r [−]	I.T.T.C. 57	CFD	EFD	CFD
1	1.400	0.215	3.357	9.138	15.436	15.194
2	1.500	0.230	3.314	7.960	18.260	17.837
3	1.600	0.245	3.276	6.996	21.329	20.963
4	1.900	0.291	3.176	4.962	32.872	32.814
5	2.000	0.307	3.147	4.478	37.736	37.920
6	2.100	0.322	3.120	4.061	42.777	42.213
7	2.200	0.337	3.094	3.701	48.661	48.094
8	2.300	0.353	3.070	3.386	56.486	56.639
9	2.400	0.368	3.047	3.110	67.597	71.916
10	2.500	0.383	3.026	2.866	83.357	87.030
11	2.600	0.399	3.005	2.650	104.441	109.546

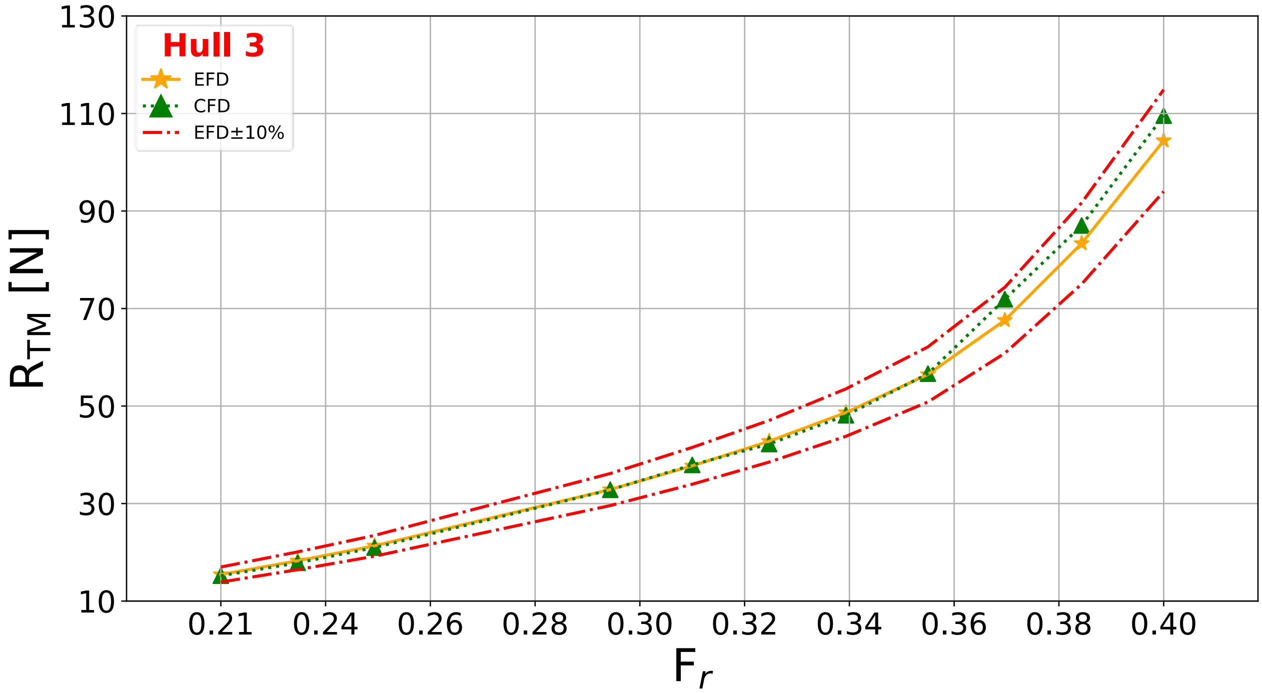

Figure 137: resistance curve, comparisons between EFD results and CFD calculations, varying speed range for the model hull 3.

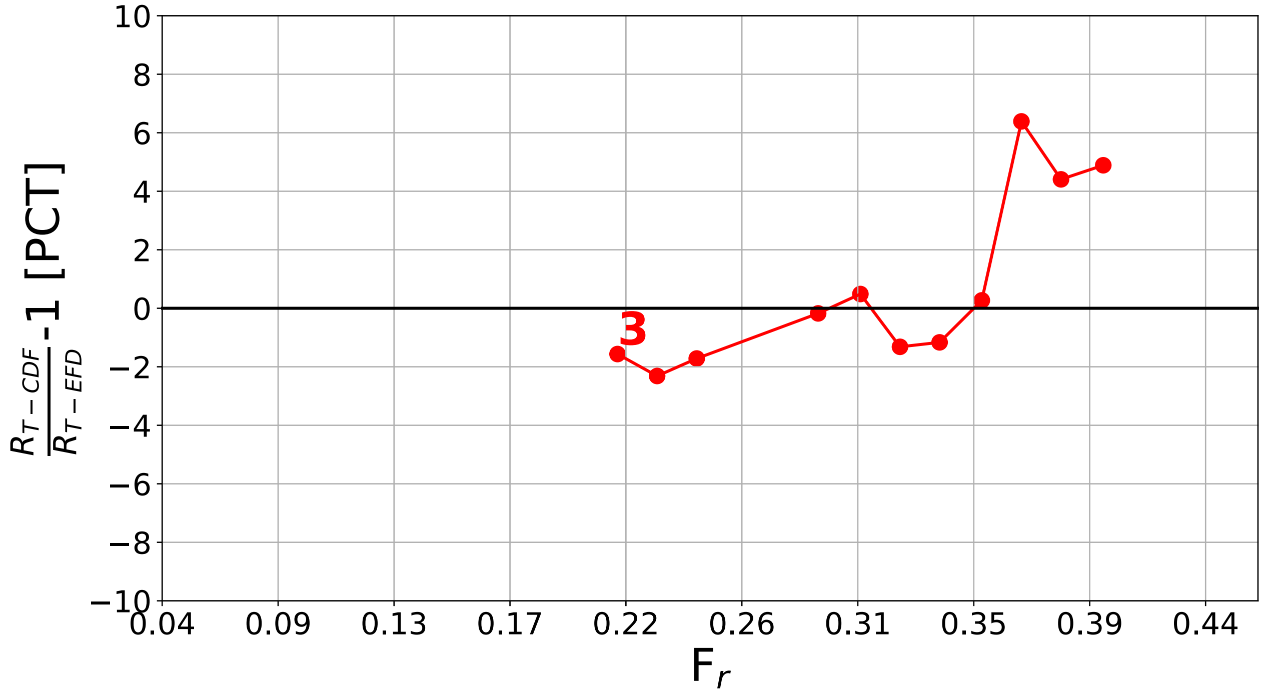

Figure 138: percentual difference between EFD results and CFD calculations, varying speed range for the model 3.

4. Hull 4.

Table 48: main characteristics for hull 4.

Model characteristics	Symbol	Values	UoM
Length between perpendiculars	L_{PP}	4.3600	m
Length, overall submerged	L_{OS}	4.3600	m
Length of waterline	L_{WL}	4.3600	m
Maximum moulded Breadth at design WL	B_{WL}	0.8300	m
Draught at forward perpendicular	T_F	0.2810	m
Draught at midship	$T_M = (T_A + T_F)/2$	0.2810	m
Draught at aft perpendicular	T_A	0.2810	m
Displacement volume	∇	0.4076	m^3
Area of wetted surface	S	3.5406	m^2
Ratio L/B	L_{WL}/B_{WL}	5.2530	-
Ratio B/T	B_{WL}/T_M	2.9537	-
Block coefficient	$C_B = \nabla/LBT$	0.4008	-
Froude's length coefficient, or length-displacement ratio	$M^C = \nabla^{1/3}$	5.8804	-
Scale ratio	$\lambda = L_s/L_M$	5.0000	-
Area of water-plane	A_W	2.5772	m^2
Longitudinal centre of flotation	L_{CF}, X_{CF}	2.0726	m
Longitudinal centre of buoyancy	L_{CB}, X_{CB}	2.0104	m

Figure 139: model scale longitudinal view for hull 4.

Table 49: towing tank and virtual towing tank results for hull 4.

RUN	Carriage speed		$10^{-3}C_{FM}[-]$		R_{TM} [N]	
	V_M [m/s]	F_r [−]	I.T.T.C. 57	CFD	EFD	CFD
1	1.400	0.214	3.439	9.543	15.298	15.122
2	1.600	0.245	3.355	7.306	21.545	20.235
3	1.700	0.260	3.318	6.472	24.517	23.152
4	1.800	0.275	3.284	5.773	27.949	26.954
5	2.000	0.306	3.222	4.676	36.383	36.348
6	2.100	0.321	3.194	3.322	41.286	41.408

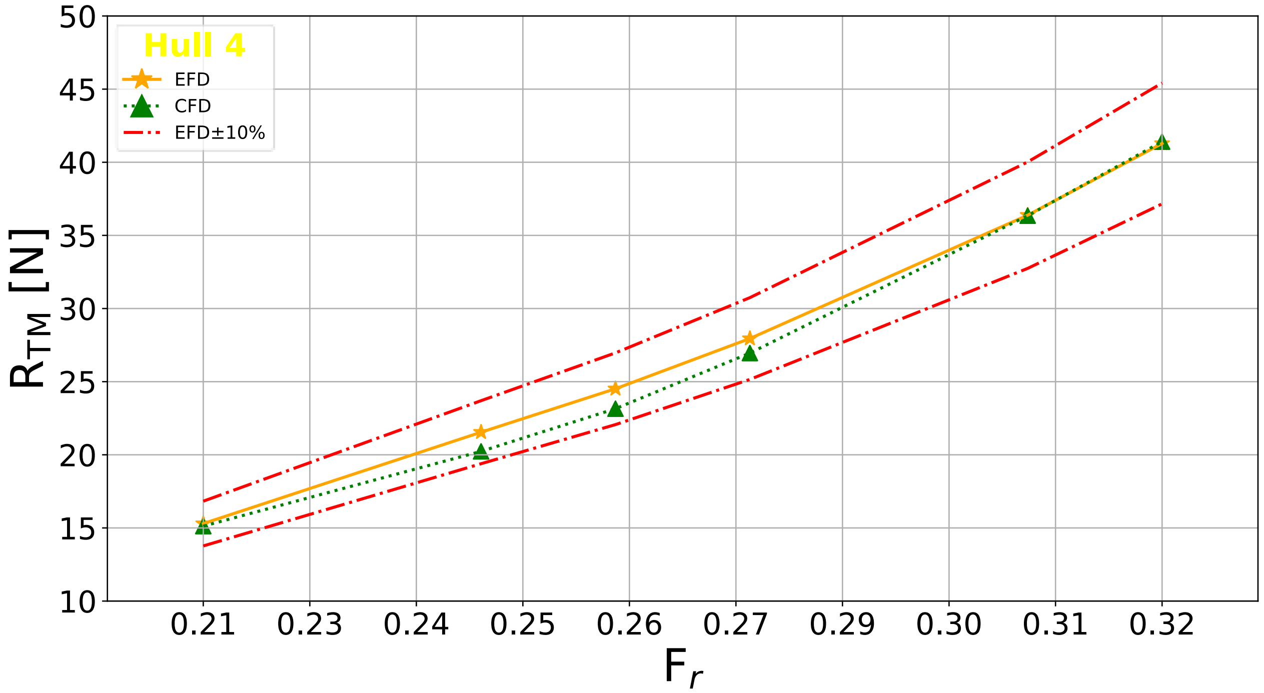

Figure 140: resistance curve, comparisons between EFD results and CFD calculations, varying speed range for the model hull 4.

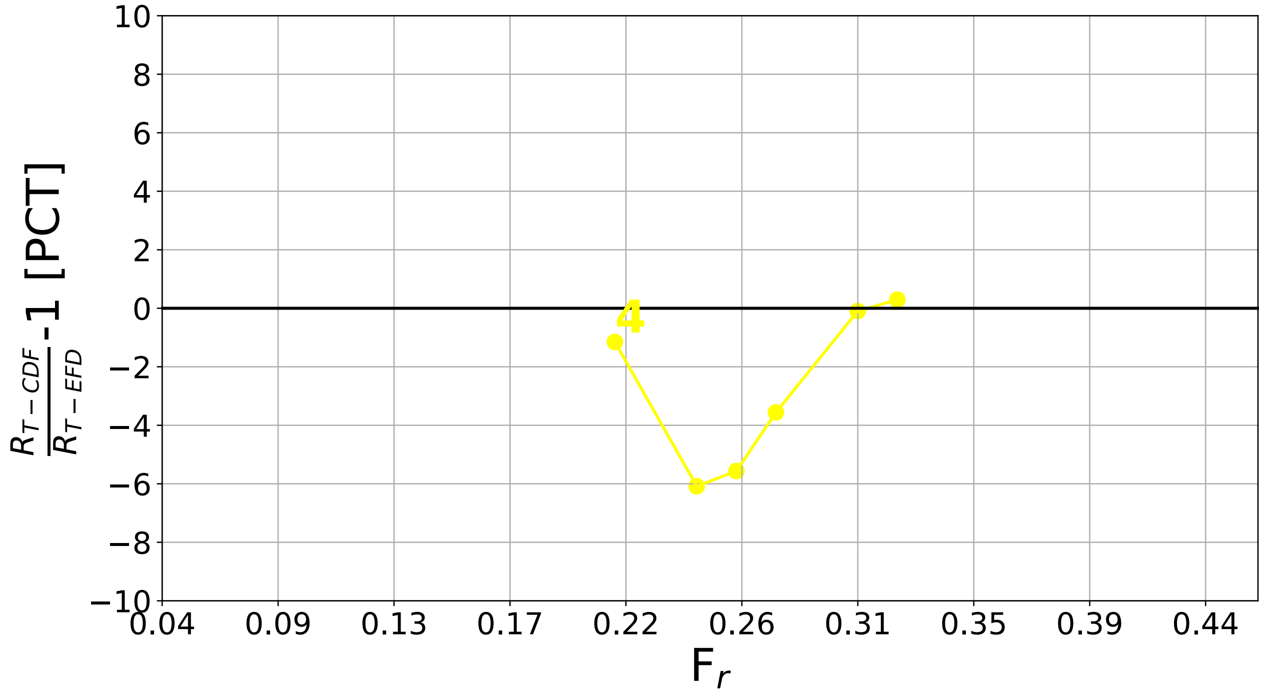

Figure 141: percentual difference between EFD results and CFD calculations, varying speed range for the model 4.

5. Hull 5.

Table 50: main characteristics for hull 5.

Model characteristics	Symbol	Values	UoM
Length between perpendiculars	L_{PP}	3.7800	m
Length, overall submerged	L_{OS}	3.7800	m
Length of waterline	L_{WL}	3.7800	m
Maximum moulded Breadth at design WL	B_{WL}	0.7480	m
Draught at forward perpendicular	T_F	0.1850	m
Draught at midship	$T_M = (T_A + T_F)/2$	0.1850	m
Draught at aft perpendicular	T_A	0.1850	m
Displacement volume	∇	0.2314	m^3
Area of wetted surface	S	2.6300	m^2
Ratio L/B	L_{WL}/B_{WL}	5.0535	-
Ratio B/T	B_{WL}/T_M	4.0432	-
Block coefficient	$C_B = \nabla/LBT$	0.4424	-
Froude's length coefficient, or length-displacement ratio	$M^C = \nabla^{1/3}$	6.1570	-
Scale ratio	$\lambda = L_s/L_M$	10.0000	-
Area of water-plane	A_W	2.0746	m^2
Longitudinal centre of flotation	L_{CF}, X_{CF}	1.7459	m
Longitudinal centre of buoyancy	L_{CB}, X_{CB}	1.7092	m

Figure 142: model scale longitudinal view for hull 5.

Table 51: towing tank and virtual towing tank results for hull 5.

RUN	Carriage speed		$10^{-3}C_{FM}[-]$		R_{TM} [N]	
	V_M [m/s]	F_r [−]	I.T.T.C. 57	CFD	EFD	CFD
1	1,100	0,181	3,502	20,639	6,767	6,868
2	1,400	0,230	3,348	12,741	11,278	11,328
3	1,700	0,279	3,232	8,641	18,633	19,158
4	2,000	0,328	3,140	6,243	30,450	32,407
5	2,400	0,394	3,040	3,196	62,959	66,131

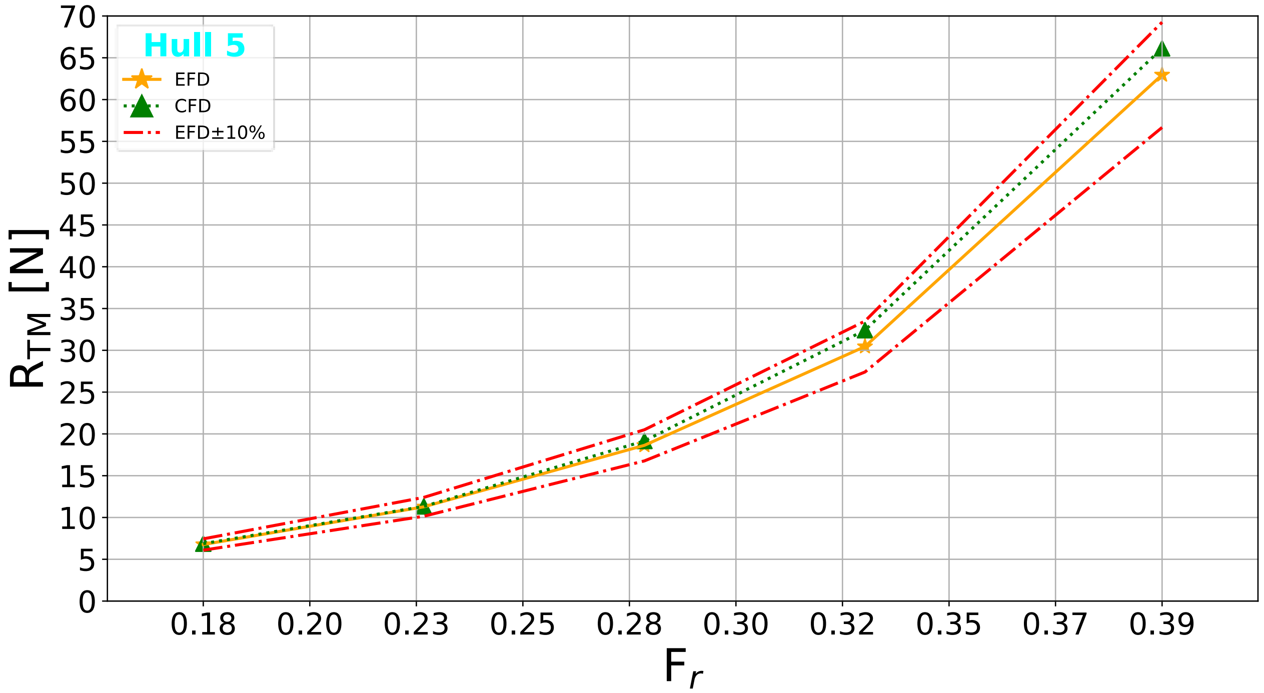

Figure 143: resistance curve, comparisons between EFD results and CFD calculations, varying speed range for the model hull 5.

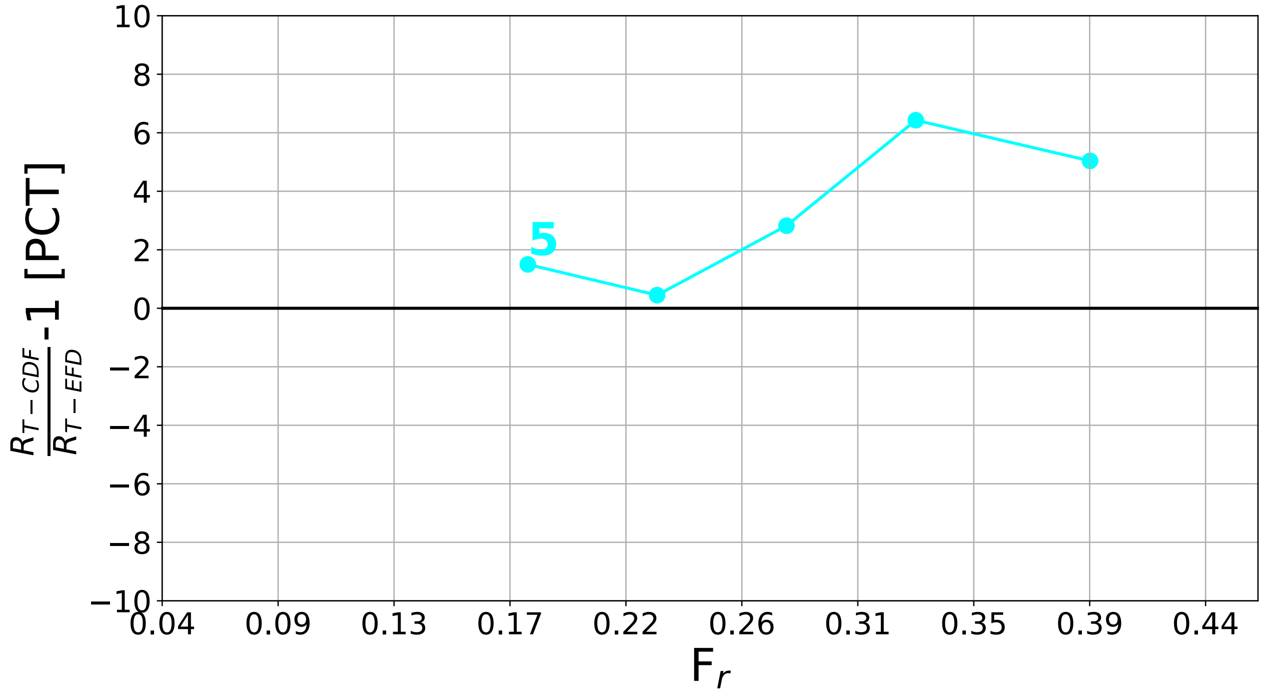

Figure 144: percentual difference between EFD results and CFD calculations, varying speed range for the model 5.

6. Hull 6, 7 and 8.

Table 52: main characteristics for hulls 6, 7 and 8.

Model characteristics	Symbol	Values Hull 06	Values Hull 07	Values Hull 08	UoM
Length between perpendiculars	L_{PP}	4,6667	4,6667	4,6667	m
Length, overall submerged	L_{OS}	4,7561	4,8387	4,6520	m
Length of waterline	L_{WL}	4,7561	4,8387	4,6520	m
Maximum moulded Breadth at design WL	B_{WL}	0,6944	0,6944	0,6900	m
Draught at forward perpendicular	T_F	0,2226	0,2600	0,1850	m
Draught at midship	$T_M = (T_A + T_F)/2$	0,2226	0,2600	0,1850	m
Draught at aft perpendicular	T_A	0,2226	0,2600	0,1850	m
Displacement volume	∇	0,3342	0,4191	0,2507	m^3
Area of wetted surface	S	3,2068	3,5707	2,8148	m^2
Ratio L/B	L_{WL}/B_{WL}	6,8488	6,9680	6,7377	-
Ratio B/T	B_{WL}/T_M	3,1203	2,6708	3,7419	-
Block coefficient	$C_B = \nabla/LBT$	0,4547	0,4798	0,4231	-
Froude's length coefficient, or length-displacement ratio	$M^C = \nabla^{1/3}$	6,8533	6,4656	7,3774	-
Scale ratio	$\lambda = L_S/L_M$	18,0000	18,0000	18,0000	-
Area of water-plane	A_W	2,2425	2,3629	2,0933	m^2
Longitudinal centre of flotation	L_{CF}, X_{CF}	2,2973	2,2212	2,2321	m
Longitudinal centre of buoyancy	L_{CB}, X_{CB}	2,1731	2,2940	2,2943	m

Figure 145: model scale longitudinal view for hulls 6, 7 and 8.

Table 53: towing tank and virtual towing tank results for hull 6.

RUN	Carriage speed		$10^{-3}C_{FM}[-]$		R_{TM} [N]	
	V_M [m/s]	F_r [−]	I.T.T.C. 57	CFD	EFD	CFD
1	1,200	0,176	3,288	13,921	8,875	8,736
2	1,400	0,205	3,198	10,228	12,209	12,110
3	1,600	0,234	3,123	7,831	16,083	16,246
4	1,800	0,264	3,058	6,187	21,182	21,467
5	2,000	0,293	3,003	5,012	27,900	29,186
6	2,200	0,322	2,954	4,142	34,912	36,558
7	2,400	0,351	2,910	2,882	45,797	46,781

Table 54: towing tank and virtual towing tank results for hull 7.

RUN	Carriage speed		$10^{-3}C_{FM}[-]$		R_{TM} [N]	
	V_M [m/s]	F_r [−]	I.T.T.C. 57	CFD	EFD	CFD
1	1,200	0,174	3,278	12,420	10,003	10,135
2	1,400	0,203	3,188	9,125	13,827	14,275
3	1,600	0,232	3,113	6,986	18,535	19,324
4	1,800	0,261	3,049	5,520	24,173	25,557
5	2,000	0,290	2,994	4,471	32,852	34,246
6	2,200	0,319	2,945	3,695	40,992	44,232
7	2,400	0,348	2,901	2,958	53,054	56,671

Table 55: towing tank and virtual towing tank results for hull 8.

RUN	Carriage speed		$10^{-3}C_{FM}[-]$		R_{TM} [N]	
	V_M [m/s]	F_r [−]	I.T.T.C. 57	CFD	EFD	CFD
1	1,200	0,178	3,301	15,902	7,600	7,402
2	1,400	0,207	3,211	11,683	10,395	10,178
3	1,600	0,237	3,135	8,945	13,631	13,533
4	2,200	0,326	2,965	4,731	29,028	28,686
5	2,500	0,370	2,901	2,886	45,111	46,138

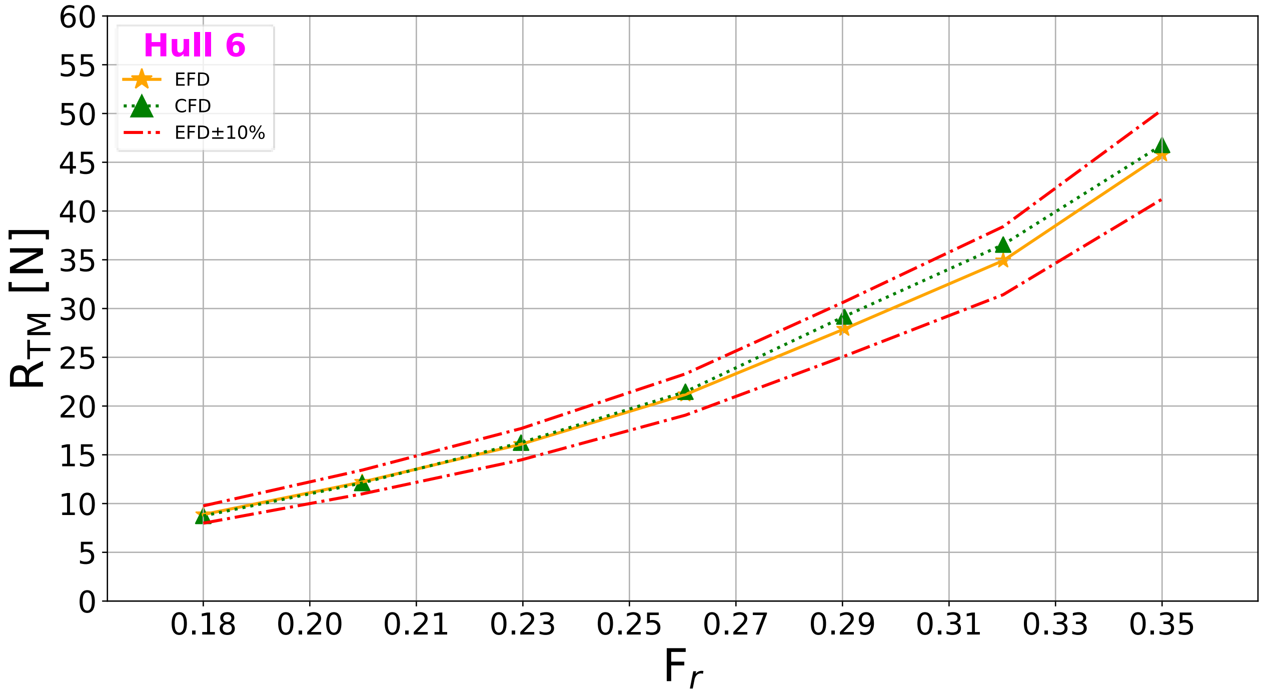

Figure 146: resistance curve, comparisons between EFD results and CFD calculations, varying speed range for the model hull 6.

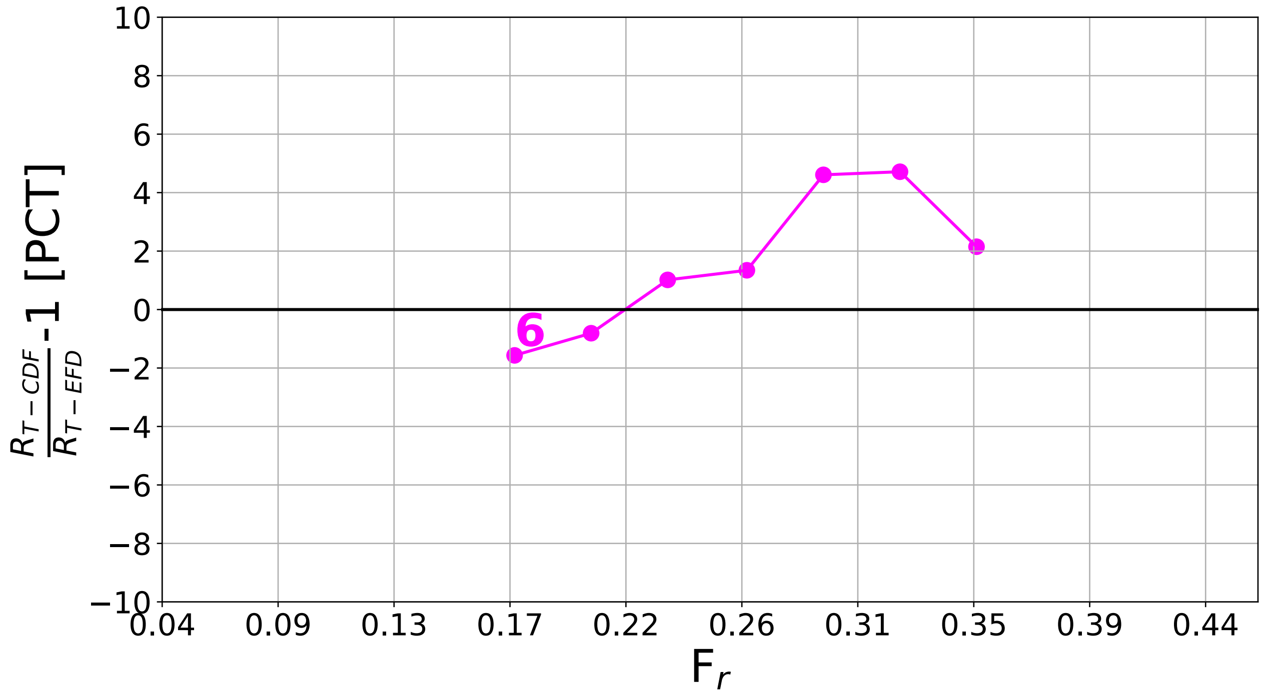

Figure 147: percentual difference between EFD results and CFD calculations, varying speed range for the model 6.

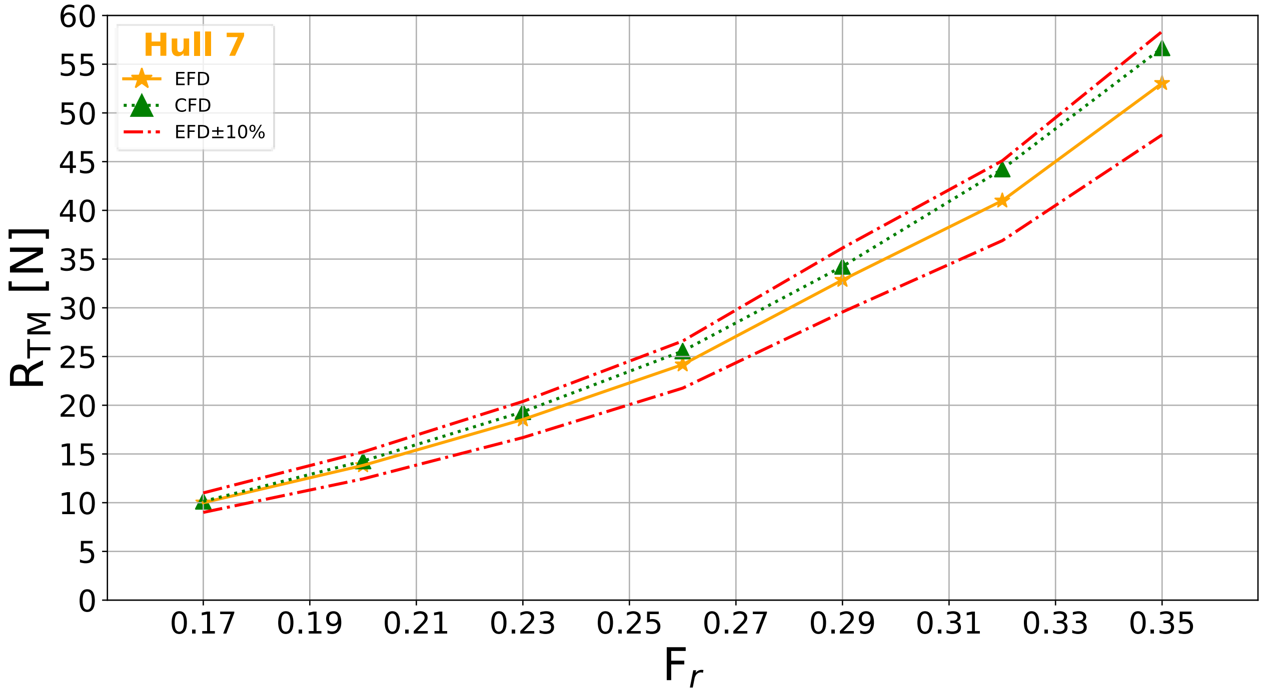

Figure 148: resistance curve, comparisons between EFD results and CFD calculations, varying speed range for the model hull 7.

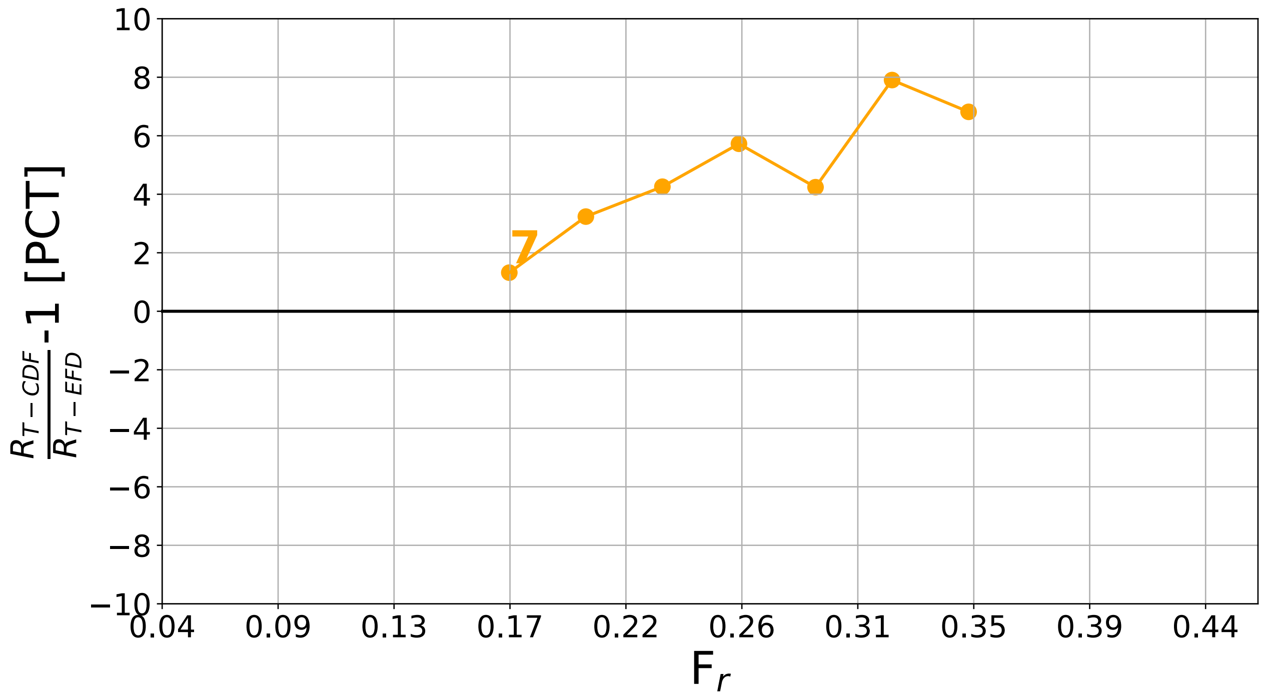

Figure 149: percentual difference between EFD results and CFD calculations, varying speed range for the model 7.

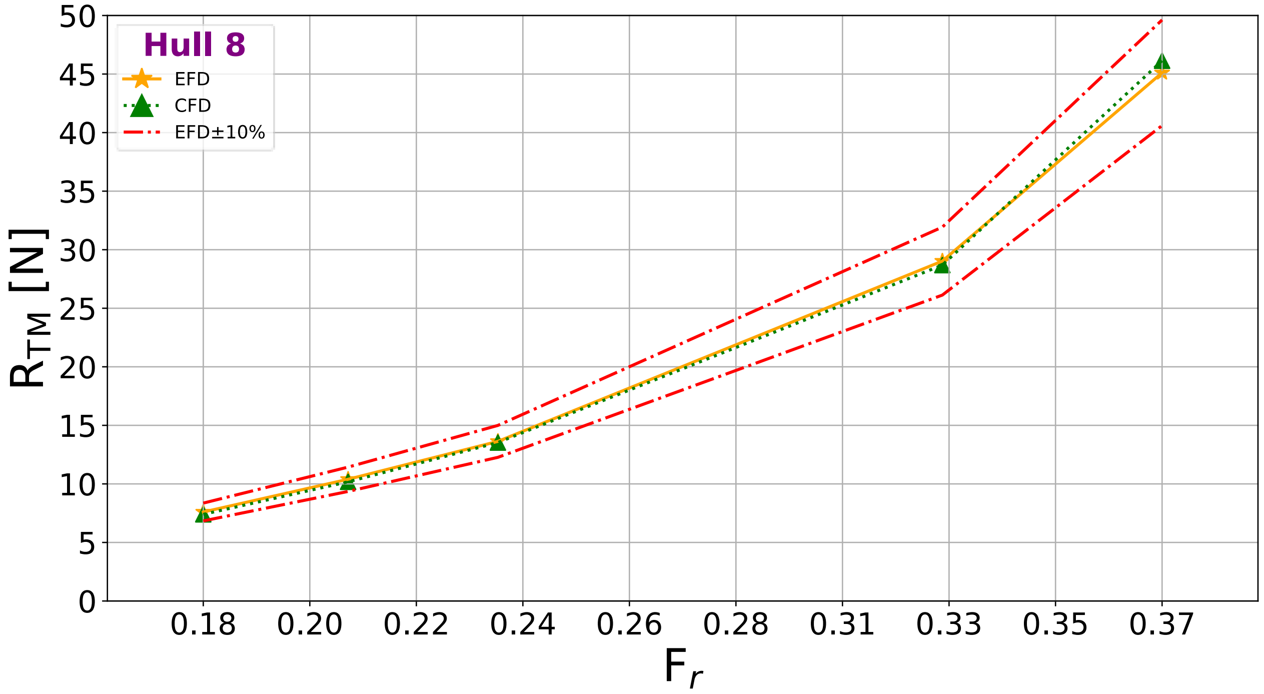

Figure 150: resistance curve, comparisons between EFD results and CFD calculations, varying speed range for the model hull 8.

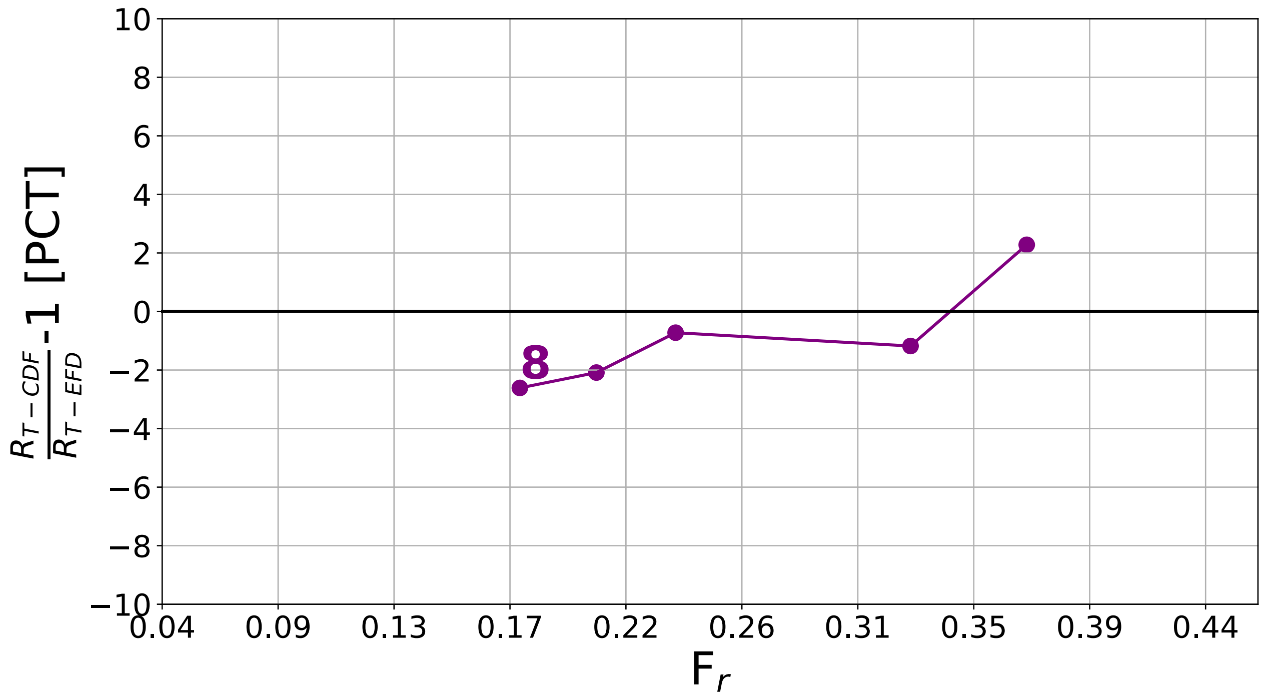

Figure 151: percentual difference between EFD results and CFD calculations, varying speed range for the model 8.

7. Hull 9.

Table 56: main characteristics for hull 9.

Model characteristics	Symbol	Values	UoM
Length between perpendiculars	L_{PP}	4,3333	m
Length, overall submerged	L_{OS}	4,3918	m
Length of waterline	L_{WL}	4,3918	m
Maximum moulded Breadth at design WL	B_{WL}	0,7500	m
Draught at forward perpendicular	T_F	0,2500	m
Draught at midship	$T_M = (T_A + T_F)/2$	0,2500	m
Draught at aft perpendicular	T_A	0,2500	m
Displacement volume	∇	0,5759	m^3
Area of wetted surface	S	4,3117	m^2
Ratio L/B	L_{WL}/B_{WL}	5,8555	-
Ratio B/T	B_{WL}/T_M	3,0000	-
Block coefficient	$C_B = \nabla/LBT$	0,6993	-
Froude's length coefficient, or length-displacement ratio	$M^C = \nabla^{1/3}$	5,2787	-
Scale ratio	$\lambda = L_s/L_M$	25,8950	-
Area of water-plane	A_W	2,6123	m^2
Longitudinal centre of flotation	L_{CF}, X_{CF}	2,2730	m
Longitudinal centre of buoyancy	L_{CB}, X_{CB}	2,1768	m

Figure 152: model scale longitudinal view for hull 9.

Table 57: towing tank and virtual towing tank results for hull 9.

RUN	Carriage speed		$10^{-3}C_{FM}[-]$		R_{TM} [N]	
	V_M [m/s]	F_r [−]	I.T.T.C. 57	CFD	EFD	CFD
1	1,012	0,154	3,443	15,282	9,120	8,569
2	1,163	0,177	3,356	11,571	11,768	11,571
3	1,404	0,214	3,243	3,275	18,927	18,090
4	1,407	0,214	3,242	7,906	18,829	18,225
5	1,539	0,235	3,190	6,608	24,909	24,600
6	1,776	0,271	3,109	4,962	46,876	48,787

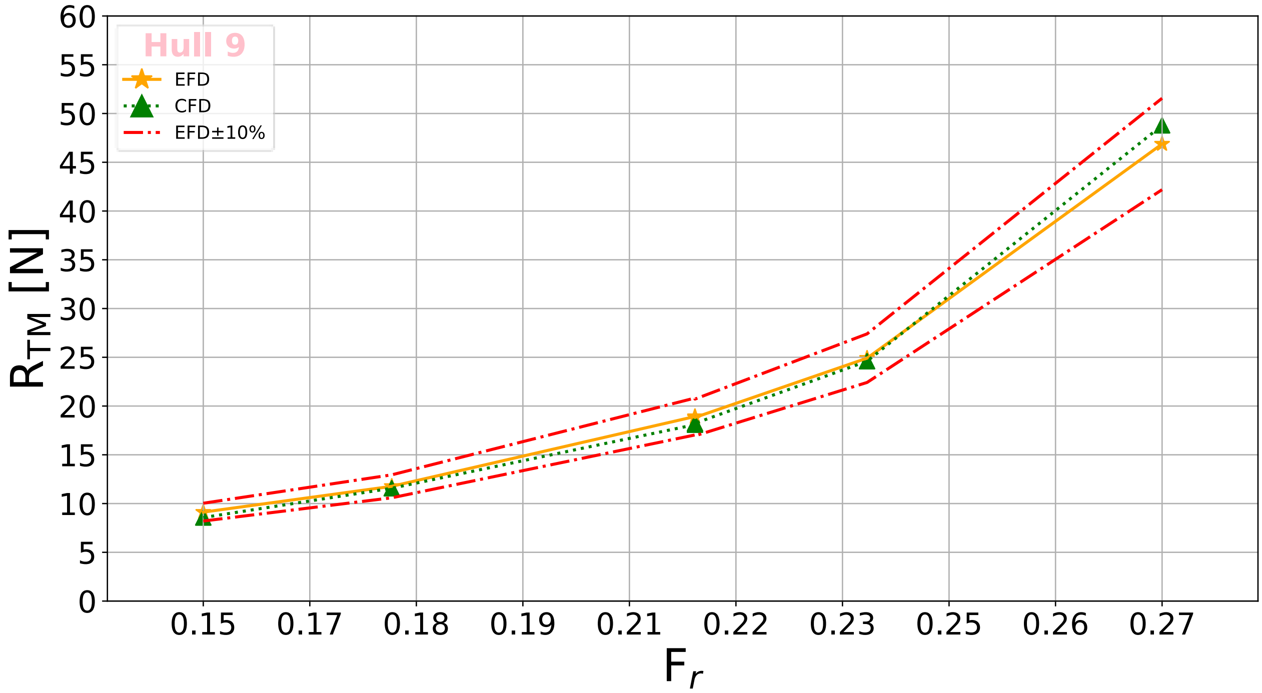

Figure 153: resistance curve, comparisons between EFD results and CFD calculations, varying speed range for the model hull 9.

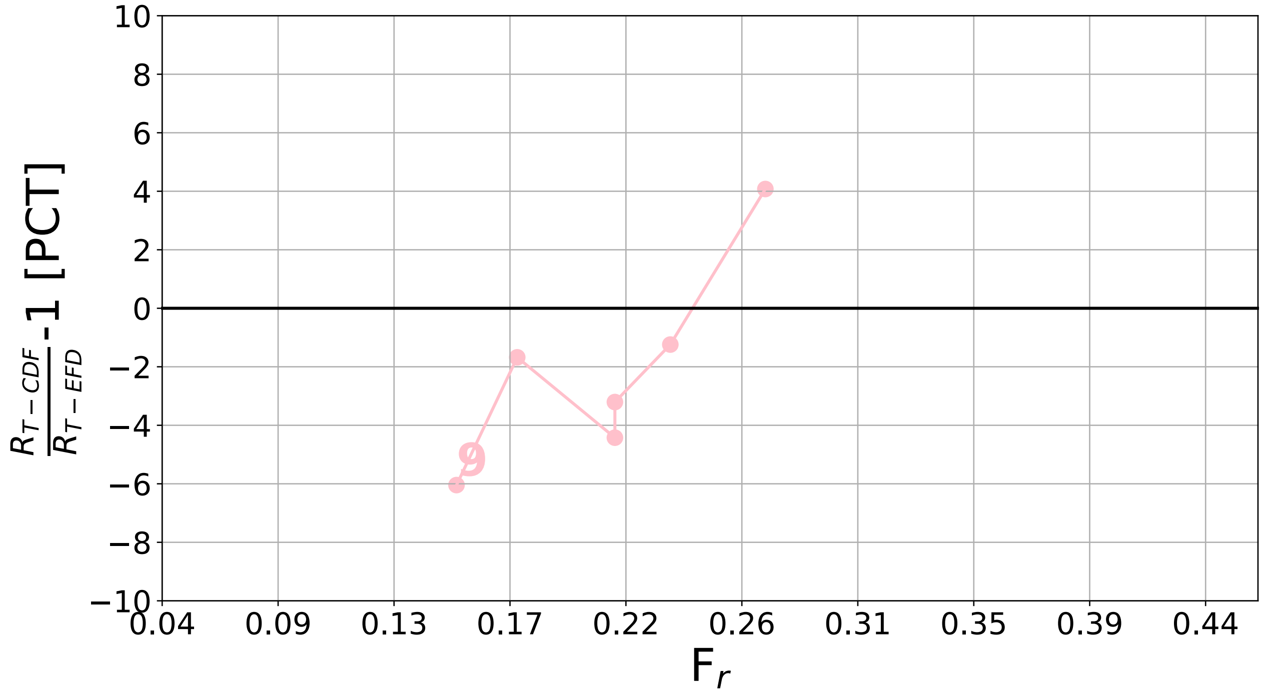

Figure 154: percentual difference between EFD results and CFD calculations, varying speed range for the model 9.

8. Hull 10.

Table 58: main characteristics for hull 10.

Model characteristics	Symbol	Values	UoM
Length between perpendiculars	L_{PP}	4,6440	m
Length, overall submerged	L_{OS}	4,7690	m
Length of waterline	L_{WL}	4,7690	m
Maximum moulded Breadth at design WL	B_{WL}	0,7880	m
Draught at forward perpendicular	T_F	0,3270	m
Draught at midship	$T_M = (T_A + T_F)/2$	0,3270	m
Draught at aft perpendicular	T_A	0,3270	m
Displacement volume	∇	0,8480	m^3
Area of wetted surface	S	5,3990	m^2
Ratio L/B	L_{WL}/B_{WL}	6,0520	-
Ratio B/T	B_{WL}/T_M	2,4098	-
Block coefficient	$C_B = \nabla/LBT$	0,6901	-
Froude's length coefficient, or length-displacement ratio	$M^C = \nabla^{1/3}$	5,0384	-
Scale ratio	$\lambda = L_s/L_M$	22,7640	-
Area of water-plane	A_W	2,9535	m^2
Longitudinal centre of flotation	L_{CF}, X_{CF}	2,3657	m
Longitudinal centre of buoyancy	L_{CB}, X_{CB}	2,2642	m

Figure 155: model scale longitudinal view for hull 10.

Table 59: towing tank and virtual towing tank results for hull 10.

RUN	Carriage speed		$10^{-3}C_{FM}[-]$		R_{TM} [N]	
	V_M [m/s]	F_r [−]	I.T.T.C. 57	CFD	EFD	CFD
1	1,039	0,152	3,390	11,387	12,160	11,069
2	1,159	0,169	3,322	9,151	14,612	13,807
3	1,330	0,194	3,240	6,949	19,711	18,361
4	1,503	0,220	3,170	5,442	26,576	25,120
5	1,533	0,224	3,159	3,125	27,998	27,092

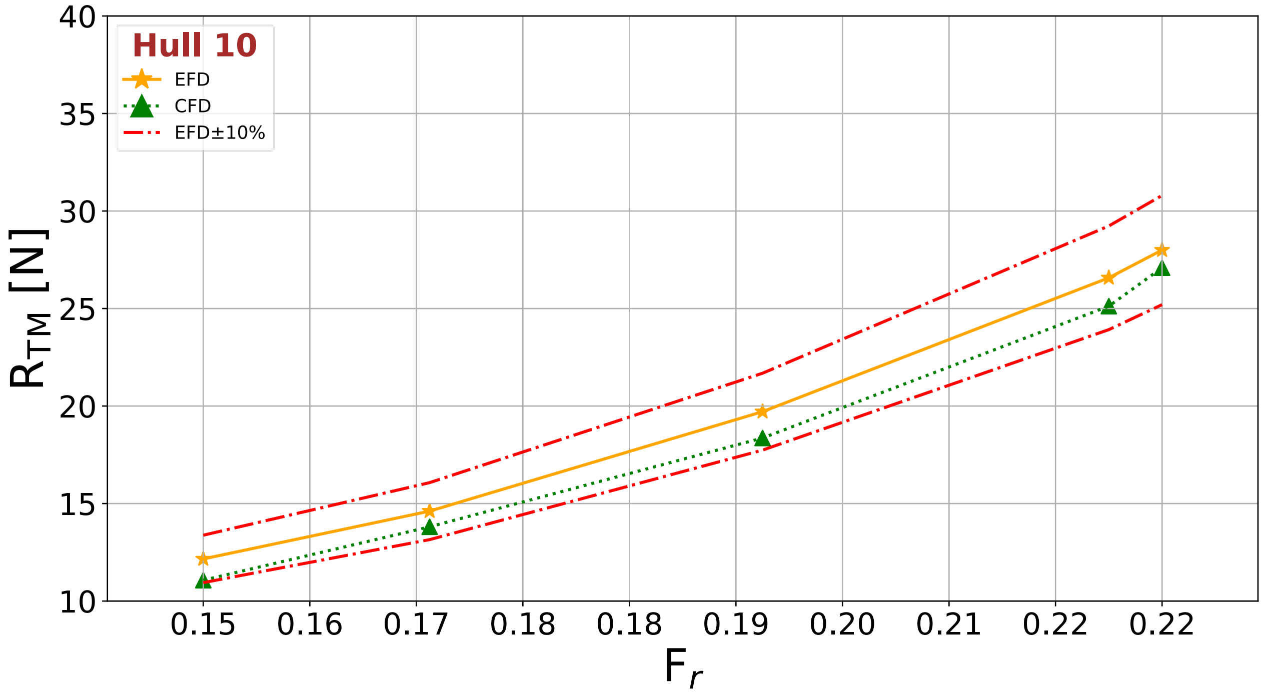

Figure 156: resistance curve, comparisons between EFD results and CFD calculations, varying speed range for the model hull 10.

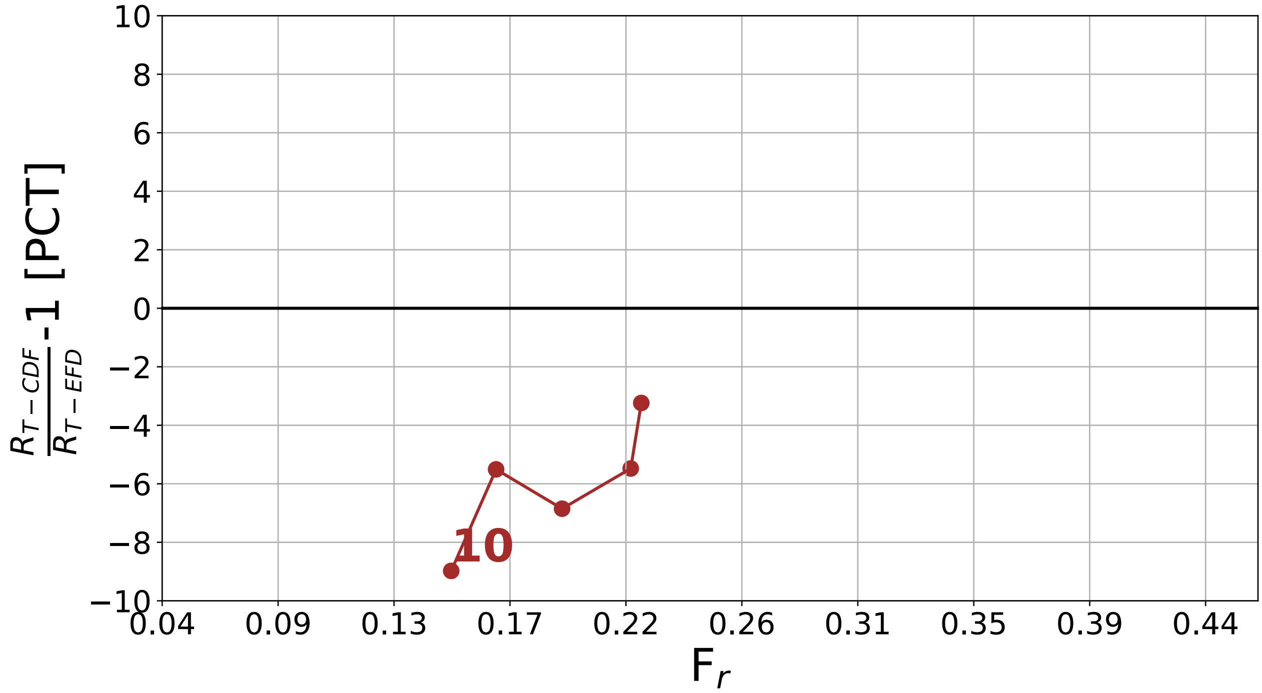

Figure 157: percentual difference between EFD results and CFD calculations, varying speed range for the model 10.

9. Hull 11.

Table 60: main characteristics for hull 11.

Model characteristics	Symbol	Values	UoM
Length between perpendiculars	L_{PP}	5,4000	m
Length, overall submerged	L_{OS}	5,5794	m
Length of waterline	L_{WL}	5,5794	m
Maximum moulded Breadth at design WL	B_{WL}	0,8390	m
Draught at forward perpendicular	T_F	0,2650	m
Draught at midship	$T_M = (T_A + T_F)/2$	0,2650	m
Draught at aft perpendicular	T_A	0,2650	m
Displacement volume	∇	0,6585	m^3
Area of wetted surface	S	4,9238	m^2
Ratio L/B	L_{WL}/B_{WL}	6,6500	-
Ratio B/T	B_{WL}/T_M	3,1699	-
Block coefficient	$C_B = \nabla/LBT$	0,5303	-
Froude's length coefficient, or length-displacement ratio	$M^C = \nabla^{1/3}$	6,4130	-
Scale ratio	$\lambda = L_s/L_M$	24,7630	-
Area of water-plane	A_W	3,2617	m^2
Longitudinal centre of flotation	L_{CF}, X_{CF}	2,6724	m
Longitudinal centre of buoyancy	L_{CB}, X_{CB}	2,4896	m

Figure 158: model scale longitudinal view for hull 11.

Table 61: towing tank and virtual towing tank results for hull 11.

RUN	Carriage speed		$10^{-3}C_{FM}[-]$		R_{TM} [N]	
	V_M [m/s]	F_r [−]	I.T.T.C. 57	CFD	EFD	CFD
1	1,828	0,247	3,102	3,957	33,146	33,197
2	2,253	0,305	2,991	2,605	53,103	53,810
3	2,323	0,314	2,975	2,450	56,928	59,463
4	2,531	0,342	2,931	2,064	72,569	76,959

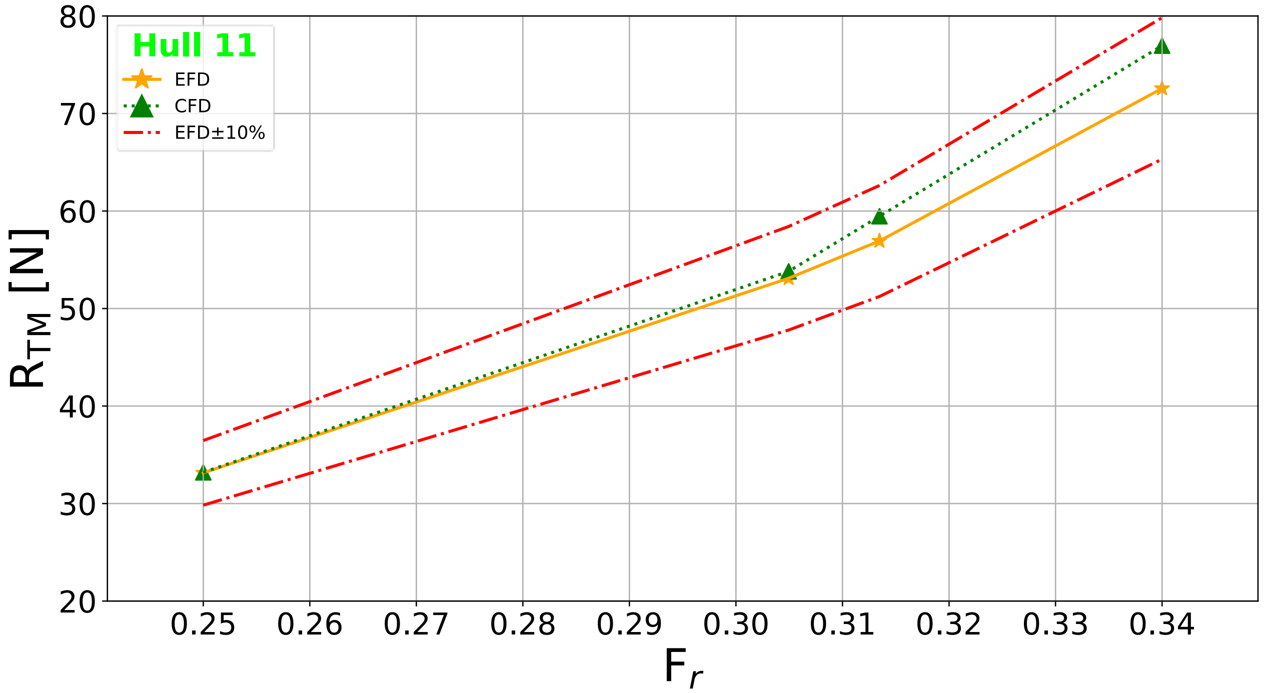

Figure 159: resistance curve, comparisons between EFD results and CFD calculations, varying speed range for the model hull 11.

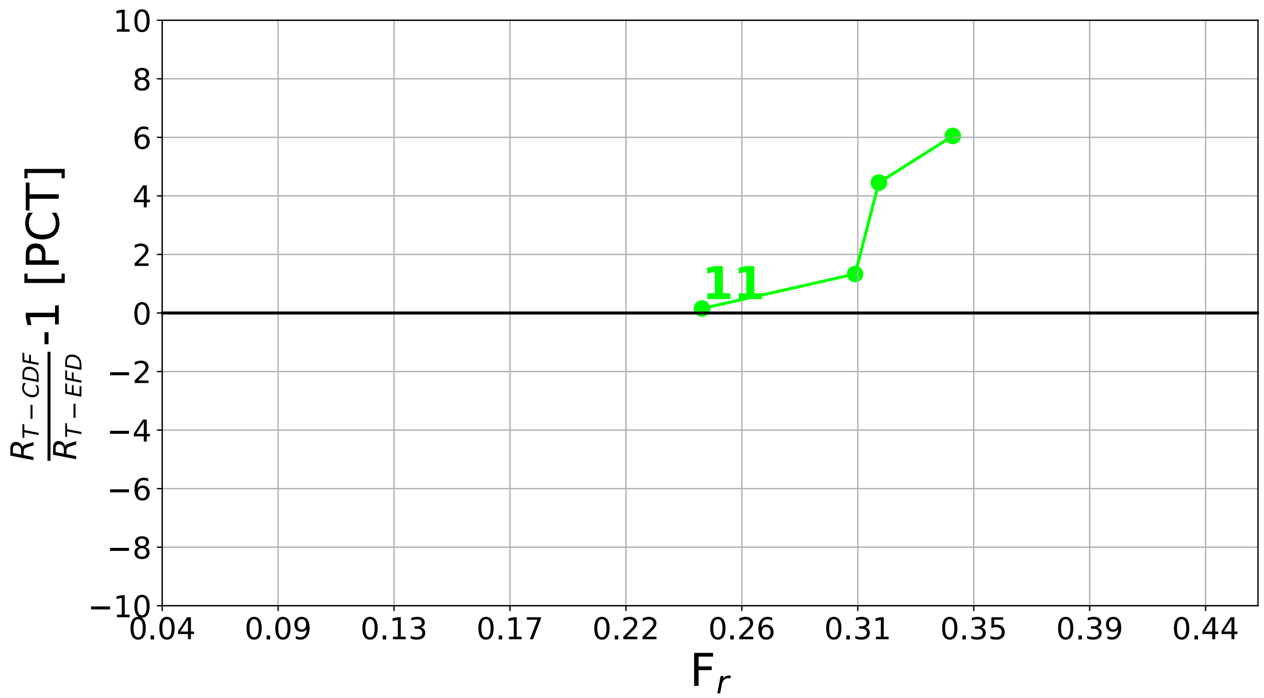

Figure 160: percentual difference between EFD results and CFD calculations, varying speed range for the model 11.

10. Hull 12 and 13.

Table 62: main characteristics for hulls 12 and 13.

Model characteristics	Symbol	Values Hull 12	Values Hull 13	UoM
Length between perpendiculars	L_{PP}	5,4000	5,4000	m
Length, overall submerged	L_{OS}	5,5703	5,5156	m
Length of waterline	L_{WL}	5,5703	5,5156	m
Maximum moulded Breadth at design WL	B_{WL}	0,8390	0,8400	m
Draught at forward perpendicular	T_F	0,2688	0,2502	m
Draught at midship	$T_M = (T_A + T_F)/2$	0,2688	0,2502	m
Draught at aft perpendicular	T_A	0,2688	0,2502	m
Displacement volume	∇	0,6585	0,5976	m^3
Area of wetted surface	S	4,9412	4,7115	m^2
Ratio L/B	L_{WL}/B_{WL}	6,6392	6,5662	-
Ratio B/T	B_{WL}/T_M	3,1246	3,3579	-
Block coefficient	$C_B = \nabla/LBT$	0,5241	0,5156	-
Froude's length coefficient, or length-displacement ratio	$M^C = \nabla^{1/3}$	6,4025	6,5484	-
Scale ratio	$\lambda = L_s/L_M$	24,7631	24,7631	-
Area of water-plane	A_W	3,2720	3,2845	m^2
Longitudinal centre of flotation	L_{CF}, X_{CF}	2,6663	2,8413	m
Longitudinal centre of buoyancy	L_{CB}, X_{CB}	2,4966	2,5529	m

Figure 161: model scale longitudinal view for hulls 12 and 13.

Table 63: towing tank and virtual towing tank results for hull 12.

RUN	Carriage speed		$10^{-3}C_{FM}[-]$		R_{TM} [N]	
	V_M [m/s]	F_r [−]	I.T.T.C. 57	CFD	EFD	CFD
1	1,830	0,248	2,967	3,905	32,754	33,907
2	2,197	0,297	2,875	2,709	50,308	53,225
3	2,394	0,324	2,834	2,282	62,763	66,811

Table 64: towing tank and virtual towing tank results for hull 13.

RUN	Carriage speed		$10^{-3}C_{FM}[-]$		R_{TM} [N]	
	V_M [m/s]	F_r [−]	I.T.T.C. 57	CFD	EFD	CFD
1	1,439	0,196	3,093	6,376	18,633	19,006
2	1,560	0,212	3,049	5,425	22,310	22,981
3	1,914	0,260	2,943	3,604	34,127	34,726
4	2,191	0,298	2,875	2,750	47,121	48,722
5	2,433	0,331	2,825	2,230	61,733	62,725
6	2,667	0,363	2,782	2,816	89,731	91,200

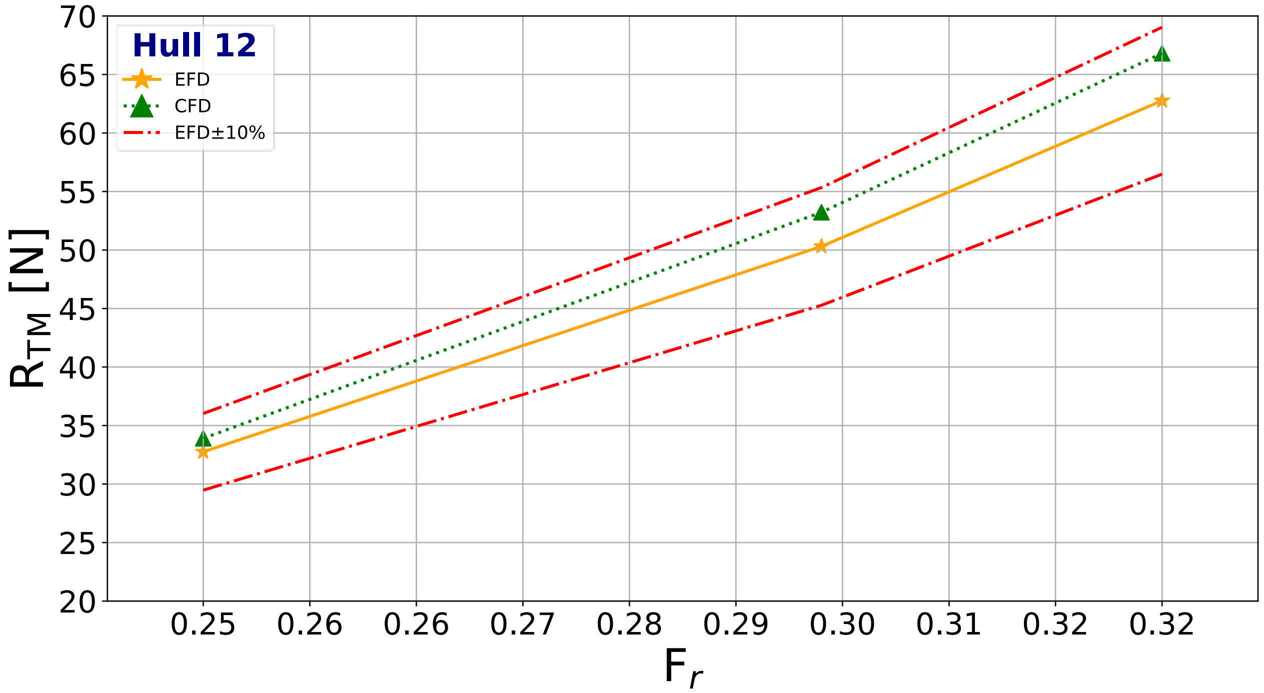

Figure 162: resistance curve, comparisons between EFD results and CFD calculations, varying speed range for the model hull 12.

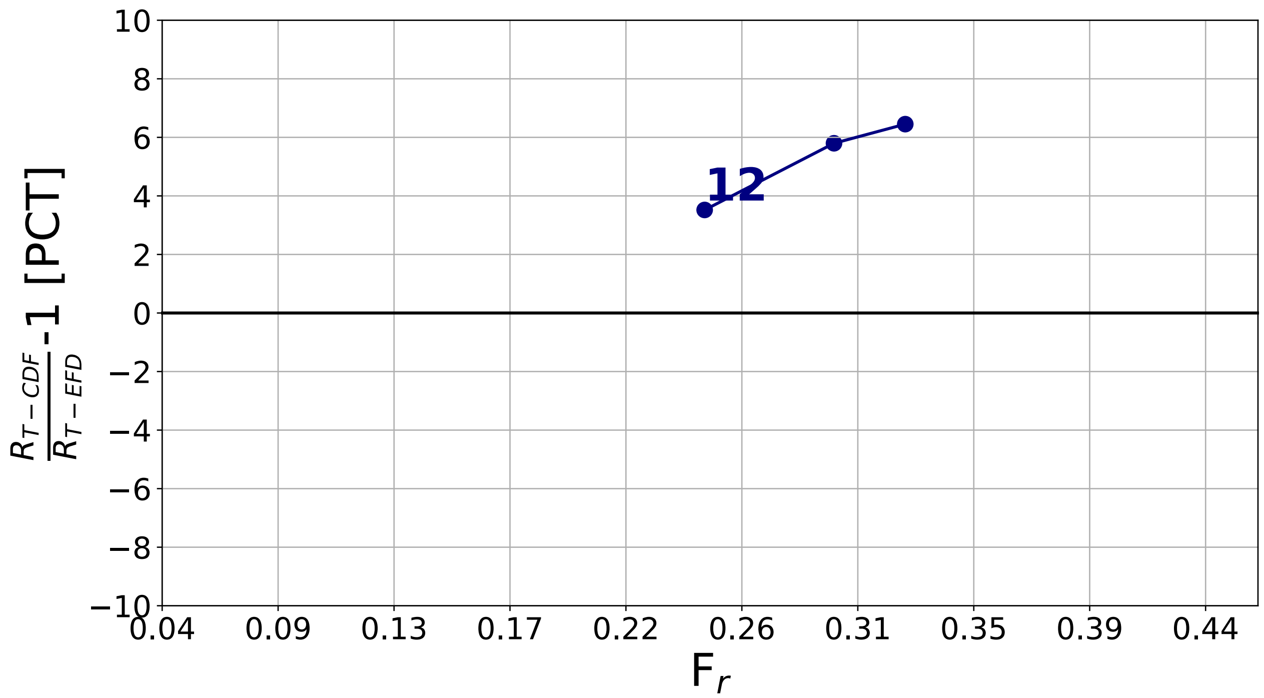

Figure 163: percentual difference between EFD results and CFD calculations, varying speed range for the model 12.

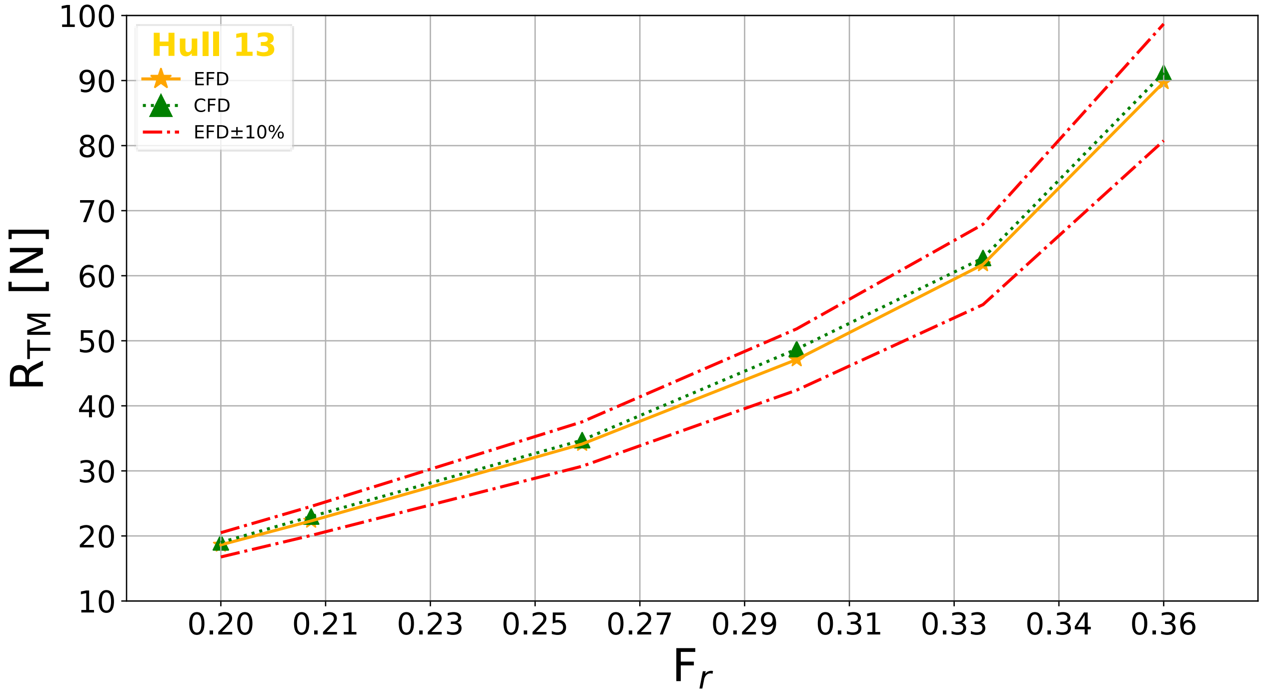

Figure 164: resistance curve, comparisons between EFD results and CFD calculations, varying speed range for the model hull 13.

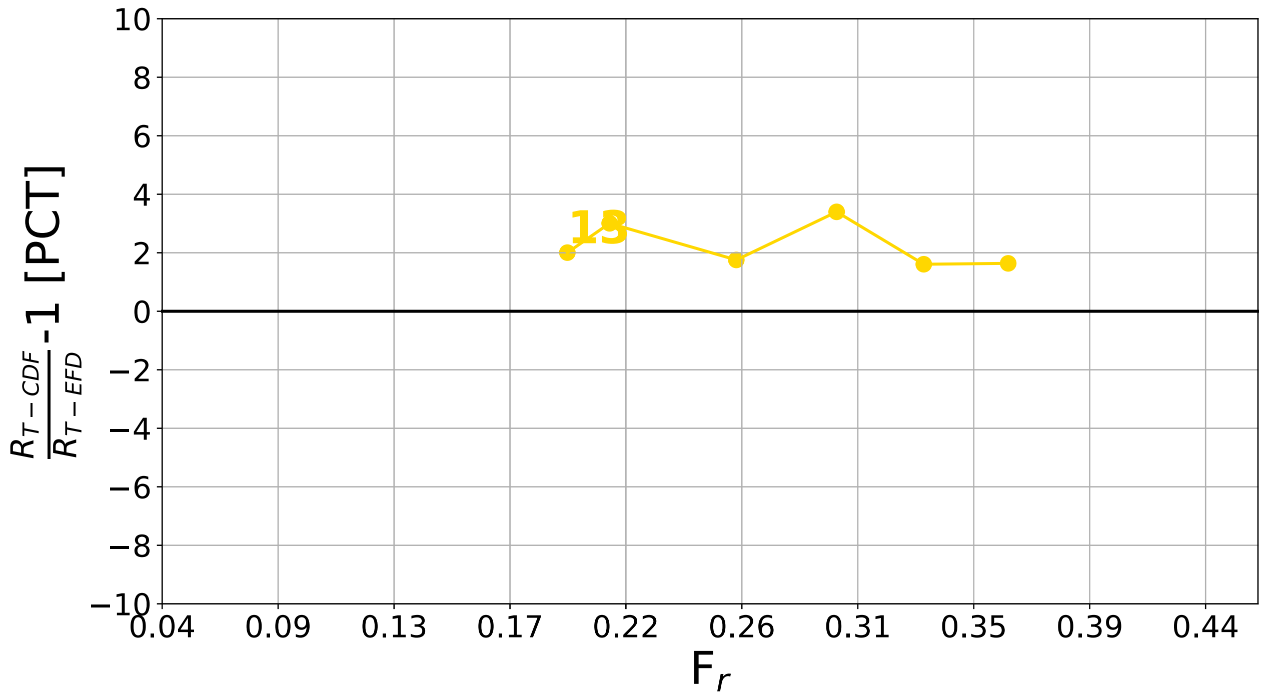

Figure 165: percentual difference between EFD results and CFD calculations, varying speed range for the model 13.

11. Hull 14.

Table 65: main characteristics for hull 14.

Model characteristics	Symbol	Values	UoM
Length between perpendiculars	L_{PP}	4,1833	m
Length, overall submerged	L_{OS}	4,2403	m
Length of waterline	L_{WL}	4,2403	m
Maximum moulded Breadth at design WL	B_{WL}	0,7533	m
Draught at forward perpendicular	T_F	0,2436	m
Draught at midship	$T_M = (T_A + T_F)/2$	0,2436	m
Draught at aft perpendicular	T_A	0,2436	m
Displacement volume	∇	0,4134	m^3
Area of wetted surface	S	3,3811	m^2
Ratio L/B	L_{WL}/B_{WL}	5,6290	-
Ratio B/T	B_{WL}/T_M	3,0925	-
Block coefficient	$C_B = \nabla/LBT$	0,5313	-
Froude's length coefficient, or length-displacement ratio	$M^C = \nabla^{1/3}$	5,6922	-
Scale ratio	$\lambda = L_s/L_M$	28,9215	-
Area of water-plane	A_W	2,3987	m^2
Longitudinal centre of flotation	L_{CF}, X_{CF}	2,2829	m
Longitudinal centre of buoyancy	L_{CB}, X_{CB}	2,1376	m

Figure 166: model scale longitudinal view for hull 14.

Table 66: towing tank and virtual towing tank results for hull 14.

RUN	Carriage speed		$10^{-3}C_{FM}[-]$		R_{TM} [N]	
	V_M [m/s]	F_r [−]	I.T.T.C. 57	CFD	EFD	CFD
1	1,591	0,247	3,310	3,184	19,221	18,709
2	1,731	0,268	3,259	3,161	24,222	23,360
3	1,992	0,309	3,178	3,104	42,414	42,514
4	2,258	0,350	3,108	3,056	59,870	59,117

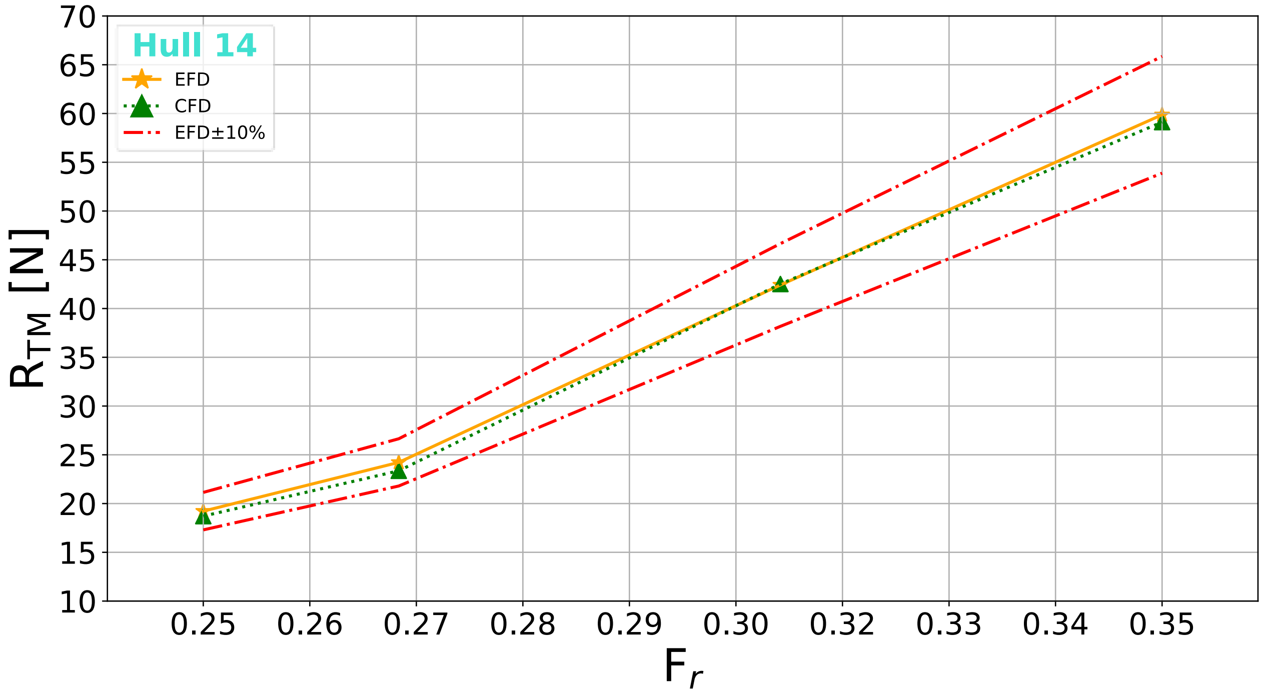

Figure 167: resistance curve, comparisons between EFD results and CFD calculations, varying speed range for the model hull 14.

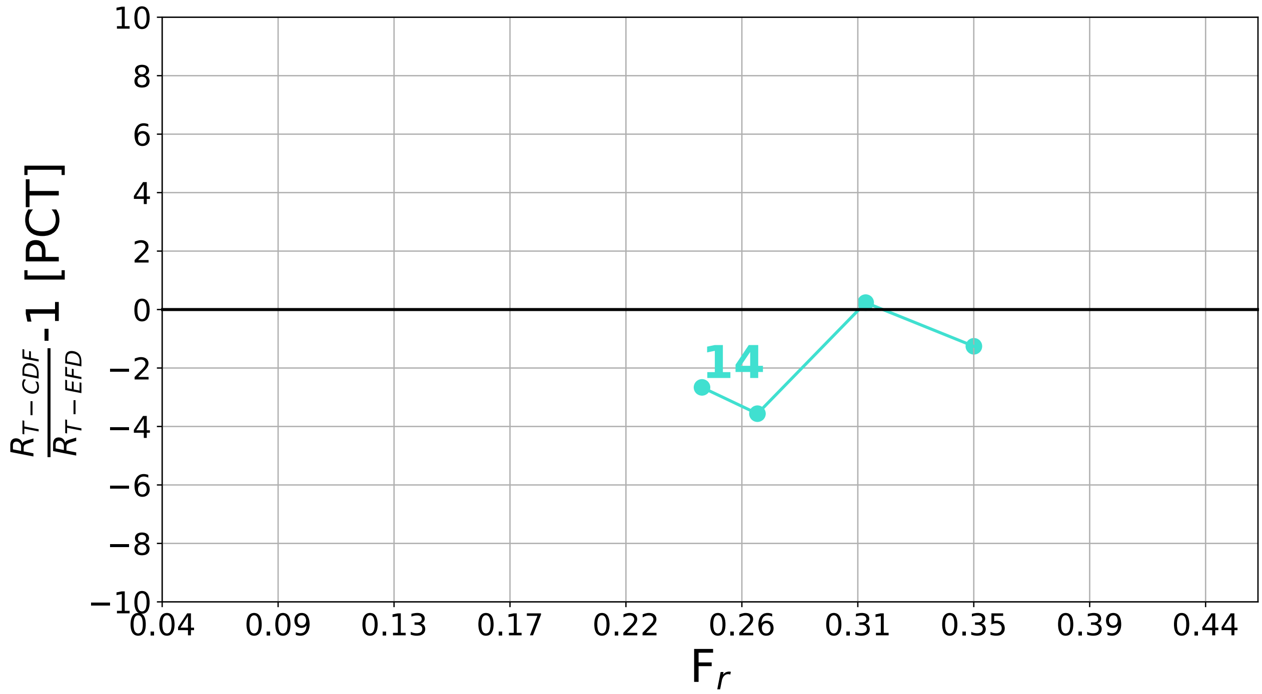

Figure 168: percentual difference between EFD results and CFD calculations, varying speed range for the model 14.

12. Hull 15.

Table 67: main characteristics for hull 15.

Model characteristics	Symbol	Values	UoM
Length between perpendiculars	L_{PP}	4,5071	m
Length, overall submerged	L_{OS}	4,8654	m
Length of waterline	L_{WL}	4,6899	m
Maximum moulded Breadth at design WL	B_{WL}	0,7715	m
Draught at forward perpendicular	T_F	0,2177	m
Draught at midship	$T_M = (T_A + T_F)/2$	0,2177	m
Draught at aft perpendicular	T_A	0,2177	m
Displacement volume	∇	0,4204	m^3
Area of wetted surface	S	3,7380	m^2
Ratio L/B	L_{WL}/B_{WL}	6,0786	-
Ratio B/T	B_{WL}/T_M	3,5440	-
Block coefficient	$C_B = \nabla/LBT$	0,5337	-
Froude's length coefficient, or length-displacement ratio	$M^C = \nabla^{1/3}$	6,2606	-
Scale ratio	$\lambda = L_s/L_M$	28,7500	-
Area of water-plane	A_W	2,5918	m^2
Longitudinal centre of flotation	L_{CF}, X_{CF}	2,1842	m
Longitudinal centre of buoyancy	L_{CB}, X_{CB}	1,9757	m

Figure 169: model scale longitudinal view for hull 15.

Table 68: towing tank and virtual towing tank results for hull 15.

RUN	Carriage speed		$10^{-3} C_{FM} [-]$		R_{TM} [N]	
	V_M [m/s]	F_r [−]	I.T.T.C. 57	CFD	EFD	CFD
1	0,672	0,097	3,774	37,982	3,373	3,384
2	1,151	0,167	3,407	12,947	9,630	9,290
3	1,535	0,222	3,233	7,279	16,867	16,555
4	1,919	0,278	3,106	4,658	26,782	26,852
5	2,303	0,333	3,009	2,937	44,640	46,091

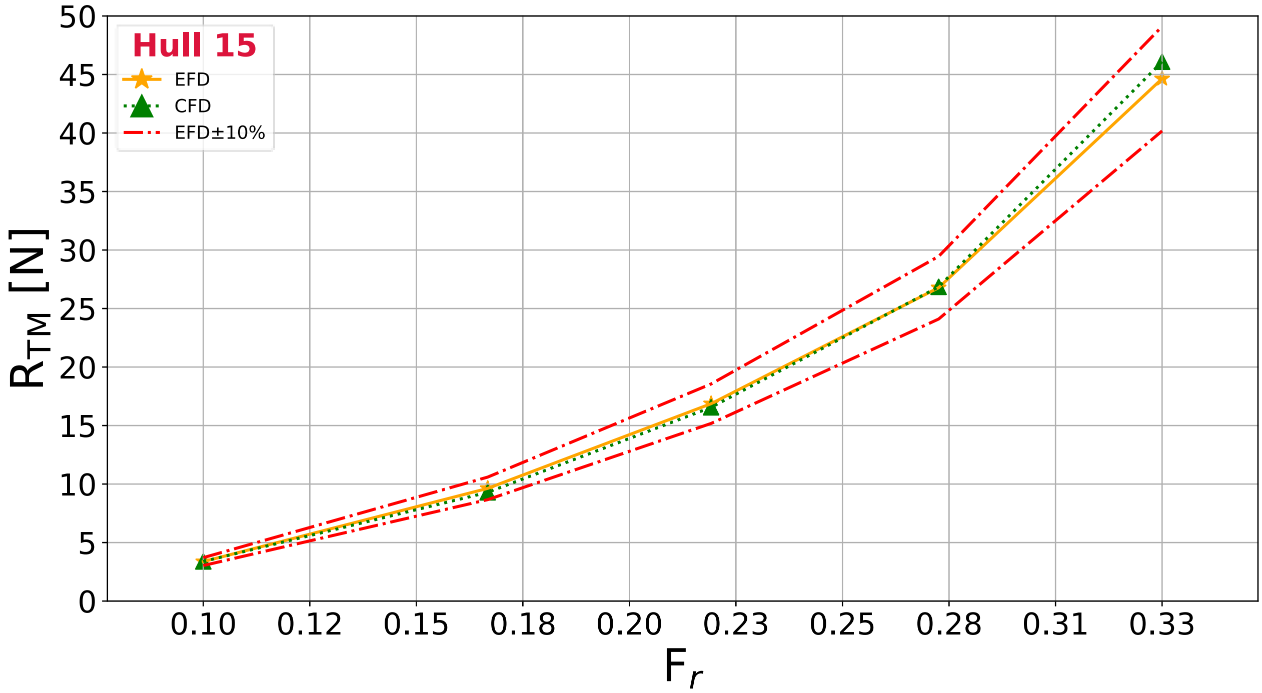

Figure 170: resistance curve, comparisons between EFD results and CFD calculations, varying speed range for the model hull 15.

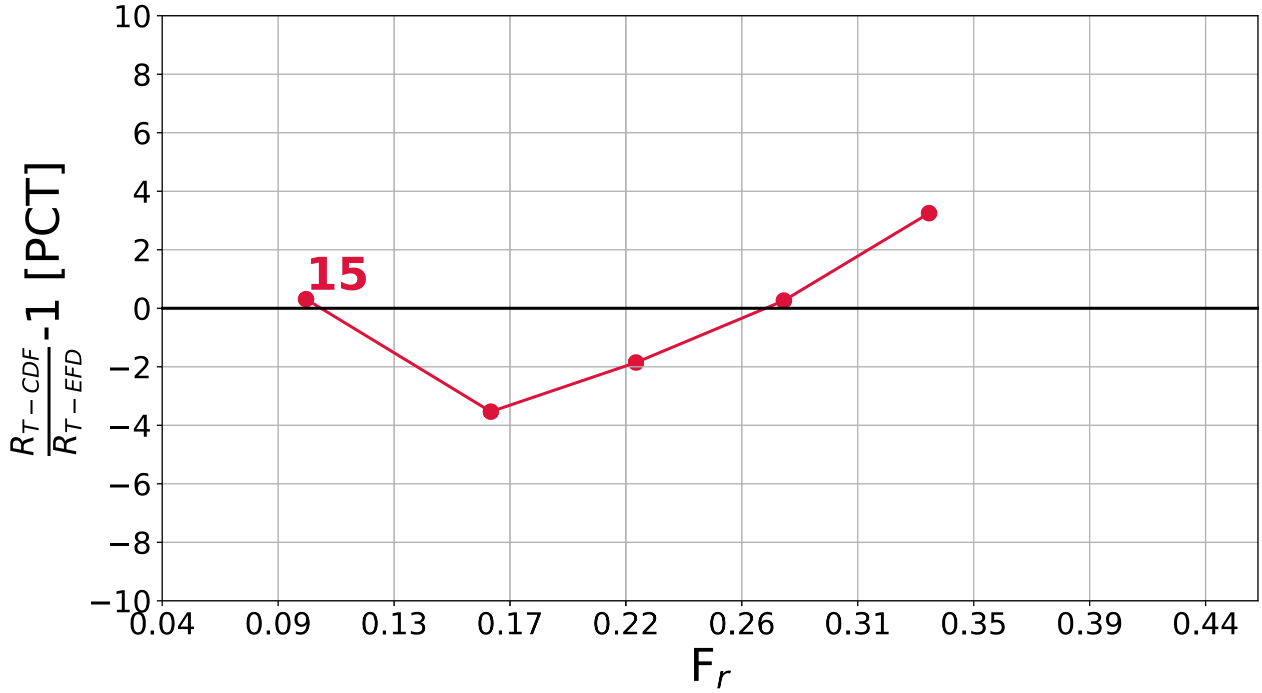

Figure 171: percentual difference between EFD results and CFD calculations, varying speed range for the model 15.

13. Hull 16.

Table 69: main characteristics for hull 16.

Model characteristics	Symbol	Values	UoM
Length between perpendiculars	L_{PP}	3,4671	m
Length, overall submerged	L_{OS}	3,7426	m
Length of waterline	L_{WL}	3,6074	m
Maximum moulded Breadth at design WL	B_{WL}	1,0030	m
Draught at forward perpendicular	T_F	0,2177	m
Draught at midship	$T_M = (T_A + T_F)/2$	0,2177	m
Draught at aft perpendicular	T_A	0,2177	m
Displacement volume	∇	0,4208	m^3
Area of wetted surface	S	3,4550	m^2
Ratio L/B	L_{WL}/B_{WL}	3,4566	-
Ratio B/T	B_{WL}/T_M	4,6073	-
Block coefficient	$C_B = \nabla/LBT$	0,5149	-
Froude's length coefficient, or length-displacement ratio	$M^C = \nabla^{1/3}$	4,8139	-
Scale ratio	$\lambda = L_s/L_M$	28,7500	-
Area of water-plane	A_W	2,5919	m^2
Longitudinal centre of flotation	L_{CF}, X_{CF}	1,6801	m
Longitudinal centre of buoyancy	L_{CB}, X_{CB}	1,5196	m

Figure 172: model scale longitudinal view for hull 16.

Table 70: towing tank and virtual towing tank results for hull 16.

RUN	Carriage speed		$10^{-3}C_{FM}[-]$		R_{TM} [N]	
	V_M [m/s]	F_r [−]	I.T.T.C. 57	CFD	EFD	CFD
1	0,480	0,079	4,256	4,037	1,844	1,946
2	0,672	0,111	3,974	41,389	3,521	3,566
3	0,863	0,142	3,783	25,096	5,707	5,573
4	1,055	0,174	3,639	16,793	8,689	8,244
5	1,535	0,253	3,391	7,932	18,741	19,444
6	2,111	0,348	3,200	4,194	54,309	55,050

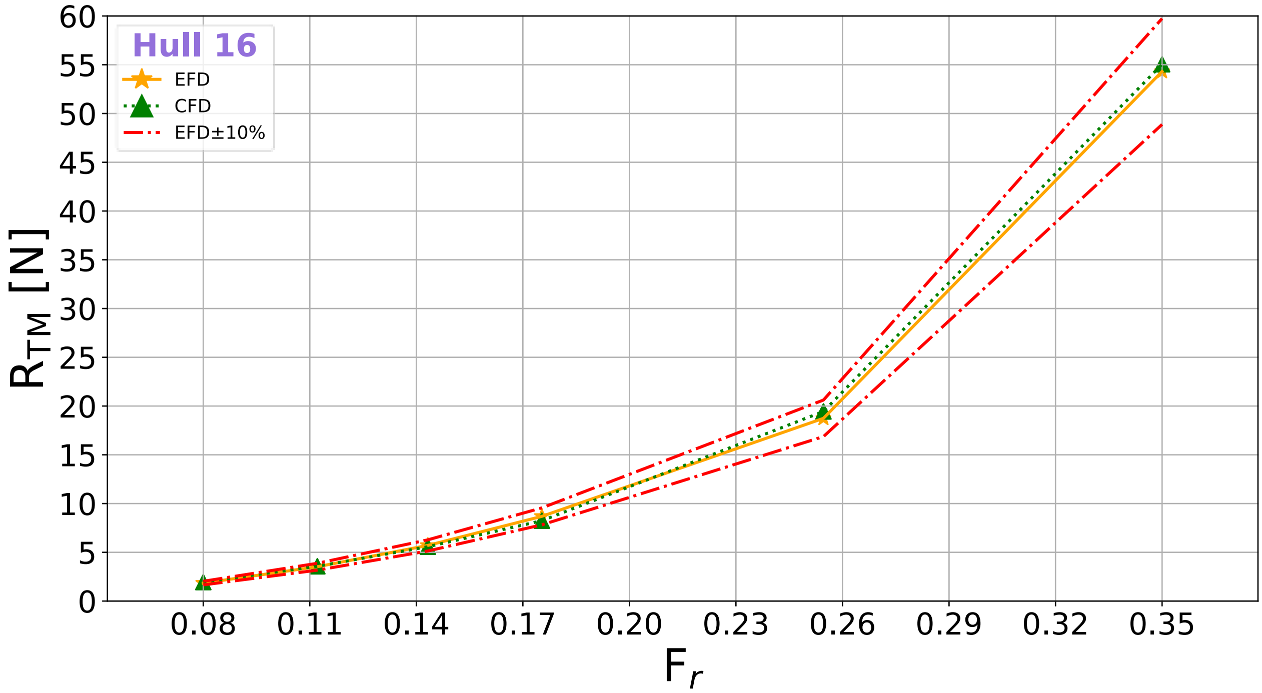

Figure 173: resistance curve, comparisons between EFD results and CFD calculations, varying speed range for the model hull 16.

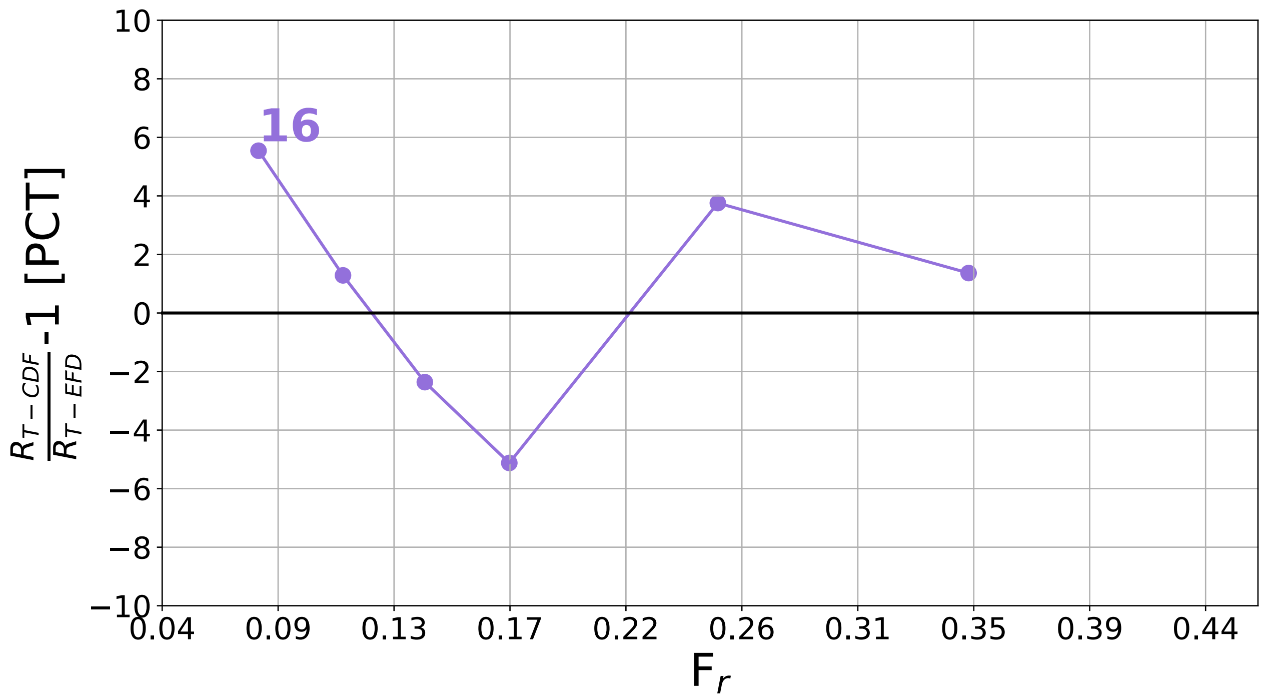

Figure 174: percentual difference between EFD results and CFD calculations, varying speed range for the model 16.

14. Hull 17 (DTMB – INSEAN model 2340).

Table 71: main characteristics for hull 17.

Model characteristics	Symbol	Values	UoM
Length between perpendiculars	L_{PP}	5,7200	m
Length, overall submerged	L_{OS}	5,7200	m
Length of waterline	L_{WL}	5,7200	m
Maximum moulded Breadth at design WL	B_{WL}	0,7600	m
Draught at forward perpendicular	T_F	0,2480	m
Draught at midship	$T_M = (T_A + T_F)/2$	0,2480	m
Draught at aft perpendicular	T_A	0,2480	m
Displacement volume	∇	0,5490	m^3
Area of wetted surface	S	4,7860	m^2
Ratio L/B	L_{WL}/B_{WL}	7,5132	-
Ratio B/T	B_{WL}/T_M	3,0682	-
Block coefficient	$C_B = \nabla/LBT$	0,5096	-
Froude's length coefficient, or length-displacement ratio	$M^C = \nabla^{1/3}$	6,9784	-
Scale ratio	$\lambda = L_s/L_M$	24,8240	-
Area of water-plane	A_W	3,3883	m^2
Longitudinal centre of flotation	L_{CF}, X_{CF}	2,8250	m
Longitudinal centre of buoyancy	L_{CB}, X_{CB}	3,1449	m

Figure 175: model scale longitudinal view for hull 17.

Table 72: towing tank and virtual towing tank results for hull 17.

RUN	Carriage speed		$10^{-3}C_{FM}[-]$		R_{TM} [N]	
	V_M [m/s]	F_r [−]	I.T.T.C. 57	CFD	EFD	CFD
1	0,374	0,050	4,010	4,301	1,667	1,801
2	0,524	0,070	3,740	3,740	2,893	2,996
3	0,674	0,090	3,570	3,484	4,403	4,568
4	1,123	0,150	3,250	3,150	12,111	12,208
5	1,947	0,260	2,950	2,913	37,559	38,016
6	2,621	0,350	2,800	2,885	80,670	80,178
7	2,921	0,390	2,750	2,863	123,387	120,035
8	3,097	0,413	2,727	2,834	158,049	152,658

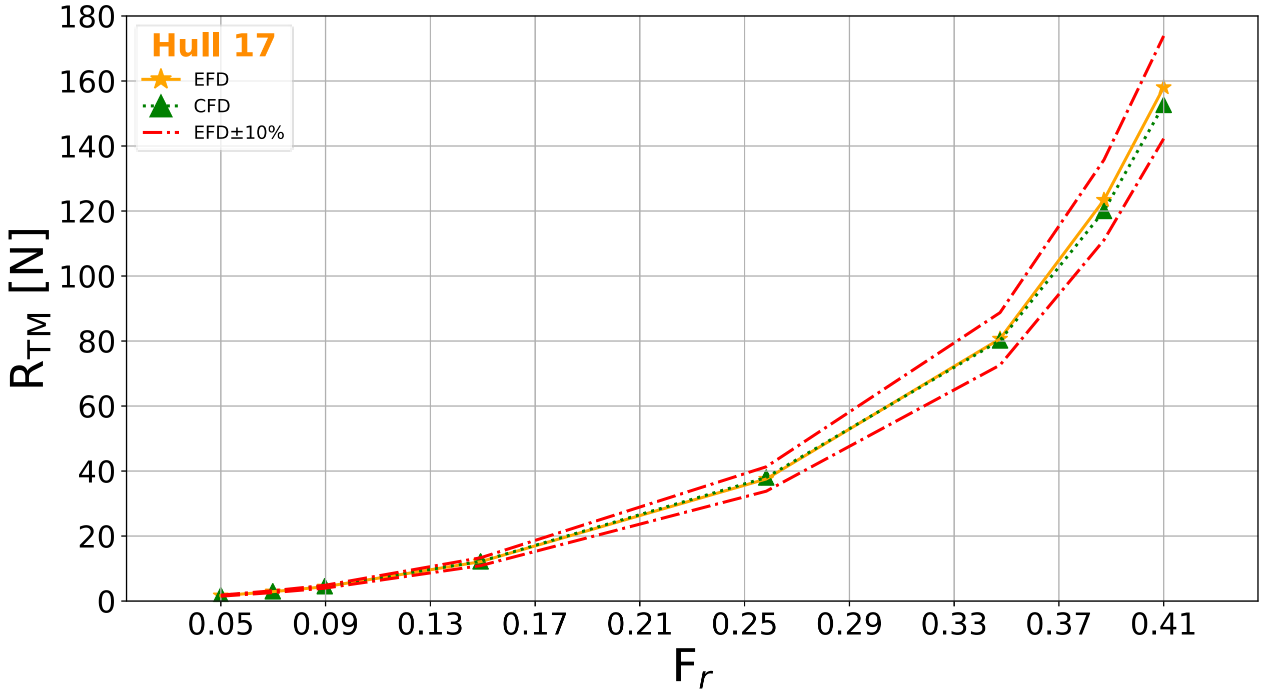

Figure 176: resistance curve, comparisons between EFD results and CFD calculations, varying speed range for the model hull 17.

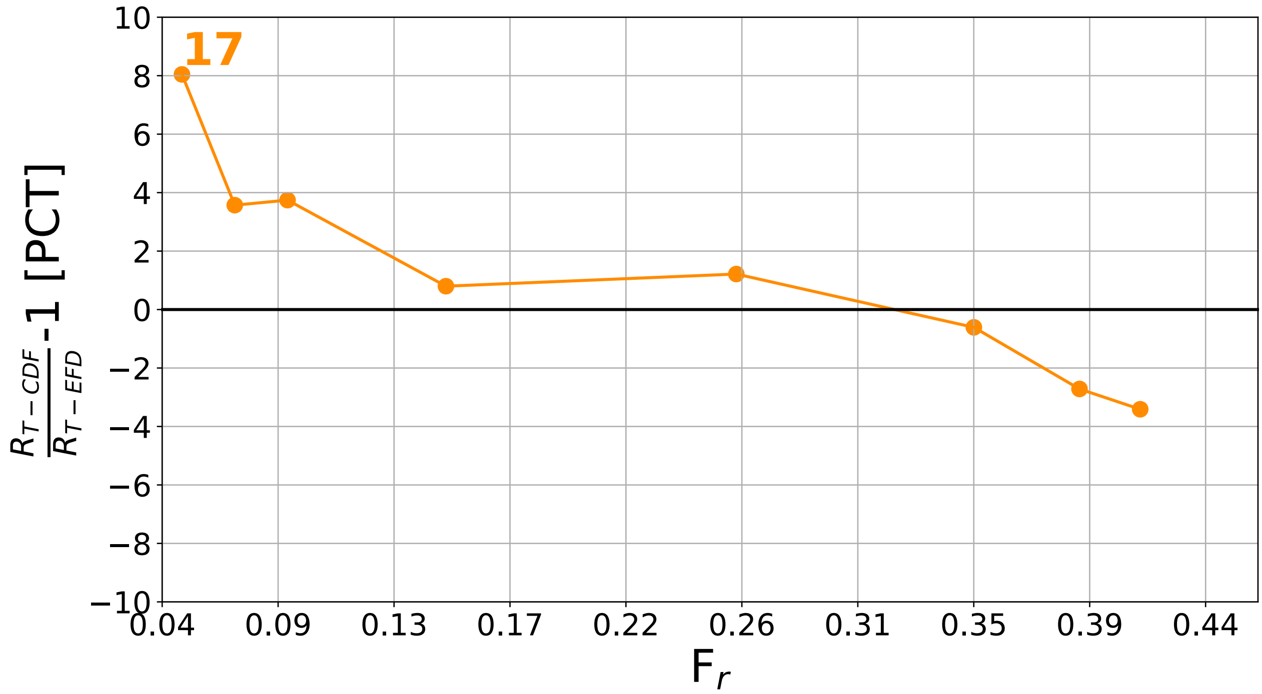

Figure 177: percentual difference between EFD results and CFD calculations, varying speed range for the model 17.

15. Hull 18 (JBC, full load condition) and 19 (JBC, ballast condition).

Table 73: main characteristics for hulls 18 and 19.

Model characteristics	Symbol	Values Hull 18	Values Hull 19	UoM
Length between perpendiculars	L_{PP}	7,0000	7,0000	m
Length, overall submerged	L_{OS}	7,1250	7,1250	m
Length of waterline	L_{WL}	7,1250	7,1250	m
Maximum moulded Breadth at design WL	B_{WL}	1,1250	1,1250	m
Draught at forward perpendicular	T_F	0,4125	0,1804	m
Draught at midship	$T_M = (T_A + T_F)/2$	0,4125	0,2154	m
Draught at aft perpendicular	T_A	0,4125	0,2504	m
Displacement volume	∇	2,7910	1,3941	m^3
Area of wetted surface	S	12,4558	9,3782	m^2
Ratio L/B	L_{WL}/B_{WL}	6,3333	6,3333	-
Ratio B/T	B_{WL}/T_M	2,7273	5,2234	-
Block coefficient	$C_B = \nabla/LBT$	0,8441	0,8075	-
Froude's length coefficient, or length-displacement ratio	$M^C = \nabla^{1/3}$	5,0605	6,3780	-
Scale ratio	$\lambda = L_S/L_M$	40,0000	40,0000	-
Area of water-plane	A_W	7,2862	6,8267	m^2
Longitudinal centre of flotation	L_{CF}, X_{CF}	3,6766	3,6065	m
Longitudinal centre of buoyancy	L_{CB}, X_{CB}	3,4554	3,6886	m

Figure 178: model scale longitudinal view for hulls 18 and 19.

Table 74: towing tank and virtual towing tank results for hull 18.

RUN	Carriage speed		$10^{-3}C_{FM}[-]$		R_{TM} [N]	
	V_M [m/s]	F_r [−]	I.T.T.C. 57	CFD	EFD	CFD
1	0,738	0,088	3,394	3,428	15,396	16,432
2	0,822	0,098	3,332	3,479	18,756	20,056
3	0,897	0,107	3,282	3,381	22,234	23,048
4	0,984	0,118	3,231	0,000	26,316	26,956
5	1,060	0,127	3,191	3,234	30,510	30,976
6	1,145	0,137	3,149	3,197	35,290	35,831
7	1,183	0,142	3,132	3,191	37,627	38,297
8	1,220	0,146	3,116	3,170	40,286	40,913
9	0,982	0,118	3,328	3,305	26,195	26,987
10	1,189	0,142	3,214	3,193	38,039	38,945

Table 75: towing tank and virtual towing tank results for hull 19.

RUN	Carriage speed		$10^{-3}C_{FM}[-]$		R_{TM} [N]	
	V_M [m/s]	F_r [−]	I.T.T.C. 57	CFD	EFD	CFD
1	0,729	0,088	3,369	3,394	10,996	11,169
2	0,812	0,098	3,307	3,334	13,521	13,682
3	0,895	0,108	3,252	3,342	16,259	16,711
4	0,976	0,118	3,205	0,000	19,352	20,008
5	1,056	0,128	3,163	3,298	22,798	23,387
6	1,131	0,137	3,127	3,274	26,197	27,167
7	1,216	0,147	3,089	3,203	30,484	30,957
8	1,254	0,152	3,074	3,189	32,593	32,878
9	1,293	0,157	3,058	3,180	34,893	35,163
10	0,980	0,119	3,203	3,337	19,510	20,149
11	1,137	0,138	3,124	3,143	26,424	25,944
12	1,271	0,154	3,067	3,075	33,533	32,467

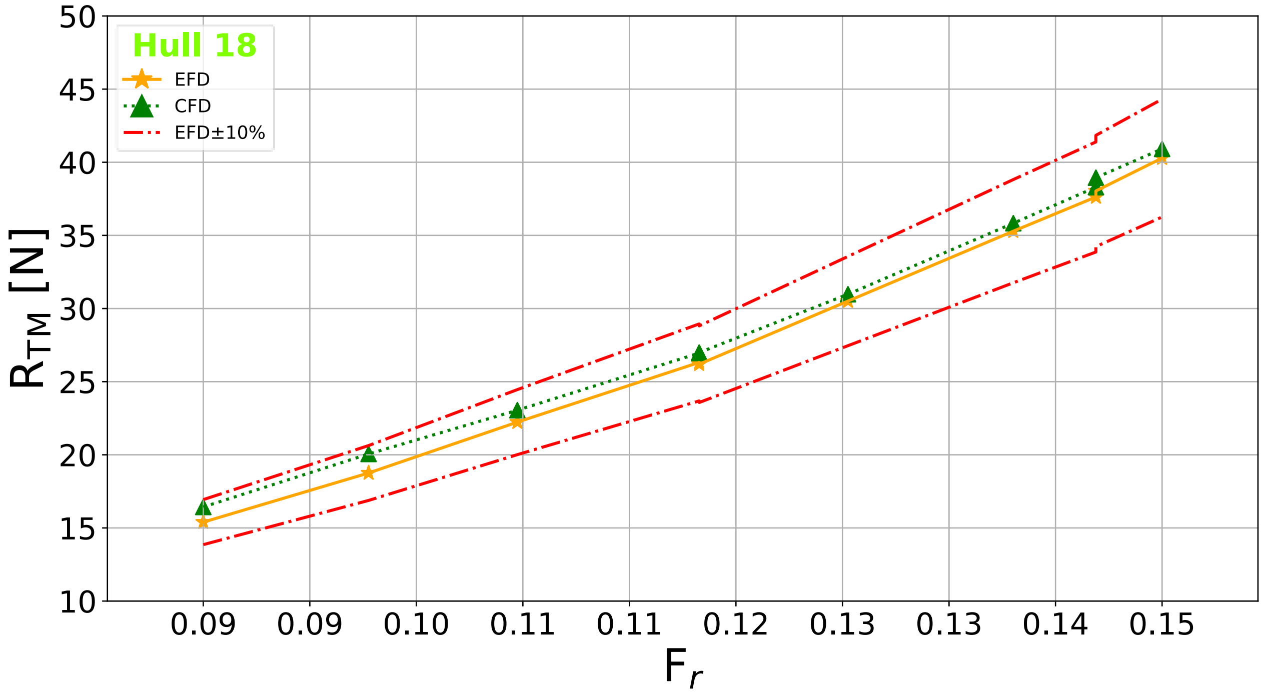

Figure 179: resistance curve, comparisons between EFD results and CFD calculations, varying speed range for the model hull 18.

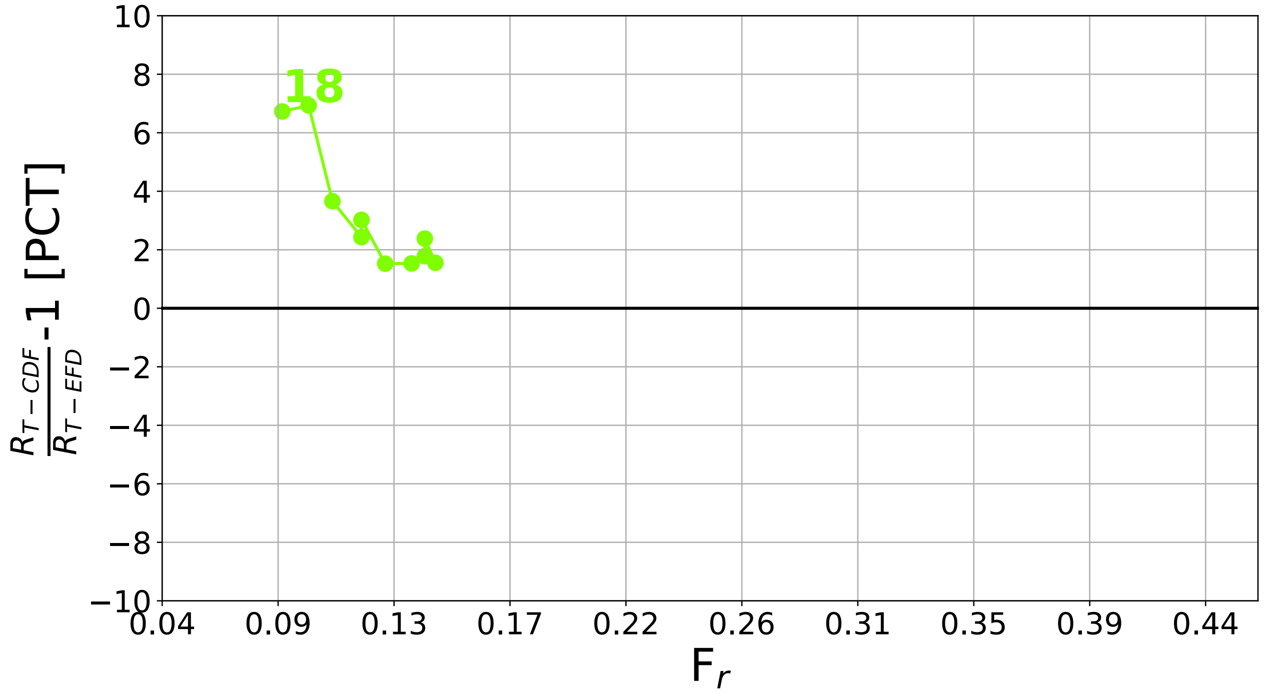

Figure 180: percentual difference between EFD results and CFD calculations, varying speed range for the model 18.

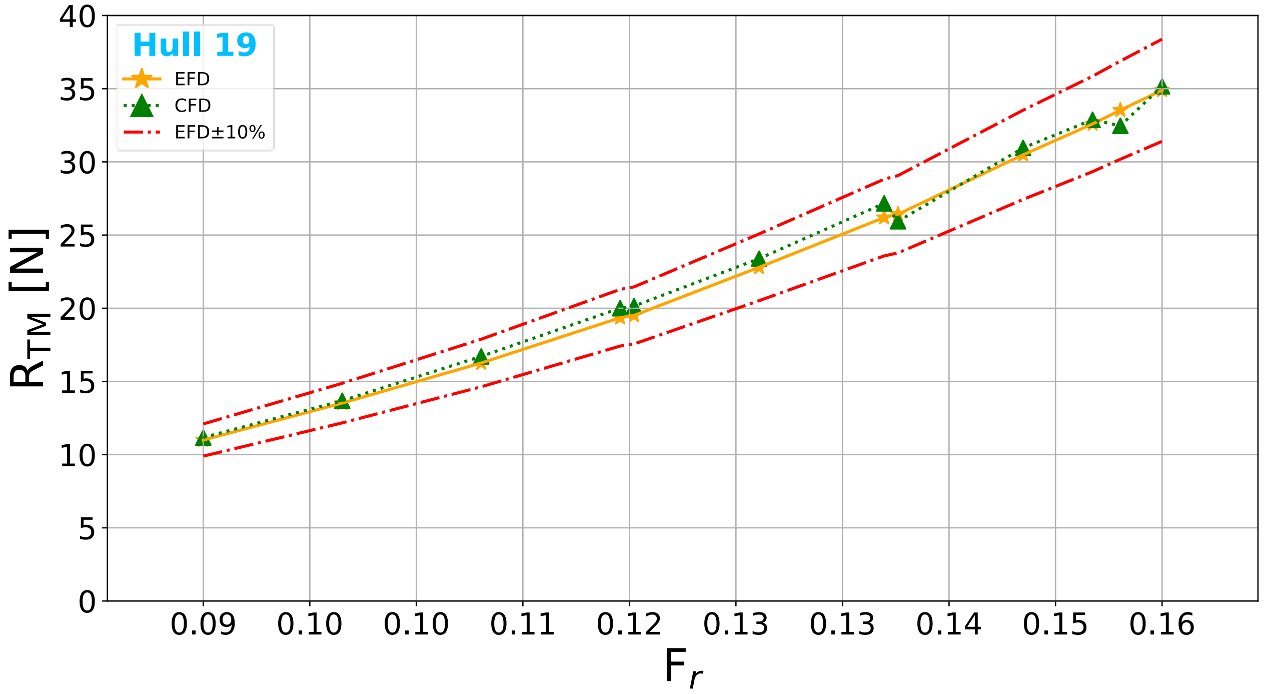

Figure 181: resistance curve, comparisons between EFD results and CFD calculations, varying speed range for the model hull 19.

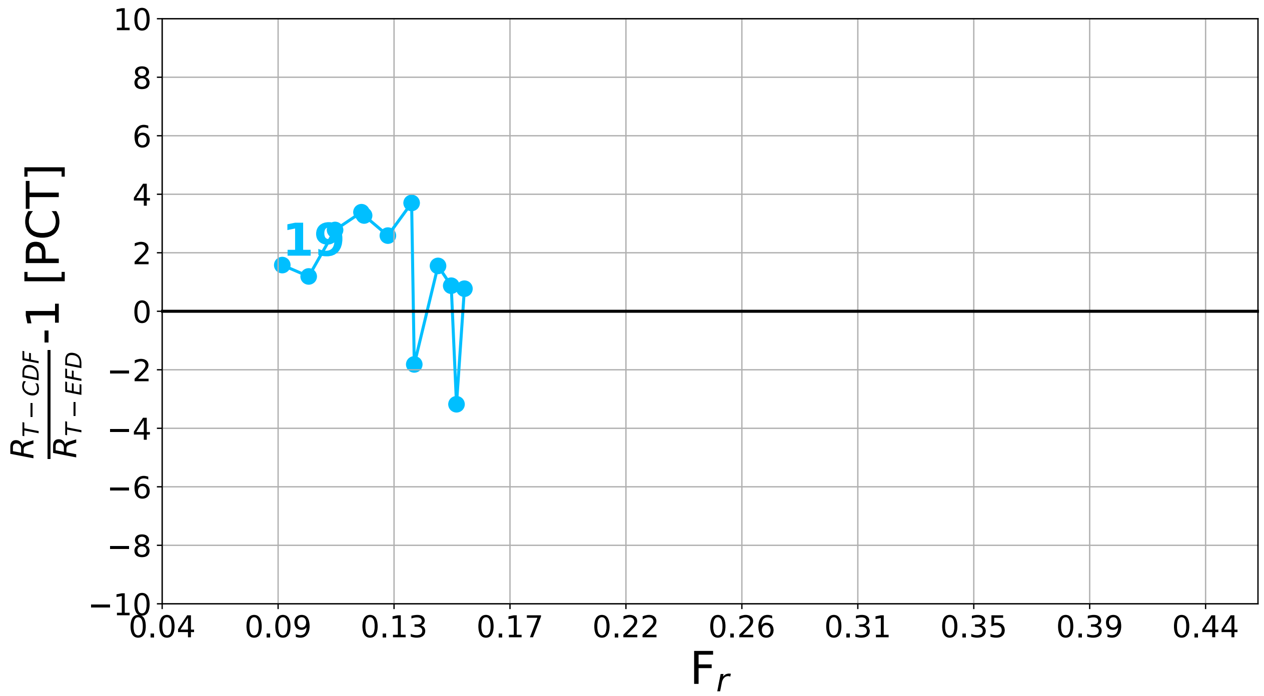

Figure 182: percentual difference between EFD results and CFD calculations, varying speed range for the model 19.

16. Hull 20 (KCS).

Table 76: main characteristics for hull 20.

Model characteristics	Symbol	Values	UoM
Length between perpendiculars	L_{PP}	7,2785	m
Length, overall submerged	L_{OS}	7,3288	m
Length of waterline	L_{WL}	7,3288	m
Maximum moulded Breadth at design WL	B_{WL}	1,0190	m
Draught at forward perpendicular	T_F	0,3418	m
Draught at midship	$T_M = (T_A + T_F)/2$	0,3418	m
Draught at aft perpendicular	T_A	0,3418	m
Displacement volume	∇	1,6489	m^3
Area of wetted surface	S	9,6589	m^2
Ratio L/B	L_{WL}/B_{WL}	7,2205	-
Ratio B/T	B_{WL}/T_M	2,9815	-
Block coefficient	$C_B = \nabla/LBT$	0,6435	-
Froude's length coefficient, or length-displacement ratio	$M^C = \nabla^{1/3}$	6,2279	-
Scale ratio	$\lambda = L_s/L_M$	31,5995	-
Area of water-plane	A_W	6,1622	m^2
Longitudinal centre of flotation	L_{CF}, X_{CF}	3,5295	m
Longitudinal centre of buoyancy	L_{CB}, X_{CB}	3,2254	m

Figure 183: model scale longitudinal view for hull 20.

Table 77: towing tank and virtual towing tank results for hull 20.

RUN	Carriage speed		$10^{-3} C_{FM} [-]$		R_{TM} [N]	
	V_M [m/s]	F_r [−]	I.T.T.C. 57	CFD	EFD	CFD
1	0,913	0,108	3,364	3,247	15,255	14,957
2	1,284	0,152	3,162	2,981	28,983	27,907
3	1,648	0,195	3,026	2,927	45,526	44,708
4	1,918	0,227	2,948	2,906	61,552	60,934
5	2,197	0,260	2,880	2,931	86,432	87,163
6	2,383	0,282	2,841	2,896	123,323	120,618

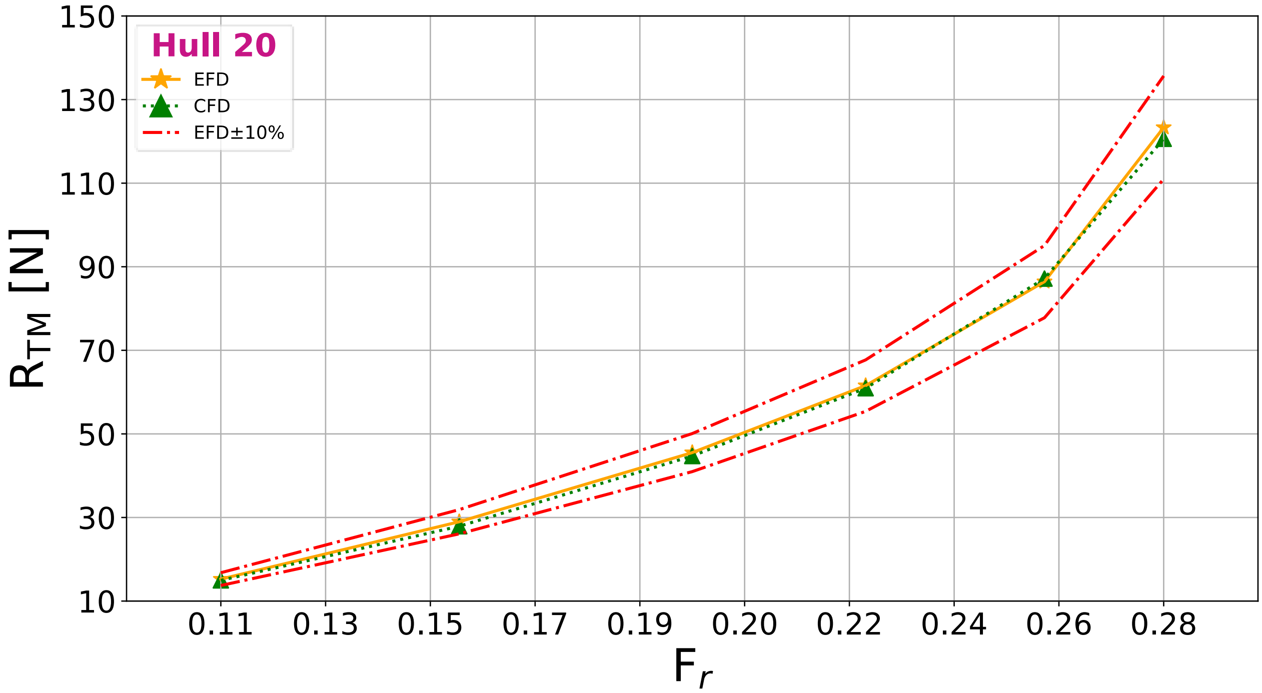

Figure 184: resistance curve, comparisons between EFD results and CFD calculations, varying speed range for the model hull 20.

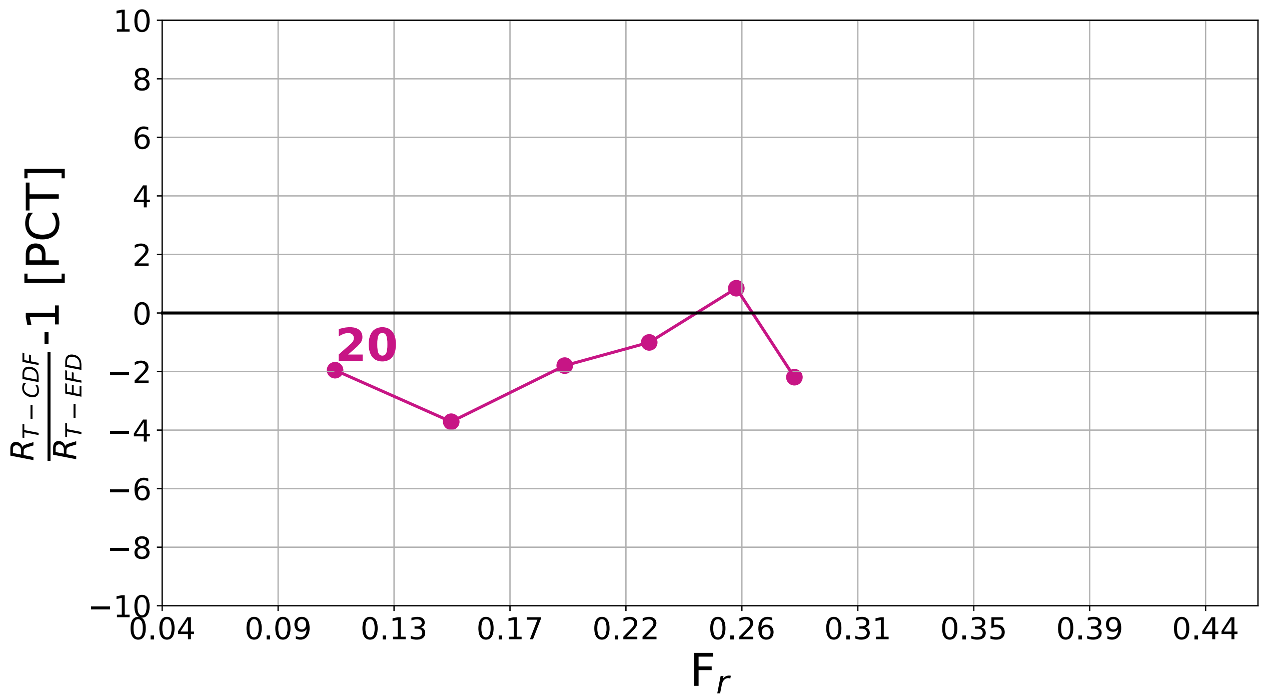

Figure 185: percentual difference between EFD results and CFD calculations, varying speed range for the model 20.

17. Hull 21 (DTC).

Table 78: main characteristics for hull 21.

Model characteristics	Symbol	Values	UoM
Length between perpendiculars	L_{PP}	5,9760	m
Length, overall submerged	L_{OS}	5,9760	m
Length of waterline	L_{WL}	5,9760	m
Maximum moulded Breadth at design WL	B_{WL}	0,8590	m
Draught at forward perpendicular	T_F	0,2440	m
Draught at midship	$T_M = (T_A + T_F)/2$	0,2440	m
Draught at aft perpendicular	T_A	0,2440	m
Displacement volume	∇	0,8270	m^3
Area of wetted surface	S	6,2430	m^2
Ratio L/B	L_{WL}/B_{WL}	6,9608	-
Ratio B/T	B_{WL}/T_M	3,5172	-
Block coefficient	$C_B = \nabla/LBT$	0,6608	-
Froude's length coefficient, or length-displacement ratio	$M^C = \nabla^{1/3}$	6,3654	-
Scale ratio	$\lambda = L_s/L_M$	59,4043	-
Area of water-plane	A_W	4,3415	m^2
Longitudinal centre of flotation	L_{CF}, X_{CF}	2,9288	m
Longitudinal centre of buoyancy	L_{CB}, X_{CB}	2,7100	m

Figure 186: model scale longitudinal view for hull 21.

Table 79: towing tank and virtual towing tank results for hull 21.

RUN	Carriage speed		$10^{-3}C_{FM}[-]$		R_{TM} [N]	
	V_M [m/s]	F_r [−]	I.T.T.C. 57	CFD	EFD	CFD
1	1,335	0,174	3,170	3,050	20,340	19,497
2	1,401	0,183	3,142	3,047	22,060	21,442
3	1,469	0,192	3,116	3,026	24,140	23,440
4	1,535	0,201	3,092	0,000	26,460	25,714
5	1,602	0,209	3,069	3,012	28,990	28,316
6	1,668	0,218	3,047	2,999	31,830	31,076

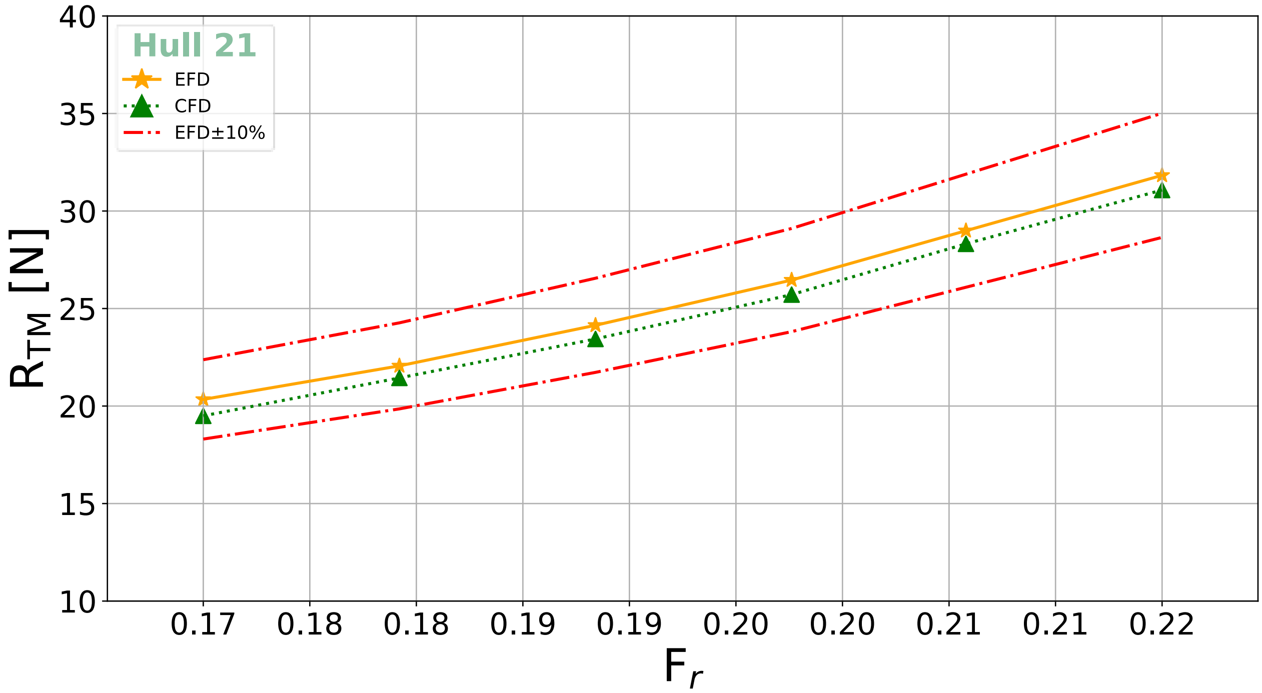

Figure 187: resistance curve, comparisons between EFD results and CFD calculations, varying speed range for the model hull 21.

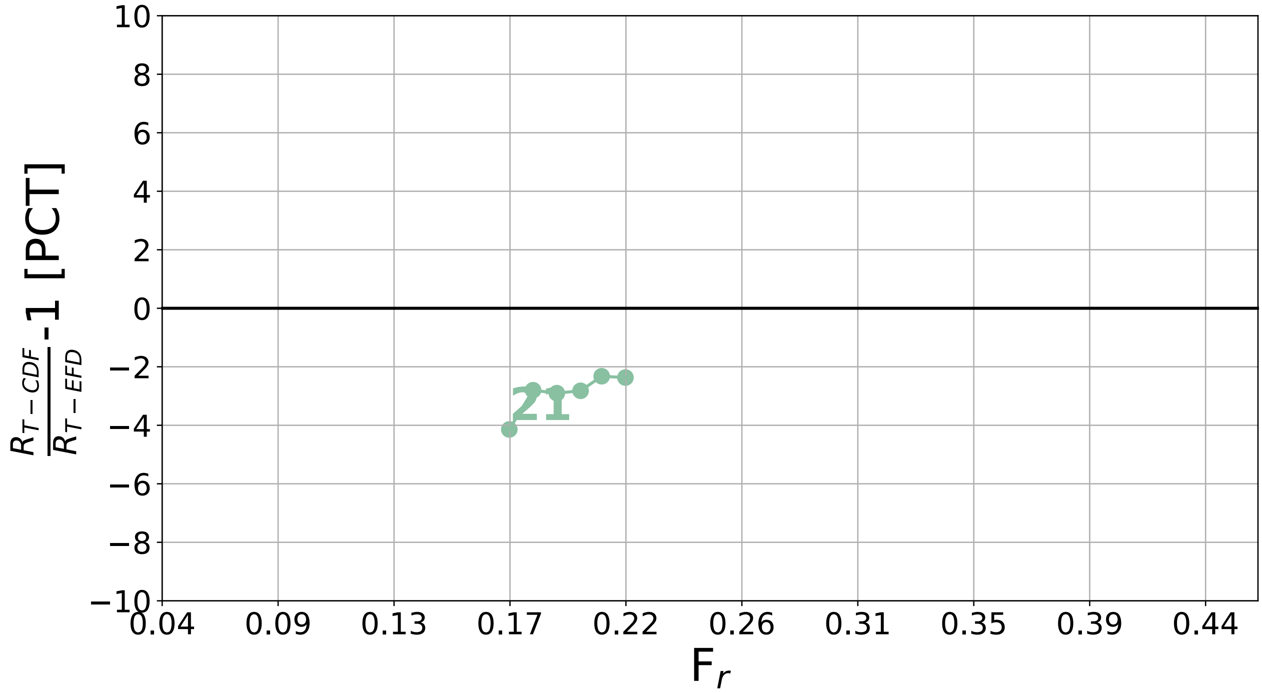

Figure 188: percentual difference between EFD results and CFD calculations, varying speed range for the model 21.

18. Hull 22 (KVLCC2 - INSEAN).

Table 80: main characteristics for hull 22.

Model characteristics	Symbol	Values	UoM
Length between perpendiculars	L_{PP}	7,0000	m
Length, overall submerged	L_{OS}	7,1203	m
Length of waterline	L_{WL}	7,0000	m
Maximum moulded Breadth at design WL	B_{WL}	1,2688	m
Draught at forward perpendicular	T_F	0,4550	m
Draught at midship	$T_M = (T_A + T_F)/2$	0,4550	m
Draught at aft perpendicular	T_A	0,4550	m
Displacement volume	∇	3,2724	m^3
Area of wetted surface	S	13,0128	m^2
Ratio L/B	L_{WL}/B_{WL}	5,5172	-
Ratio B/T	B_{WL}/T_M	2,7885	-
Block coefficient	$C_B = \nabla/LBT$	0,8098	-
Froude's length coefficient, or length-displacement ratio	$M^C = \nabla^{1/3}$	4,7149	-
Scale ratio	$\lambda = L_s/L_M$	45,7143	-
Area of water-plane	A_W	8,0090	m^2
Longitudinal centre of flotation	L_{CF}, X_{CF}	3,7433	m
Longitudinal centre of buoyancy	L_{CB}, X_{CB}	3,5020	m

Figure 189: model scale longitudinal view for hull 22.

Table 81: towing tank and virtual towing tank results for hull 22.

RUN	Carriage speed		$10^{-3} C_{FM} [-]$		R_{TM} [N]	
	V_M [m/s]	F_r [−]	I.T.T.C. 57	CFD	EFD	CFD
1	0,989	0,119	3,241	3,163	26,368	25,371
2	1,141	0,138	3,159	3,108	34,436	33,070
3	1,179	0,142	3,141	3,088	36,640	35,379
4	1,217	0,147	3,123	3,075	38,950	37,460
5	1,255	0,152	3,106	3,058	41,336	39,782

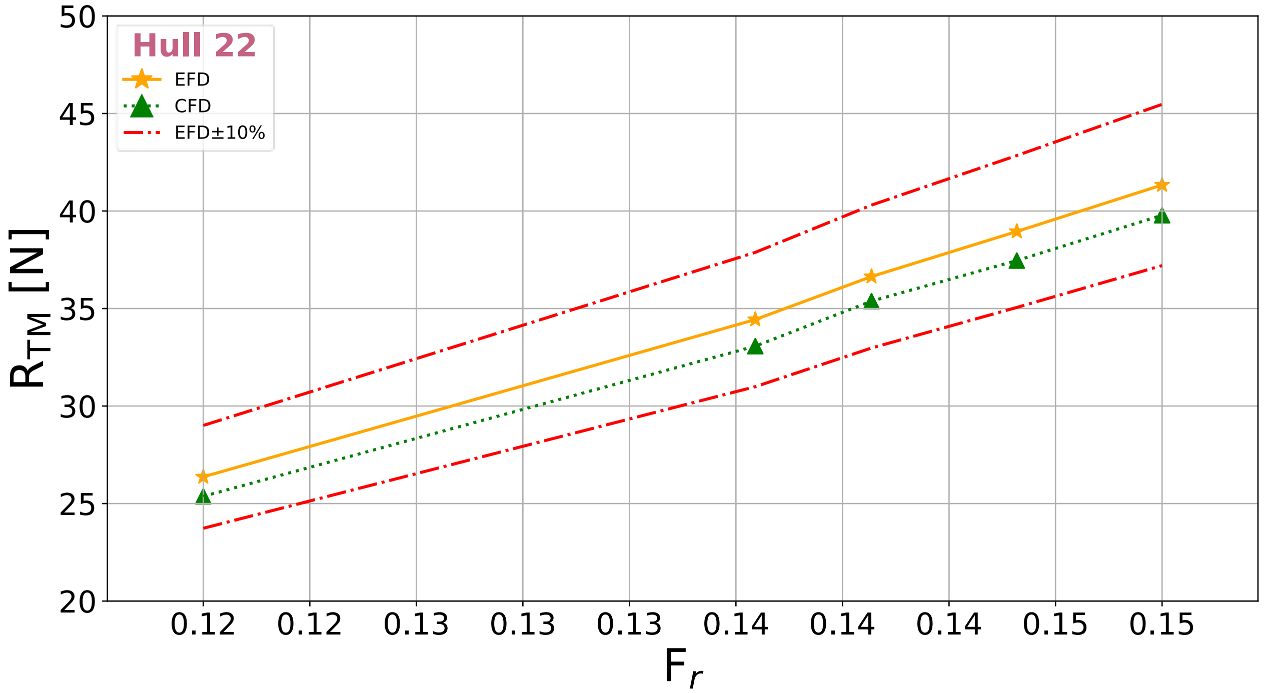

Figure 190: resistance curve, comparisons between EFD results and CFD calculations, varying speed range for the model hull 22.

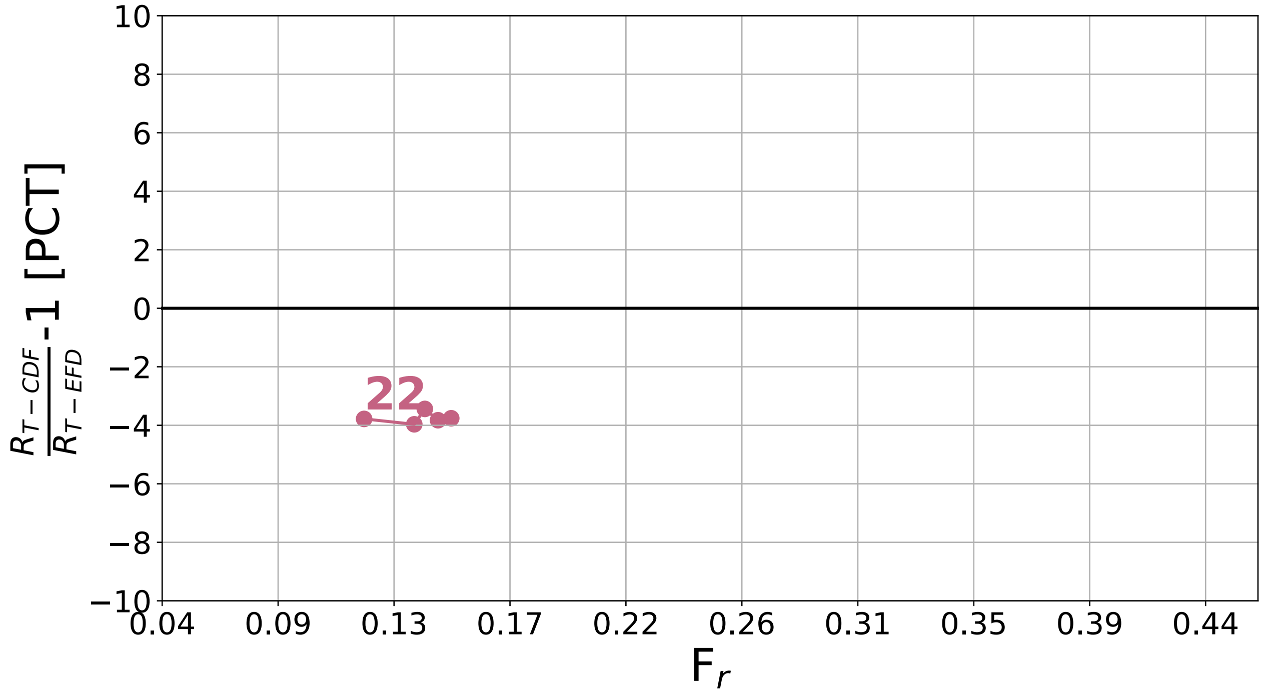

Figure 191: percentual difference between EFD results and CFD calculations, varying speed range for the model 22.

This page is intentionally left blank

Annex 2 - Mesh sensitivity analysis

The subsequent sections present the main features of the 72 simulations performed to get the uncertainty assessment for two test hulls: Hull_A and Hull_B, respectively. The simulations have been divided in 9 families clustered by the speed and the configuration, as described below:

- Hull_A, has been tested in free trim-sinkage configuration for 3 different speeds (F_r = 0.276, 0.314, 0.342);
- Hull_B, has been tested in free trim-sinkage configuration for 4 different speeds (F_r = 0.158, 0.222, 0.285, 0.348);
- Hull_B*, has been tested in free trim-sinkage configuration for 2 different speeds (F_r = 0.285, 0.348).

With the respect to the advance resistance, for each case a table reporting all the differences recorded is present along with a graph. Considering the graph, the hulls can be graphically identified through the color (Hull_A is always marked with a fuchsia color and the other in dark green) and by the condition for the test looking at the marker (a triangular shape for the free trim-sinkage configuration and a pentagonal one for the fix trim-sinkage). Each graph reports on x-axis the grid refinement factor $r_{(k,k+1)} = h_k/h_{k+1}$, where subscript "k" indicates a finer mesh compared with the "$k+1$" and on y-axis the differences among CFD and EFD for each simulation; moreover, an additional scaled axis is available to get the information about the number of cells (referred to half domain because of the symmetry condition) used to perform each simulation.

1. Hull_A-1.

Table 82: main characteristics for Hull_A-1.

RUN	Hull_ID	F_r [-]	Cells 10^6 [-]	$r_{(k,k+1)}$ [-]	ΔR_{T_M} [-]
1	Hull_A-1.1	0,276	0.735	1.76	2.40%
2	Hull_A-1.2	0.276	1.019	1.58	-1.50%
3	Hull_A-1.3	0.276	1.32	1.45	-1.21%
4	Hull_A-1.4	0.276	1.718	1.33	-1.71%
5	Hull_A-1.5	0.276	2.478	1.17	-2.20%
6	Hull_A-1.6	0.276	2.943	1.11	-1.18%
7	Hull_A-1.7	0.276	4.018	1.00	-1.79%
8	-	-	-	-	-
9	-	-	-	-	-
10	-	-	-	-	-
11	-	-	-	-	-
12	-	-	-	-	-
13	-	-	-	-	-

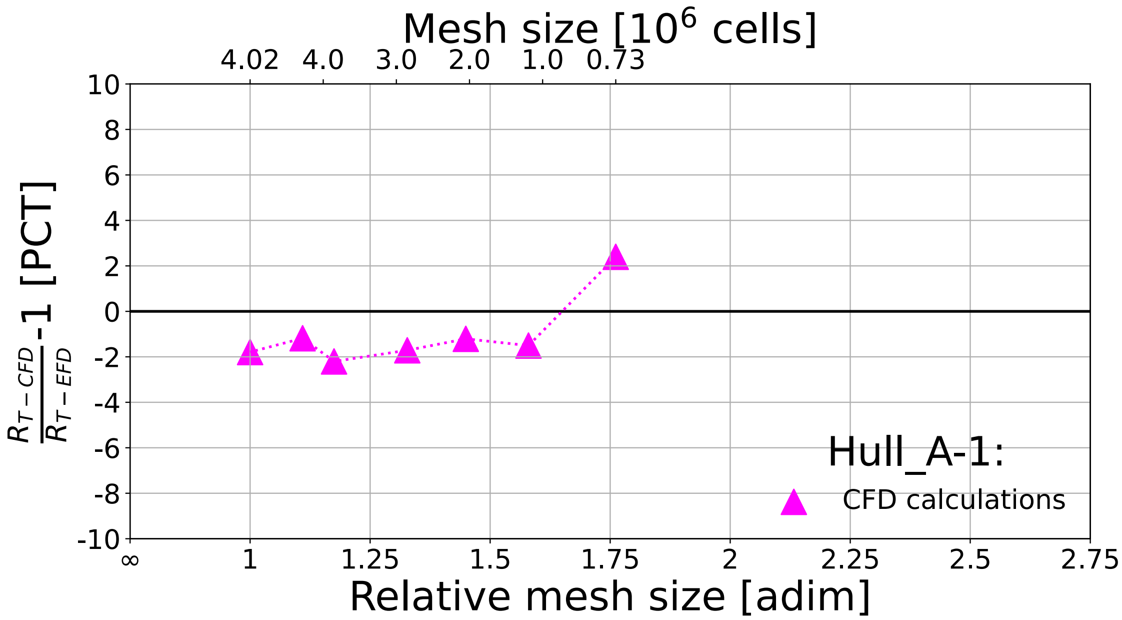

Figure 192: mesh depending analysis for Hull_A-1.

2. Hull_A-2.

Table 83: main characteristics for Hull_A-2.

RUN	Hull_ID	F_r [-]	Cells 10^6 [-]	$r_{(k,k+1)}$ [-]	ΔR_{T_M} [-]
1	Hull_A-2.1	0.314	0.735	1.59	3.35%
2	Hull_A-2.2	0.314	1.048	1.41	2.18%
3	Hull_A-2.3	0.314	1.321	1.31	-0.19%
4	Hull_A-2.4	0.314	1.717	1.20	-0.74%
5	Hull_A-2.5	0.314	2.34	1.08	-1.19%
6	Hull_A-2.6	0.314	2.956	1.00	-0.28%
7	-	-	-	-	-
8	-	-	-	-	-
9	-	-	-	-	-
10	-	-	-	-	-
11	-	-	-	-	-
12	-	-	-	-	-
13	-	-	-	-	-

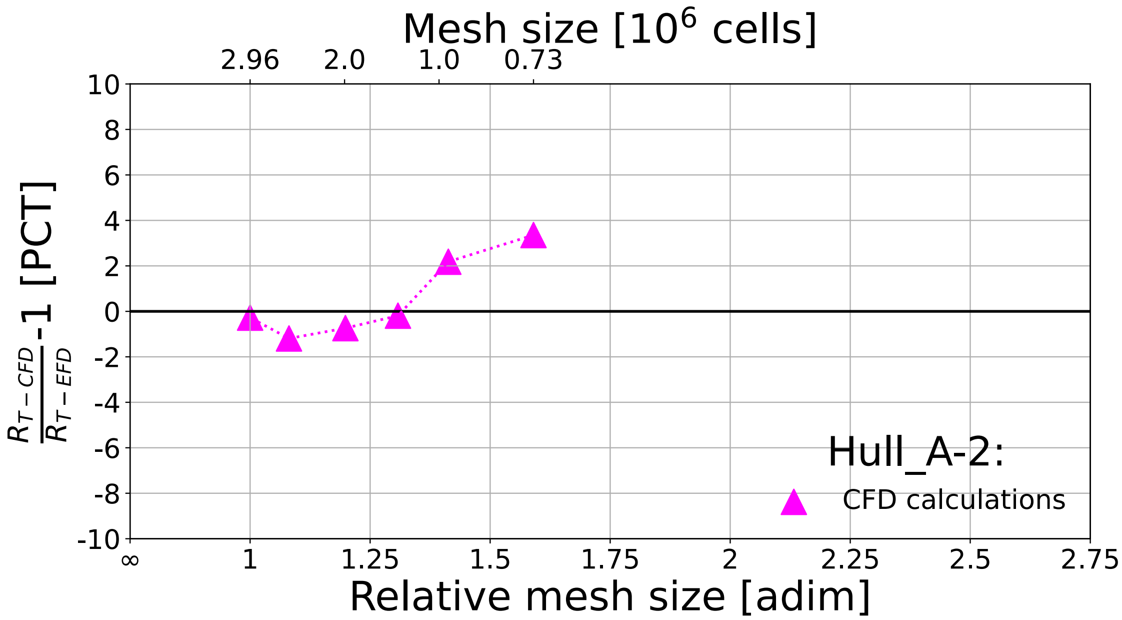

Figure 193: mesh depending analysis for Hull_A-2.

3. Hull_A-3.

Table 84: main characteristics for Hull_A-3.

RUN	Hull_ID	F_r [-]	Cells 10^6 [-]	$r_{(k,k+1)}$ [-]	ΔR_{T_M} [-]
1	Hull_A-3.1	0.342	0.743	1.77	6.19%
2	Hull_A-3.2	0.342	1.048	1.57	5.03%
3	Hull_A-3.3	0.342	1.356	1.45	5.19%
4	Hull_A-3.4	0.342	2.174	1.23	2.26%
5	Hull_A-3.5	0.342	2.492	1.18	2.20%
6	Hull_A-3.6	0.342	2.956	1.11	2.86%
7	Hull_A-3.7	0.342	4.092	1.00	3.00%
8	-	-	-	-	-
9	-	-	-	-	-
10	-	-	-	-	-
11	-	-	-	-	-
12	-	-	-	-	-
13	-	-	-	-	-

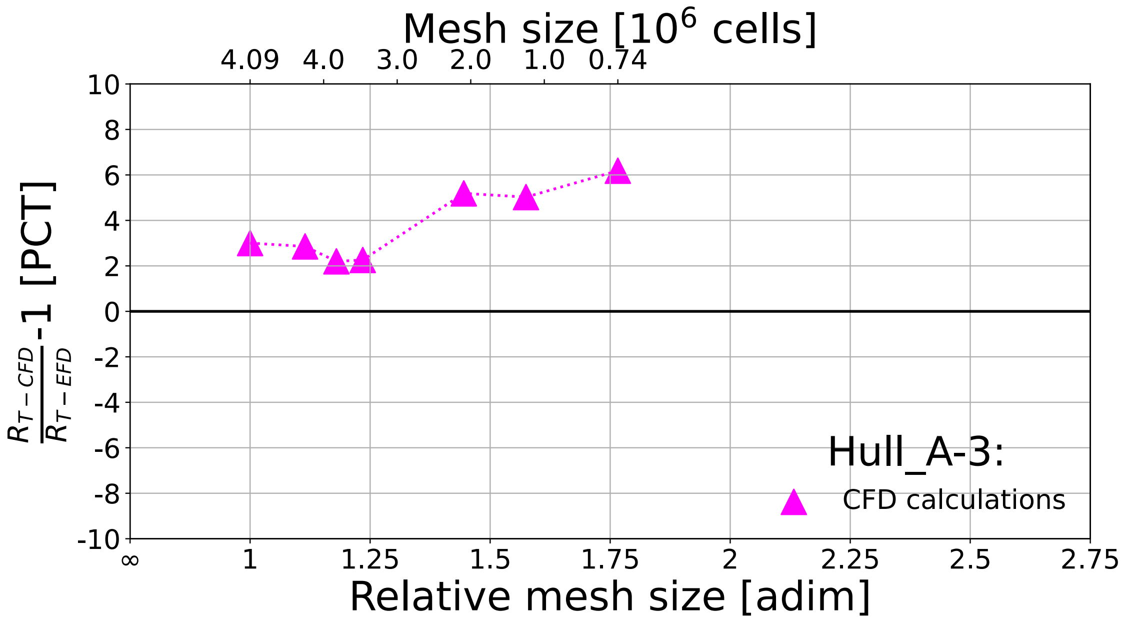

Figure 194: mesh depending analysis for Hull_A-3.

4. Hull_B-1.

Table 85: main characteristics for Hull_B-1.

RUN	Hull_ID	F_r [-]	Cells 10^6 [-]	$r_{(k,k+1)}$ [-]	ΔR_{T_M} [-]
1	Hull_B-1.1	0.158	0.941	1.46	-2.86%
2	Hull_B-1.2	0.158	1.389	1.28	-3.65%
3	Hull_B-1.3	0.158	1.619	1.22	-3.82%
4	Hull_B-1.4	0.158	1.939	1.15	-3.57%
5	Hull_B-1.5	0.158	2.238	1.09	-3.15%
6	Hull_B-1.6	0.158	2.39	1.07	-3.14%
7	Hull_B-1.7	0.158	2.93	1.00	-2.62%
8	-	-	-	-	-
9	-	-	-	-	-
10	-	-	-	-	-
11	-	-	-	-	-
12	-	-	-	-	-
13	-	-	-	-	-

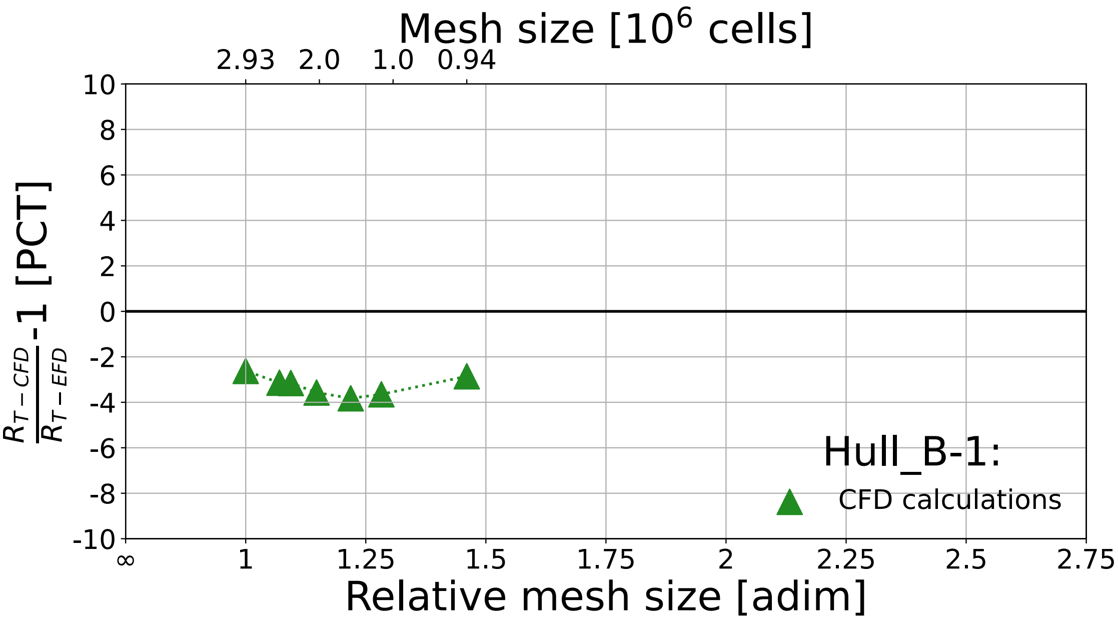

Figure 195: mesh depending analysis for Hull_B-1.

5. Hull_B-2.

Table 86: main characteristics for Hull_B-2.

RUN	Hull_ID	F_r [-]	Cells 10^6 [-]	$r_{(k,k+1)}$ [-]	ΔR_{T_M} [-]
1	Hull_B-2.1	0.222	0.709	1.79	3.64%
2	Hull_B-2.2	0.222	1.073	1.56	3.60%
3	Hull_B-2.3	0.222	1.404	1.43	2.24%
4	Hull_B-2.4	0.222	1.619	1.36	1.64%
5	Hull_B-2.5	0.222	1.939	1.28	1.35%
6	Hull_B-2.6	0.222	2.238	1.22	1.41%
7	Hull_B-2.7	0.222	2.391	1.20	1.61%
8	Hull_B-2.8	0.222	2.878	1.12	1.68%
9	Hull_B-2.9	0.222	4.089	1.00	1.29%
10	-	-	-	-	-
11	-	-	-	-	-
12	-	-	-	-	-
13	-	-	-	-	-

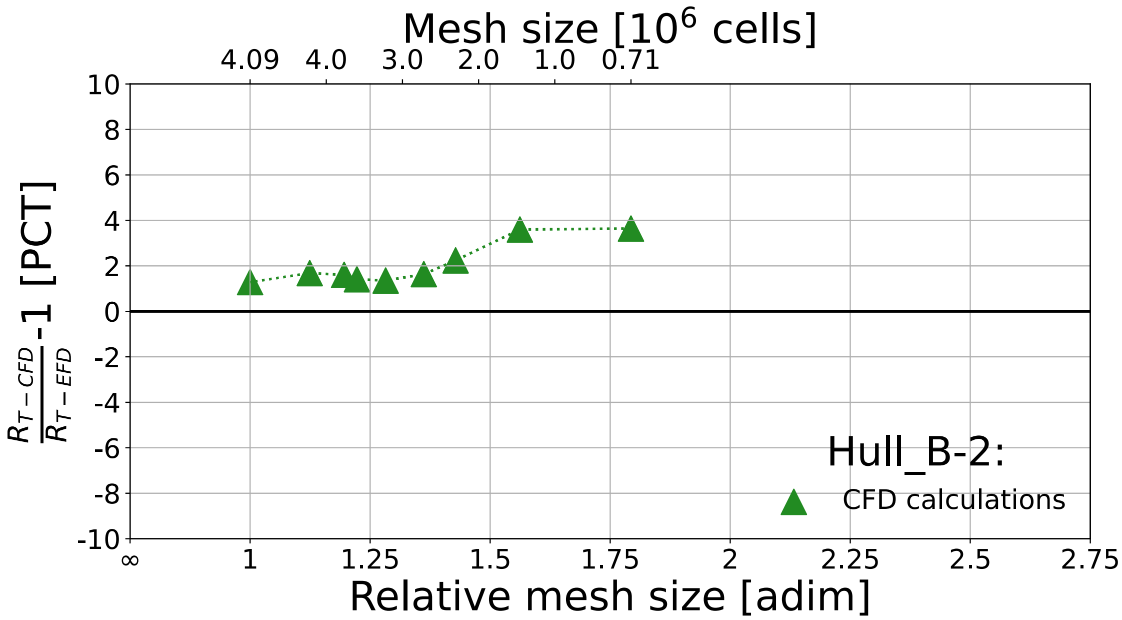

Figure 196: mesh depending analysis for Hull_B-2.

6. Hull_B-3.

Table 87: main characteristics for Hull_B-3.

RUN	Hull_ID	F_r [-]	Cells 10^6 [-]	$r_{(k,k+1)}$ [-]	ΔR_{T_M} [-]
1	Hull_B-3.1	0.285	0.965	1.74	4.57%
2	Hull_B-3.2	0.285	1.404	1.54	4.29%
3	Hull_B-3.3	0.285	1.636	1.46	3.29%
4	Hull_B-3.4	0.285	1.957	1.38	2.46%
5	Hull_B-3.5	0.285	2.257	1.31	2.47%
6	Hull_B-3.6	0.285	2.39	1.29	3.00%
7	Hull_B-3.7	0.285	2.878	1.21	3.89%
8	Hull_B-3.8	0.285	5.096	1.00	2.14%
9	-	-	-	-	-
10	-	-	-	-	-
11	-	-	-	-	-
12	-	-	-	-	-
13	-	-	-	-	-

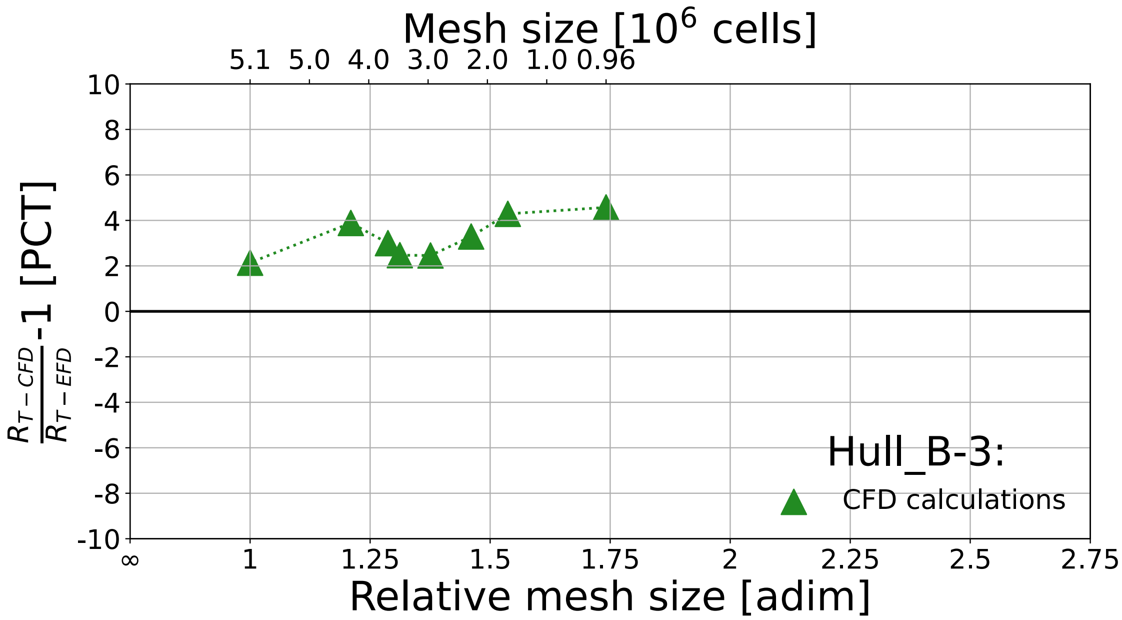

Figure 197: mesh depending analysis for Hull_B-3.

7. Hull_B-3*.

Table 88: main characteristics for Hull_B-3.*

RUN	Hull_ID	F_r [-]	Cells 10^6 [-]	$r_{(k,k+1)}$ [-]	ΔR_{T_M} [-]
1	Hull_B-3*.1	0.285	0.964	1.72	4.52%
2	Hull_B-3*.2	0.285	1.404	1.51	3.20%
3	Hull_B-3*.3	0.285	1.633	1.44	2.08%
4	Hull_B-3*.4	0.285	1.952	1.36	1.72%
5	Hull_B-3*.5	0.285	2.384	1.27	1.87%
6	Hull_B-3*.6	0.285	2.868	1.19	2.33%
7	Hull_B-3*.7	0.285	4.868	1.00	0.88%
8	-	-	-	-	-
9	-	-	-	-	-
10	-	-	-	-	-
11	-	-	-	-	-
12	-	-	-	-	-
13	-	-	-	-	-

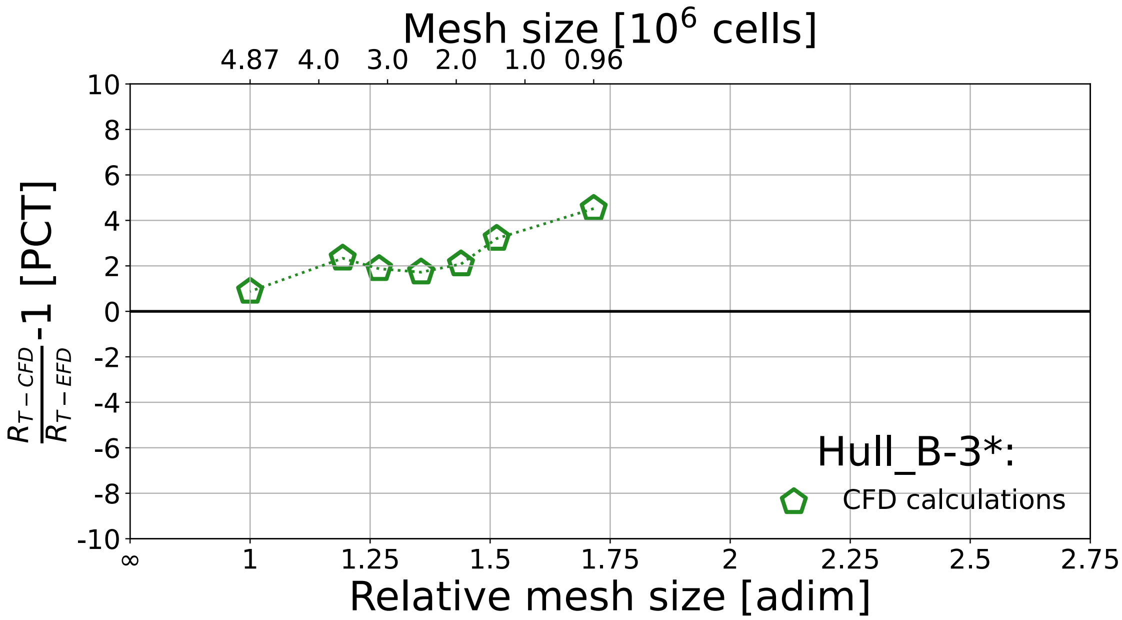

Figure 198: mesh depending analysis for Hull_B-3.*

8. Hull_B-4.

Table 89: main characteristics for Hull_B-4.

RUN	Hull_ID	F_r [-]	Cells 10^6 [-]	$r_{(k,k+1)}$ [-]	ΔR_{T_M} [-]
1	Hull_B-4.1	0.348	0.965	1.74	5.64%
2	Hull_B-4.2	0.348	1.419	1.53	5.01%
3	Hull_B-4.3	0.348	1.636	1.46	5.27%
4	Hull_B-4.4	0.348	1.957	1.38	4.02%
5	Hull_B-4.5	0.348	2.257	1.31	3.80%
6	Hull_B-4.6	0.348	2.411	1.28	3.13%
7	Hull_B-4.7	0.348	2.952	1.20	3.21%
8	Hull_B-4.8	0.348	5.096	1.00	4.59%
9	-	-	-	-	-
10	-	-	-	-	-
11	-	-	-	-	-
12	-	-	-	-	-
13	-	-	-	-	-

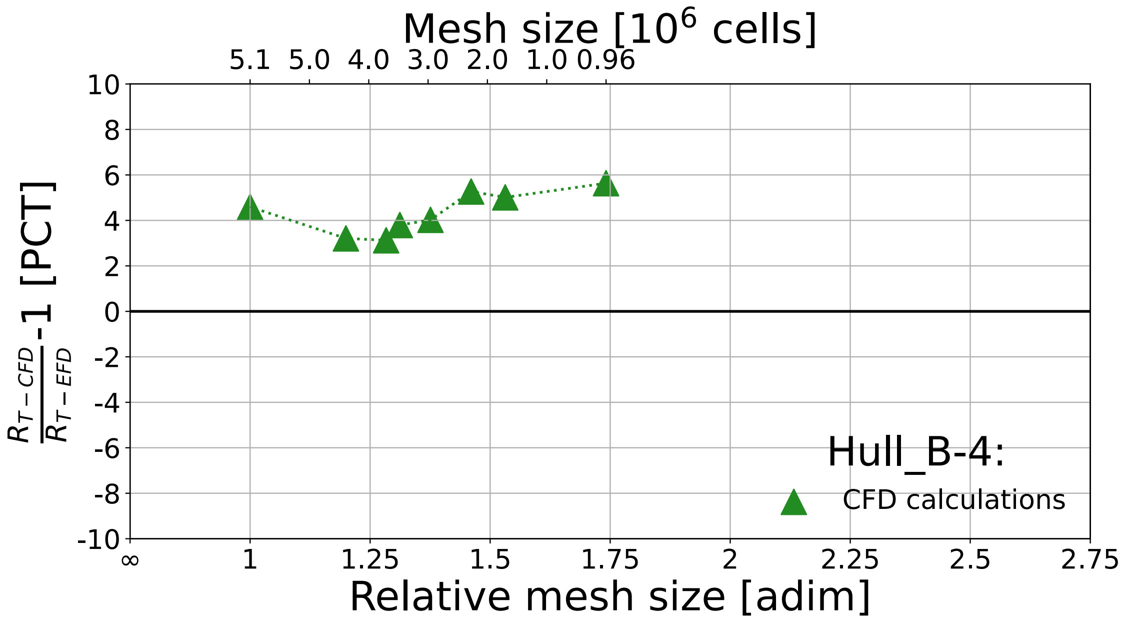

Figure 199: mesh depending analysis for Hull_B-4.

9. Hull_B-4*.

Table 90: main characteristics for Hull_B-4.*

RUN	Hull_ID	F_r [-]	Cells 10^6 [-]	$r_{(k,k+1)}$ [-]	ΔR_{T_M} [-]
1	Hull_B-4*.1	0.348	0.611	2.52	4.80%
2	Hull_B-4*.2	0.348	0.747	2.35	3.80%
3	Hull_B-4*.3	0.348	0.787	2.31	3.61%
4	Hull_B-4*.4	0.348	0.963	2.16	4.25%
5	Hull_B-4*.5	0.348	1.091	2.07	4.16%
6	Hull_B-4*.6	0.348	1.42	1.90	4.00%
7	Hull_B-4*.7	0.348	1.633	1.81	3.00%
8	Hull_B-4*.8	0.348	1.951	1.71	2.54%
9	Hull_B-4*.9	0.348	2.403	1.59	1.67%
10	Hull_B-4*.10	0.348	2.94	1.49	2.01%
11	Hull_B-4*.11	0.348	5.064	1.24	1.68%
12	Hull_B-4*.12	0.348	5.894	1.18	1.46%
13	Hull_B-4*.13	0.348	9.725	1.00	2.11%

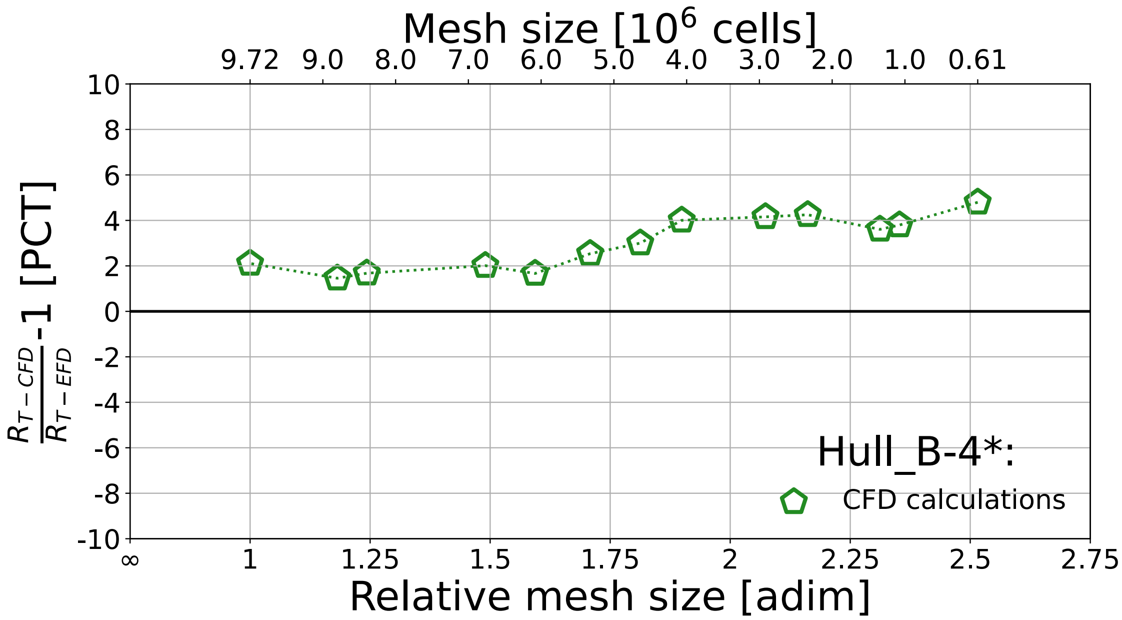

Figure 200: mesh depending analysis for Hull_B-4.*

Index of Figures

Index of Tables

This page is intentionally left blank

List of acronyms

AEW	Admiralty Experiment Works
AH	All Hulls
ASME	American Society of Mechanical Engineers
A_W	Area of water-plane
S	Area of wetted surface
A_T	Area, Transversal cross section
A_{V_S}	Area, Transversal cross section above the water plane
AHR	Average Hull Roughness
C_B	Block coefficient
BL	Boundary layer
CDS	Central Differencing Scheme
J	Coefficient, advance
ARC	Coefficient, Ahead Resistance
C_{AA_S}	Coefficient, Air resistance
C_{APP_M}, C_{APP_S}	Coefficient, appendages resistance (model, ship)
η_B	Coefficient, efficiency behind hull
η_H	Coefficient, hull efficiency
ΔC_F	Coefficient, hull roughness allowance

C_A	Coefficient, incremental resistance for model ship correlation
η_O	Coefficient, propeller open-water efficiency
η_D	Coefficient, propulsive efficiency
η_R	Coefficient, Relative rotation efficiency
C_R	Coefficient, Residuary resistance
C_{F_M}, C_{F_S}	Coefficient, Resistance Frictional (model, ship)
k_S	Coefficient, roughness
K_T	Coefficient, thrust
t	Coefficient, Thrust deduction
$\mathrm{K}_{T,\mathrm{OW}}$	Coefficient, thrust experienced through the open-water test
$\mathrm{K_Q}$	Coefficient, torque
$\mathrm{K_{Q,OW}}$	Coefficient, torque experienced through the open-water test
C_{T_M}, C_{T_S}	Coefficient, Total resistance (model, ship)
w	Coefficient, Wake fraction
CIPM	Comité International des Poids et Mesures
COMPDB	Comparisonal DataBase
CFD	Computational Fluid Dynamics
CGPM	Conférence Générale des Poids et Mesures
KCS	Container Ship from KRISO
R	Convergence ratio parameter
C_O	Courant number
C_CURV	Curved surface, Original
C_CURV_STL	Curved surface, STL (approx.)
Δ_S	Data range parameter
DTMB	David Taylor Model Basin
DoF	Degree of Freedom
$(\overline{\Delta R}_{T_M})$	Delta Resistance, mean value

$\lvert \Delta R_{T_M} \rvert_i$	Delta Resistance, module for the mean value
ρ	Density
∇	Displacement volume
y^+	Distance, non-dimensional from the wall
T_A	Draught at aft perpendicular
T_F	Draught at forward perpendicular
T_M	Draught at midship
ESD	Energy Saving Device
δ_{S_C}	Error, correct simulation
ε_{SN}	Error, estimation for the numerical part
$\delta^*_{RE_k}$	Error, extrapolated value based on RE
δ_{SPD}	Error, from use of previous data
δ_G	Error, grid size
δ_I	Error, iteration number
δ_{SM}	Error, modelling
δ_{SMA}	Error, modelling assumption
δ_{SN}	Error, numerical
δ_P	Error, other parameters
δ^*_{SN}	Error, sign with the magnitude for the numerical simulation error
δ_S	Error, simulation
δ_T	Error, time step
EFD	Experimental Fluid Dynamics
F_S	Factor of safety approach
FDM	Finite Difference Method
FEM	Finite Element Method
FVM	Finite Volume Method
1+k	Form factor

FSTP	Four STeps Procedure
F_r	Froude number
M^C	Froude's length coefficient, or length-displacement ratio
g	Gravity acceleration
GCI	Grid Convergence Index
GUM	Guide to the expression of uncertainty in measurement
HPC	High-Performance Computing
RI1	Industrial Revolution I, first
RI2	Industrial Revolution II, second
RI3	Industrial Revolution III, third
RI4	Industrial Revolution IV, fourth
RI5	Industrial Revolution V, fifth
ICT	Information Communication Technology
IGES	Initial Graphics Exchange Specification
INM	Institute of Marine Engineering (Istituto di Ingegneria del Mare)
IBM	International Business Machines Corporation
ISO	International Organization for Standardization
ITTC	International Towing Tank Conference
JBC	Japan Bulk Carrier
KVLCC2	Korean Very Large Crude Carrier 2
LRS	Least Squares Root
L_{PP}	Length between perpendiculars
L_{WL}	Length of waterline
L_{OS}	Length, overall submerged
LSM	Level Set Method
LTS	Local Time Step
L_{CB}, X_{CB}	Longitudinal centre of buoyancy

L_{CF}, X_{CF}	Longitudinal centre of flotation
$\overline{BM}_L$	Longitudinal metacentre above centre of buoyancy
M_a	Mach number
MAC	MArker and Cell method
B_{WL}	Maximum moulded Breadth at design WL
D	Measured data value
MAD	Median Absolute Deviation about the median
PIMPLE	Merged PISO-SIMPLE algorithm
MPTO	Multiple Participants To One
n	Number of combinations
N	Number, total of cells
ASUP	Numerical set-up, Alpha Set-Up defined as STD
BSUP	Numerical set-up, Bravo Set-Up
CSUP	Numerical set-up, Charlie Set-Up
DSUP	Numerical set-up, Delta Set-Up
ONR	Office of Naval Research
ONRT	Office of Naval Research model Tumblehome
p	Order of accuracy, apparent
p_{th}	Order of accuracy, theoretical
r_{xy}	Pearson's correlations factor
P_{E_S}	Power, effective (ship)
P	Pressure
PISO	Pressure-Implicit with Splitting of Operators
P_ORIG	Prismatic surface, Original
P_ORIG_STL	Prismatic surface, STL
PDF	Probability Density Function
C_T	Propeller load coefficient

QUICK	Quadratic Upstream Interpolation for Convective Kinetics
h_i	Refinement factor
r_K	Refinement ratio parameter
R_F	Resistance, Frictional component
R_{F_0}	Resistance, Frictional component for a flat wetted surface
R_P	Resistance, Pressure component
R_R	Resistance, Residuary component
$R_{TM_{EFD}}$	Resistance, Total component for the Model assessed by EFD test
R_V	Resistance, Viscous component
R_{VP}	Resistance, Viscous Pressure
R_{WB}	Resistance, Wavebreaking Pressure
R_W	Resistance, Wavemaking
R_{WP}	Resistance, Wavemaking wave Pattern
RANS	Reynolds Averaged Navier-Stokes
R_e	Reynolds' number
RE	Richardson Extrapolation
λ	Scale ratio
RT-NS	Self-propulsion Test, Resistance Test – No Symmetry
RT-S	Self-propulsion Test, Resistance Test – Symmetry
SP-NTNS	Self-propulsion Test, Self Propulsion - No Torque No Symmetry
SP-NTS	Self-propulsion Test, Self Propulsion - No Torque Symmetry
SP-TNS	Self-propulsion Test, Self Propulsion - Torque No Symmetry
SIMPLE	Semi-Implicit Method for Pressure-Linked Equations
SLIC	Simple Line Interface Method
SPTM	Single Participant To Multiple
SPTO	Single Participant To One
F_D, SFC	Skin Friction Correction

σ	Standard deviation
STD	Standard numerical set-up
STL	STereoLithography
S	Surface, wetted
S_{WBK}	Surface, wetted part of appendages
TVD	Total Variation Diminishing
UA	Uncertainty Assessment
UA	Uncertainty Assessment
U_E	Uncertainty, comparison error
U_{S_CN}	Uncertainty, correct simulation
U_D	Uncertainty, estimated data
U_{SPD}	Uncertainty, from use of previous data
U_G	Uncertainty, grid size
U_I	Uncertainty, iteration number
U_{SMA}	Uncertainty, modelling assumption
U_P	Uncertainty, other parameters
U_S	Uncertainty, simulation
U_T	Uncertainty, time step
U_V	Uncertainty, validation
UDS	Upwind Differencing Scheme
E	Value, comparison error
S_C	Value, correct simulation
S_{ext}^{21}	Value, extrapolated value for an infinite number of cells
M	Value, model
S	Value, simulation result
$\hat{S}_{UP}$, $\hat{S}_{LOW}$	Value, simulation result (higher, lower results)
$\hat{S}_i$	Value, simulation result for the i-th grid

T	Value, Truth
σ^2	Variance
	Velocity, increase
u^+	Velocity, non-dimensional in BL
V_D	Velocity, propeller disk
V&V	Verification and Validation
VVUA	Verification, Validation, and Uncertainty Assessment
VD_CFD	Virtual Disk, CFD
VD_MAT	Virtual Disk, MAThematical
υ	Viscosity, kinematic
VoF	Volume Of Fluid
1G1980	Workshop, Gothenburg 1980
2G1990	Workshop, Gothenburg 1990
4G2000	Workshop, Gothenburg 2000
6G2010	Workshop, Gothenburg 2010
8V2024	Workshop, Lucy Ashton blind full-scale CFD 2024
3T1994	Workshop, Tokyo 1994
5T2005	Workshop, Tokyo 2005
7T2015	Workshop, Tokyo 2015
9W2025	Workshop, Wageningen 2010

Acknowledgements

"I treni non camminano con la Divina Commedia"

(Pino Costa)

Un dottorato di ricerca contempla al suo interno esclusivamente accezioni massime afferenti ai seguenti aspetti: impegno, dedizione e sacrifici. Mi sia concesso di poter sfruttare il parallelo con una esperienza personale per formulare questi miei ringraziamenti finali. A similitudine di una competizione di canottaggio olimpico nella specialità del singolo, solo affrontando il lungo percorso formativo con modalità agonistica, è possibile arrivare all'ambito traguardo finale rappresentato dalla *Final Defence,* certi di avere profuso il massimo impegno senza recriminarsi possibili negligenze.

Se è vero che la mentalità agonistica possa pervadere uno spirito e non distaccarsi mai da esso, come un vaccino contro l'astenia, sono conscio di aver affrontato questo percorso profondendo un impegno massimale, spesso andando nella regione fisica del sovraccarico e troppo spesso non rispettando i "cicli di scarico" canonici. In questo lasso temporale e nell'ottica di centrare la prestazione, il *team* che mi ha affiancato è sicuramente un aspetto non trascurabile. Pertanto, sono onorato di poter "spendere" qualche riga al fine di citare tutti i membri del *team* che mi ha supportato (e talvolta sopportato) in questo lungo e stimolante percorso, con l'auspicio di non dimenticarne nessuno. In primo luogo ringrazio mia moglie per la Sua giornaliera complicità; senza il Tuo continuo supporto non avrei avuto abbastanza Joule da impiegare in questo ambizioso percorso. Ringrazio i miei figli, non solo per i preziosi sorrisi che mi hanno sempre regalato prima d'iniziare le lunghe notti in compagnia di "*Peter*", ma anche per l'affetto e le soddisfazioni che quotidianamente continuano a darmi. Soddisfazioni che aumentano in me la convinzione di fare sempre del mio meglio per essere il più cristallino possibile ed addivenire a rappresentare un punto di riferimento per loro (auspicabilmente positivo). Ringrazio i miei genitori, mio fratello, mia cugina, mia nonna e mio zio per avere creduto ancora una volta in me. Spiace dover inserire una nota malinconica, ma mi ritengo onorato di poter ricordare anche tutte le persone che mi hanno guidato in varie fasi della mia vita e che ora continuano a farlo sotto una forma che dal punto di vista della fisica classica una spiegazione non è ancora stata trovata. In particolare il mio pensiero di commiato va a miei nonni ed alla zia. Non vanno dimenticati anche gli amici, quelli con la "A" maiuscola che hanno sfruttato tutta la paletta colori per dipingere i pochi momenti in cui mi sono concesso il lusso tralasciar le "sudate carte".

Non posso non citare il mio *tutor* universitario; senza il Suo prezioso contributo non sarei mai riuscito a concludere il percorso e riconosco in un lui sia una professionalità sia una dedizione che difficilmente ho riscontrato in altre persone. Ricorderò con piacere e vivido apprezzamento le nostre conversazioni nei momenti in cui gli "uffici" sono solitamente con le luci spente.

Ho anche il privilegio di poter ringraziare un Professore in particolare, sia per la generosa condivisone del Suo sapere che per il costante supporto professionale, puntelli fondamentali per addivenire a questo risultato.

Per ultimo, ma non in ordine di priorità, ringrazio la Marina Militare per avermi concesso l'opportunità di compiere il più alto tra i possibili percorsi formativi del mondo Accademico. In particolare ringrazio tutti i Comandanti, colleghi ed Amici che a partire dalle fasi di selezione del dottorato nel 2022 mi hanno accompagnato e guidato fino ad oggi; sono certo che i diretti interessati colgano il mio ringraziamento anche se i nomi non sono stati inseriti.